# Rubber Structures in Oil and Gas Equipment

Jie Zhang
Chuanjun Han

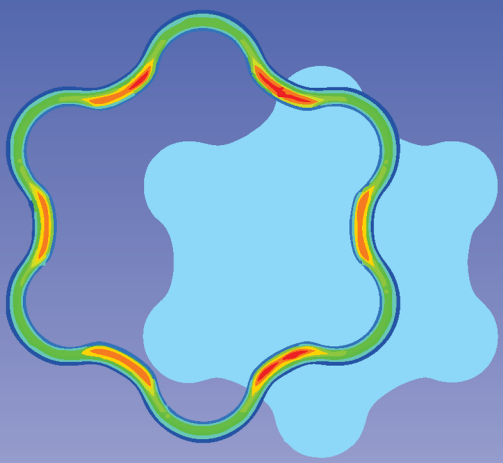

CRC Press
Taylor & Francis Group

A SCIENCE PUBLISHERS BOOK

# Rubber Structures in Oil and Gas Equipment

**Jie Zhang**
Southwest Petroleum University
Chengdu, Sichuan
China

**Chuanjun Han**
Southwest Petroleum University
Chengdu, Sichuan
China

CRC Press
Taylor & Francis Group
Boca Raton London New York

CRC Press is an imprint of the
Taylor & Francis Group, an **informa** business
A SCIENCE PUBLISHERS BOOK

*Cover credit*: Cover illustration reproduced by kind courtesy of the authors.

First edition published 2022
by CRC Press
6000 Broken Sound Parkway NW, Suite 300, Boca Raton, FL 33487-2742

and by CRC Press
2 Park Square, Milton Park, Abingdon, Oxon, OX14 4RN

© 2022 Taylor & Francis Group, LLC

*CRC Press is an imprint of Taylor & Francis Group, LLC*

Reasonable efforts have been made to publish reliable data and information, but the author and publisher cannot assume responsibility for the validity of all materials or the consequences of their use. The authors and publishers have attempted to trace the copyright holders of all material reproduced in this publication and apologize to copyright holders if permission to publish in this form has not been obtained. If any copyright material has not been acknowledged please write and let us know so we may rectify in any future reprint.

Except as permitted under U.S. Copyright Law, no part of this book may be reprinted, reproduced, transmitted, or utilized in any form by any electronic, mechanical, or other means, now known or hereafter invented, including photocopying, microfilming, and recording, or in any information storage or retrieval system, without written permission from the publishers.

For permission to photocopy or use material electronically from this work, access www.copyright.com or contact the Copyright Clearance Center, Inc. (CCC), 222 Rosewood Drive, Danvers, MA 01923, 978-750-8400. For works that are not available on CCC please contact mpkbookspermissions@tandf.co.uk

*Trademark notice*: Product or corporate names may be trademarks or registered trademarks and are used only for identification and explanation without intent to infringe.

*Library of Congress Cataloging-in-Publication Data*

```
Names: Zhang, Jie, 1987- author. | Han, Chuanjun, 1978- author.
Title: Rubber structures in oil and gas equipment / Jie Zhang, School of
   Mechatronic Engineering, Southwest Petroleum University, Chengdu,
   Sichuan, China, Chuanjun Han, Southwest Petroleum University, Chengdu,
   Sichuan, China.
Description: First edition. | Boca Raton : CRC Press, Taylor & Francis
   Group, 2022. | Includes bibliographical references and index.
Identifiers: LCCN 2021047226 | ISBN 9780367897239 (hardcover)
Subjects: LCSH: Petroleum industry and trade--Equipment and supplies. |
   Petroleum industry and trade--Materials. | Gas industry--Equipment and
   supplies. | Gas industry--Materials. | Sealing (Technology)--Materials.
   | Sealing compounds. | Rubber.
Classification: LCC TN871.5 .Z485 2022 | DDC 622/.3382--dc23/eng/20211103
LC record available at https://lccn.loc.gov/2021047226
```

ISBN: 978-0-367-89723-9 (hbk)
ISBN: 978-1-032-27879-7 (pbk)
ISBN: 978-1-003-02073-8 (ebk)

DOI: 10.1201/9781003020738

Typeset in Times New Roman
by Radiant Productions

# Preface

Oil and gas industry is an important part of energy structure. They are a strategic industry for the development of any country. Oil and gas equipment is very important to establish a leading oil and gas industry system. Good sealing environment is very important for exploration equipment, drilling and production equipment, storage and transportation equipment. The damage of sealing system will lead to equipment failure, high-pressure medium leakage, and then blowout and other disastrous consequences.

Rubber products are widely used in all aspects of oil and gas drilling and production and play an important role in oil and gas development. The performance of rubber products determines the safe and efficient development of oil and gas. In this book, rubber experiment and the constitutive model have been introduced. Rubber sealing ring, metal-rubber sealing structure, stator rubber of PDM, wellhead BOP and downhole rubber packer have been investigated. The mechanical properties and sealing properties of rubber structure in different working environments were studied. These contents can provide a basis for the design, manufacture and maintenance of rubber structures.

In the process of writing this book, Master Wenjie Jiang, Master Pai Zhu, Master Ruichuan Wang and Dr. Hu Yang paid great efforts to it. Dr. Yang Liu, Dr. Jipeng Zheng, Master Xuyun Ren and Master Fei Chen gave great help to rubber tests. We thank all references and publisher.

Jie Zhang

Taylor & Francis
Taylor & Francis Group
http://taylorandfrancis.com

# Contents

# 1
# Background

## 1.1 Introduction

Rubber is a highly elastic polymer material with reversible deformation, which has the characteristics of good elasticity, insulation, and impermeability to water and air. Under normal atmospheric temperature, it can be deformed by a small external force. When the external force is relieved, rubber can quickly return to its original state, and with excellent elasticity, flexibility and energy accumulation.

Rubber can be divided into natural rubber and synthetic rubber (Figure 1-1). Natural rubber is formed by coagulation, washing, molding, and drying of the sap collected directly from rubber trees. However, with the development of science and technology, natural rubber gradually cannot meet the complex requirements of civilization. Humans have begun to seek rubber with more superior performance. Thus, synthetic rubbers synthesized from various monomer materials have begun to be developed.

Synthetic rubber can be divided into general rubber and special rubber according to its use. The general rubber meets general needs, and includes styrene butadiene rubber, butadiene rubber, butyl rubber, etc. The special rubber can meet specific conditions, such as nitrile rubber, silicone rubber, fluorine rubber, etc.

(a) Natural rubber (b) Synthetic rubber

**Fig. 1-1.** Different types of rubber.

## 1.2 Rubber used in the field of oil and gas equipment

Oil and natural gas are basic energy sources and the main pillars of national economic development. Rubber products are widely used in all aspects of oil and

gas drilling and production, and play an important role in oil and gas development. The performance of rubber products determines whether oil and gas exploration can be carried out safely and efficiently. During the oil and gas development process, the service environment of the equipment is even worse. The harsh environmental conditions such as downhole high temperature, high pressure, and acidity have a great impact on the life of rubber products.

### *1.2.1 Rubber sealing ring*

The rubber ring is a kind of squeeze type sealing ring, which relies on its elastic deformation to obtain the sealing effect, by preventing the fluid leakage. It is annular and composed of one or several parts. It's widely used in surface equipment and downhole tools of oil and gas exploitation, as shown in Figure 1-2.

O-ring is named for its circular cross-section. The O-ring has the advantages of a simple structure and reliable sealing performance. It is widely used in various sealing structures and it is one of the most common seals used in static seals, reciprocating seals and rotary seals [1].

The O-ring can be easily twisted and worn down during installation, which reduces the cross-section of the ring. In a reciprocating dynamic seal, the O-ring is easy to twist and turn over. When the friction of the ring is uneven in the circumferential direction, the distortion is more serious. The service life of seal ring is greatly shortened due to the distortion [2, 3].

There are many seal rings with different cross-section shapes are widely used apart from the O-ring [4]. For example, the X-ring has the advantages of not rolling in the reciprocating motion, a small radial compression ratio, a lubricating cavity, limited friction resistance, and good pressure distribution on the cross section; however, it is prone to fatigue failure. The D-ring and the rectangular base can ensure that the sealing ring is properly installed, and reduce the distortion and damage of the sealing ring during the installation process [2]. In the reciprocating seal, the possibility of distortion can be reduced, and its semicircular cross-section has the advantage of self-sealing. Rectangular sealing rings are usually used for static seals. In dynamic seals, rectangular seals release heat slowly, which leads to a deterioration in the sealing performance [5].

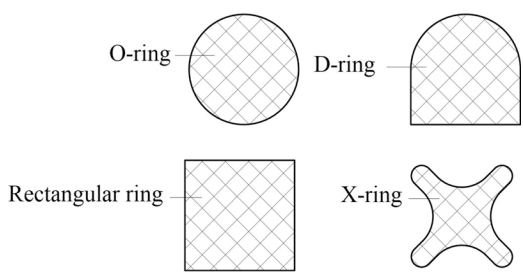


**Fig. 1-2.** A structural diagram of different types of sealing rings.

### *1.2.2 Metal-rubber sealing structure in roller cone bit*

A cone bit is usually used to break hard formations. It is used in the creation of deep wells, ultra-deep wells and geothermal wells, which require a higher performance and a longer life [6]. Bearing is one of the core structures of a cone bit, and bearing service life affects the service life and reliability of the cone bit [7]. The metal sealing structure in the bit can prevent the bottom hole drilling fluid from entering into the bearing, ensure the stable working environment of the bearing, and prolong its service life [8].

There are mainly two kinds of metal seals: single metal seal and double metal seal.

A single metal seal is composed of moving ring, static ring, O-ring, and rubber support ring. Its structure is shown in Figure 1-3. The sealing principle is that the O-ring respectively contacts with the journal and the static ring to form a static seal. Under the action of O-ring, the dynamic ring and the static ring always keep close contact, and a layer of oil film is formed between the contact surface of the dynamic ring and the static ring to realize the dynamic seal of the cone bit [9].

A bimetal seal is composed of static rubber ring, dynamic rubber ring, dynamic ring and static ring. The static rubber ring is in contact with the static ring and the bearing shaft, respectively. The moving rubber ring is in contact with the moving ring and the inner hole of the cone bit, respectively. The moving ring and the inner ring are closely bonded under the action of the two sealing rings. The moving ring

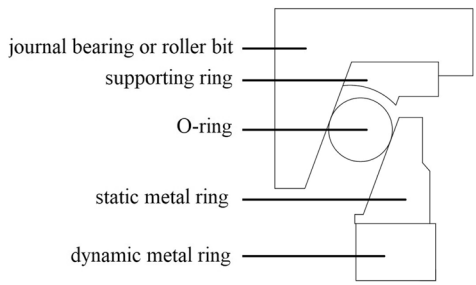


(a) Single metal sealing system

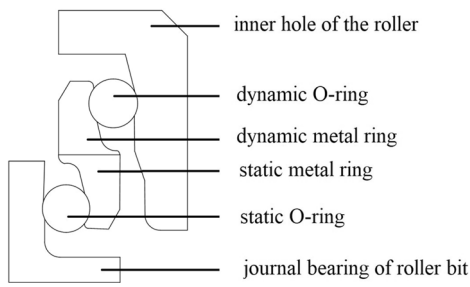


(b) Double metal sealing system

**Fig. 1-3.** A structural diagram of a metal seal [7].

and the static ring closely fit under the action of the two sealing rings, and an oil film is formed between the bonding surfaces to ensure the sealing performance [10].

The structure of a single metal seal is simpler than that of a double metal seal, but it is easier to fail under the condition of high speed and high WOB. The metal seal structure can float to a certain extent because of the elasticity of rubber, and the metal seal has a certain anti-vibration performance. The bimetallic seal has better anti-vibration performance.

Failure of the metal seal mainly comprises the following two aspects: (1) The high temperature of the bottom hole and self-generated change the performance of lubricating oil and rubber seal ring, which reducing the failure of the sealing performance. (2) Abrasive wear and bottom hole debris in the sealing surface and the rubber ring contact ring surface, result in the wear of the dynamic ring, static ring and rubber ring.

### *1.2.3 Screw drill rubber lining*

A screw drill is a kind of positive displacement downhole power drill, which can directly provide power for the bit at the bottom of the well. It is the most widely used downhole power tool at present. It has the advantages of low speed, large torque, large displacement and so on.

As shown in Figure 1-4. A screw drill is composed of bypass valve, motor, universal shaft and transmission shaft. The motor is the core part of screw drill [11]. The motor is mainly composed of a rotor and a stator. The rotor is a steel screw plated with corrosion-resistant material, and the stator is a steel pipe with rubber bushing on the inner wall [12]. The working principle of the screw drilling tool is that when the drilling fluid driven from one end of the motor to the other end, it drives the screw rotor to rotate in the stator and converts the liquid pressure into mechanical energy, driving the drilling tool to rotate and break the rock.

Rubber bushing is a part of the stator of screw drill, and its main material is rubber. In actual production, because of the high temperature of the bottom hole environment, friction and heat generation between stator and rotor, the rubber performance changes. The wear of the stator and rotor reduces the service life of stator. When the drilling fluid contains large solid particles, it will aggravate the wear of the stator and rotor, and even cause sand sticking fault of the drilling tool [13, 14, 15].

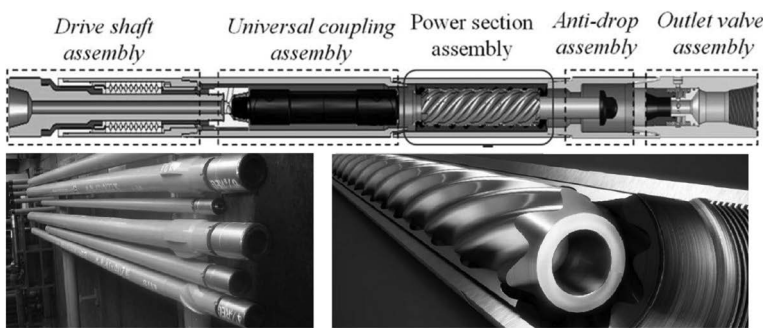


**Fig. 1-4.** A schematic diagram of the screw drilling tool structure [13].

### *1.2.4 Seal structure of the pump*

The mud pump is called the "heart" of the drilling circulation system. In the drilling operation, the mud pump transports a large amount of mud to the bottom of the well, which can carry out the debris and cool down the bit. Mud fluid can also be used as the power fluid in the downhole power drilling tool [16].

The piston is one of the core parts of the mud pump, which can be divided into integral piston and assembled piston (as shown in Figure 1-5). The integral piston is made of rubber vulcanized in the steel core as one whole, but the cup falls off easily during the piston movement. The cup is sleeved on the steel core in the assembled piston, and the piston is fixed by the clamp spring and the clamp plate. The structure is firm, and the interference amount of the piston cup can be adjusted by adjusting the tightness of the clamp plate and clamp spring [17].

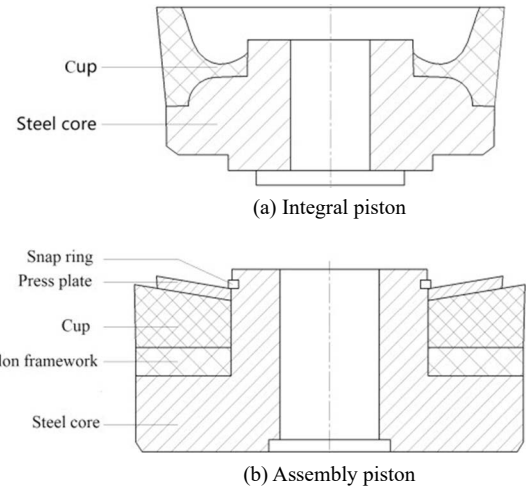


(a) Integral piston

(b) Assembly piston

**Fig. 1-5.** A schematic diagram of the piston structure [17].

Sealing performance of the piston is related to the performance and efficiency of mud pump, and the piston is one of the main vulnerable parts of mud pump. The failure forms and causes of the piston are as follows: [18, 19] (1) The friction between the piston and cylinder liner produces a lot of heat in a reciprocating motion, which leads to the piston temperature's increasing, the piston's material aging and service life decreasing. When the temperature rises, the piston will be heated and expanded, which will aggravate the wear of the piston and cylinder liner. (2) There are a certain amount of solid particles in the mud. During the working process, the solid particles enter into the contact surface between the piston and cylinder liner, which causes abrasive wear on component surface and aggravates the piston failure. The mud has certain corrosiveness. If the piston is immersed in the mud for a long time, the piston's material properties will be changed and its service life will be reduced. (3) There is a small gap between the steel core and cylinder liner, the rubber material is squeezed into the gap during the working process, which leads to the bite and crack at the root of the piston and affects its normal use.

### *1.2.5 Wellhead blowout preventer*

A blowout preventer (BOP) is one of the core equipment for the well control operation, which can ensure the safe and normal operation of oil and gas drilling engineering. In drilling operation, when the liquid column pressure in the well is less than the formation pressure, blowout may occurs. The blowout preventer can quickly close the wellhead to prevent blowout accidents. While, the blowout preventer also plays an important role in underbalanced drilling, pressure operation and other processes [20]. The blowout preventer failure causes serious environment pollution and life threatening. The rubber core is one of the key components of the blowout preventer. The rubber core performance determines the sealing performance of the blowout preventer and the oil and gas exploitation progress.

The blowout preventer is mainly composed of the ram blowout preventer and the annular blowout preventer (as shown in Figure 1-6).

The main structure of ram BOP includes a shell, an oil cylinder, a cylinder head, a piston, a piston rod, a seal, a ram, etc. The working principle of a ram BOP is that the piston is driven by hydraulic pressure, and the piston drives the ram to close. The arc rubber core is placed in the concave part of the ram. Under the action of the ram, the rubber core gradually contacts with the drill pipe. The rubber core is deformed by extrusion, which produces contact pressure and realizes sealing.

According to the shape of the rubber core, the annular BOP can be divided into conical annular BOP and spherical BOP. The annular BOP structure is mainly composed of a shell, a top cover, a rubber core and a piston. The working principle is that when the hydraulic oil enters into the closing cavity of the lower part of the piston from the lower oil port, which push the piston upward. The ball rubber core moves upward along the ball surface, and the rubber core moves closer to the center under the restriction of the top cover and the extrusion of the inner cone surface of the piston. Then the drilling tool is tightened and encircled, which helps to realize the wellhead closure.

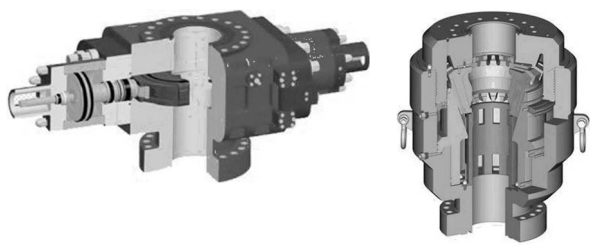

(a) Ram BOP (b) Annular BOP

**Fig. 1-6.** A schematic diagram of the blowout preventer structure.

### *1.2.6 Packer*

A packer is an essential downhole tool in oil and gas production (as shown in Figure 1-7). It is mainly used for fracturing, acidizing, water plugging, and other high-pressure seal layer construction technology to meet the process requirements of layered testing, layered oil production, layered water injection, and layered

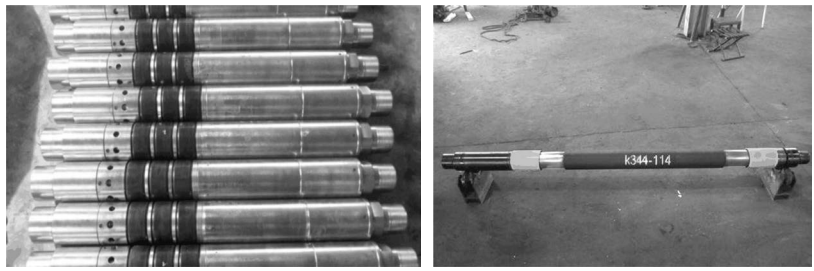


(a) Compression packer (b) Expansion packer

**Fig. 1-7.** An image of the different types of packers.

transformation [21, 22]. Rubber cylinder is the core component of the packer. The performance and service life of the rubber cylinder determines the sealing performance and effective sealing time [23, 24].

The sealing principle of the packer is based on the rubber cylinder expanding gradually in the annular space encased by mechanical or hydraulic action. This can increase the cylinder's radial diameter, and allowing it to finally come into contact with the inner wall of the casing to complete the sealing and realize the annular stratification. There are four categories of packer sealing: the self-sealing packer, which is realized by the interference between the outer diameter of packer and the inner diameter of casing and the working pressure difference; the compression packer, which compresses the rubber cylinder by axial force to make its outer diameter larger; the expansion packer, which makes the rubber cylinder expand radially by increasing the hydraulic pressure in the inner cavity of rubber cylinder; and the combined packer, which is sealed by the arbitrary combinations of the above three. The compression packer and expansion packer are the most widely used.

In the working process of packer, the rubber cylinder always maintains large deformation. The forms and characteristics of the failure of the rubber cylinder include the following aspects: the rubber cylinder works in high temperature, high pressure and even an acidic environment for a long time; the rubber material easily ages, its stress relaxation, hardness, and tensile resistance become poor, and its pressure bearing capacity is reduced [25]. Due to the structural design of the packer, the "shoulder convex" phenomenon occurs on the rubber barrel shoulder, where the "shoulder convex" part becomes prone to failure. The residual deformation of the rubber cylinder leads to the difficulty known as packer unsealing. The fretting wear of the rubber cylinder is caused by external environment. When the rubber cylinder is immersed in the mixture of crude oil and water for a long time, some solutes enter into the molecular structure of rubber, which changes its properties [26].

## References

[1] Zhang, J. and Xie, J. 2018. Investigation of static and dynamic seal performances of a rubber O-Ring. Journal of Tribology 140.

[2] Mo Li and Wang Jun. 2016. Finite element analysis and structural optimization of rubber D-ring. Mechanical Science and Technology for Aerospace Engineering 35(07): 1018–1022 (Chinese).

[3] Zhang, H. and Zhang, J. 2016. Static and dynamic sealing performance analysis of rubber D-ring based on FEM. Journal of Failure Analysis and Prevention 16: 165–172.
[4] Han Chuanjun, Zhang Han and Zhang Jie. 2015. Sealing performance analysis and cross section melioration of X-ring. Machine Design & Research 31(04): 90–94 (Chinese).
[5] Han, C., Zhang, H. and Zhang, J. 2015. Structural design and sealing performance analysis of biomimetic sealing ring. Applied Bionics and Biomechanics 1–11.
[6] Yang Linjun. 2017. Research on Metal Seal of Bit Bearing. B.S. Thesis, Southwest Petroleum University, Chengdu, China (Chinese).
[7] Zhang, J. and Hu, Y. 2019. Mechanical behavior and sealing performance of metal sealing system in roller cone bits. Journal of Mechanical Science and Technology 33: 2855–2862.
[8] Song Baojian, Zou Chun, Sun Kai, Ming Xin and Ren Wuhua. 2019. Numerical simulation and optimization research on single metal sealing of cone bit. Oil Field Equipment 48(04): 47–51 (Chinese).
[9] Ma Yi, Ni Yang, Meng Xiangkai, Peng Xudong and Jiang Jinbo. 2020. Thermal-fluid-solid coupling model and performance analysis of single metal seals in cone bits. China Mechanical Engineering 31(19): 2295–2303 (Chinese).
[10] Zhou Yi, Huang Zhiqiang, An Xianbin and Tan Jun. 2011. Failure analysis and improvement of high-speed roller bit bearing Bi-metal seal. Oil Field Equipment 40(08): 50–53 (Chinese).
[11] Han Chuanjun, Zheng Jipeng and Zhang Jie. 2016. Friction regularity of screwdrill's stator lining in different hot muds. China Mechanical Engineering 27(14): 1948–1952 (Chinese).
[12] Su Yinao. 2001. Research and Application of Screw Drilling Tools. Petroleum Industry Press, Beijing (Chinese).
[13] Zhang, J., Han, C. and Liang, Z. 2016. Physics of failure analysis of power section assembly for positive displacement motor. Journal of Loss Prevention in the Process Industries 44: 414–423.
[14] Han Chuanjun, Zhang Jie and Liu Yang. 2013. Thermal-structure coupling analysis for general stator lining of PDM. Journal of Central South University (Science and Technology). 44(06): 2311–2317 (Chinese)
[15] Zheng Bin. 2017. Failure Analysis and Precautions of PDM. B.S. Thesis, Northeast Petroleum University, Daqing, China (Chinese).
[16] Ru Shaofeng. 2015. Optimization Design of Mud Pump Piston Biomimetic Surface and Research on Wear-resistance and Sealing. B.S. Thesis, Jilin University, Jilin, China (Chinese).
[17] Cheng Xuejing. 2020. Optimal Design and Experimental Study of the Bionic Piston for F-1300 Mud Pump. B.S. Thesis, Jilin University, Jilin, China (Chinese).
[18] Huang Shengxue. 2007. Optimization Design of Mud Pump Piston. Daqing Petroleum Institute. B.S. Thesis, Daqing, China (Chinese).
[19] Sun Yiwen. 2017. Experimental Study and Mechanism Analysis of High Seal Ability Mud Pump Piston. B.S. Thesis, Jilin University, Jilin, China (Chinese).
[20] Chen Ting, Ma Weiguo and Wang Wei. 2020. Wear behavior of packer of ram blowout preventer in snubbing service. Lubrication Engineering 45(01): 74–80 (Chinese).
[21] Zhong Weiping. 2016. Sealing Performance Research on the Compression Packer Rubbers. B.S. Thesis, China University of Petroleum, Beijing China (Chinese).
[22] Zhang Zhipeng. 2015. New Y441Type Packer Design and Specificity Analysis. B.S. Thesis, China University of Petroleum, Beijing, China (Chinese).
[23] Li Ming. 2014. Study on Calculation Model of Pressure Difference Capacity of Rubber Cylinder of Compression Packer. B.S. Thesis, Southwest Petroleum University, Chengdu, China (Chinese).
[24] Jiang Xiangmin. 2017. Research on Sealing Performance and Reliability Analysis for Compression Packer Rubber Tube. B.S. Thesis, Tianjin University of Science and Technology, Tianjin China (Chinese).
[25] Yang Yong. 2020. Application of rubber products in oil drilling and production engineering. Equipment Technology (11): 0058–0058 (Chinese).
[26] Zhang Yufei. 2019. Research on the Structure Optimization and Stability of Fracturing Packer Rubber Tube. Tianjin University of Science & Technology (Chinese).

# 2

# A Rubber Experiment and the Constitutive Model

## 2.1 Rubber's material properties

Rubber is a polymer material with high flexibility and excellent elasticity. Compared to metals and other polymeric materials, rubber materials have unique properties, such as softness, elasticity, wear resistance, strong bonding capacity, and low breathability. Additionally, some special synthetic rubbers have better heat resistance (the heat resistance can be as high as 180~350ºC) and oil resistance. Lastly, it has good resistance to the swelling of fuel oil, lubricating oil, fatty oil, hydraulic oil, and solvent oil [1]. These excellent characteristics make rubber an excellent industrial material for sealing, shock absorption, wear resistance, corrosion resistance, noise, insulation, and bonding [2].

During the process of oil and gas exploitation, the high temperature and pressure at the bottom of the well and the high sand content in heavy oil put require reliable rubber seals, and high performance. For example strength, fatigue-resistant aging, metal and rubber bonding strength, etc., while the cost is secondary. Traditional stator rubber materials (mostly Nitrile Butadiene Rubber (NBR)) are prone to swelling in such an environment, resulting in material softening and hardness reduction, which makes the interference fit between stator and rotor develop into an interference fit and increases the friction torque between the stator and rotor, so that the rapid aging of the rubber results in seal failure. Hydrogenated butyrubber (HNBR) is highly regarded for its excellent comprehensive ability in underground mechanical seal rubber selection. Although the cost of HNBR is higher than that of NBR, it is more economy as well as more suitable for use in a harsh environment.

## 2.2 Nonlinear characteristics

### *2.2.1 Material nonlinearity*

Material nonlinearity mainly contains the following characteristics: plasticity, creep, hyper-elasticity, viscoelasticity, visco-plasticity, etc. [3] A simple description of material properties is as follows:

(1) Plasticity

The ability of a material to deform permanently without compromising its integrity under external forces is called plasticity. Most engineering materials are divided into two main deformation behaviors: elastic deformation and plastic deformation. When the stress of a material is below the elastic limit (proportional limit), the stress-strain relationship changes linearly, which is in the elastic deformation. When the stress exceeds the elastic limit, plastic deformation occurs.

(2) Creep

Under the action of constant load, the irreversible strain of the material increases continuously, which causes the creep phenomenon, which is different from the plastic deformation. The creep occur when the stress is less than the force exerted by the elastic limit as long as the stress action time is quite long. It is divided into display creep and implicit creep. The correlation between creep deformation and stress, strain, time, and temperature is generally simulated in a similar form:

$$\varepsilon_{cr} = f_1(\sigma) f_2(\varepsilon) f_2(t) f_4(T) \tag{2-1}$$

The $f_{1-4}$ function in the series is related to the creep law selected.

(3) Hyper-elasticity

The strain of the material produced by the external force is much higher than the elastic limit strain. When the pressure is unloaded, its strain is restored to its original state. This kind of material is called hyper-elastic. Hyper-elastic materials can withstand large, recoverable (elastic) deformations and have a strain rate of up to 300%. Hyper-elastic materials are commonly used to simulate rubber and other polymer-like materials. At the same time, the elastic range of materials with hyper-elasticity properties is much higher than that of conventional materials.

(4) Viscoelasticity

Viscoelasticity is a kind of nonlinear material with an elastic deformation component (recoverable) and a viscous deformation component (irrecoverable). It can be used to simulate the viscoelastic behavior of amorphous solids and amorphous polymers.

(5) Visco-plasticity

At a certain critical value of stress, the deformation rate of a body is related to the viscosity of the fluid pressure, and has the characteristics of yielding and flowing, this phenomenon is called the visco-plasticity of the material.

### *2.2.2 Geometry nonlinearity*

The characteristic of geometric nonlinearity is that the object structure produces large displacement and rotation during the process of adding a load. Meanwhile, the load and displacement do not obey the linear relationship. The quadratic term of displacement must be included in the expression of strain [4]. During rubber sealing, there is a large deformation under working pressure and extrusion pressure. Therefore, this type of contact problem is geometrically nonlinear.

This geometric nonlinear problem is solved by using the principle of virtual work displacement to establish finite object balance equations. According to the principle of virtual work displacement, the supply made by external forces due to false work is equal to the strain energy produced by the structure due to virtual strain; the following equations shed more light on it:

$$d\boldsymbol{u}^T\boldsymbol{\psi}(\boldsymbol{u}) = \int d\boldsymbol{\varepsilon}^T\boldsymbol{\sigma}dV - d\boldsymbol{u}^T F = 0 \tag{2-2}$$

where, $\psi$ is the sum of the node's broad inner and broad external force vectors. $du$ is virtual displacement. $d\varepsilon$ is virtual strain, and $F$ is all load arrays.

The form of displacement and strain is given as $d\boldsymbol{\varepsilon} = \bar{\boldsymbol{B}}d\boldsymbol{u}$ by using the incremental form of strain. The equilibrium equation of nonlinear problems can be derived by bringing it into the upper equation:

$$\boldsymbol{\psi}(\boldsymbol{u}) = \int \bar{\boldsymbol{B}}^T\boldsymbol{\sigma}dV - \boldsymbol{F} = 0 \tag{2-3}$$

The integral operation in the system is made up of the sum of the integrals of each element to the node balance, which is fully applicable to large displacement (strain) and small displacement (strain).

For a linear finite problem, the relationships between strain and displacement, as well as between stress and strain, are linear; the relationship can be seen in $\boldsymbol{\varepsilon} = \boldsymbol{B}(\boldsymbol{u})$, $\boldsymbol{\sigma} = \boldsymbol{D}(\boldsymbol{\varepsilon})$ the equation:

$$\int B^T\boldsymbol{D}\boldsymbol{B}dV\boldsymbol{u} - \boldsymbol{F} = 0 \tag{2-4}$$

In the case of large displacements, the relationship between the strain and displacement in the formula $d\varepsilon = \bar{\boldsymbol{B}}d\boldsymbol{u}$ is nonlinear, so the matrix $\bar{\boldsymbol{B}}$ is a function of $u$, which can be broken $\bar{\boldsymbol{B}}$ down into the following equation:

$$\bar{\boldsymbol{B}} = \boldsymbol{B}_0 + \boldsymbol{B}_L \tag{2-5}$$

where, $\boldsymbol{B}_0$ is matrix item for linear strain analysis, independent of $u$. $\boldsymbol{B}_L$ is caused by nonlinear deformation, is a linear function of the displacement column array $u$.

In most cases, although the displacement is large, the structural strain is not large, and the stress and strain relationship is still a line elasticity relationship, so:

$$\boldsymbol{\sigma} = \boldsymbol{D}(\boldsymbol{\varepsilon} - \boldsymbol{\varepsilon}_0) + \boldsymbol{\sigma}_0 \tag{2-6}$$

where, $D$ is the elastic matrix of the material. $\varepsilon$ is initial strain array. $\varepsilon_0$ is initial stress array.

Equation (2-3) is usually used by the Newton-Lafayette solution, so the relationship between the two needs to be established by the Equation (2-3) method of division:

$$d\boldsymbol{\psi} = \int d\bar{\boldsymbol{B}}^T\boldsymbol{\sigma}dV + \int \bar{\boldsymbol{B}}^T d\boldsymbol{\sigma}dV \tag{2-7}$$

Ignoring the effects of initial strain and initial stress, the equation $d\boldsymbol{\sigma} = \boldsymbol{D}\, d\varepsilon = \boldsymbol{D}\,\overline{\boldsymbol{B}}d\boldsymbol{u}$ can be obtained from the formula (2-3). Because B0 and u are independent. Then,

$$\begin{aligned} d\boldsymbol{\psi} &= \int d\boldsymbol{B}_L^T \boldsymbol{\sigma} dV + \overline{\boldsymbol{K}}^T d\boldsymbol{u} \\ \overline{\boldsymbol{K}} &= \int \overline{\boldsymbol{B}}^T \boldsymbol{D}\overline{\boldsymbol{B}} dV = \int [\boldsymbol{B}_0 + \boldsymbol{B}_L]^T \boldsymbol{D}[\boldsymbol{B}_0 + \boldsymbol{B}_L] dV = \boldsymbol{K}_0 + \boldsymbol{K}_L \\ \boldsymbol{K}_0 &= \int \boldsymbol{B}_0^T \boldsymbol{D}\boldsymbol{B}_0 dV \\ \boldsymbol{K}_L &= \int (\boldsymbol{B}_0^T \boldsymbol{D}\boldsymbol{B}_L + \boldsymbol{B}_L^T \boldsymbol{D}\boldsymbol{B}_L + \boldsymbol{B}_L^T \boldsymbol{D}\boldsymbol{B}_0)\, dV \end{aligned} \tag{2-8}$$

where, $\boldsymbol{K}_0$s a linear stiffness matrix that represents a small displacement. $\boldsymbol{K}_1$ represents the initial displacement matrix (also known as the large displacement matrix).

The first item to the right of the second expression in Equation (2-8) can be written as:

$$\int d\boldsymbol{B}_L^T \sigma dV = \boldsymbol{K}_\sigma d\boldsymbol{u} \tag{2-9}$$

where, $\boldsymbol{K}$ is asymmetrical matrix of $\sigma$ stress, called a primary stress matrix, or a geometric stiffness matrix.

Therefore, the first expression of Equation (2-8) can be written as:

$$d\boldsymbol{\psi} = (\boldsymbol{K}_0 + \boldsymbol{K}_\sigma + \boldsymbol{K}_L) d\boldsymbol{u} = \boldsymbol{K}_T d\boldsymbol{u} \tag{2-10}$$

where, $\boldsymbol{K}_1$ represents tangent stiffness matrix, $\boldsymbol{K}_T = \boldsymbol{K}_0 + \boldsymbol{K} + \boldsymbol{K}_L$.

For large displacement problems, the Newton-Lafayette method is usually used to solve the problem, and its iterative formula is:

$$\Delta\boldsymbol{u}_n = -\boldsymbol{K}_T^{-1}\boldsymbol{\psi}_n, \Delta\boldsymbol{u}_{n+1} = \boldsymbol{u}_n + \Delta\boldsymbol{u}_n \tag{2-11}$$

The solution for Newton-Lafayette's iterative approach is divided into the following steps:

1) Use line elastic solution u as the first approximation of $\boldsymbol{u}_1$;
2) The stress $\overline{B}$ is calculated by the formula (2-5), the stress $\sigma$ is calculated by the formula in Equation (2-6), and then the imbalance force $\psi_1$ is calculated by the formula in Equation (2-4);
3) Calculate the shed steel stiffness of the $K_T$ matrix;
4) Calculate $\Delta u_1$, $u_2$ using the formula in Equation (2-11);
5) Return to the second step and repeat the iteration until $\psi_n$ is small enough.

### *2.2.3 Contact nonlinearity*

The contact problem is an important nonlinear problem in state nonlinearity. Seals are made of rubber, which makes such contact difficult to analyze. In view of the contact problem, the variables should not only satisfy the basic equation of solid metal, the given boundary conditions, and the initial conditions in the study model,

but also satisfy the contact conditions of the objects on the contact surface. That is to say, the two objects in contact must satisfy the non-penetration constraint condition. The contact state of the interface can be divided into three kinds: separation state, bond contact state, and sliding contact state. For three states, the displacements and force conditions of the contact interface are also different. It is the transformation of the actual contact state in the above three states that leads to the highly nonlinear characteristics of the contact problem [5].

The methods of implementing no penetration constraints in contact problems include the Lagrange multiplier method, the penalty method, the augmented Lagrange multiplier method, and the hybrid finite element method.

The contact method between rigid bodies and rubber parts studied in this book is the penalty function method, and the algebraic equation system of the constraint algorithm is [6]:

$$(K + \alpha K_P^T)u = R - \alpha\gamma_p \tag{2-12}$$

where, $\alpha$ represents the penalty function. $\alpha K_P^T$ represents the stiffness matrix of the logic unit. $R$ represents a load vector. $\alpha\gamma_p$ represents the cell load vector.

## 2.3 Rubber constitutive model

### *2.3.1 The constitutive relation of rubber*

As a kind of hyper-elastic material, rubber has good elasticity and resilience. The nonlinear characteristics of hyper-elastic materials are very obvious. The rubber is under great strain, and the stress-strain relationship is highly nonlinear [7]. Its mechanical properties are greatly affected by temperature, which is opposite to the characteristics of solid expansion after heating; that is, rubber shows the thermodynamic characteristics of shrinkage after heating [8–9].

Research on the rubber constitutive relationship mainly focuses on the stress-strain relationship of rubber using phenomenological theory [10–14].

The image theory treats rubber material as a continuous unity. Based on the assumption that the rubber is isotropic and the volume is approximately incompressible, a unified physical quantity is used to characterize its mechanical properties. This physical quantity is called the strain energy density function. This function is a scalar function of strain tensor, and the derivative of its corresponding variable component is the corresponding stress component, and its expression is:

$$S_{ij} = \frac{\partial W}{\partial E} \tag{2-13}$$

where, $S_{ij}$ is II Piola-Kirchhoff stress level. $\boldsymbol{W}$ is strain energy density function per unit volume. $\boldsymbol{E}$ is Lagrange strain sheet.

The strain energy function is:

$$W = (I_1, I_2, I_3) \text{ or } W = (\lambda_1, \lambda_2, \lambda_3) \tag{2-14}$$

Elongation:

$$\lambda = \frac{L}{L_0} = \frac{L_0 + \Delta u}{L_0} = 1 + \varepsilon_E \tag{2-15}$$

$I_1$, $I_2$, $I_3$ are called the Green first, second, and third strain invariants, and the relationship between them and elongation is:

$$\begin{cases} I_1 = \lambda_1^{\,2} + \lambda_2^{\,2} + \lambda_3^{\,2} \\ I_2 = \lambda_1^{\,2}\lambda_2^{\,2} + \lambda_2^{\,2}\lambda_3^{\,2} + \lambda_3^{\,2}\lambda_1^{\,2} \\ I_3 = \lambda_1^{\,2}\lambda_2^{\,2}\lambda_3^{\,2} \end{cases} \tag{2-16}$$

For limited compressible materials, the model generally takes the following form:

$$W = W(I_1, I_2, J) = W(\lambda_1, \lambda_2, \lambda_3) \tag{2-17}$$

Compression volume ratio is:

$$J = \lambda_1\lambda_2\lambda_3 = \frac{V}{V_0} \tag{2-18}$$

(in thermal expansion $J_{th} = (1 + \varepsilon_{th})^3$).

If rubber is considered an incompressible material ($J = 1$), the strain energy density function can be reduced to:

$$W = W(I_1, I_2) = W(\lambda_1, \lambda_2) \tag{2-19}$$

For several major forms of deformation, the stress strain relationship of the non-compressible hyper-elastic structure model is:

$$T_1 = 2\lambda_1\left(1 - \frac{1}{\lambda_1^{\,4+2\alpha}}\right)\left(\frac{\partial W}{\partial I_1} + \lambda_1^{\,2\alpha}\frac{\partial W}{\partial I_2}\right) \tag{2-20}$$

where, $T_1$ is stress. $\alpha = -1/2, 0, 1$: corresponding to unidirectional, planar and Equal biaxial tension, and compression deformation state, respectively.

### *2.3.2 Structural model of synthetic rubber*

Typical representations of the rubber-based model are Heo-Hookean strain energy functions, the exponential-hyperbolic law, the Mooney-Rivlin model, the Yeoh model, the Ogden model, and the Gent model. The structure models commonly used for rubber in finite element simulations are the Mooney-Rivlin model and Yeoh models.

(1) Mooney-Rivlin model

The Polynomial Model proposed by Rivlin in 1948 can simulate almost all the mechanical properties of rubber and is the most frequently cited basic rubber model.

It uses the idea of the Taylor series to express the strain energy density function in the form of the series expansion of the strain tensor invariant. Its most general form is:

$$W = \sum_{i+j=1}^{N} C_{ij}(I_1 - 3)^i (I_2 - 3)^j + \sum_{i=1}^{N} \frac{1}{D_i}(J-1)^{2i} \tag{2-21}$$

where, $N$ is Polynomial order. $C_{ij}$ is Rivlin coefficients, which are regression coefficients obtained from experimental data analysis. $D_i$ is the compression amount of the material depends on whether the material can be pressurized.

Taking $N = 1$, treat rubber as an incompressible material, after which the formula in Equation (2-20) can be simplified as:

$$W = C_{10}(I_1 - 3) + C_{01}(I_2 - 3) \tag{2-22}$$

where, $W$ is the strain energy density. $C_1$, $C_2$ are Mooney-Rivlin coefficients. $I_1$, $I_2$ are the first and second strain tensor invariants.

This has exactly the same form as the strain energy density function proposed by Mooney in 1940, so it is usually called the Mooney-Rivlin model. $C_{10}$ and $C_{01}$ are Mooney-Rivlin constants.

(2) Yeoh model

In 1951, Rivlin and Saunders found that when a hyper-elastic material undergoes large deformation ($I_1$, $I_2 \geq 5$), $\partial W/\partial I_2$ is only about 1/8~1/30 of $\partial W/\partial I_1$ from a biaxial tensile experiment. This shows that $\partial W/\partial I_2$ is the main contributor to stress, while $\partial W/\partial I_1$ is the secondary factor. In 1990, Yeoh et al. pointed out that when describing the large deformation mechanical characteristics of filled rubber, the influence of $\partial W/\partial I_2$ can be ignored, and the $I_2$ term in the expression of the strain energy density function can be ignored, which can often enhance the Drucke stability of the constitutive model [15–17]

The polynomial model with $I_2$ omitted terms is usually called Reduced Polynomial Model, and its expression is:

$$W = \sum_{i=1}^{N} C_{i0}(I_1 - 3)^i + \sum_{i=0}^{N} \frac{1}{D_i}(J-1)^{2i} \tag{2-23}$$

When $N = 3$, the reduced polynomial is the Yeoh model. For incompressible materials, the expression is:

$$W = C_{10}(I_1 - 3) + C_{20}(I_1 - 3)^2 + C_{30}(I_1 - 3)^3 \tag{2-24}$$

### *2.3.3 The constitutive model*

In this book, the Mooney-Rivlin model was selected to describe the mechanical characteristics of the rubber O-ring.

The relationship of stress and strain can be expressed as follows:

$$\sigma = \partial W/\partial \varepsilon \tag{2-25}$$

## 2.4 Single-axis stretching experiment

### *2.4.1 Experiment design*

The high temperature environment and the heavy oil environment will greatly affect the mechanical properties of rubber materials, and then affect the normal operation of seals. The material mechanical parameters are very important for simulation. Therefore, the rubber experiment can not only provide a valuable reference for mechanical properties of rubber materials in underground oil and gas mining machinery, but also provide a strong basis in finite element analysis. The rubber sample is a dumbbell type I made of hydrogenated butyl rubber material, which complies with the GB/T528-2009. The sample is selected standard size—thickness 2 mm, width 6 mm, gauge length 25 mm, and its shape is shown in Figure 2-1.

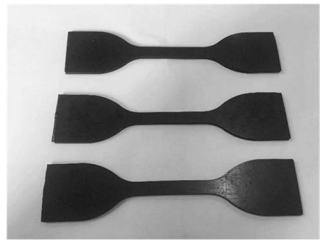

**Fig. 2-1.** A tensile specimen of rubber material.

Before the test begins, the heavy oil is heated on the friction wear test machine, and then the rubber sample is immersed in the heavy oil, which is heated for two hours. In order to facilitate stretching and assess the effect of the cleaning agent on the test results, only wipe the heated rubber sample. Since the heating equipment and the stretch tester are located in different laboratories, the sample needs to be placed in a heating tank for insulation before being removed from the heated heavy oil and stretched. The test temperature is 30ºC, 60ºC, 90ºC, 120ºC, and 150ºC. Each group stretches three samples and averages them as test data to reduce the test error. Using a moving speed of 200 mm/min.

### *2.4.2 Experiment results*

#### *2.4.2.1 Fatigue damage resistance*

According to Figure 2-2 and Table 2-1, hydrogenated butyl rubber still has well-functioning mechanical properties at high temperatures of 150ºC, but a significantly lower performance than at normal temperatures. With the increasing of temperature, the maximum load and stretch strength of rubber material are gradually reduce, the rip elongation increases slightly and then gradually decreases. The fatigue-resistant damage performance of rubber material is gradually reduced. Which is less affected by temperature at temperatures below 60ºC, and it decreases sharply when the temperature is above 60ºC, especially at 60–90ºC. At high temperatures of 150ºC, the tear elongation, maximum load and extrusion strength of the rubber were reduced by 58.88%, 78.12%, and 77.92%, respectively.

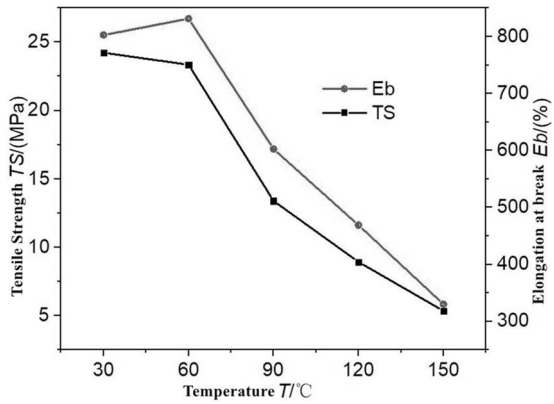


**Fig. 2-2.** The temperature dependence curve of fatigue resistance of the rubber specimen.

**Table 2-1.** The uniaxial tensile test data of rubber in heavy oil at different temperatures.

| Test temperature | Sample number | Tear elongation % | Maximum load/N | Stretch strength/MPa |
|---|---|---|---|---|
| 30ºC | 1-1 | 834.333 | 324.462 | 27.0385 |
| | 1-2 | 771.451 | 296.765 | 22.5848 |
| | 1-3 | 802.053 | 303.690 | 23.0487 |
| | Average | 802.612 | 308.306 | 24.2240 |
| 60ºC | 2-1 | 800.828 | 274.240 | 22.2589 |
| | 2-2 | 836.846 | 281.422 | 23.7339 |
| | 2-3 | 856.572 | 289.003 | 24.0836 |
| | Average | 831.415 | 281.555 | 23.3588 |
| 90ºC | 3-1 | 643.004 | 174.239 | 14.6198 |
| | 3-2 | 575.775 | 150.291 | 12.3007 |
| | 3-3 | 588.841 | 158.991 | 13.2493 |
| | Average | 602.540 | 161.174 | 13.3899 |
| 120ºC | 4-1 | 487.998 | 114.287 | 9.7835 |
| | 4-2 | 455.721 | 106.564 | 8.6638 |
| | 4-3 | 459.644 | 106.514 | 8.3344 |
| | Average | 468.788 | 109.122 | 8.9272 |
| 150ºC | 5-1 | 326.715 | 66.563 | 5.2594 |
| | 5-2 | 343.363 | 70.724 | 5.6162 |
| | 5-3 | 320.055 | 65.052 | 5.1689 |
| | Average | 330.044 | 67.446 | 5.3482 |

### *2.4.2.2 Stress-strain curve*

The stress-strain curves of rubber samples at different temperatures in heavy oil are shown in Figure 2-3. With the temperature increases, the mechanical properties of

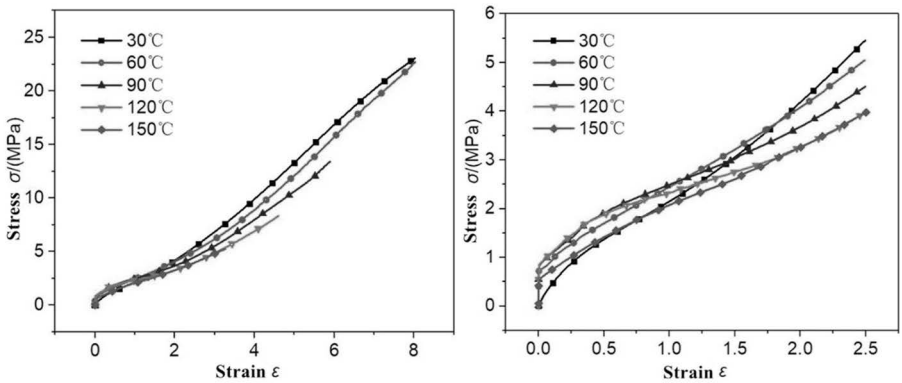


(a) The rubber breaks (b) The rubber strain is 2.5

**Fig. 2-3.** The stress-strain curves of the rubber materials at different temperatures.

rubber gradually decrease. Because the maximum strain of rubber at 150ºC is only 3.30, which is 8 when the temperatures below 60ºC. Figure 2-3(b) extracts the stress-strain curve at 2.50 before rubber deformation. The stress-strain relationship of rubber material shows obvious nonlinear characteristics. When the strain is less than 1, the stress-strain relationship of the rubber material is a curve with outward convexity. When the strain is 1~2, the stress-strain relationship is an inward concave curve. When the strain exceeds 2, the stress-strain relationship is approximately a straight line, and the growth of the stress accelerates with the strain increases. Temperature has a great influence on the stress-strain relationship of rubber. When the temperature is no higher than 60ºC, the mechanical properties of rubber do not change much, and the curve is a smoother curve on the whole. When rubber is heated, its stress-strain curve can be divided into three stages. Small deformation (less than 0.011), the thermodynamic properties of the rubber's heat contraction make a large transient stress in the initial stage of stretching, and the stress-strain curve is close to a straight line parallel to the ordinate. When the strain is less than 1, the stress-strain curves basically coincide under different temperatures. When the strain is greater than 1.50, the overall slope of the curve decreases with the increasing of temperature, and the stress growth slows down.

### *2.4.2.3 Elastic modulus*

The elastic modulus is defined as the stress required for a material to produce unit elastic deformation under the action of external forces. It is a measure of the size of an object's resistance to elastic deformation, and it is also the characterization of the difficulty of elastic deformation. As can be found from the previous analysis, the stress-strain relationship of rubber material shows nonlinear characteristics, and the elastic modality $E$ is not a constant but a function of the deformation process. When the deformation of rubber material is very less, the relationship between stress and strain can be approximated as linear.

The elastic modulus of the synth rubber material in the small deformation range can be found by the rubber stretch test. With a sample thickness of 2 mm and a width

of 6 mm, the cross-sectional area $\boldsymbol{A}_0$ is 12 mm$^2$ and the pitch $\boldsymbol{L}_0$ is 25 mm. The elastic modality of the rubber is obtained by the definition as:

$$E = \frac{F/A_0}{\Delta L/L_0} = \frac{F}{A_0 \cdot \varepsilon_y} \tag{2-26}$$

$\varepsilon_y$ can be directly calculated by the displacement extrusion meter, and $\boldsymbol{E}$ in the case of small deformations (within the strain range of 0.01~0.1 can be matched by using origin's data analysis capabilities of linear regression). The solution process of rubber elastic modulus at 30ºC is shown in Figure 2-4. The slope is the elastic modulus to be sought, and the solution methods for elastic modulus at other temperatures are the same as that at 30°C.

The elastic modulus of three samples at different temperatures are calculated separately, and the average is taken as the elastic modality of the sage rubber, and the curve as shown in Figure 2-5. With the temperature increases, the elastic modulus of the rubber material decreases sharply and then slowly increases, which reaches its highest value at normal atmospheric temperature. When the lowest temperature is at 90°C, the difference is 1.88 MPa, which is consistent with the mechanical property of rubber. As the temperature rises, there is a large difference in the elastic modal variation of the rubber material. When the temperature is heated from normal atmospheric temperature to 60°C, the elastic modulus change is the largest with a reduction of 1.49 MPa. When the temperature is higher than 60°C, the elastic modulus changes less with the temperature. As a result, the elastic modulus is much lower when heated at a higher temperature. It can be speculated that rubber seals are more prone to elastic deformation when working in high-temperature environments.

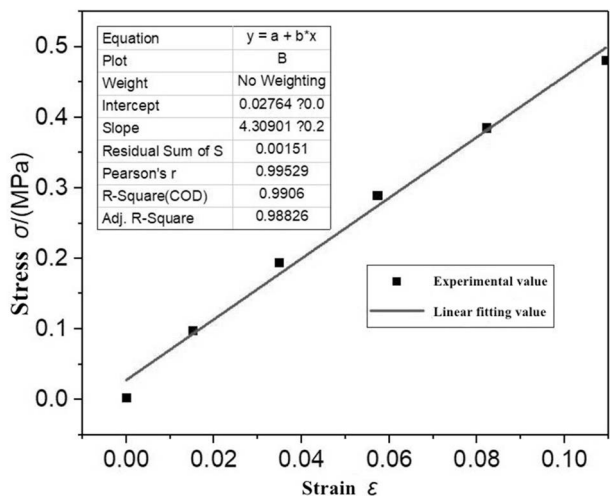


**Fig. 2-4.** A linear fitting curve of the rubber's stress and strain (at 30ºC).

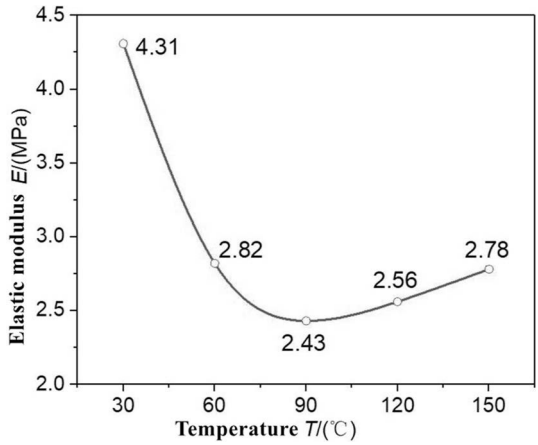


**Fig. 2-5.** The rubber's elastic modulus with temperature.

## 2.5 Rubber friction wear

Wear is one of the main forms of seal failure. By the friction wear test of rubber in high-temperature sand-containing heavy oil, the friction coefficient of rubber in heavy oil heat extraction is studied.

### *2.5.1 Test materials and processes*

*2.5.1.1 Testing material*

(1) Crude oil

The parameters of crude oil are shown in Table 2-2:

**Table 2-2.** Heavy oil parameters.

| The layer bit | Ina | The initial temperature of the oil layer | Viscosity (50°C) | Density | Gel content | Wax content |
|---|---|---|---|---|---|---|
| N/S | 350 m | 20ºC | 3219 mpa·s | 0.9627 g/cm$^3$ | 0 | 0 |

(2) Solid-phase particles

The diameter of the selected sand is 40 to 60 mesh and sand particles taken from the Kramay oil field.

(3) Test rubber

The test rubber is butyl rubber provided by Chengdu Hanguang Rubber Co., Ltd. Butyl rubber has good oil, wear, and high-temperature resistance. The formula: butyl glue 100, high wear-resistant carbon black 110, fatty acids 4, zinc oxide 8, fatty acids 4, improver 12, anti-age agent D5, vulcanizer 3 and promoter TMTD4. Using a vulcanization process, the formulated rubber is vulcanized on a hard steel disc with a diameter of 50 mm as shown in Figure 2-6. The mechanical properties of Butyl rubber are shown in Table 2-3.

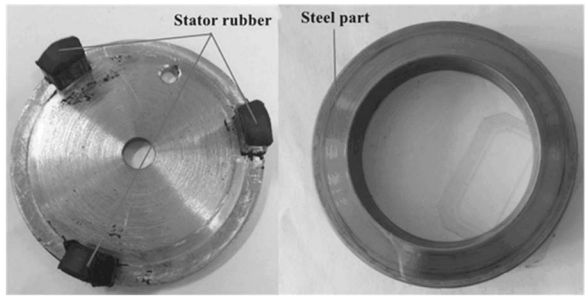


**Fig. 2-6.** A rubber test piece and a steel ring test piece.

**Table 2-3.** Major thermic properties of butyl rubber.

| Major aesthetic properties | Unit | Experience standard values | NBR |
|---|---|---|---|
| Shore Type A hardness | — | 65 ± 5 | 72 |
| Stretch strength | MPa | ≥ 12 | 22.5 |
| Break elongation | % | 500 ± 50 | 579 |
| 200% Tensile strength | MPa | ≥ 8.5 | 11 |
| Tear strength | kN/m | 30~50 | 63 |

(4) Steel for testing

Combined with the tester loading device base and rubber friction test piece, the steel ring conforming to the test requirements is designed with an internal diameter of 38mm, an outer diameter of 54 mm and a height 10.5 mm. As shown in Figure 2-6, the test steel ring is 45# steel-plated on the surface.

### *2.5.1.2 Experiment process*

Before the start of the test, the rubber and steel ring fittings are installed on the test bench, and then the sand-containing heavy oils are rationed to mass fractions (0, 5%, 10%, 15%) and stirred well. The sand-containing heavy oil is then poured into the steel groove at the top of the loading device to ensure that the liquid surface is completely covered with the contact surface of the rubber test piece and the metal ring. The oil is heated to 55°C.

After the test, the rubber test part was cleaned with petroleum ether and the ultrasonic generator, the crude oil and sand grains are removed. The rubber test part was measured and the wear amount was calculated.

In order to ensure the accuracy of the test results and eliminate the effects caused by the differences in surface roughness of the material, the rubber test surface was pre-grinded before the start of the test, so that the roughness of the rubber surface is as consistent as possible.

### *2.5.2 Test results*

#### *2.5.2.1 Effect of speed on the friction coefficient*

It can be seen from Figure 2-7 that when the normal load is constant, the friction coefficient of the stator rubber first increases and then decreases with the increasing of the speed, which reaches the maximum at 250 r/min. The friction coefficient of rubber in a sandy 5% heavy oil is greater than that in a sand-containing oil. The main reason is that the presence of sand grains increases the friction between rubber and steel sleeves. The increasing speed that result in heat can't be dissipated in time and accumulates in the contact area of rubber and steel parts (rubber thermal conductivity difference), resulting in the rubber-surface-appearing-like-glue phenomenon. When the speed increases, heat continues to accumulate, the bonding phenomenon evolves into a melting phenomenon, and a layer of melting layer is formed in the rubber surface, which plays a certain lubrication effect. Therefore, the friction between rubber and steel parts reduce.

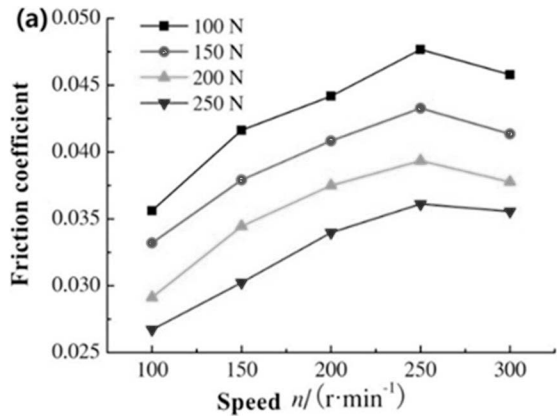


(a) Sand content 0%

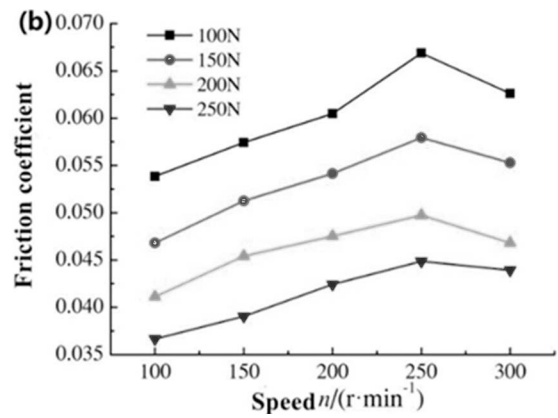


(b) Sand content 5%

**Fig. 2-7.** The friction coefficient of rubber with different speeds.

Figure 2-8 shows the rubber friction coefficient curve with different speeds. At the same ambient temperature and speed, the friction coefficient decreases gradually with the increasing of the legal load, and which in the sand-containing oil is greater than that without sand. During the test process, the sand particles in the heavy oil enter the area where the rubber is in contact with the steel part as the test piece rotates, which seeps into the rubber surface and increases the friction between the rubber and steel part, then resulting in an increase of the friction coefficient. The friction coefficient decreases as the load increases. The reason is that the contact area between rubber and steel increases when the load increases, which results in a reduction in the contact pressure per unit area. Meanwhile, the formation of the oil film area also increases, which resulting in a reduction of friction coefficient.

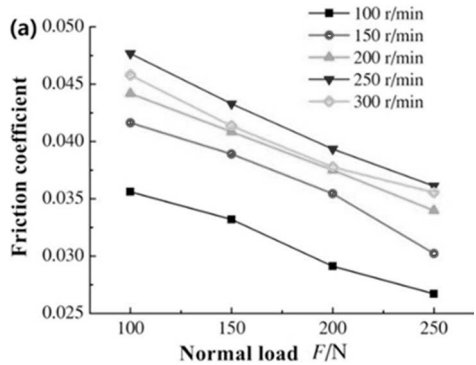


(a) Sand content 0%

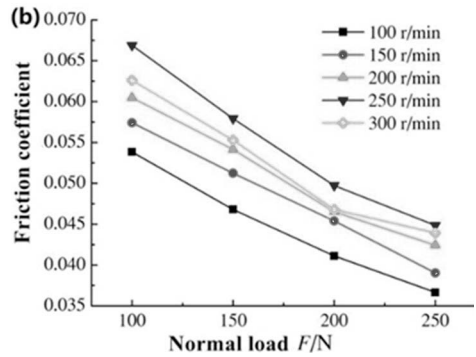


(b) Sand content 5%

**Fig. 2-8.** The friction coefficient curves with different loads.

### *2.5.2.2 Effect of sand content on friction coefficient and wear*

As shown in Figure 2-9, the friction coefficient increases with the load increases, which first increases and then decreases with the speed increases. Under the same load and speed, as the concentration of sand particles increases, and the force of the sand particles on the rubber surface increases, then resulting an increase of friction

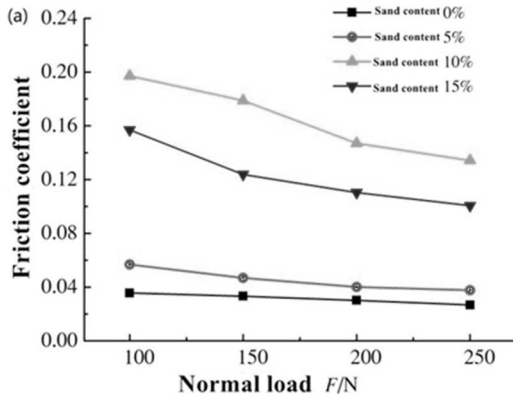


(a) The load

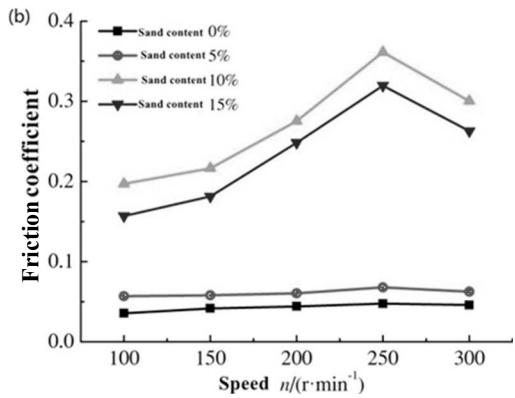


(b) The speed

**Fig. 2-9.** The friction coefficient curves with different sand content.

coefficient. When the sand concentration increase to a certain concentration, the number of sand particles entering the contact surface of the friction pair increase, and the mutual interference behavior between the sand particles increases. That results in a decrease of the force of the sand particles acting on the rubber surface, which leads to friction coefficient decreases.

It can be seen from Figure 2-10 that the rubber wear in heavy oil with different sand content increases with the increasing of load and speed. As the sand content increases, the rubber wear first increases and then decreases, which reaches the maximum value with a sand content of 10%. When the sand particles in the heavy oil increase, the content of sand particles entering the surface of the friction pair will increase accordingly, leading to the force acting on the rubber surface to increase, which resulting in wear increases. When the concentration of sand particles continues to increase a certain value, adjacent sand particles will interfere with each other, then the interference effect increases. When the interference force is greater than its force on the rubber, the number of the sand particles act on the rubber surface will decrease, and the corresponding friction will decrease, which reduces the rubber

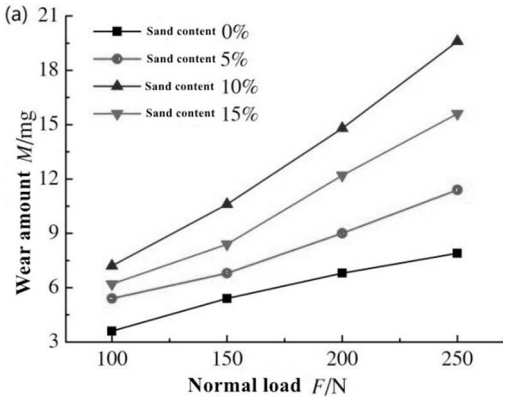


**Fig. 2-10.** The rubber wear curves under different sand content.

wear. Therefore, the amount of rubber wear increases with the increasing of sand grain concentration, and which decreases gradually after reaching the maximum value.

### *2.5.3 Surface morphology of rubber wear*

In Figure 2-11, there are many parallel but unequal spacing tear stripes on the worn surface of Butyl rubber in high-temperature heavy oil with sand content, and there are scratches and furrows in heavy oil with high sand content. In Figure 2-11(a), the rubber surface presents a curly tongue-like substance with stripe-like distribution. In the high-temperature environment, the heat generated on the rubber surface can't be eliminated, then resulting in a melting layer on the rubber surface. This morphology appears under the action of friction. However, scratches also appear in Figures 2-11(b), (c) and (d), and the number of scratches first increases and then decreases with the increasing of sand content. This is because the number of sand particles entering the rubber surface increases with the increasing of sand content,

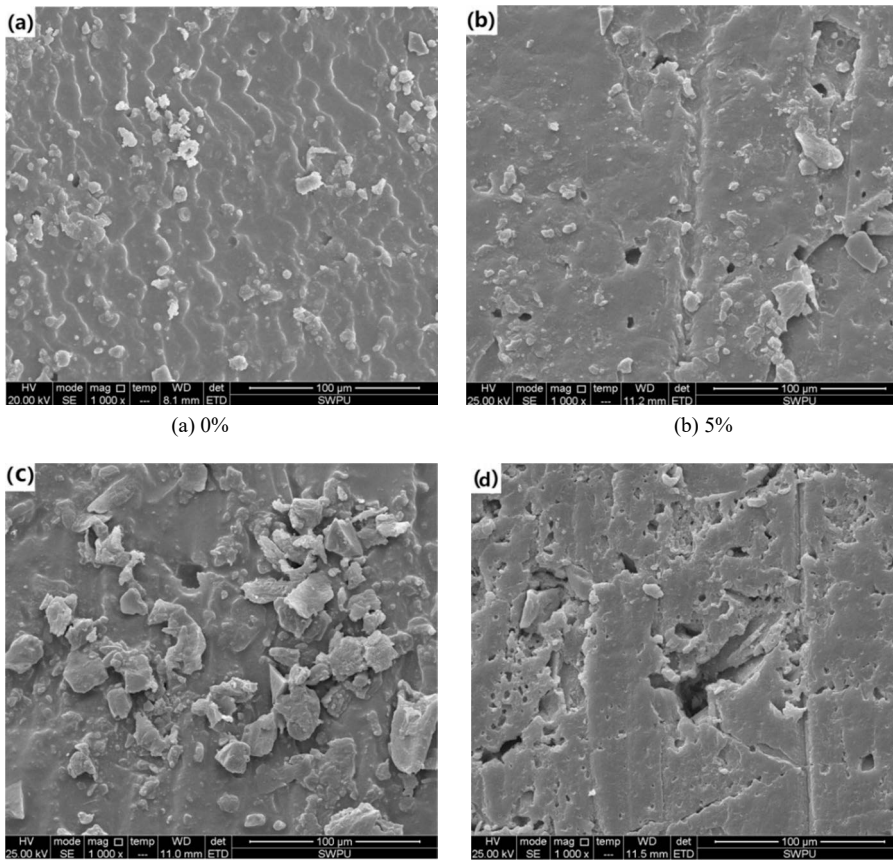


(a) 0% (b) 5%

(c) 10% (d) 15%

**Fig. 2-11.** An abrasion SEM topography of the rubber surface with different percentages of sand-bearing crude oil.

and the interaction force between sand particles also increases, which leads to the decrease of the force acting on the rubber surface and rubber wear. The morphology in Figure 2-11(c) shows that the rubber wear is the most serious. The surface layer shows a large area of rubber shedding due to wear. The number of sand scratches is the largest, and the morphology after wear is also more complex. In Figure 2-11(b), (c) and (d), the tearing stripes on the worn rubber surface are irregular, because there is not only sliding friction, but also rolling friction on the rubber surface, which is caused by the irregularity of sand particles and the interaction of friction force.

## References

[1] Jiacai Zhu, Yeying Ma and Hua Li. 1992. Nonmetallic Materials and Their Applications. Hu Bei Science and Technology Press, Wuhan (Chinese).

[2] Lingyan Wang. 2010. Study on Adhesion Mechanisms and Technological Parameters Optimization of Heat Vulcanization of Natural Rubber and Metal Composite Structure. Ph.D. Thesis, Xidian University, Xian, China (Chinese).

[3] Schiavone, P. and Hibbeler, R.C. 2020. Engineering Mechanics Statics Twelfth Edition Si Units Statics Study Pack Worldwide Edition. Pearson Publishers, England.
[4] Zhuo Zhuang, Timu Guo and Weiming Tao. 2005. Linear and Nonlinear Finite Elements and Their Applications. China Machine Press, Beijing.
[5] Xiuping Yang and Jinjin Guo. 2007. Study of contact abrasion for stator rubber of eccentric screw pump. Lubrication Engineering (04): 33–35 (Chinese).
[6] Gent, A.N. and Campion, R.P. 2001. Engineering with Rubber, how to Design Rubber Components. Hanser Gardner Publications, Carl Hanser Publishers, Munich.
[7] Mark, J.E. and Erman, B. 2005. Science and Technology of Rubber (Third Edition). Academic Press, New York.
[8] Zheng, M., Cui, Y. and Sun, F. 1998. Analysis of static temperature field of vehicle's solid rubber tire. Journal of Beijing Institute of Technology 7(2): 135–140.
[9] Yi-hu Song, Miao Du, Hong-mei Yang and Qiang Zheng. 2013. Structure and viscoelasticity of rubber materials. Acta Polymerica Sinica (09): 1115–1130 (Chinese).
[10] Jiazhao Chen, Minxiang Huang and Xueren Wang. 2015. Typical constitutive models of rubber materials and their ranges of application. Materials Reports (s1): 118–120 (Chinese).
[11] Rivlin, R.S. 1997. Large Elastic Deformations of Isotropic Materials. I. Fundamental Concepts. Collected Papers of R.S. Rivlin. Springer, New York.
[12] Dai, H.H. 1998. Model equations for nonlinear dispersive waves in a compressible Mooney-Rivlin rod. Acta Mechanical 127(1-4): 193–207.
[13] Seibert, D.J. and Schöche, N. 2000. Direct comparison of some recent rubber elasticity models. Rubber Chemistry & Technology 73(2): 366–384.
[14] Yeoh, O.H. 1993. Some forms of the strain energy function for rubber. Rubber Chemistry & Technology 66(5): 754–771.
[15] Yeoh, O.H. 2012. Characterization of elastic properties of carbon-black-filled rubber vulcanizates. Rubber Chemistry & Technology 63(5): 792–805.
[16] State Bureau of quality and technical supervision of the people's Republic of China. 2009. Rubber, Vulcanized or Thermoplastic - Determination of Tensile Stress-Strain Properties. China Standards Press, Beijing (Chinese).
[17] Lv, X.R., Song, S.Y. and Wang, H.M. 2015. Effect of $CO_2$ gas on the swelling and tribological behaviors of NBR Rubber in water. Journal of Materials Science & Technology (12): 1282–1288.

# 3

# Mechanical Behavior and Sealing Performance of the Rubber Sealing Rings

## 3.1 Materials and methods

The sealing performances of the rubber seal rings were examined numerically by using advanced computational tools in a rigorous manner, considering the nonlinear geometry of rubber material. Two-dimensional axisymmetric finite element models of the rubber rings, sealing groove, and cylinder liner were established based on the actual structure of sealing systems. Fluid carbon quenched and tempered steel are the materials used for the sealing groove and cylinder liner. The density is 7800 kg/$m^3$, Poisson's ratio is 0.3, and the elasticity modulus is 210 GPa. A contact penalty algorithm was employed to simulate the interactions between the ring and the steel. A contact algorithm was defined based on contact pairs between ring's surface and groove surfaces, and also between ring's surface and the cylinder liner surface.

As rubber has material nonlinearity, geometrical nonlinearity, and contact nonlinearity, it is necessary to make the following assumptions for mechanical and sealing performance research:

1) The rubber material used for a sealing ring has a determined Poisson's ratio and elasticity modulus.
2) Fluid will not corrode the rubber sealing ring.
3) The rubber sealing ring will not be affected by the fluid's temperature.
4) The volume of the sealing ring does not change with creep deformation.
5) The compression and tension of the rubber material have the same creeping property.

In practice, the rubber sealing ring has to face two different working conditions: static seal and dynamic seal.

## 3.2 O-ring

Two-dimensional axisymmetric finite element models of the O-ring, sealing groove and cylinder liner were established based on the actual structure of the sealing system. Cross-sectional diameter of the O-ring is 5.33 mm. The depth of the groove is 4.14 mm, width of the groove is 7.3 mm, and chamfer of the groove is 0.2 mm. Inner diameter of the O-ring is 90.7 mm. Inner diameter of the cylinder liner is 101.31 mm. A contact penalty algorithm with a friction coefficient equal to 0.12 was employed to simulate the interactions between the ring and steel material.

Static and reciprocating dynamic sealing performances were researched in this study. In accordance with actual conditions, pre-compression (0.5 mm) was completed to simulate the installation process of the sealing ring. Then, medium pressure ($P$ = 3 MPa) was loaded on the working surface of the sealing ring. The relative velocity ($v$ = 0.3 m/s) was applied in the reciprocating dynamic seal process. There are two movement directions in the reciprocating motion. One is the outward stroke, which is defined as the sealing groove moves against the direction of fluid pressure action. The opposite motion is when sealing groove moves towards the same direction of the fluid pressure, it is called inward stroke.

### *3.2.1 Tribology experiment*

The friction coefficient between rubber and steel was tested using a MMW-1 friction testing machine. The rubber samples were fixed on the steel plate by vulcanization. Nitrile butadiene rubber (NBR) is one of the most common rubber materials, and it is widely used in sealing components, gaskets, hoses, cables, and so on. The hardness of NBR is 80 Hr, with a tensile strength not less than 16 MPa, tensile elongation not less than 2, and volume change rate less than 15%.

The steel sample was a cylinder made from medium carbon quenched and tempered steel. The friction coefficients between rubber and steel sample under different lubricating conditions (including no lubricant condition, water lubrication condition, and oil lubrication condition) were tested when an axial compressive force ($F$ = 30 N) was applied.

Figure 3-1 shows the friction coefficient curves between rubber and steel samples under different lubricating conditions. The friction coefficients are different in different lubricating conditions. The maximum friction coefficient appears in the no lubricant condition while the minimum friction coefficient appears in the oil lubricant condition. In spite of different lubricating conditions, the friction coefficient fluctuates up and down around a fixed value respectively. The friction coefficients are 0.095, 0.32, and 0.515 in the oil lubrication, water lubrication and no lubrication, respectively. Oil lubrication is the most common in most traverse seals.

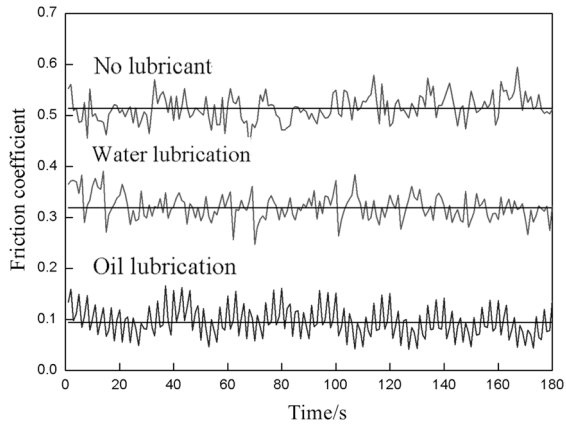


**Fig. 3-1.** The friction coefficient between rubber and steel in different lubricating conditions.

### *3.2.2 Static sealing performance*

#### *3.2.2.1 Sealing performance*

The rubber O-ring is in an interference assembly state after it is installed in the sealing groove. The stress and contact pressure distributions on the O-ring are shown in Figure 3-2. In the assembly state, the O-ring is compressed. The von-Mises stress distribution has a dumbbell shape. The maximum stress is on the inner surface of the ring's cross-section. The contact pressure is the gradient on the contact surfaces.

Under the action of fluid pressure, the O-ring comes into closer contact with the inner surfaces of the groove and cylinder liner. The contact pressure between the contact surfaces can prevent fluid leakage, which may occur when the maximum contact pressure is lesser than the fluid pressure.

According to the seal system structure, the leak occurs in two directions: one is in the clearance between the cylinder liner and the O-ring; the other is in the clearance between the groove and O-ring. Although there are two contact surfaces between the O-ring and the groove, there is only one contact surface between the O-ring and cylinder liner. Due to the relative motion of the O-ring and cylinder liner, the contact surface between them is weak, and it is the primary sealing surface. In Figure 3-2, the stress distribution undergoes a great change under the action of fluid pressure. There are three high-stress areas, close to three contact surfaces. In this condition, the fluid pressure is 3 MPa. The maximum contact pressures on the three surfaces are greater than 3 MPa, respectively. Therefore, the static sealing performance is reliable.

#### *3.2.2.2 Effect of the fluid pressure*

Under the action of different fluid pressures, the deformation and stress on the O-ring are different. As shown in Figure 3-3, the high-stress areas change from two to three with increasing fluid pressure. The maximum stress is close to the side surface of the grove; it also increases when the fluid pressure increases. There is a lower-stress area in the middle part of the cross-section. Additionally, the low-stress area also extends to the middle part with the fluid pressure increases. Therefore, it is suggested that material failure occurs first in the high-stress area of the cross-section.

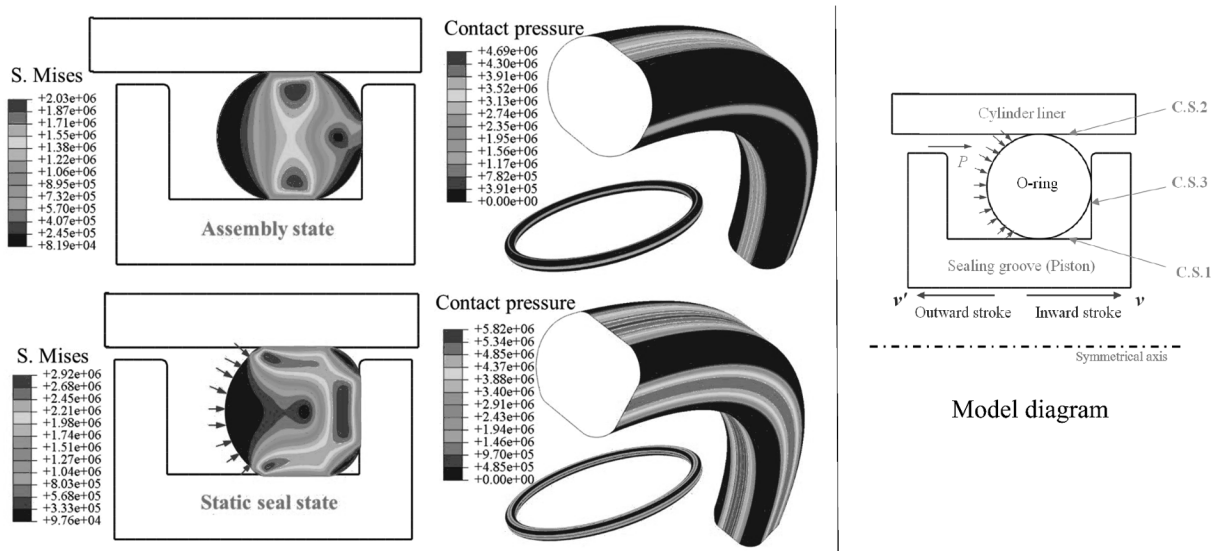


**Fig. 3-2.** The static seal performance of the O-ring.

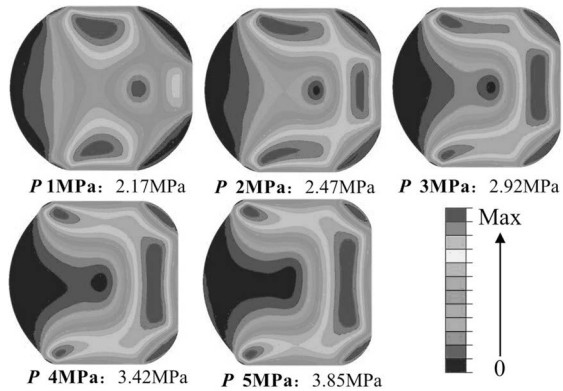


**Fig. 3-3.** The stress distribution on the O-ring under different fluid pressures.

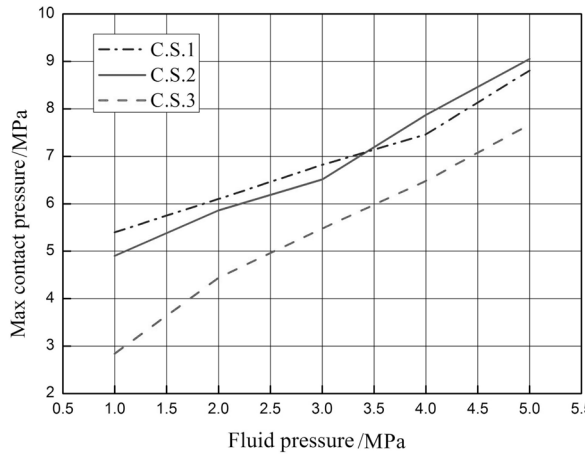


**Fig. 3-4.** The maximum contact pressure on the O-ring under different fluid pressures.

For the three contact surfaces (shown in Figure 3-2), the maximum contact pressures on the surfaces are shown in Figure 3-4. The maximum contact pressure on C.S.3 is the smallest, and it is still greater than the fluid pressure in any conditions. Therefore, the static sealing performance is very good in this seal range. The difference between the C.S.1 and C.S.2 is very small. The fluid pressure 3.4 MPa is a critical point of this difference. The maximum contact pressure curves have nonlinearity along with the fluid pressure.

### *3.2.2.3 Effect of the friction coefficient*

Oil lubrication is used in the vast majority of the seal systems. The friction coefficient ranges 0.05~0.2 was considered. Figure 3-5 shows the von-Mises stress distributions on the O-ring with different friction coefficients. In the static seal, the action process of fluid pressure is still affected by the friction coefficient. In the static sealing state, the stress distributions in the cross-section are different. The location of the high-

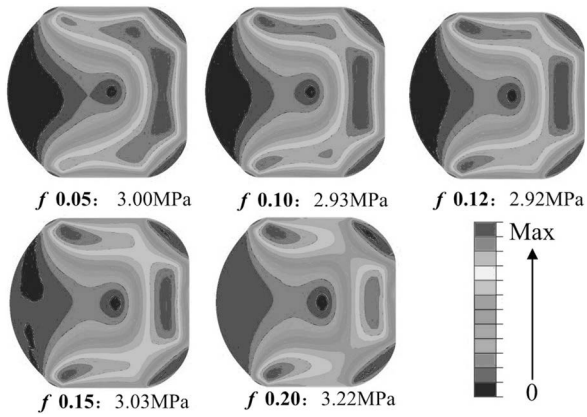


**Fig. 3-5.** The stress distribution on the O-ring with different friction coefficients.

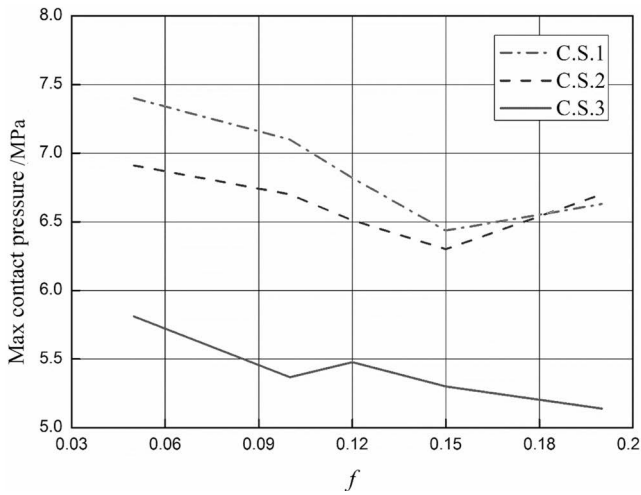


**Fig. 3-6.** The maximum contact pressure on the O-ring with different friction coefficients.

stress area changes when the friction coefficient increases, but the change in the maximum-stress is small.

Figure 3-6 shows the maximum contact pressure on the three surfaces under different friction coefficients. The contact pressure on C.S.3 is the least. For C.S.1 and C.S.2, the contact pressures decrease first and then increase with the increasing friction coefficient, but they are both greater than the fluid pressure 3 MPa. The difference between the contact pressures on C.S.1 and C.S.2 decreases when the friction coefficient increases. Therefore, the friction coefficient between the O-ring and cylinder liner also affects the static sealing performance.

### *3.2.2.4 Effect of the compression ratio*

The O-ring is pre-compressed in the process of assembling. Therefore, the compression ratio affects its sealing performance. The von-Mises stress on the

O-ring under different ratios between the compression and the O-ring's diameter is shown in Figure 3-7. The stress distributions on the cross-section are different under different compression ratios. The location of the high-stress area changes along with the compression ratio. The maximum stress decreases first and then increases with the increasing of compression ratio, and the high-stress area changes to three areas at first, and then to two.

Figure 3-8 shows the maximum contact pressure on the three contact surfaces under different compression ratios. The contact pressure on C.S.3 changes very slightly. Therefore, the compression ratio has little effect on the sealing performance between the O-ring and side wall of the groove. When the compression ratio is smaller than 4%, the contact pressure on the C.S.3 is the greatest. The contact pressure on the other contact surfaces increases with the increasing of the compression ratio. Therefore, compression can enhance the sealing performance of the O-ring.

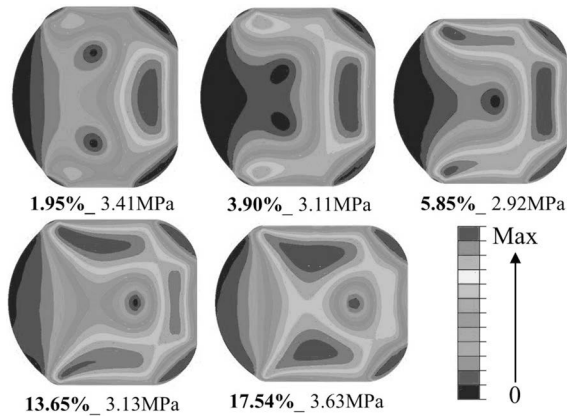


**Fig. 3-7.** The stress distribution on the O-ring under different compression ratios.

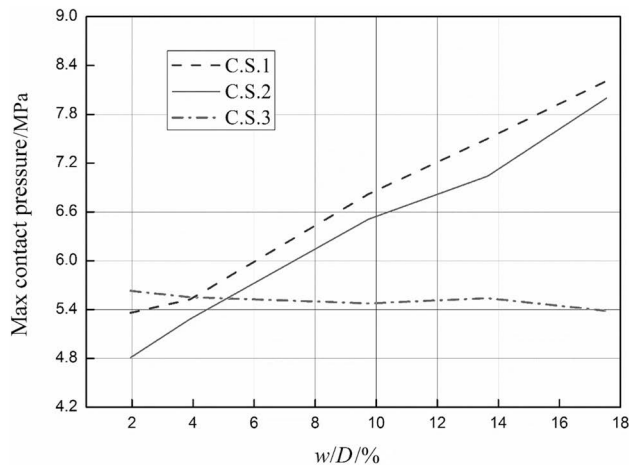


**Fig. 3-8.** The maximum contact pressure on the O-ring under different compression ratios.

### *3.2.3 Dynamic sealing performance*

#### *3.2.3.1 Sealing performance*

In the reciprocating seal system, there is a relative motion between the O-ring and cylinder liner. Therefore, the deformation and stress on the O-ring change according to the rubber material's approximate incompressibility. Figure 3-9 shows the typical stress distribution on the O-ring during the outward stroke and inward stroke when the velocity is 3 m/s. During the outward stroke, there is a persistent high-stress area and a changed high-stress area created near the side wall of the groove. During the inward stroke, one high-stress area occurs near the cylinder liner, and the other high-stress area occurs near the groove's side wall. Stress changes may result in changes of the O-ring's internal heat due to the rubber's lag effect caused by its viscoelasticity. These phenomena aggravate the failure of the O-ring.

Take the key points A, B, C, and D as examples (as shown in Figure 3-9); the stress curves of the four points are shown in Figure 3-10. The stress curves of any points are fluctuate in a reciprocating motion. Stress fluctuations are different when they occur during the inward stroke and outward stroke. The difference between the average stresses on point A in the two strokes is the greatest. The stress difference at points B and D during the two strokes is smaller. Stress fluctuation in the cross-section near the cylinder liner is greater than the fluctuation in the lower part of the O-ring during the reciprocating process. Sharp fluctuations in stress will lead to material fatigue failure. Therefore, the upper part of the O-ring is more prone to failure than the lower part. On the whole, the area around point A is dangerously weak due to great fluctuations in stress.

Figure 3-11 shows the maximum contact pressure on the seal surfaces during the dynamic seal process. The maximum contact pressure curves of sealing surfaces fluctuate. The contact pressure fluctuation in C.S.3 is serious. The amplitude changes in the contact pressure curves of C.S.1 and C.S.2 are smaller. The minimum contact pressure are greater than the fluid pressure 3 MPa. Therefore, the dynamic sealing performance is reliable. The sealing performance during the outward stroke is better

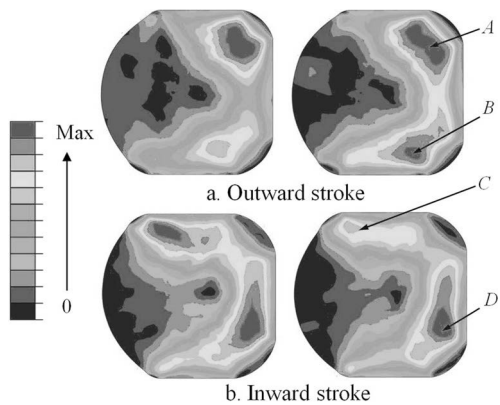


**Fig. 3-9.** The typical stress distribution on the O-ring in a dynamic seal.

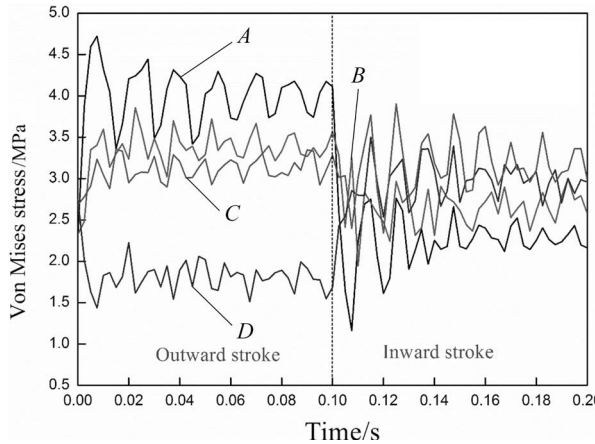


**Fig. 3-10.** The stress-time curves of the four points in the dynamic seal.

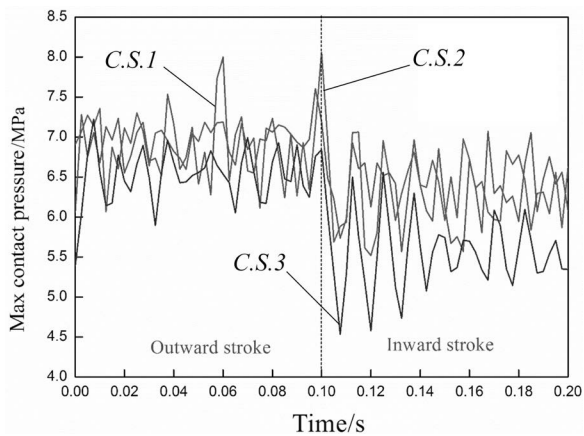


**Fig. 3-11.** The maximum contact pressure curves of the three seal surfaces in the dynamic seal.

than it is during the inward stroke. The fluctuation degree of the contact pressure is more serious during the inward stroke.

### *3.2.3.2 Effect of the fluid pressure*

The maximum contact pressure curves of the main seal surface (C.S.2) under different fluid pressures are shown in Figure 3-12. The greater the fluid pressure is, the greater the contact force between the O-ring and seal groove is. The contact pressure increases with the fluid pressure increases. The average value of the contact pressure during the outward stroke is greater than it is during the inward stroke. The difference also increases with an increase in fluid pressure.

Figure 3-13 shows the frictional force curves of the main seal surface under different fluid pressures. The frictional force curves fluctuate in a reciprocating motion because of the stick-slip phenomenon of the rubber material during the outward or inward stroke. The first wave crest of the frictional force in the outward stroke is the

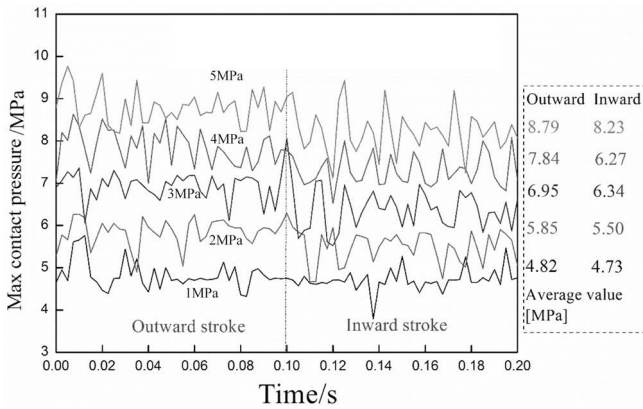


**Fig. 3-12.** The contact pressure curves of the main seal surface under different fluid pressures.

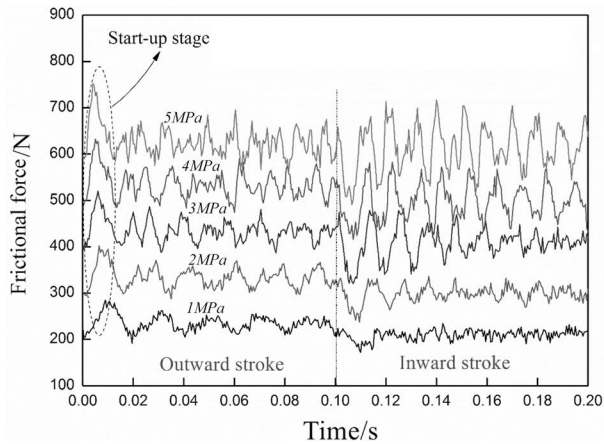


**Fig. 3-13.** The frictional force curves of the main seal surface under different fluid pressures.

transition from static seal to dynamic seal. In the starting phase of the dynamic seal, the frictional force between the O-ring and cylinder liner increases, and it reaches its maximum value in this process. Then the frictional force decreases and fluctuations in the stable movement occur during the second phase. From the outward stroke to inward stroke, the frictional force decreases, and it reaches its minimum value in this process. The volatility of the frictional force increases when the fluid pressure increases. The average frictional resistance also increases. Therefore, more energy is consumed in a reciprocating seal under higher fluid pressure, while designing the reciprocating seal system, frictional resistance and dynamic sealing performance need to be considered together.

### *3.2.3.3 Effect of the friction coefficient*

The friction coefficient between the O-ring and cylinder liner has a great effect on the dynamic sealing process. Figure 3-14 shows the maximum contact pressure on the main contact surface under different friction coefficients. The volatility of the

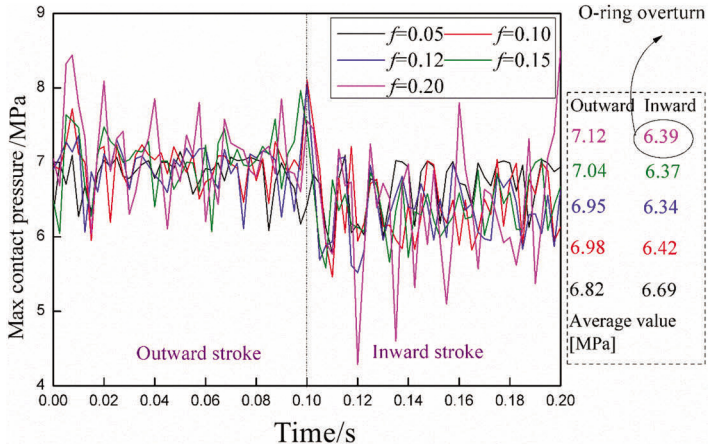


**Fig. 3-14.** The contact pressure curves of the main seal surface under different friction coefficients.

contact pressure increases with the increasing of the friction coefficient. Therefore, fluid leakage may occur during the dynamic seal under a bigger friction coefficient. Smoothing the parts' surfaces with a high machining precision and keeping them in good lubrication condition can help reduce the friction coefficient; then the fluid leakage can be reduced. The contact pressure during the inward stroke is lesser than during the outward stroke. The friction coefficient has a small effect on the average contact pressure during the dynamic seal. When the friction coefficient is 0.2, the O-ring overturns in the groove. The O-ring's contact surface changes in the dynamic process.

Figure 3-15 shows the frictional force curves of the main seal surface with different friction coefficients. When the frictional force is 0.05, fluctuation in the force curve is very small. It increases when the friction coefficient increases. In the initial stage, the frictional resistance is 1 kN when the friction coefficient is 0.2. So, the starting resistance is very large when the lubrication condition is poor. During the

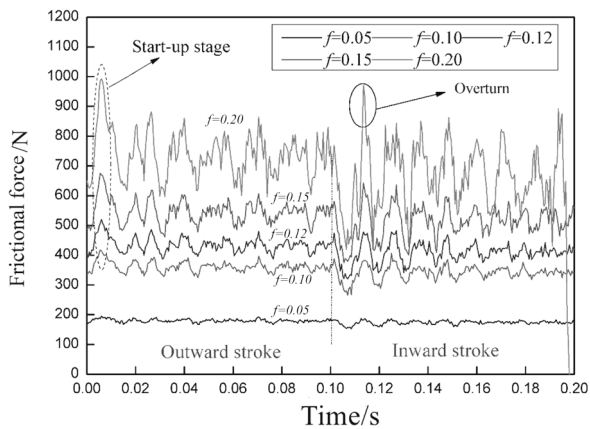


**Fig. 3-15.** The friction force curves of the main seal surface with different friction coefficients.

inward stroke, the fluctuation in the frictional force is more severe than it is during the outward stroke. When the friction coefficient is less than 0.15, the frictional force distribution laws are the same. Therefore, the friction coefficient doesn't affect the change rate of the frictional force. However, the fluid pressure has little effect on the distribution rule of the frictional force (as shown in Figure 3-13).

When the friction coefficient is 0.2, the distribution rule changes over time. During the outward stroke, the distribution rule of the frictional force is similar to the smaller friction coefficient conditions. The O-ring does not get overturned in this process. But the distribution rule of the frictional force changes quite differently from the others in inward stroke. It means that the O-ring has overturned in this process. Therefore, the frictional force curve can be used to judge the state of the O-ring in the groove.

In order to better investigate the motion state of the O-ring in the reciprocating dynamic seal, the deformations of the O-ring in a dynamic seal are shown in Figure 3-16 and Figure 3-17. When the friction coefficient is 0.15, the deformations in the O-ring are basically stable during the outward and inward strokes. Compared to the static seal, the upper part of O-ring is partially in contact with or away from the external gap due to the action of cylinder liner. Deformations on the O-ring are different in the two processes. Therefore, fatigue failure is more likely to occur in the dynamic seal.

In Figure 3-17, deformation of the O-ring is relatively stable in the outward stroke, and the ring doesn't overturn in this process. The overturn phenomenon occurs with difficulty also because it is hindered by the groove's side wall. But during the inward stroke, the deformation of the O-ring is different at different times. Overturn occurs along the counterclockwise direction in this process. Because the length of the groove is longer than the O-ring's diameter, there is a space occupied by fluid in the groove. Under the action of the cylinder liner's frictional force, overturn may occur

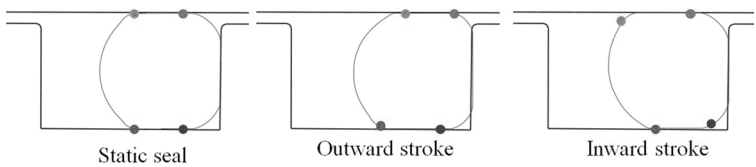


**Fig. 3-16.** The deformation of O-ring in the dynamic seal when f = 0.15.

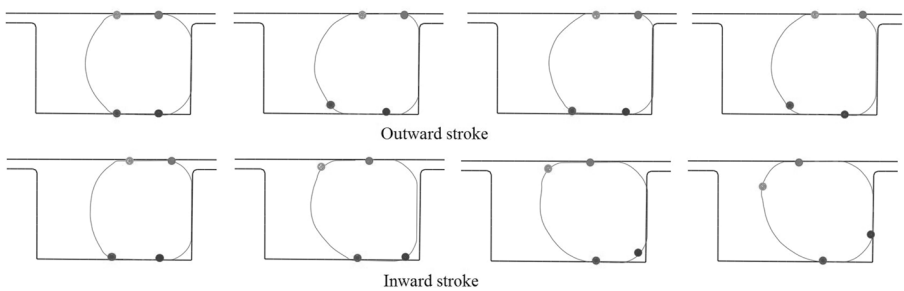


**Fig. 3-17.** The deformation of O-ring in the dynamic seal when f = 0.2.

when the friction torque is greater than the torque produced by the fluid pressure. The O-ring's overturn could result in fluid leakage. If the friction coefficients are different along the circumferential direction, the frictional forces are also different. That may cause the torsion angles to be different in different sections. Then, distortion of the O-ring occurs, which can lead to sealing failure. Therefore, a good lubrication condition and surface machining accuracy are essential for effective sealing.

### *3.2.3.4 Effect of the compression ratio*

Compression ratio directly affects the contact pressure between the O-ring and cylinder liner. Figure 3-18 shows the maximum contact pressure curves of the main seal surface under different compression ratios. The contact pressure on the O-ring increases with the increase in compression ratio. When the compression ratio is smaller than 9.4%, the difference between the average contact pressures in the outward stroke and inward stroke is small. With the compression ratio increases, the ring overturns during the inward stroke, and there is only a slight change in the average contact pressure. However, the ring doesn't overturn during the outward stroke.

Figure 3-19 shows the frictional force curves under different compression ratios. In the outward stroke, the distribution rules of the frictional force are the same. The

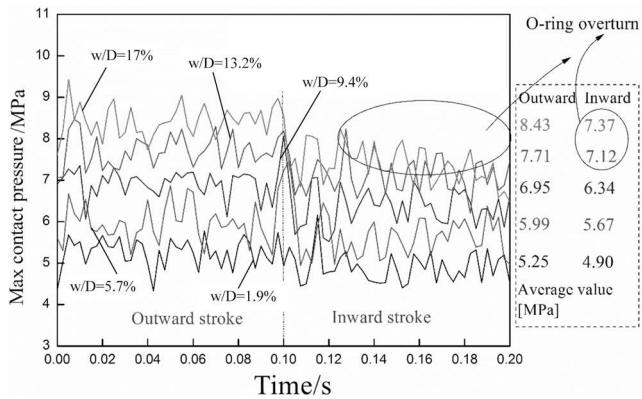


**Fig. 3-18.** The contact pressure curves of the main seal surface under different compression ratios.

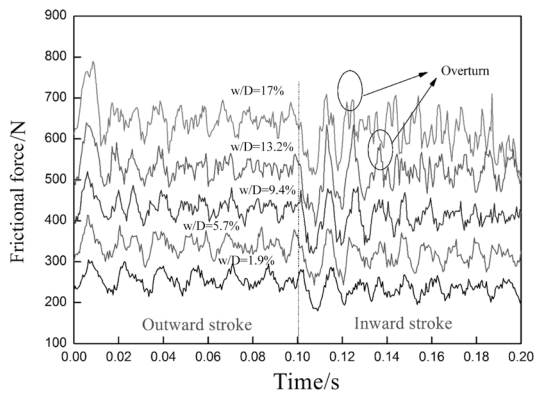


**Fig. 3-19.** The friction force curves of the main seal surface under different compression ratios.

frictional force increases when the compression ratio increases at a uniform rate. But during the inward stroke, the ring overturns when the compression ratio is greater than 9.4%. The frictional force distributions are random. However, the overturn time is later during the process when the compression ratio is 13.2% than when it is 17.6%. This is because the friction torque is greater when the compression ratio is 17.6%. Therefore, groove depth and the installation process need to be designed carefully to avoid O-ring's overturn during the dynamic seal.

### *3.2.4 Bitten failure analysis*

An improper design of the groove will result in bitten failure of the O-ring. Depth and chamfer are very important aspects of the groove design. Take for example, the three structures shown in Figure 3-20. There is no chamfer in structure 1, but the curvature radius of the chamfer is 0.2 mm in structure 2 and structure 3. At the same compression ratio, the gap between the cylinder liner and the groove is 1.46 mm for structure 1 and structure 2, but it is 0.96 mm for structure 3.

Figure 3-20 shows the von-Mises stress and contact pressure on the O-ring in static seal. The stress distributions on structure 1 and structure 3 are the same. But, for structure 1, there is a small extrusion part of the O-ring in the gap. This extrusion is the biggest for the gaps where distance is greater than 1.46 mm. This is because the gap distance is the sum of 1.46 mm and 0.2 mm. So, there is an obvious stress concentration near the gap. The maximum stress of structure 2 is 5.1 MPa, which is about greater than others by 19%. The contact pressures on structure 1 and structure 3 are evenly distributed. But there is a contact pressure concentration on

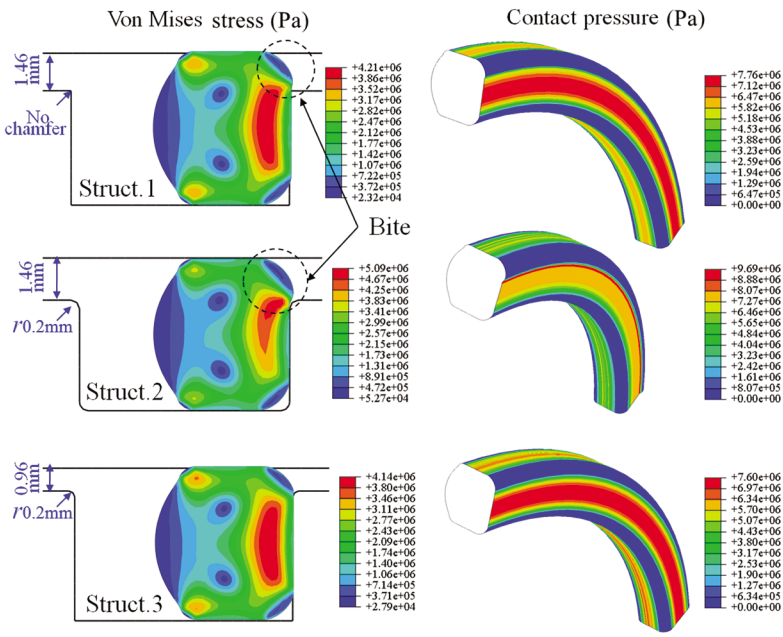


**Fig. 3-20.** The static seal performance of the O-ring in different grooves.

structure 2. Compared to structure 1, structure 3 is more efficient, the maximum stress is lesser, and there is no cutting effect subjected to the hard edge.

The von-Mises stress distributions on the O-ring in different grooves are shown in Figure 3-21. The stress concentrations on the O-ring are very obvious in the dynamic seal process. During the outward stroke, there is a big extrusion part of the O-ring in the gap for both structure 1 and structure 2. The high-stress area lies near the edge of the groove in both. However, the maximum stress on structure 2 is a little less than structure 1, and it is twice than that on structure 3. Therefore, excessive clearance distance will lead to a bitten failure of the O-ring. During the inward stroke, there is no extrusion phenomenon when the direction of the frictional force is different from the fluid pressure direction. The difference between the maximum stress on the three structures is small during the ward stroke. Bitten failure often occurs in structure 1 and structure 2 during the reciprocating movement. Therefore, the gap distance after the completion of the assembly should be considered carefully.

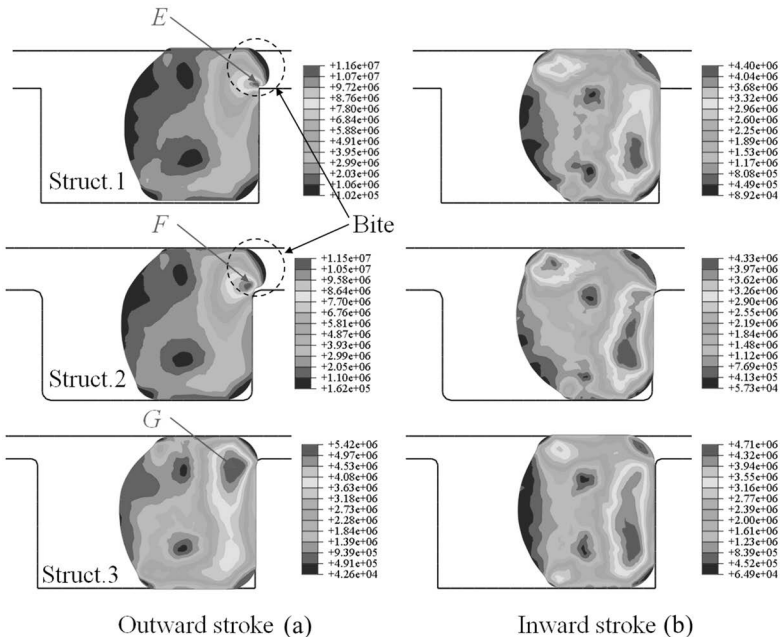


**Fig. 3-21.** The von-Mises stress distributions on the O-ring in different grooves.

The von-Mises stress curves of the key points (as shown in Figure 3-21) in the O-ring are shown in Figure 3-22. The curve change rules in structure 1 and structure 2 are the same; however, there is only a small difference in terms of stress. While the maximum stress on structure 3 is the least, the difference between the stress in the outward and inward strokes is smaller than it is in the other two structures.

The maximum contact pressure curves of the main seal surface in different grooves are shown in Figure 3-23. The fluctuation of the contact pressure on structure 2 is more severe than it is in the other structures; however, the average

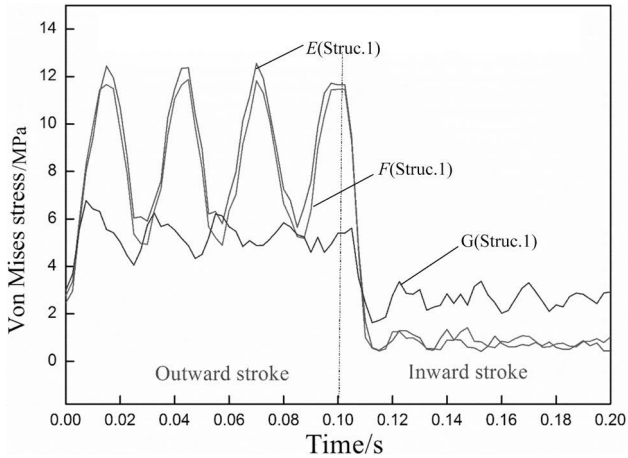


**Fig. 3-22.** The stress distribution on the three points in the dynamic seal.

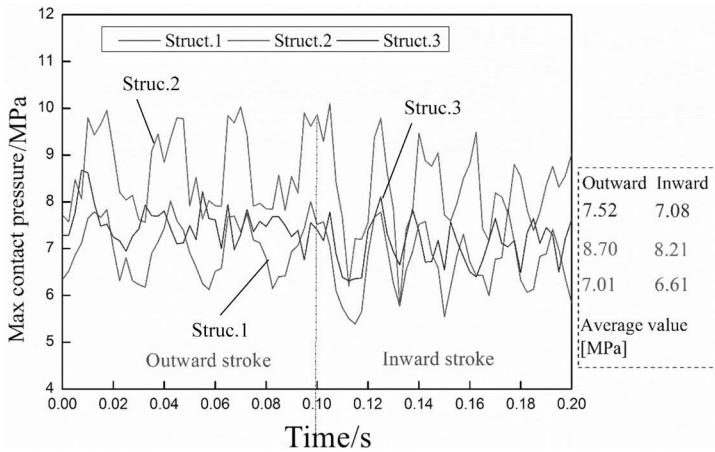


**Fig. 3-23.** The contact pressure curves of the main seal surface in different grooves.

contact pressure on it is greater than it is in the others. The contact pressure fluctuation in structure 3 is the smallest, and the average value of structure 3 is greater than structure 1. Therefore, after a comprehensive comparison, it can be said that structure 3 is a better structure than the others.

Under the same compression ratio, frictional forces on the main seal surface in different grooves are shown in Figure 3-24. The frictional force on structure 2 is little greater than it in on structure 1. It means that the chamfer can increase the friction resistance. The frictional force and its fluctuation are both the least in structure 3. The smaller width of the gap can reduce the friction resistance of the O-ring in the reciprocating motion. Thus, structure 3 is the best in terms of the parts moving smoothly and the friction energy consumption.

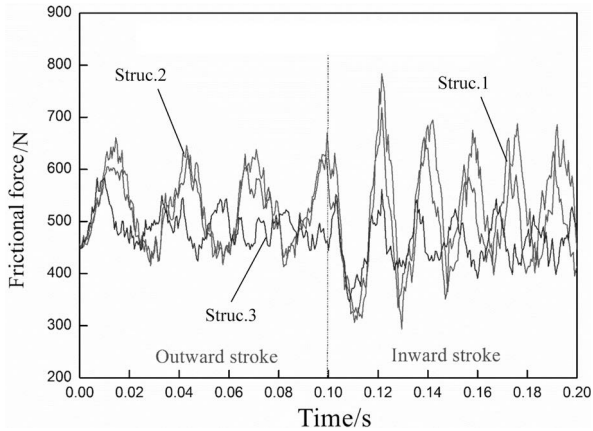


**Fig. 3-24.** The friction force curves of the main seal surface in different grooves.

## 3.3 D-ring

D-ring, O-ring, groove and slide bar were established by an advanced finite element program based on the actual structure of sealing system. As per related standard, the cross-section diameter of O-ring and the section length of D-ring are both 5.33 mm. The inner diameters of the sealing rings are both 45.20 mm.

### *3.3.1 Sealing performance*

When the compression amount is 0.3 mm, the von-Mises stress distributions on the D-ring and O-ring are shown in Figure 3-25. As Figure 3-25(a) shows, the high-stress area appears on the right end of the D-ring (in the semicircular convex) under none-pressure working condition. The maximum von-Mises stress of the D-ring is 1.757 MPa, which appears inside the sealing ring instead of the surface. Meanwhile, the von-Mises stress on the rectangular part of the D-ring is relatively slight. The von-Mises stress distribution on the D-ring is not symmetrical and the high-stress area is more concentrated on the top inner area of the D-ring. The high-stress area on the O-ring is distributed in a dumbbell shape. The maximum von-Mises stress on the O-ring is 1.287 MPa, 26.7% smaller than it is on the D-ring. When the fluid pressure is 3 MPa, the von-Mises stress distribution on the O-ring is shown in Figure 3-25(b). There is a big difference between the von-Mises stress on the sealing ring under none-pressure working condition and when it was under the pressured working condition. The maximum von-Mises stress on the D-ring appears on the surface when it comes into contact with the slide bar, but the high-stress area still appears on the right part of the D-ring. Under the action of fluid pressure, the high-stress area on the O-ring gradually transferred from its center to underside, and gets distributed in a rectangular shape. However, the high-stress area in the center of the O-ring is replaced by low-stress area. Under the pressured working condition, the maximum von-Mises stress on the O-ring is 3.491 MPa, while on the D-ring it is 19.7 percentage points lower (about 2.8 MPa). Therefore, compared with D-ring, the O-ring is more likely to failure.

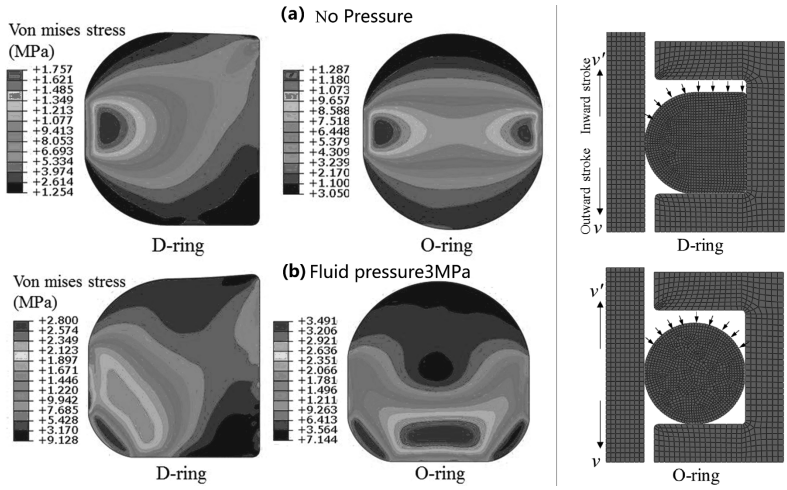


**Fig. 3-25.** The von-Mises stress distribution on the sealing ring.

Figure 3-26 shows the contact pressure distributions on the D-ring and the O-ring. While the sealing rings are under the none-pressure working condition, the maximum contact pressure appears on the main sealing surface, which is in contact with the slide bar. Also, the contact width of D-ring is larger than that of the O-ring. The maximum contact pressure on the D-ring is 2.8 MPa while it is 2 MPa on the O-ring. When the fluid pressure is 3 MPa, the contact pressure distributions on these two sealing rings are shown in Figure 3-26b. Under the action of fluid pressure, the rubber sealing rings come into contact with the slide bar and groove to achieve self-sealing. The contact pressure on the main surface of the D-ring is the maximum while it is relatively small on the other side. Both on the main surface and the other

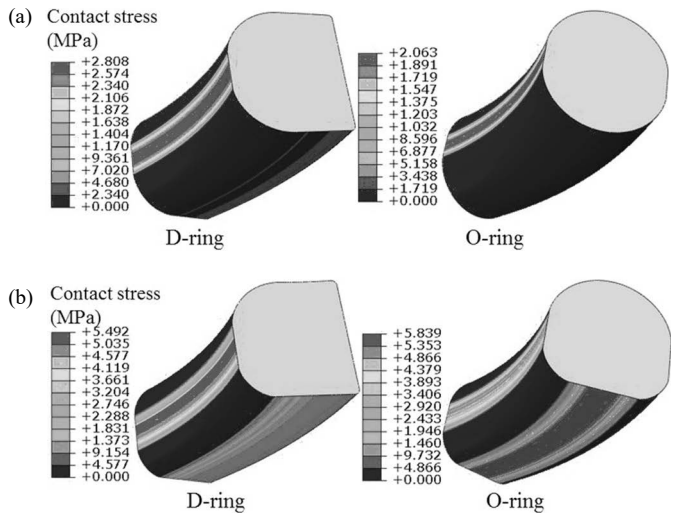


**Fig. 3-26.** (a) The contact pressure distribution on the sealing ring (no-pressure). (b) The contact pressure distribution on the sealing ring (fluid pressure 3 MPa).

side, the maximum contact pressures are more than 3 MPa which means D-ring can achieve good self-sealing. As for the O-ring, it can achieve good sealing despite the maximum contact pressure, which appears on the other side instead of on the main surface. Since there is no great difference in the maximum contact pressures on these two kinds of rubber sealing rings, the O-ring could be easily replaced by the D-ring in static sealing. In addition, when considering the function of the main sealing surface, the D-ring is much more reliable than O-ring.

### *3.3.2 Effect of the compression amount*

The appropriate compression amount can maintain the stable and reliable self-sealing nature of the rubber sealing ring. Figure 3-27a shows the curves of the maximum contact pressure on the main sealing surface of the D-ring and O-ring under different compression amounts with no fluid pressure for both. For both the D-ring and the O-ring, the maximum contact pressures on the main sealing surfaces increase with the increasing of the compression amount. Besides, the contact pressure on the D-ring

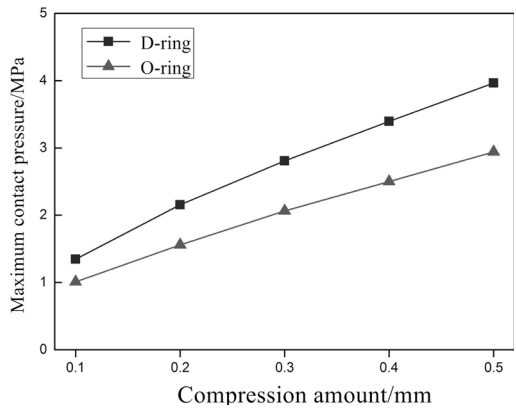


(a) None-pressure

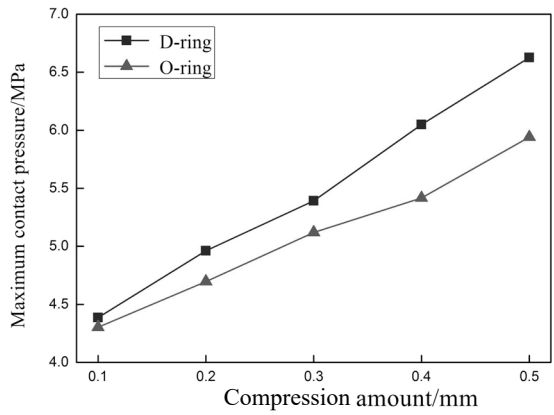


(b) Fluid pressure 3 MPa

**Fig. 3-27.** The contact pressure on the sealing ring under different compression amounts.

is always higher than it is on the O-ring. The maximum contact pressure curves of the main sealing surfaces on the D-ring and O-ring under different compression amounts when fluid pressure 3 MPa are shown in Figure 3-27b. The maximum contact pressure on both the rubber sealing rings is larger than the fluid pressure 3 MPa, which means they can well achieve the expected sealing performance. The maximum contact pressure on both rubber rings increases with the increasing of compression amount. However, compared to the O-ring, the D-ring has a higher growth rate of contact pressure when there is a change in compression amount. This ultimately causes the difference in the value of contact between the D-ring and the O-ring to greatly increase, when the compression amount increases.

### *3.3.3 Effect of the fluid pressure*

When compression amount is 0.3 mm, the maximum contact pressure curves of the main sealing surface of both D-ring and O-ring under different fluid pressures are shown in Figure 3-28. With the increase in fluid pressure, the maximum contact pressure on both the rubber sealing rings, which is also larger than its corresponding fluid pressure. Hence, well-performing sealing can be ensured. The difference in the contact pressure value between the D-ring and O-ring decreases as the fluid pressure increases. The D-ring's static sealing performance excelled that of the O-ring for the larger maximum contact pressure.

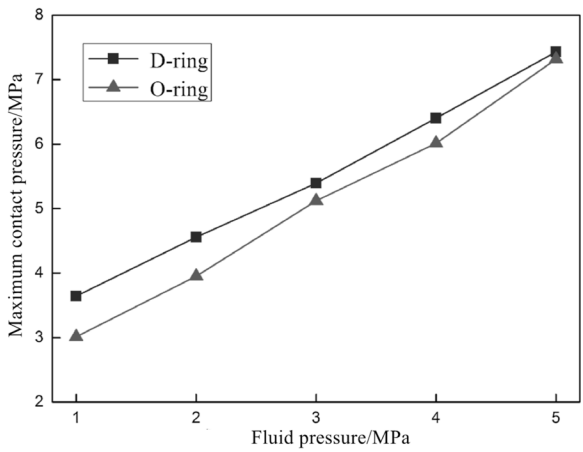


**Fig. 3-28.** The contact pressure on the sealing ring under different pressures.

### *3.3.4 Effect of the rubber hardness*

The Shore hardness of rubber sealing rings which are generally applied in multiple fields is from 70~90 Hr. [2] derived physical parameters (C1 and C2) which are quite consistent with engineering practice for creating rubber materials under different hardness. The parameters are shown in Table 3-1.

Figure 3-29a shows the curves of the maximum contact pressures on the two rings' main sealing surfaces with different rubber hardness, when the compression

**Table 3-1.** Parameters of rubber materials with different levels of hardness [2].

| Hardness/Hr | $C_1$ | $C_1$ |
|---|---|---|
| 70 | 1.137 | 0.023 |
| 75 | 1.444 | 0.0165 |
| 80 | 1.833 | –0.003 |
| 85 | 2.334 | –0.034 |
| 90 | 2.972 | –0.082 |

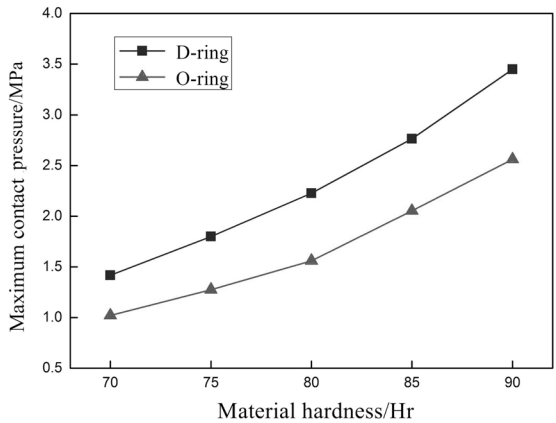


(a) None-pressure

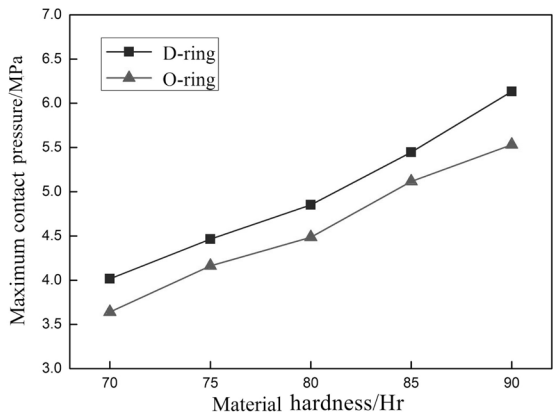


(b) Fluid pressure 3 MPa

**Fig. 3-29.** The contact pressure on the sealing ring with differences in rubber hardness.

amount is 0.3 mm and fluid pressure is 0. With the increasing of the rubber hardness, the maximum contact pressures on the main sealing surfaces of both rubber sealing rings increase nonlinearly. In addition, when fluid pressure is 3 MPa, the maximum contact pressures on the two sealing rings increase nonlinearly as well (as shown in Figure 3-29b). Whether under none-pressure condition or a pressured condition, the maximum contact pressure on the D-ring is greater than that on the O-ring, with a

corresponding increase in rubber hardness, which ensures the D-ring having a stable and better sealing performance.

### *3.3.5 Dynamic sealing performance*

In order to compare the dynamic sealing performance of the two sealing rings, the entire process of the reciprocating dynamic seal was simulated. The maximum contact pressures on the D-ring and O-ring in a reciprocating dynamic seal when axial velocity is 0.2 m/s, compression amount is 3 mm, and fluid pressure is 3 MPa are shown in Figure 3-30. To ensure its own viscoelasticity, the rubber sealing rings' maximum contact pressures fluctuate greatly when the reciprocating motion begins. By contrast, the stress fluctuation in the D-ring is much greater at this stage of the reciprocating motion. But when the reciprocating motion reaches the stable stage during the outward or inward stroke, the maximum contact pressure on the D-ring is always greater than it is on the O-ring. Besides, contact pressure fluctuation on the D-ring is relatively small and the sealing performance is more stable which makes the D-ring meet the sealing requirements satisfactorily. Since the semicircular structure of the D-ring's inner surface inherits a good self-sealing function from the O-ring and the structure of D-ring's outside has the same advantages as a rectangular ring, a D-ring can effectively avoid the damages of distortion and scroll. In addition, these factors prolong its working life.

The friction coefficient between the rubber sealing ring and the steel mechanism plays an important role in the reciprocating dynamic seal process. It has a significant impact on the ring's sealing performance, operation stability, and frictional wear. According to the experimental test, friction coefficients under the oil lubricating condition, the water lubricating condition, and the no lubricant condition are around 0.1, 0.3 and 0.5, respectively. Therefore, five working conditions under different friction coefficients (0.1, 0.2, 0.3, 0.4, 0.5) were analyzed. The maximum contact pressure curves of D-ring with different friction coefficients when reciprocating velocity is 0.2 m/s are shown in Figure 3-31. At the stable stage of the outward stroke, the maximum contact pressure on the D-ring increases with the increasing of the friction coefficient. Nevertheless, friction coefficient has little influence on the maximum contact pressure when the reciprocating motion occurs at the stable

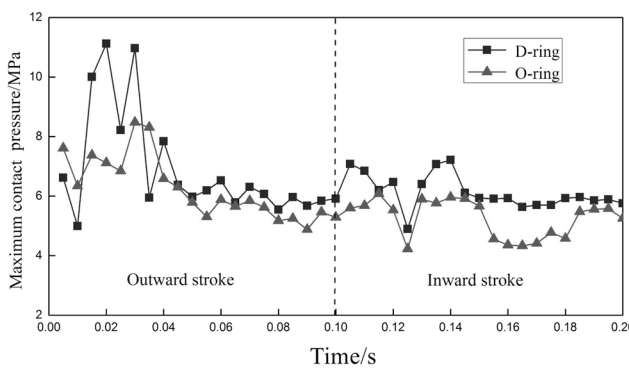


**Fig. 3-30.** The contact pressure on the sealing ring during the reciprocating motion.

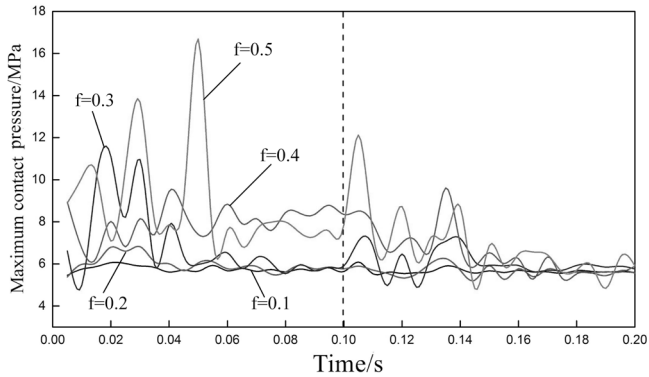


**Fig. 3-31.** The contact pressure on the sealing ring with different friction coefficients.

stage of the inward stroke. During the whole process of the reciprocating motion, the amplitude of contact pressure fluctuation increases with the increasing of the friction coefficient.

The maximum amplitude of the contact pressure fluctuation appears at the beginning of both the outward stroke and the inward stroke. When friction coefficient is 0.1, the contact pressure variation on the D-ring is the smoothest. When friction coefficient is 0.5, the contact pressure on the D-ring fluctuates wildly and the difference between the maximum and the minimum values is 11.84 MPa. Additionally, the creeping phenomenon appears at the beginning of the outward stroke, which could have a serious effect on the sealing performance. Meanwhile, a high friction coefficient may not only lead to a severe deformation of the sealing ring's cross-section but also greatly reduce the working life of the sealing ring.

## 3.4 X-ring

The cross-section length of X-ring is 5.33 mm and the inner diameter is 45.20 mm. The initial preloading shrinkage of the sealing ring is 0.3 mm. In the static seal, the pressure of fluid medium is 3 MPa.

### *3.4.1 Static seal characteristics*

Figure 3-32(a) shows the stress distribution on the sealing ring with no pressure after installation. The maximum von-Mises stress is 1.302 MPa, and the maximum stress does not appear on the contact surface of the sealing ring, but it is in the four antennae of the sealing ring, which is at a certain distance from the contact position. The stress distribution conforms to the Hertz classical contact mechanics theory. With the increase in the compression amount, the stress concentration begins to appear at the bottom of the two large arcs. When the compression amount increases to a certain value, the maximum stress position on the sealing ring is transferred to the bottom of the two large arcs. There is no fluid pressure, the four contact angles of the sealing ring come into contact with the sliding rod and the bottom of the groove, and the maximum contact pressure is 2.222 MPa.

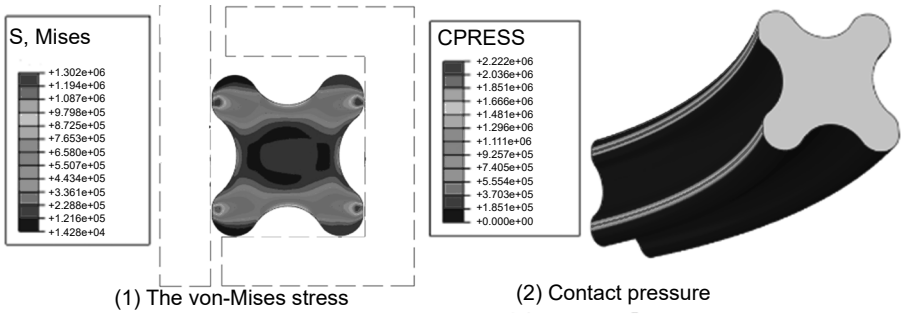


(a) None-pressure

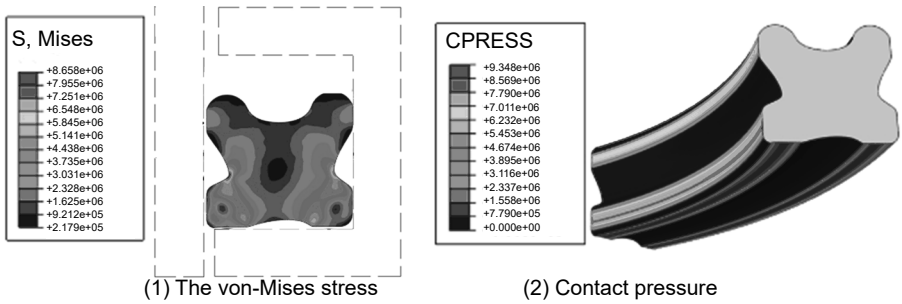


(b) Fluid pressure 3 MPa

**Fig. 3-32.** The stress distribution of the X-ring.

Figure 3-32(b) shows the stress distribution of the sealing ring when the fluid pressure is 3 MPa. Under the action of fluid pressure, the sealing ring is compressed, and the contact pressure between the sealing ring and the sliding rod and groove increases, so as to realize self-sealing. The maximum von Mises stress is 8.658 MPa at the bottom of the left and right circular arc, which is 7.356 MPa higher than it under no pressure condition. The maximum contact pressure occurs when the ring comes into contact with the groove side. Because the contact surface between the sliding rod and the sealing ring is the main sealing surface, when the maximum stress on the contact surface is greater than the fluid pressure, effective sealing can be achieved, otherwise leakage will occur. Therefore, the main sealing surface is as the research object. Under these condition, the maximum contact pressure on the main sealing surface is 8.55 MPa, which is higher than the fluid pressure, and thus the sealing occurs safely.

### *3.4.1.1 Effect of the compression amount*

The proper compression amount is a necessary condition to ensure the self-sealing effect of the sealing ring. Figure 3-33(a) shows the stress curve of the X-ring with different compression amounts under no pressure condition. The maximum von Mises stress and contact pressure on the sealing ring increase with the increasing of compression amount, and their change rates are close. The stress curve with different compression amounts when the fluid pressure is 3 MPa is shown in Figure 3-33(b).

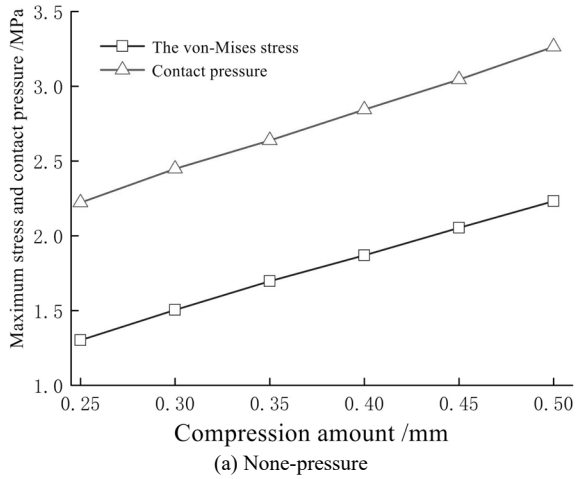


(a) None-pressure

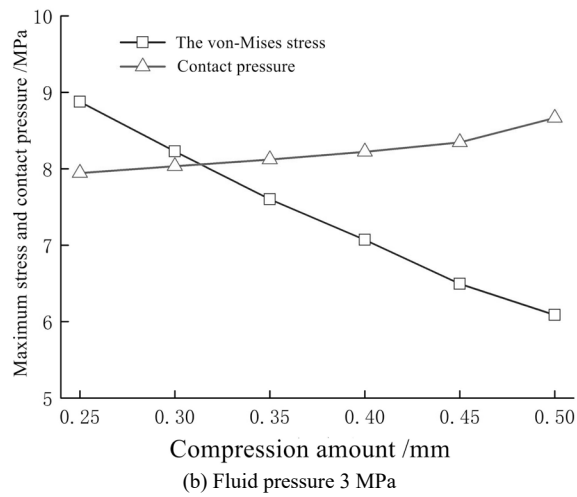


(b) Fluid pressure 3 MPa

**Fig. 3-33.** The stress curve on the sealing ring under different compression amounts.

Under the working pressure, the maximum von Mises stress on the sealing ring decreases with the increasing of the compression amount, while the contact pressure increases. This is caused by the special structure of the X-shaped sealing ring. It can be seen from Figures 3-32 and 3-33 that the working fluid pressure causes the axial deformation of the sealing ring, resulting in the change of the maximum von Mises stress position of the sealing ring, and the stress concentration appears at the bottom of the left and right large arc. With the increase of the compression amount, the radial deformation of the sealing ring is larger, which makes the left and right large arc surfaces close to the plane, offsets part of the axial deformation due to the pressure effect, so as to reduce the deformation of the sealing ring and improve the stress concentration. Because the contact pressure is caused by radial deformation, which increases with the increase of the compression amount.

### *3.4.1.2 Effect of the friction coefficient*

The friction coefficient between the rubber sealing ring and the sliding rod is affected by the surface roughness of the sliding rod, the number of abrasive particles and the lubrication condition. The preloading shrinkage is 0.35 mm, and the variation curve of the maximum von-Mises stress and contact pressure of the sealing ring with the friction coefficient are shown in Figure 3-34. When there is no fluid pressure, with the increase of friction coefficient, the maximum von-Mises stress and contact pressure of the sealing ring increase according to the nonlinear law. When the fluid pressure exists, the von-Mises stress and contact pressure of the sealing ring gradually decrease with the increase of the friction coefficient, but the maximum contact pressure is still higher than the fluid pressure, so a good seal can be achieved.

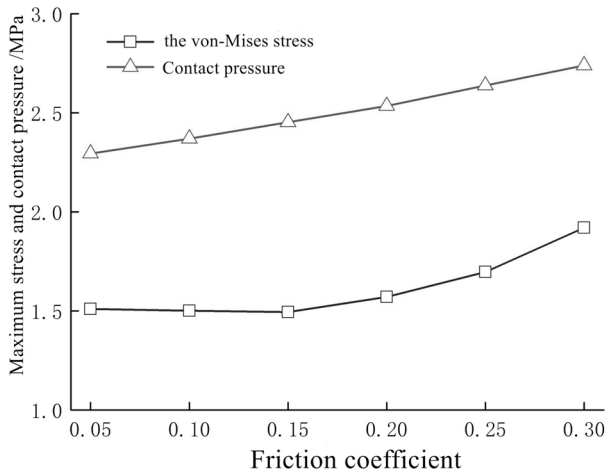


(a) None-pressure

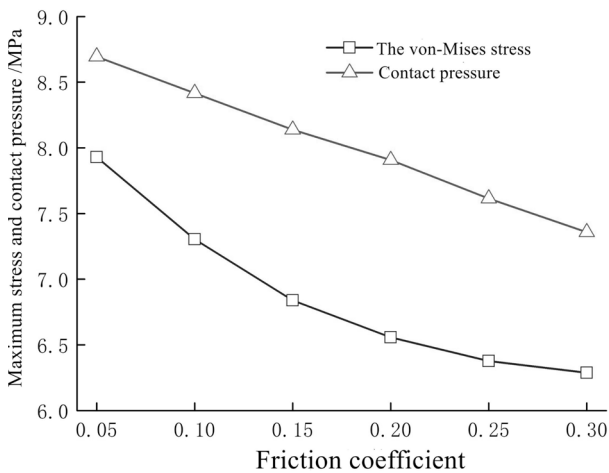


(b) Fluid pressure 3 MPa

**Fig. 3-34.** The stress curve on the sealing ring with different friction coefficients.

#### *3.4.1.3 Effect of the fluid pressure*

The maximum working pressure on the X-ring is 5 MPa without the retaining ring. When the compression amount is 0.35 mm, the maximum von-Mises stress and contact pressure on the sealing ring under different fluid pressures are shown in Figure 3-35. The maximum von-Mises stress and contact pressure increase with the fluid pressure increases. The contact pressure is always greater than the corresponding fluid pressure, so good sealing can be achieved.

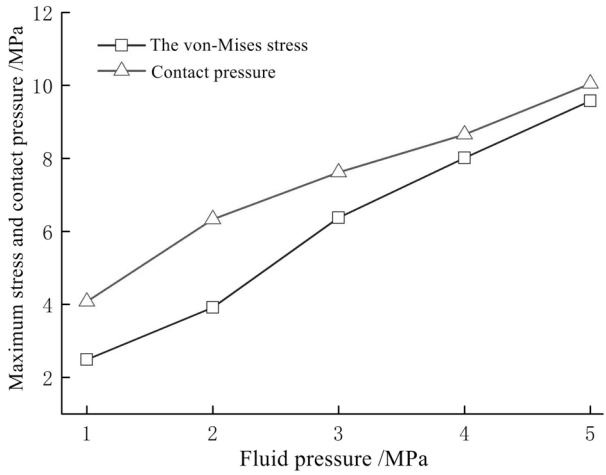


**Fig. 3-35.** Stress and contact pressure curve on the sealing ring under different fluid pressures.

#### *3.4.1.4 Effect of the rubber hardness*

Except for a few special cases, the shore hardness of a rubber sealing ring is generally 70 ~ 90. The parameters are shown in Table 3-1.

When the preloading shrinkage is 0.3 mm, the maximum von Mises stress and contact pressure on the sealing ring under different fluid pressures as shown in Figure 3-36. When there is no fluid pressure, the von-Mises stress and contact pressure increase nonlinearly with the rubber hardness increases. When the fluid pressure is 5 MPa, the von Mises stress and contact pressure on the sealing ring also increase with the increase of hardness, but their change rate first increases and then decreases. Although the greater the rubber hardness, the greater the contact pressure and the better the sealing performance is, the von-Mises stress on the sealing ring body also gradually increases, which easily leads to premature failure of the sealing ring.

### *3.4.2 Improvement of the sealing ring section*

It can be seen from the previous analysis that the stress concentration easily appear at the bottom of the left and right large arcs of the X-shaped sealing ring, especially for the reciprocating motion condition. The stress value is in a fluctuating state, which will greatly reduce the fatigue life of the sealing ring. Therefore, it is necessary to improve the cross-section shape of the sealing ring. The basic principle of improving the performance of the sealing ring is to reduce the equivalent stress on it, and make

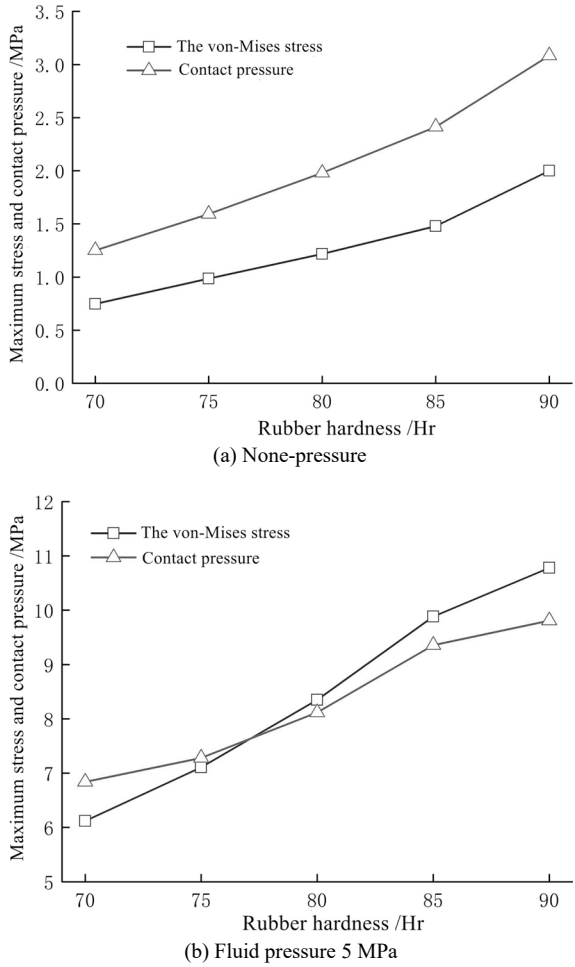


**Fig. 3-36.** The stress change on the sealing ring with different rubber hardness.

the stress distribution more uniform for reducing the stress fluctuation and improving the sealing performance and service life. For the optimization of the shape curve, the semicircular curve is used for the three protrusions of the sealing surface based on the good self-sealing advantages of the circular section. The new structure is improved by having the two large arcs of the sealing ring come into contact with the sliding rod and the bottom surface of the groove. The improved section shape is shown in Figure 3-37. One large cavity in the initial structure is changed into two small cavities, and three contact bumps are formed on the main sealing surface. Based on the drag reduction mechanism of a non-smooth surface in bionics, the concave and convex arc are transited to avoid stress concentration and reduce the surface resistance while ensuring a good sealing performance. The improved sealing ring inherits the advantages of the traditional X-ring, such as it not being easy to twist and roll, and its structure can effectively reduce the stress concentration. With special

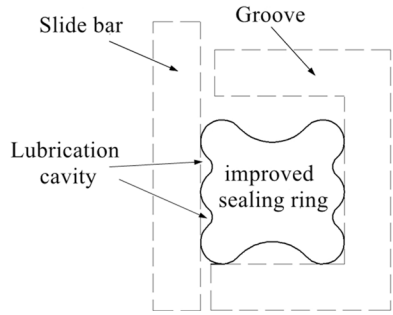


**Fig. 3-37.** A schematic diagram of the improved sealing ring.

importance for the reciprocating seal process, the new structure effectively avoids the reciprocating torsion of the upper-left corner bulge in the X-shaped sealing ring and improves the service life of the sealing ring.

### *3.4.2.1 Performance of the static seal*

In order to verify the rationality of the designed sealing ring, the numerical calculation model of the improved structure is established, and the static seal is analyzed. The stress and contact pressure distributions of the improved sealing ring are shown in Figure 3-38. When the preload shrinkage is 0.35 mm, under the pressure conditions of 0 and 3 MPa, the von-Mises stress on the middle bulge of the ring is the largest, and the contact pressure between the middle bulge and the sliding rod is also the greatest. The maximum stress appears at the bottom of the small cavity on both sides. The

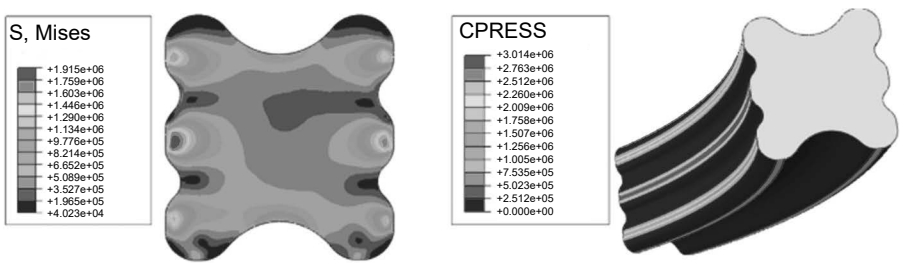


(a) None-pressure condition

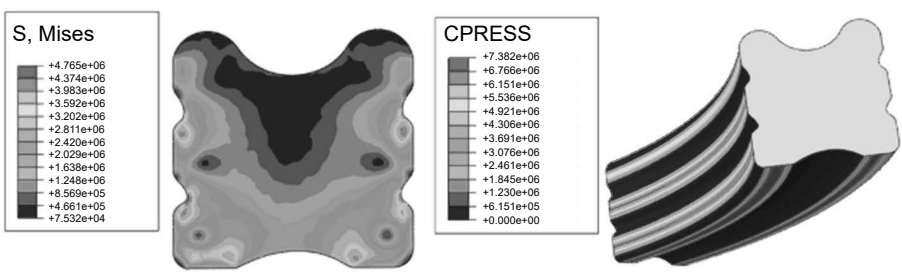


(b) Fluid pressure 3 MPa

**Fig. 3-38.** Stress and contact pressure distributions of the improved sealing ring.

maximum contact pressure on the whole sealing ring is still on the contact surface with the groove side wall, while the contact pressure on the two outer protrusions on the main sealing surface is larger, thus forming three sealing lines, which fully ensures the sealing performance.

Table 3-2 shows the stress comparison of two sealing rings under different fluid pressures. It can be seen that the stress and contact pressure on the improved structure is less than that on the original structure. The von-Mises stress reduction on the improved structure increases with the fluid pressure increases, which indicates that the higher the pressure, the more stable the improved structure is, and the premature failure caused by excessive stress is avoided. Although the contact pressure on the improved structure is lower than that on the original structure, the variation is small. The fluctuation in the contact pressure is small when there is fluid pressure. And the contact pressure is greater than fluid pressure under various working conditions, which can ensure good sealing. Therefore, the mechanical performance of the improved structure is better than that of the original structure, and the sealing safety is better guaranteed.

**Table 3-2.** Comparison of two kinds of sealing rings under different pressures.

| Stress/MPa | The von-Mises stress (MPa) | | | Contact pressure (MPa) | | |
|---|---|---|---|---|---|---|
| | Initial | Improvement | Increment | Initial | Improvement | Increment |
| 1 | 2.485 | 2.361 | –0.124 | 4.074 | 4.426 | 0.352 |
| 2 | 3.915 | 3.711 | –0.204 | 6.332 | 5.878 | –0.454 |
| 3 | 6.377 | 4.642 | –1.735 | 7.615 | 7.197 | –0.418 |
| 4 | 8.010 | 5.400 | –2.610 | 8.653 | 7.934 | –0.719 |
| 5 | 9.576 | 6.257 | –3.319 | 10.05 | 9.314 | –0.734 |

The stress comparison of two sealing rings under different compression amounts when the fluid pressure is 3 MPa is shown in Table 3-3. It can be seen that the von-Mises stress of the improved structure remains basically unchanged when the preloading shrinkage increases. At the same time, the difference between the contact pressure on the improved structure and the initial structure is less affected by the compression amount.

**Table 3-3.** A comparison of two kinds of sealing rings under different preloaded pressures.

| Compression/ mm | The von-Mises stress (MPa) | | Contact pressure (MPa) | | | |
|---|---|---|---|---|---|---|
| | Initial | Improvement | Initial | Improvement | Initial | Improvement |
| 0.25 | 8.878 | 4.666 | –4.212 | 7.945 | 6.717 | –1.228 |
| 0.3 | 8.228 | 4.494 | –3.734 | 8.034 | 7.218 | –0.816 |
| 0.35 | 7.601 | 4.624 | –2.977 | 8.122 | 6.729 | –1.393 |
| 0.4 | 7.071 | 4.691 | –2.38 | 8.223 | 7.195 | –1.028 |
| 0.45 | 6.494 | 4.813 | –1.681 | 8.347 | 7.284 | –1.063 |
| 0.5 | 6.089 | 4.960 | –1.129 | 8.666 | 7.599 | –1.067 |

### *3.4.2.2 Performance of the reciprocating seal*

Reciprocating dynamic seal performance is an important standard to evaluate the performance of a high-pressure generator. The stress history of initial structure and improved structure with time when the reciprocating speed is 0.2 m/s is shown in Figure 3-39. In Figure 3-39(a), the maximum stress on the sealing ring in the reciprocating seal is in a fluctuating state, and the mean value of the maximum stress in the internal and external stroke of the improved structure is less than that on the original structure, which indicates that an improved sealing ring structure can reduce its failure probability and prolong its service life in the reciprocating seal. In Figure 3-39(b), the contact pressure fluctuation in the improved structure is more stable than in the reciprocating motion process. Average contact pressure in the whole motion process is higher than that of the original structure, which indicates that the working state of the improved structure in the dynamic seal is more stable, and the sealing performance is better.

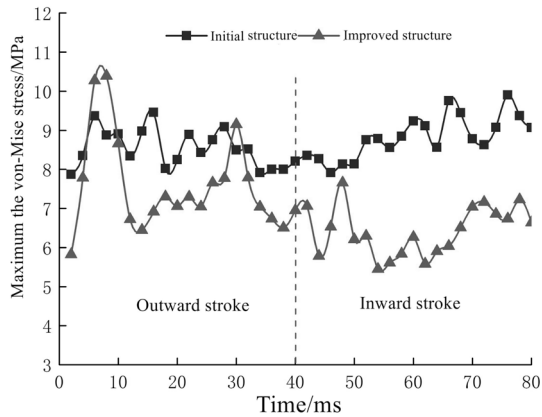


(a) The von-Mises stress

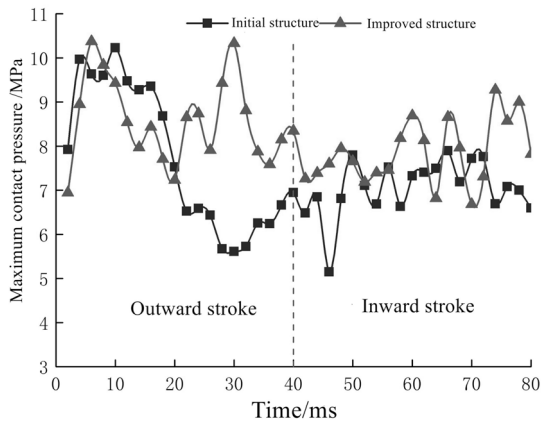


(b) Contact pressure

**Fig. 3-39.** Stress change process in reciprocating seals.

Figure 3-40 shows the cross-section deformation of the two sealing rings during the reciprocating motion. By comparing the section shape of the sealing ring in the inner and outer stroke, the feeler swing of the X-ring in the inner and outer stroke is more intensely. The high-frequency reciprocating motion will lead to fatigue failure of the feeler. At the same time, there is a hysteresis heat caused by the viscoelasticity of rubber material, as well as the friction heat of the contact surface will greatly reduce the mechanical properties of the rubber material, which may lead to fatigue failure of the feeler tear. In an improved sealing ring, the cross-section deformation in the internal and external stroke is small, which can greatly reduce the fatigue failure probability of the sealing ring.

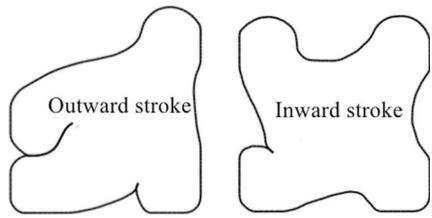


(a) Initial structure

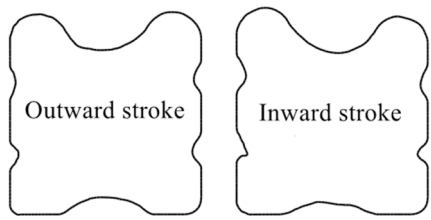


(b) Improved structure

**Fig. 3-40.** Deformation diagram of a sealing ring in reciprocating seal.

## 3.5 Rectangular ring

### *3.5.1 Effect of the initial compression ratio*

To achieve sealing, the compression ratio of the rectangular sealing ring should reach 8%~–14% [1]. For this rectangular ring, inner diameter is 45 mm, the section size is 5.16 mm, the compression ratio is 0.412–0.722 mm.

The von-Mises stress distribution on the sealing ring when there is no working fluid pressure is shown in Figure 3-41(a), and the von-Mises stress and contact pressure distributions on the sealing ring under a working pressure of 10 MPa are shown in Figures 3-41(b) and 3-41(c), respectively. The relationship between the maximum contact pressure and compression ratio of the rectangular sealing ring under no working pressure and 10 MPa is shown in Figure 3-42.

The maximum von-Mises stress on the sealing rings under no working pressure is concentrated on the two corners of the working edge. As the initial compression ratio increases, the maximum contact pressure also increases. The increase rate of contact pressure increases when the compression ratio is greater than 11%. When

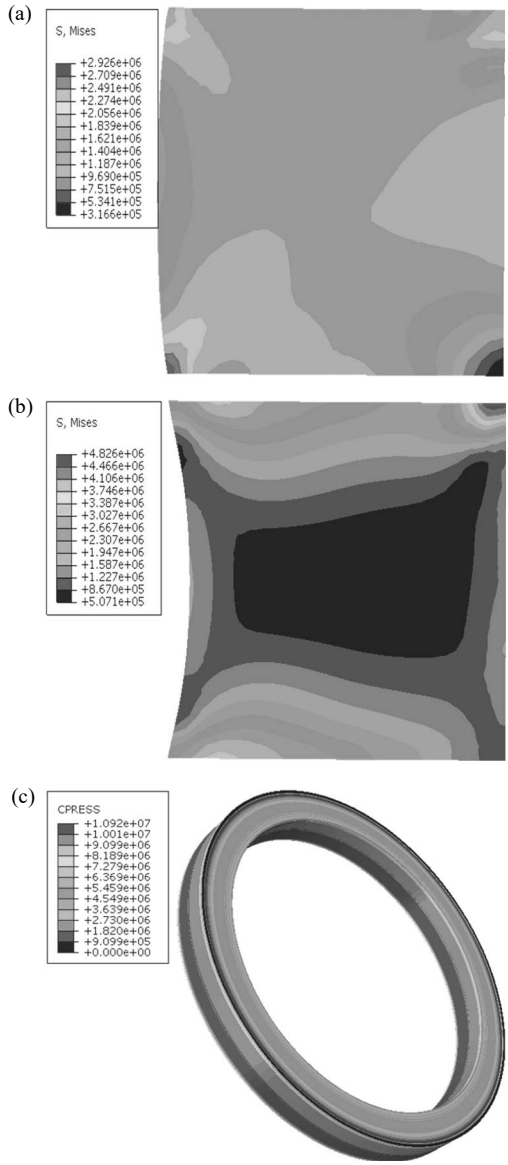


**Fig. 3-41.** The stress distribution on a rectangular sealing ring.

there is media pressure, the maximum von-Mises stress is concentrated on the upper contact surface near the gap between the shaft barrel and the groove, which indicate that the sealing rubber body is very easily sheared and fractured. As the compression ratio increases, the maximum contact pressure also increases slightly. The contact pressure is greater than the fluid pressure (10 MPa), so the rectangular sealing ring has a good sealing performance. The greater the initial compression ratio is, the better the sealing performance is.

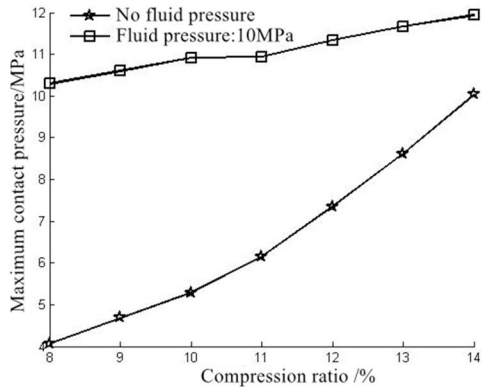


**Fig. 3-42.** The maximum contact pressure under different compression ratios.

### *3.5.2 Effect of the fluid pressure*

When the initial compression ratio is 10%, the maximum contact pressure and von-Mises stress on the sealing ring under different working pressures are shown in Figure 3-43. The contact pressure and von-Mises stress both increase with the increasing of working pressure and show a linear relationship. The maximum contact pressure on each point is greater than the corresponding working pressure value, which indicate that the sealing performance of the rectangular sealing ring is better.

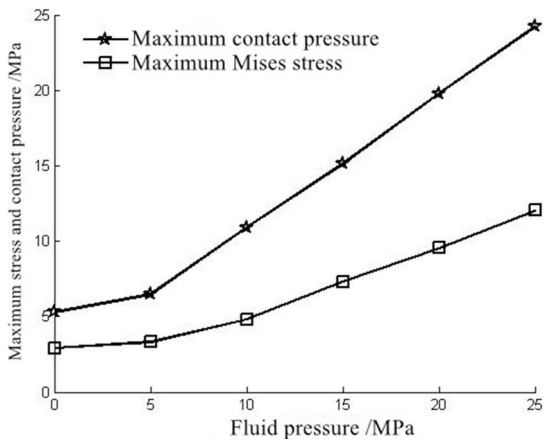


**Fig. 3-43.** The maximum stress under different fluid pressures.

### *3.5.3 Effect of the friction coefficient*

Manufacturing accuracy, immersion of fluid pressure, friction and wear may cause the friction coefficient change between the sealing ring and the groove wall. When the initial compression ratio is 10%, the maximum stress on the sealing ring with different friction coefficients under no pressure (after initial compression) and fluid pressure 10 MPa as shown in Figure 3-44. The maximum von-Mises stress and contact pressure both increase with the friction coefficient increases. The

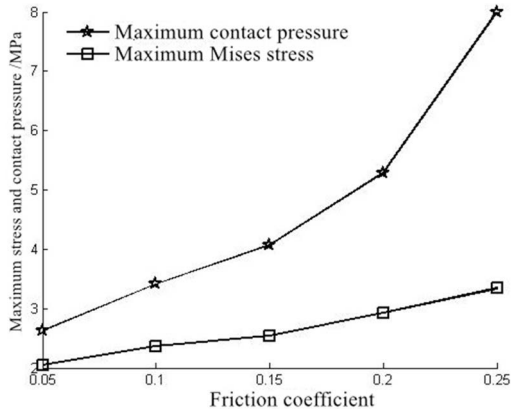


(a) None Pressure

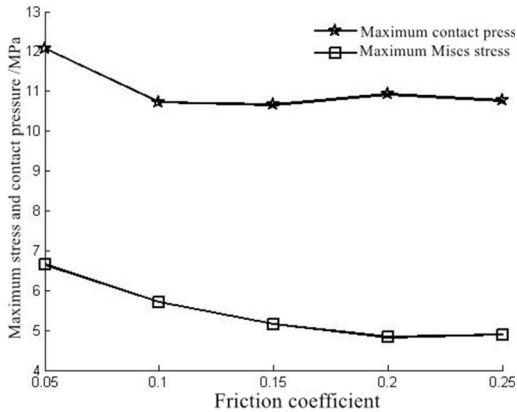


(b) Fluid pressure 10 MPa

**Fig. 3-44.** The maximum stress with different friction coefficients.

maximum von-Mises stress has a linear relationship with the friction coefficient, but the maximum contact pressure curve shows nonlinear characteristics. When there is a working pressure, the maximum von-Mises stress decreases with the friction factor increases, while the maximum contact pressure gradually decreases within the friction coefficient range of 0.05–0.15, and slightly increases within the range of 0.15–0.25. The friction coefficient has a great influence on the sealing performance and service life of the rectangular sealing ring, which must be considered in the design and research.

### *3.5.4 Effect of the rubber hardness*

The maximum stress of the rectangular sealing ring with different hardness when the initial compression ratio is 10% is shown in Figure 3-45. The maximum contact pressure and von-Mises stress increase linearly with the increasing of rubber hardness under no pressure. When the fluid pressure is 10 MPa, the maximum contact pressure of the sealing ring increases slightly with the increasing of rubber hardness.

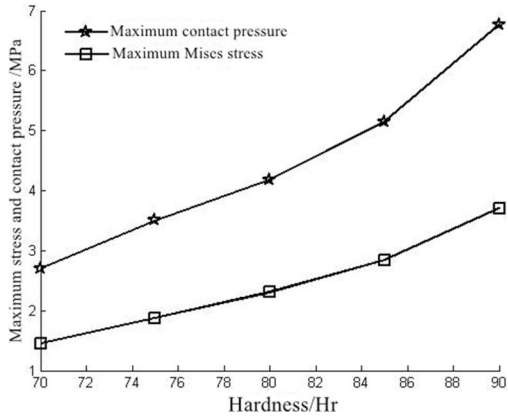


(a) None-pressure

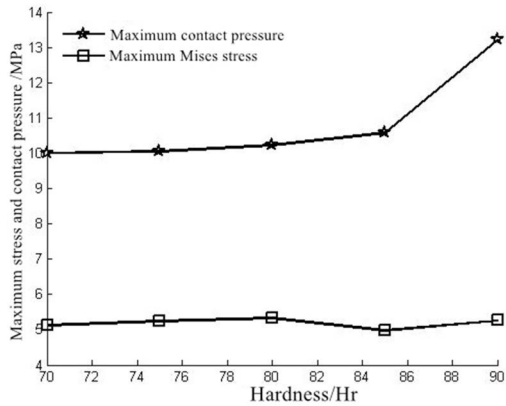


(b) Fluid pressure 10 MPa

**Fig. 3-45.** The maximum stress with different hardness.

## 3.6 Bio-mimetic ring

Bionics is built on the research of the features of animal anatomies, functional skins, and plant structures. In order to face the survival challenges and adapt to the harsh environment, many creatures improved their anatomies and epidermis micro-morphologies which made them survived. In recent years, with the development of manufacturing technology, it becomes possible to imitate the structures or functional skin of creatures.

### *3.6.1 Structure design*

Inspired by the functional surface of earthworm, morphological and structural bionics were used in the design of sealing ring. As shown in Figure 3-46, a new bio-mimetic sealing ring was designed based on the O-ring, the rectangular ring, and the X-ring. There are three concave ridges and three convex bulges on each side of the bio-mimetic ring, which is very similar to the surface of earthworm. In order to

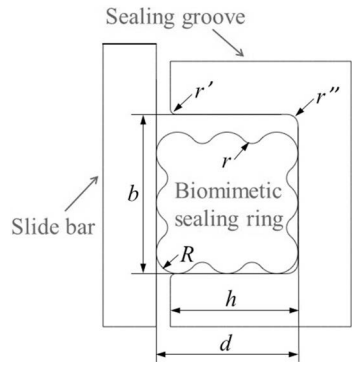


**Fig. 3-46.** A schematic diagram of the bio-mimetic sealing ring.

take advantages of the features of the O-ring like homogeneous stress distribution, all the bulges were designed as circular. Similar to the X-ring, the four corners of bio-mimetic sealing ring have circular arc transition.

This new structure has many advantages:

1) Under the lubrication condition, the concave ridges can serve as fluid dynamic bearing to generate additional fluid dynamic pressure.
2) When the concave ridge has enough volume, it can store lubricants and lubricate tribo-pair in the dynamic seal.
3) The concave ridge has the capacity of storing abrasive impurities to lower the abrasion caused by particles.
4) Under the action of compression amount and fluid pressure, the bulges can achieve self-sealing very well and three sealing tapes work in the main sealing surface, which can ensure excellent sealing performance.
5) In the reciprocating dynamic seal, the bio-mimetic sealing ring can avoid rolling and distortion, and the working life of the ring can be prolonged.
6) Due to the smaller contact area between the bio-mimetic sealing ring and the rigid wall, not only can friction and energy consumption be reduced but work efficiency can also be improved.

### *3.6.2 Static sealing performances*

#### *3.6.2.1 Stress on the sealing ring*

Stress distributions on the bio-mimetic sealing ring under none-pressure condition are shown in Figure 3-47. The von-Mises stress on the ring is distributed symmetrically with respect to a center line on the cross-section (as seen in Figure 3-47a). The maximum von-Mises stress is 3.72 MPa, and it appears on the second bulge on the inner surface. The von-Mises stress distribution on the bio-mimetic sealing ring agrees with the Hertz contact theory that stress does not appear on the contact surface but on the inside surface of the ring. As shown in Figure 3-47b, the maximum contact pressure is 4.856 MPa, and high contact pressure is concentrated on the three left

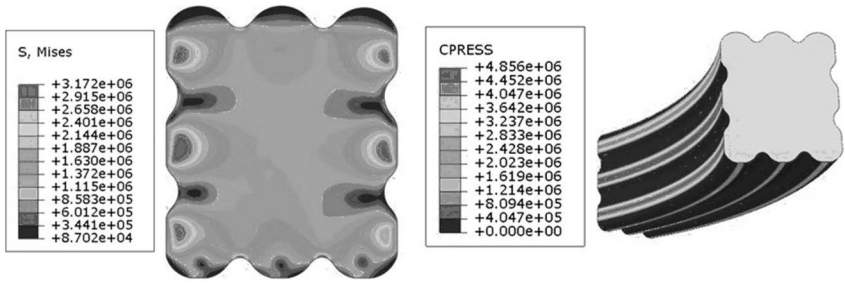


(a) The von-Mises stress (b) The contact pressure

**Fig. 3-47.** The stress distribution on the sealing ring under none-pressure condition.

bulges, which are also called the main sealing surface. Since the fluid pressure is 0 MPa, contact pressure on the bottom of the sealing ring is very slight.

When fluid pressure is 3 MPa, stress distribution on the bio-mimetic sealing ring is as shown in Figure 3-48. The contact pressure between the ring and rigid body increased after the ring was compressed by fluid pressure. In other words, the self-sealing of the ring has been achieved by fluid pressure. The von-Mises stress on the bottom increased and the stress distribution became more uneven with the increasing of fluid pressure. The maximum von-Mises stress is 4.976 MPa, which is about 1.804 MPa higher than it is in the none-pressure condition. The maximum stress still appears on the second bulges despite fluid pressure playing an important role in this sealing condition. Meanwhile, the maximum contact pressure (8.73 MPa) appears on the main sealing surface under none-pressure condition. According to the criteria, the maximum contact pressure has to be greater than or equal to the fluid pressure to meet the requirements of sealing, otherwise it may cause leakage. Therefore, this paper mainly focused on the stresses on the main sealing surface.

Figure 3-49(a) shows the deformation of the sealing ring under none-pressure condition. Under the action of compression amount, the sealing ring is squeezed, and its height increases by 0.288 mm along the axial. Figure 3-49(b) shows the deformation of the sealing ring when the fluid pressure is 3 MPa. Since the action of fluid pressure offsets the action of the radial compression amount, the axial deformation of the sealing ring is small, which is only 0.09307 mm.

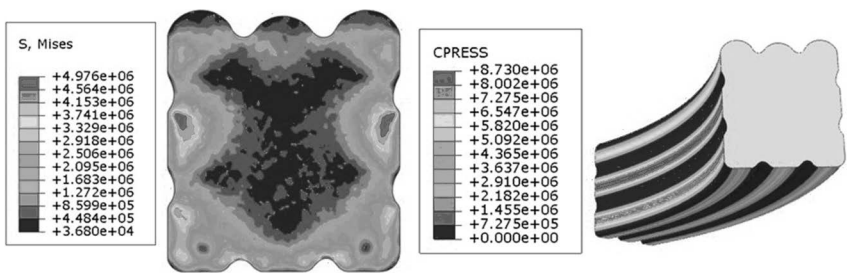


(a) The von-Mises stress (b) The contact pressure

**Fig. 3-48.** The stress distribution on the sealing ring when $P = 3$ MPa.

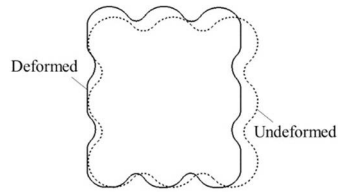


(a) None-pressure

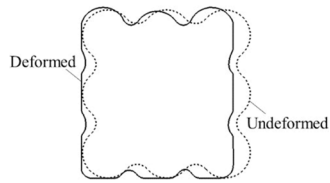


(b) Fluid pressure 3 MPa

**Fig. 3-49.** An image of the deformation in the sealing ring.

### *3.6.2.2 Effect of the compression amount*

The appropriate compression amount is an essential factor for the sealing ring to achieve a stable and reliable self-tightening seal. Figure 3-50 shows the maximum von-Mises stress and contact pressure on the bio-mimetic ring under different

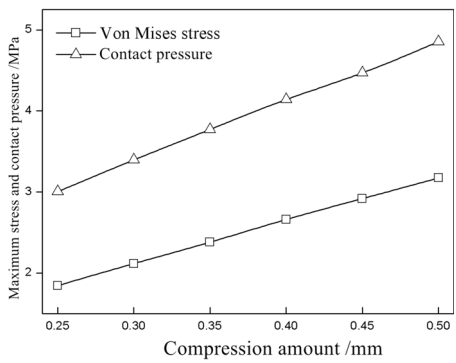


(a) None-pressure

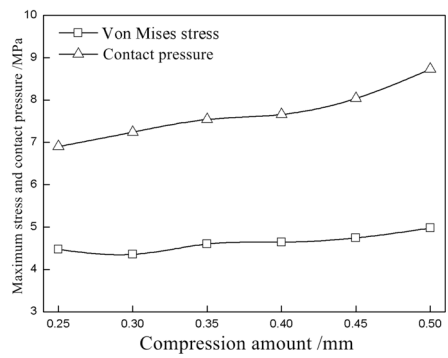


(b) Fluid pressure 3 MPa

**Fig. 3-50.** The stress on the bio-mimetic sealing ring under different compression amounts.

compression amounts. Both in none-pressure condition and the pressured condition, the von-Mises stress and contact pressure increase with the increasing of the compression amount. Two kinds of stress grow linearly under the non-pressure condition, but nonlinearly under the pressured condition. The stress curves of the ring present fluctuations with small amplitude under pressure, but the growth rate of the von-Mises stress is smaller. It means that compression amount has a lesser effect on the von-Mises stress under the pressured condition than under the none-pressure condition, because the axial strain caused by the fluid pressure can resist the radial strain caused by compression amount.

### *3.6.2.3 Effect of the friction coefficient*

According to the experimental result, the friction coefficient under different lubricating conditions is different. The structure of the bio-mimetic sealing ring is designed to store the lubricating fluid so that all the working conditions should be postulated as lubricated. Numerical simulations with a friction coefficient range from 0.15–0.35 were investigated, and the stress distributions are shown in Figure 3-51.

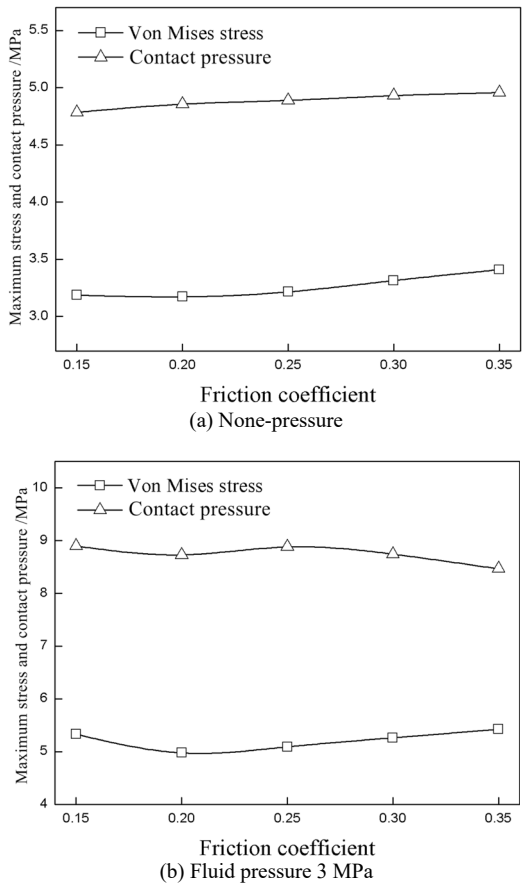


**Fig. 3-51.** Stress of the bio-mimetic sealing ring under different friction coefficients.

Under the none-pressure condition, both the von-Mises stress and contact pressure increase with the increasing of the friction coefficient, but within a small margin. As is shown in Figure 3-51b, when the fluid pressure is loaded, the bio-mimetic ring's contact pressure reduces with the increasing of the friction coefficient, which means the sealing performance has been weakened but can still meet the sealing requirement. However, the von-Mises stress first decreases and then increases with the increasing of the friction coefficient.

#### *3.6.2.4 Effect of the fluid pressure*

Figure 3-52 shows the curves of the maximum von-Mises stress and contact pressure under different fluid pressures. Both the von-Mises stress and contact pressure increase with the pressure, but grow nonlinearly. The maximum contact pressure on the main sealing surface is much higher than the fluid pressure which makes it possible for the bio-mimetic sealing ring to maintain a good performance in static seal.

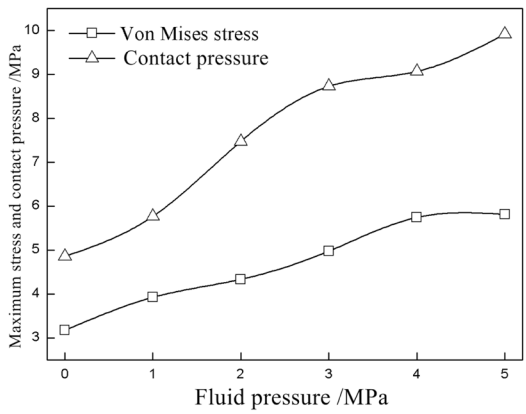


**Fig. 3-52.** Stress on the bio-mimetic sealing ring under different fluid pressures.

#### *3.6.2.5 Effect of the rubber material*

Figure 3-53 shows the maximum stresses on the ring with different material hardness. Both in the none-pressure condition and the pressured condition, the maximum contact pressure increases nonlinearly and the sealing performance becomes better with the increasing of the hardness of the rubber material.

When P = 3 MPa, the growth rates of the stress and contact pressure reduce gradually with the increasing of the hardness.

### *3.6.3 Dynamic sealing performances*

#### *3.6.3.1 Comparison with other sealing rings*

In order to research the reciprocating dynamic sealing performance of the bio-mimetic sealing ring, the sealing performance is compared with other kinds of sealing rings. The reciprocating dynamic sealing processes of these three rings are simulated.

The maximum von-Mises stress and contact pressure on the sealing rings mentioned above is shown in Figure 3-54. The maximum stress is fluctuant in the

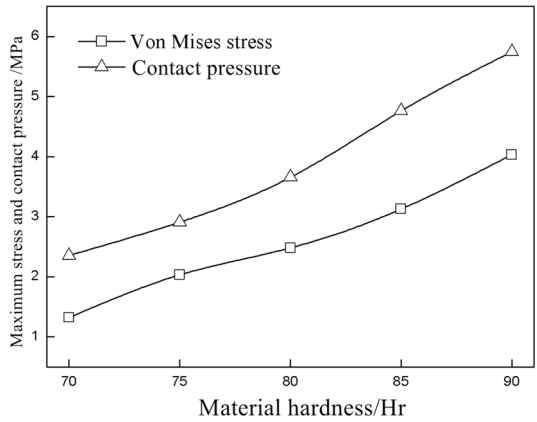


(a) None-pressure

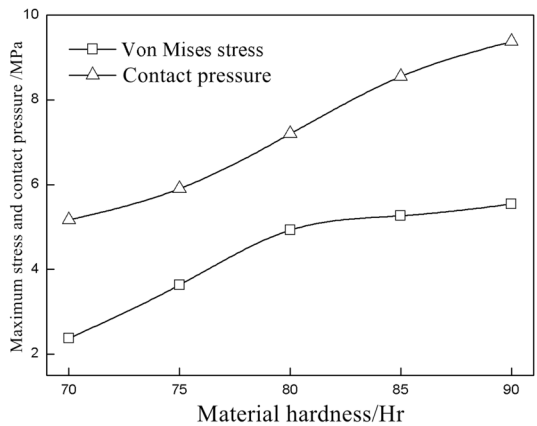


(b) Fluid pressure 3 MPa

**Fig. 3-53.** The stress on the bio-mimetic sealing ring under different hardness.

dynamic process for the rubber viscoelasticity. As shown in Figure 3-54(a), the von-Mises stress on the rectangular ring is higher than it is on the O-ring and the bio-mimetic ring, and its stress fluctuation is the greatest. It means that the rectangular ring is prone to tearing or resulting in fatigue failure. The von-Mises stress distributions on the O-ring and the bio-mimetic ring are more even in both the outward stroke and inward stroke. Therefore, the bio-mimetic ring can avoid premature failure.

As shown in Figure 3-54b, the contact pressure fluctuation on the rectangular ring is greater during the outward stroke, and a severe creeping phenomenon appeared. So, the rectangular ring is not suitable for dynamic sealing. The contact pressure on the bio-mimetic ring and O-ring are approximately the same, and so are their variation tendencies. Therefore, the bio-mimetic ring has the same sealing performance as O-ring, but the bio-mimetic ring can avoid rolling and distortion in reciprocating dynamic seal. So, the working life of bio-mimetic is much longer than that of the O-ring.

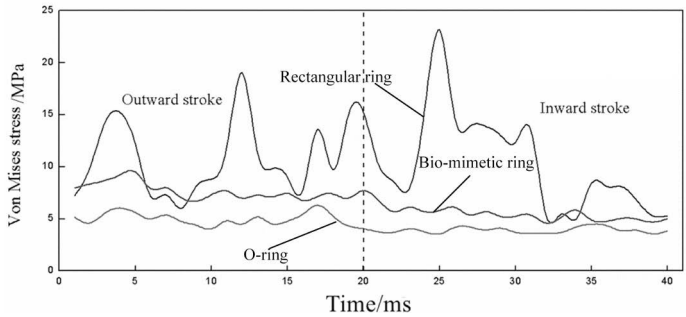


(a) The maximum von-Mises stress

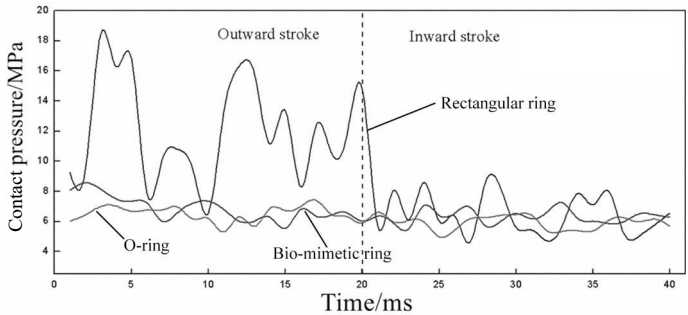


(b) The maximum contact pressure

**Fig. 3-54.** The stress and contact pressure on the sealing rings in the reciprocating dynamic seal.

### *3.6.3.2 Effect of compression amount*

Figure 3-55 shows the maximum von-Mises stress and contact pressure on the bio-mimetic sealing ring under different compression amounts. Before 7 ms, the maximum static friction is overcome and the reciprocating motion begins. The compression amount has a small effect on the stress fluctuation rule. As shown in Figure 3-55a, the maximum von-Mises stress increases with the increase in the compression amount during the outward stroke, but the effect of the compression amount on the von-Mises stress is slight during the inward stroke. As shown in Figure 3-55b, the maximum contact pressure increases with the increasing of the compression amount. The contact pressure is higher at the beginning of the reciprocating motion. The contact pressure fluctuation in the inward stroke is higher than it is in the outward stroke.

### *3.6.3.3 Effect of friction coefficient*

Figure 3-56 shows the von-Mises stress and contact pressure on the bio-mimetic sealing ring under different friction coefficients. At the beginning of the reciprocating motion, the von-Mises stress and contact pressure are higher than they are later during the reciprocating motion. The von-Mises stress and contact pressure increase with the increase of the friction coefficient, but the change rates in the inward stroke are higher than they are in the outward stroke. When friction coefficient is larger than

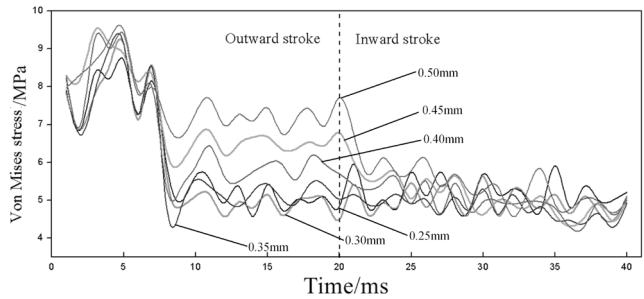


(a) The maximum von-Mises stress

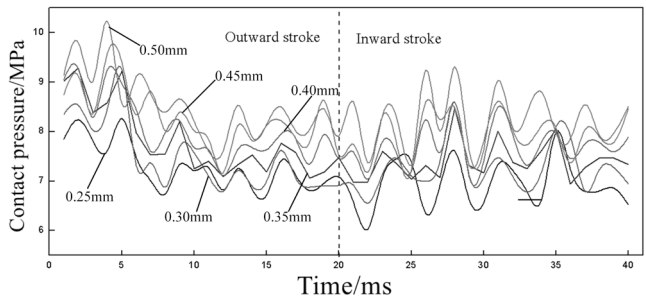


(b) The maximum contact pressure

**Fig. 3-55.** The stress and contact pressure on the bio-mimetic sealing ring under different compression amounts.

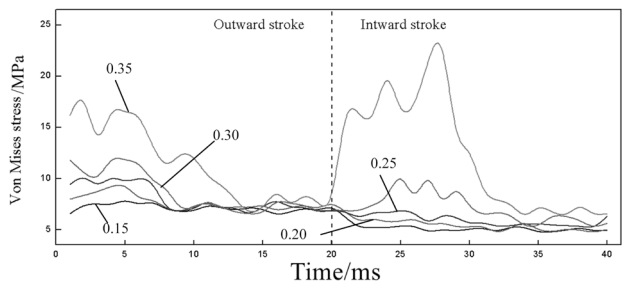


(a) The maximum von-Mises stress

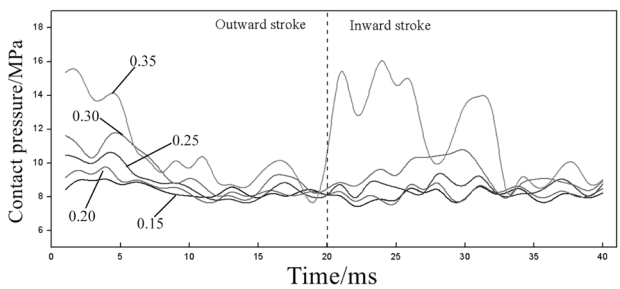


(b) The maximum contact pressure

**Fig. 3-56.** The stress and contact pressure on the bio-mimetic sealing ring under different friction coefficients.

0.3, the creeping phenomenon appears. Therefore, lubrication is an important part of the reciprocating dynamic seal. The concave ridges of the bio-mimetic ring could store lubricant to ensure the ring remain be lubricated for a longer time.

### *3.6.3.4 Effect of fluid pressure*

Figure 3-57 shows the von-Mises stress and contact pressure on the bio-mimetic sealing ring under different fluid pressures. With the increasing of fluid pressure, the von-Mises stress and contact pressure increase gradually, but the stress fluctuation also increases. The maximum contact pressure on the main sealing surface of bio-mimetic ring is higher than the fluid pressure when $P \leq 5$ MPa. Therefore, the reciprocating dynamic sealing performance of the bio-mimetic sealing ring is stable and reliable.

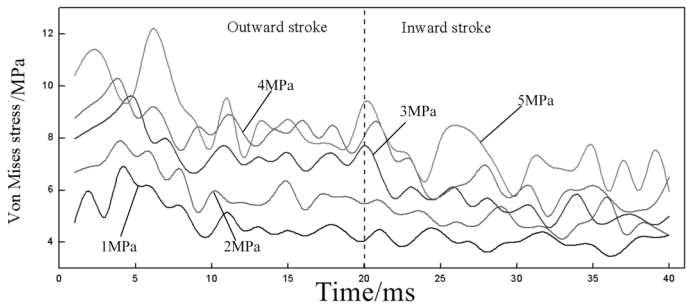


(a) The maximum von-Mises stress

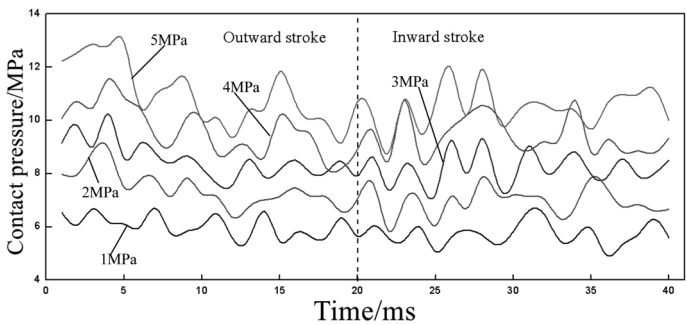


(b) The maximum contact pressure

**Fig. 3-57.** The stress and contact pressure on the bio-mimetic sealing ring under different fluid pressures.

### *3.6.3.5 Effect of rubber hardness*

Figure 3-58 shows the von-Mises stress and contact pressure on the bio-mimetic sealing ring under different material hardness. As shown in Figure 3-58a, with the increasing of the material hardness, the von-Mises stress increases gradually. The von-Mises stress during inward stroke is lesser than it is in the outward stroke. As shown in Figure 3-58(b), contact pressure increases gradually with the increasing of the material hardness. When material hardness is 70 Hr or 90 Hr, the stress on the bio-mimetic ring fluctuates severely. Therefore, it is essential for the bio-mimetic

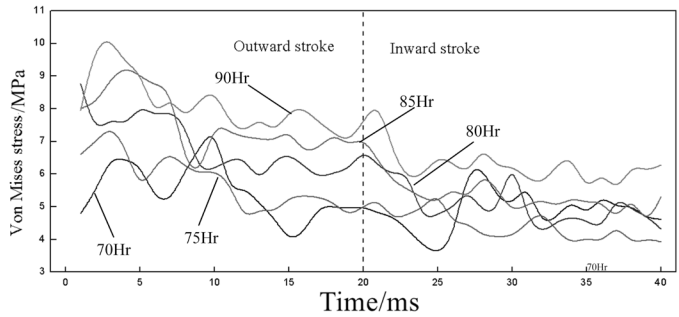


(a) The maximum von-Mises stress

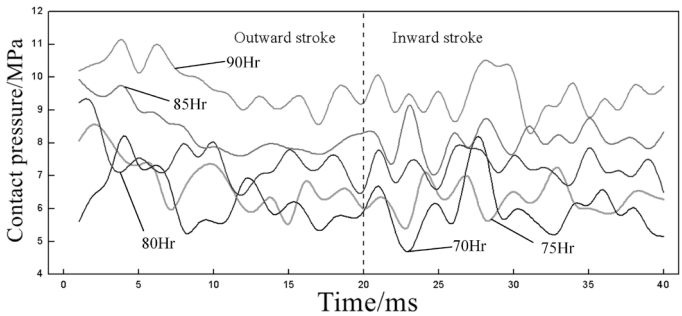


(b) The maximum contact pressure

**Fig. 3-58.** The stress and contact pressure on the bio-mimetic sealing ring under different hardness.

ring to have a reasonable hardness to ensure a good reciprocating dynamic sealing performance.

## References

[1] Tan jing, Yangweimin and Ding Yumei. 2007. Finite element analysis of rectangular rubber sealing ring. Lubrication & Sealing 32(2): 36–39.

[2] Liu, J., Qiu, X.Q., Bo, W.S. and Xu, J.L. 2010. Numerical analysis on the maximum contact pressure of rubber O-ring. Lubrication Engineering 36(1): 41–44.

# 4

# Metal-rubber Sealing Structure in the Roller Cone Bit

## 4.1 Sealing structure

Figure 4-1 shows the cross-section diagram of the roller bit with metal sealing system. The metal sealing system is located at tooth root of the roller bit. Figure 4-2 is a larger version of sealing parts in Figure 4-1. The double metal sealing system consists of a dynamic metal ring, a dynamic O-ring, a static metal ring, a static O-ring, the inner hole of the roller, and the journal bearing of the roller bit [1]. The single metal sealing system consists of a dynamic metal ring, a static metal ring, an O-ring, a supporting ring, and the journal bearing of the roller bit. In the double metal sealing system, a pair of high-precision metal rings is completely suspended in the sealed chamber, which has an axial seal. This seal can greatly reduce the friction and friction heat generation. Under the action of pressure difference, metal rings frequent emit axial and radial vibrations. The two high elastic O-rings are located in the seal area of the roller and the journal bearing to achieve the comprehensive seal. In a single metal sealing system, there is a support ring between the static ring and the journal bearing of the roller bit, which can make the contact pressure distribution of

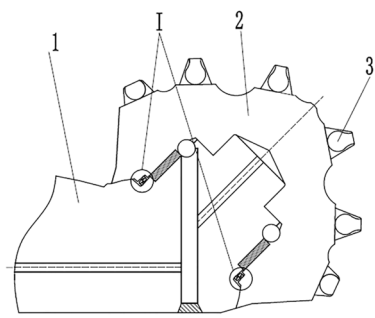


**Fig. 4-1.** A section diagram of the roller cone bit. 1-claw; 2-cone; 3-tooth.

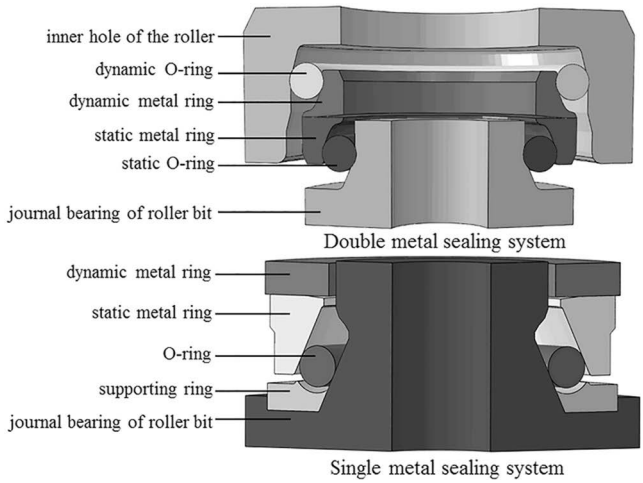


**Fig. 4-2.** The two metal sealing system in the roller cone bit.

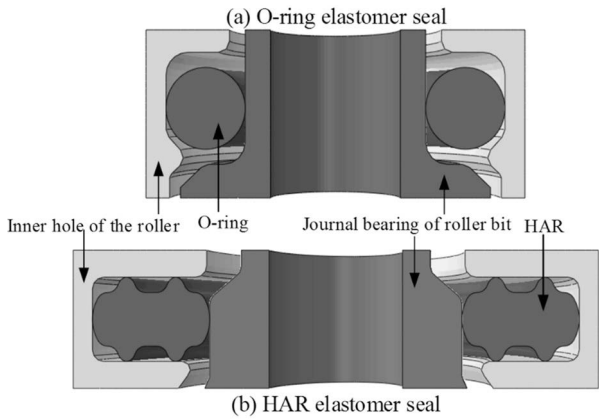


**Fig. 4-3.** The two kinds of sealing structures.

the sealing surface even. The sealing pressure and reliability of the sealing surface are improved effectively at the same time.

HAR (High Aspect Ratio) is a new rubber sealing technology proposed by Baker Hughes. The special shape of the rubber sealing system is the main characteristic of this technology. As shown in Figure 4-3, compared with the O-type sealing ring, the HAR sealing ring achieves a high compression ratio and the wear of the sealing surface is compensated, improving the working life and reliability of the seal [2].

## 4.2 Materials and models

The sealing performance of two metal sealing systems were examined considering the nonlinear geometry of mechanical deformation and the constitutive relation of rubber material. Two-dimensional axisymmetric models are established based on

the geometrical shape, material, and boundary condition. The material of both the dynamic metal ring and static metal ring is a hard alloy (YG8). The Poisson's ratio is 0.3, and elasticity modulus is 510 GPa. The material of both the inner hole and journal bearing is an alloy material (20CrNiMo). The material of O-ring is NBR, according to the rubber compression test, $C_1 = 1.79$ MPa, $C_2 = 0.4$ MPa. The diameter of O-ring is 3.66 mm. The material of the supporting ring is PTFE. Its density is 2200 kg/m$^3$, with elastic modulus 280 MPa, and a Poisson's ratio of 0.4.

The contact between surfaces was simulated by using the penalty element method, and two contact pairs, between the shaft cylinder and the sealing ring, and the sealing ring and the groove, were established. The initial friction coefficient was 0.2, from the Coulomb friction model.

## 4.3 Metal sealing system

### *4.3.1 Effect of the fluid pressure*

#### *4.3.1.1 No fluid pressure*

There are many research projects currently investigating the sealing performance and mechanical behavior in pressure difference conditions only. The maximum von-Mises stress and stress distributions on the dynamic O-ring, static O-ring, and O-ring are as shown in Figure 4-4. With an increase in the pressure difference, the maximum von-Mises stress on the static O-ring and O-ring increases and the dynamic O-ring's stress decreases. Under the same conditions, the stress on the O-ring in the double metal seal system is greater than that in the single metal seal system. The shape of the von-Mises stress distribution in the single metal seal system is a dumb-bell.

Under the action of pressure difference, the maximum contact pressure distribution of the two O-rings are different in the double metal sealing system. As is shown in Figure 4-5, with the increasing of pressure difference, the maximum contact pressure of S.S.1 and S.S.2 increase. For S.S.3, the contact pressure decreases first

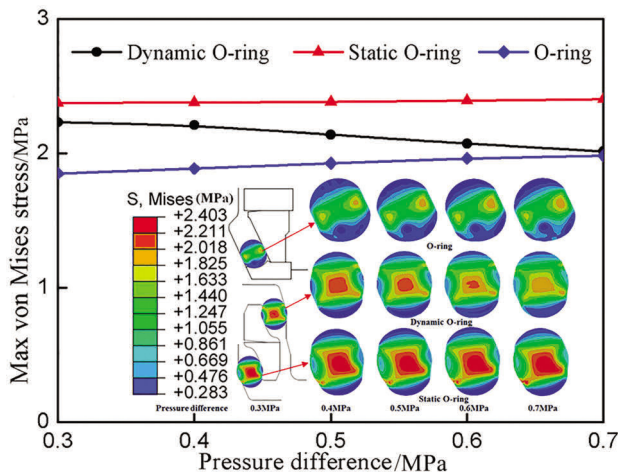


**Fig. 4-4.** The stress distribution of O-rings under different pressure differences.

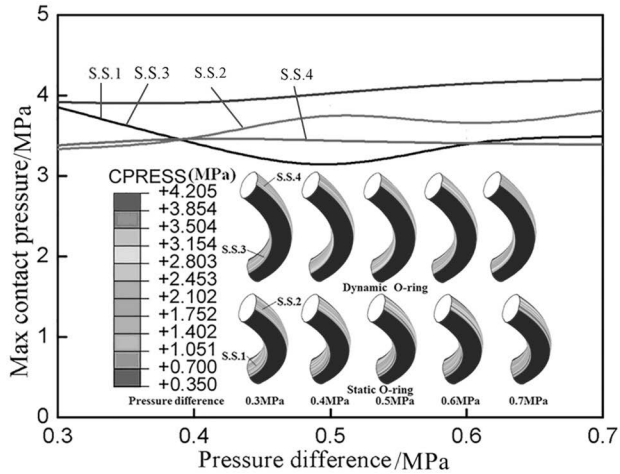


**Fig. 4-5.** The contact pressure of the double metal sealing system under different pressure differences.

and then increases with the increasing of pressure difference. The reason for this phenomenon is that the sealing structure is special. A lager deformation occurs in a small sealing area with the increasing of pressure difference, which resulting in irregular stress changes. But there is no significant change in S.S.4. And the contact pressures are greater than the pressure difference that can achieve the sealing.

As shown in Figure 4-6, with the increasing of the pressure difference, the maximum contact pressure of S.S.1 increases. But the curve of S.S.2 and S.S.3 exhibit a wave variation. For S.S.2, the contact pressure decreases first and then increases and finally decreases again. And the change in the front of S.S.3 is the same as S.S.2, but it increases at the end. The reason for this phenomenon is similar to the S.S.3 of the double metal sealing system.

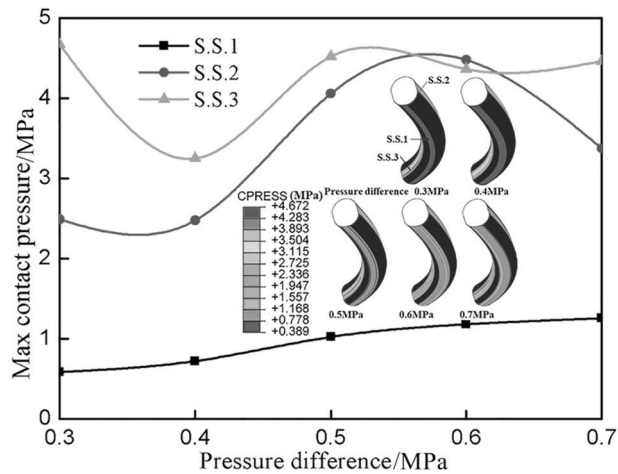


**Fig. 4-6.** The contact pressure of the single metal sealing system under different pressure differences.

The contact pressure of two sealing systems on the metal sealing surface (M.S.S.) under various pressure differences are shown in Figure 4-7. With the increasing of pressure difference, the contact pressure of the double metal sealing system on the M.S.S. increases. However, the contact pressure on the M.S.S. of the single metal sealing system decreases first and then increases and finally decreases again. Under the same conditions, the sealing performance of the double metal sealing system is better than that of the single metal sealing system.

The effect of pressure difference on the metal sealing system's mechanical behavior and sealing performance without fluid pressure is easily affected by excessive deformation in a small area. Therefore, it is necessary to study the influence of pressure difference under fluid pressure.

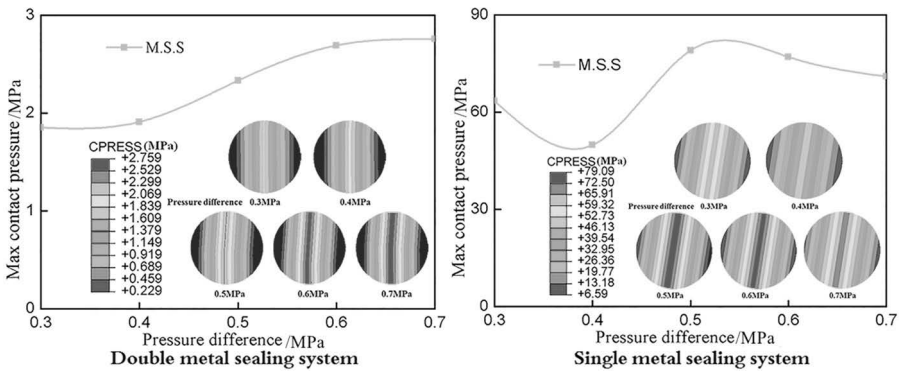


**Fig. 4-7.** The contact pressure on the two sealing systems under different pressure differences.

### *4.3.1.2 Fluid pressure*

Under the actual working conditions, the basic fluid pressure also needs to be considered. The maximum von-Mises stress and stress distributions on the dynamic O-ring, the static O-ring, and the O-ring under fluid pressure 5 MPa are shown in Figure 4-8. With the increasing of the pressure difference, the maximum von-Mises stress on the static O-ring and O-ring increases, and the dynamic O-ring decreases. The reduction of the von-Mises stress on the dynamic O-ring is not obvious from 0.3 to 0.5 MPa, but it is obvious from 0.5 to 0.6 MPa. The maximum stress concentration position on the dynamic O-ring changes from the upper to the lower part. In the single metal seal system, the high-stress area is near the side wall of the static metal ring and the low-stress area is inside the cross-section. The stress is close to the inner surface on the O-rings' cross-section in the double metal seal system but the maximum stress is concentrated at the edges of the sealing surfaces due to the structure features. Under the same conditions, the stress on the static O-ring is greater than that on the dynamic O-ring.

Under the joint action of the 5 MPa fluid pressure and the pressure difference, the variations in the maximum contact pressure and the distribution of the contact pressure are the same for the double metal seal system. Figure 4-9 shows the maximum contact pressure of the double metal sealing system under various pressure differences. The contact pressure of S.S.1 and S.S.2 are changed slightly, but S.S.3

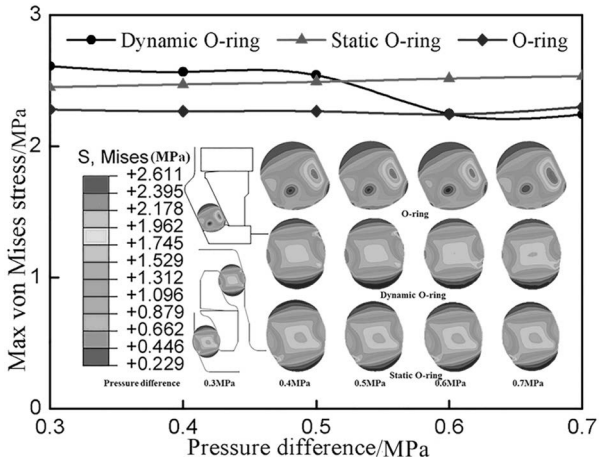


**Fig. 4-8.** The stress distribution on O-rings in 5 MPa under different pressure differences.

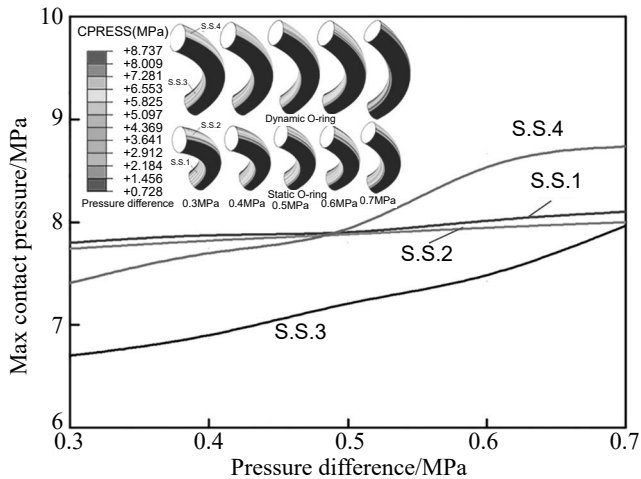


**Fig. 4-9.** The contact pressure on the double metal sealing system in 5 MPa under different pressure differences.

and S.S.4 changed greatly. Therefore, the pressure difference has a greater effect on the sealing performance on the dynamic O-ring than the static O-ring. When the pressure difference is more than 0.5 MPa, the contact pressure of S.S.4 is the most. But in the range of 0.3 to 0.7 MPa, although the contact pressure of S.S.3 is minimized, it is still more than the pressure difference.

Contact pressure of single metal sealing system in 5 MPa under various pressure difference is shown in Figure 4-10. With an increase in the pressure difference, the contact pressure of S.S.1 and S.S.2 increase. For S.S.3, the contact pressure increases slowly first and then sharply at 0.5 MPa. Therefore, pressure difference can enhance the sealing performance of the single metal sealing system.

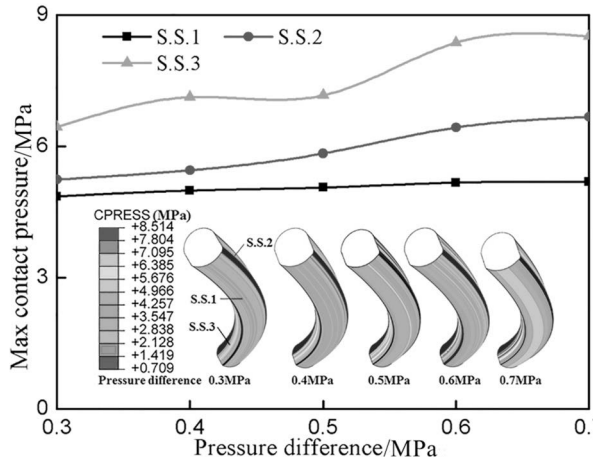


**Fig. 4-10.** The contact pressure on the single metal sealing system in 5 MPa under different pressure differences.

The contact pressure of two sealing system on M.S.S. in 5 MPa under various pressure difference is shown in Figure 4-11. With the increasing of the pressure difference, the contact pressure of the double metal sealing system increases, and the increase rate is the most between 0.4 to 0.5 MPa. For the M.S.S. of the single metal sealing system, the increase rate is the most between 0.5 to 0.6 MPa. The maximum contact pressure on the double metal sealing system is smaller than that on the single metal sealing system, and it is still greater than the pressure difference in any condition. Therefore, the performance of the M.S.S. is very great in the sealing range.

The effect of the pressure difference on the sealing performance and mechanical behavior under considering fluid pressure and no fluid pressure are different. To avoid a big deformation in a small area and to apply theoretical knowledge to actual conditions, it is more reliable to study the metal sealing system under fluid pressure.

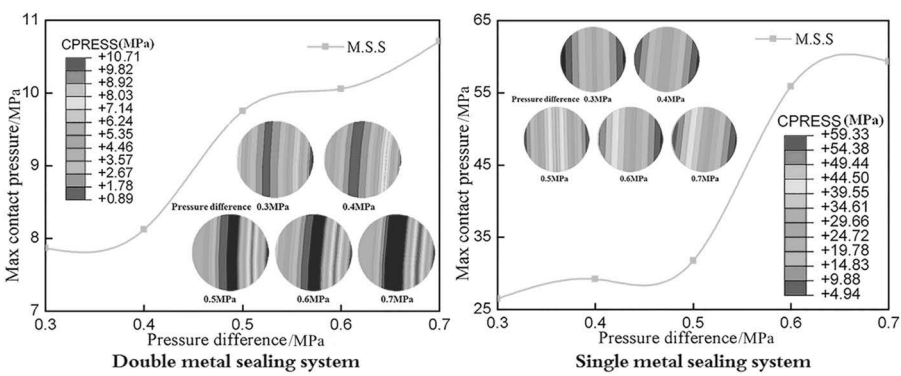


**Fig. 4-11.** The contact pressure on two sealing system on the M.S.S. in 5 MPa under different pressure differences.

### *4.3.2 Effect of the compression ratio*

The assembly compression ratio is one of the important factors that affects the sealing performance. The von-Mises stress distributions on the O-rings under different compression ratios are shown in Figure 4-12. In the assembly state, the dynamic O-ring and static O-ring are compressed. The maximum stress is on the inner surface on the O-rings' cross-section. The stress on the dynamic O-ring is greater than that on the static O-ring. The material easily becomes loose and causes the loss of stiffness of the material over the long term. With the compression ratio increases, the deformation on the dynamic O-ring and the static O-ring increase.

For the four contact surfaces, the contact pressure distributions on the surfaces are shown in Figure 4-13. With the compression ratio increases, the maximum contact pressures of the surfaces increase. In the 4%~16%, the maximum contact pressure of S.S.2 and S.S.3 is greater than that of S.S.1 and S.S.4. When the compression ratio is above 16%, the growth rate of S.S.1 and S.S.4 increase greatly. When the compression ratio is 20%, the contact pressure of S.S.4 is the highest.

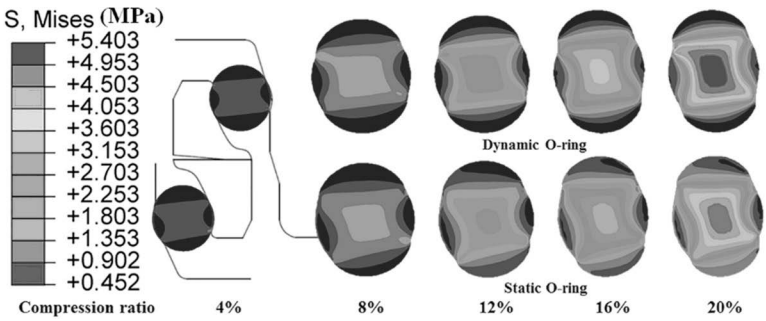


**Fig. 4-12.** The stress distribution of O-rings under different compression ratios.

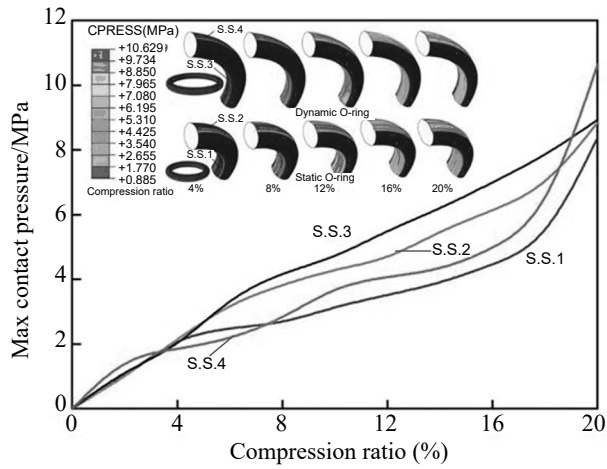


**Fig. 4-13.** The contact pressure of O-rings under different compression ratios.

### *4.3.3 Effect of fluid pressure*

As shown in Figure 4-14, with the increasing of fluid pressure, the maximum stresses on the dynamic O-ring and the static O-ring increase and the deformation is obvious. When the fluid pressure is greater than 1 MPa, the contact pressure on the dynamic O-ring is the greatest. There is a low-stress area in the middle area of the cross-section with the fluid pressure increases. Therefore, material failure occurs first in the high-stress area of the dynamic O-ring.

The maximum contact pressures on four surfaces are shown in Figures 4-15. With the increasing of fluid pressure, the maximum contact pressure on the surfaces increase linearly. The maximum contact pressure on S.S.2 and S.S.3 is higher than that on S.S.1 and S.S.4. But the difference between the four sealing surfaces is very small. For S.S.1, the contact pressure is the least, and it is still greater than the

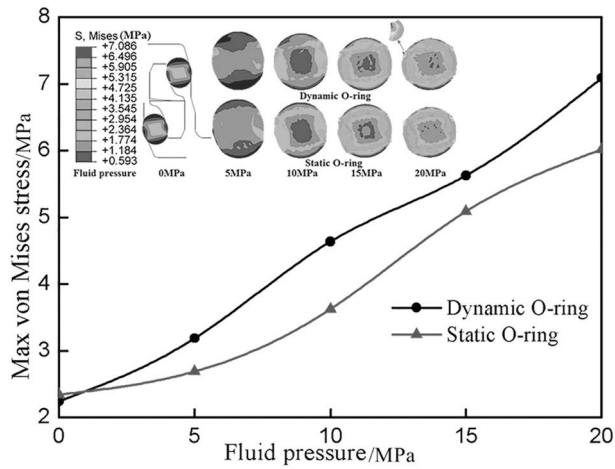


**Fig. 4-14.** The stress distribution on O-rings under different fluid pressures.

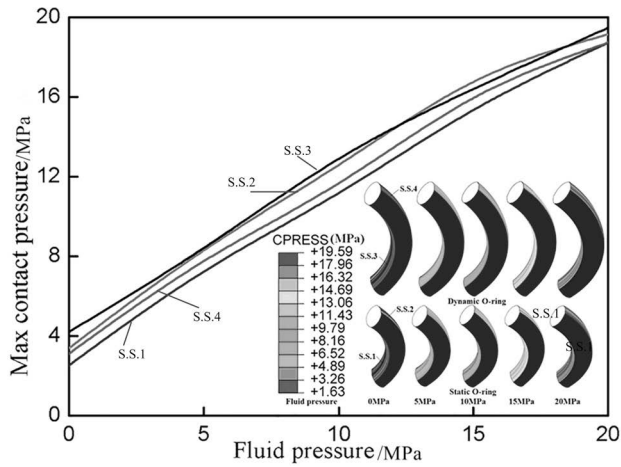


**Fig. 4-15.** The contact pressure on O-rings under different fluid pressures.

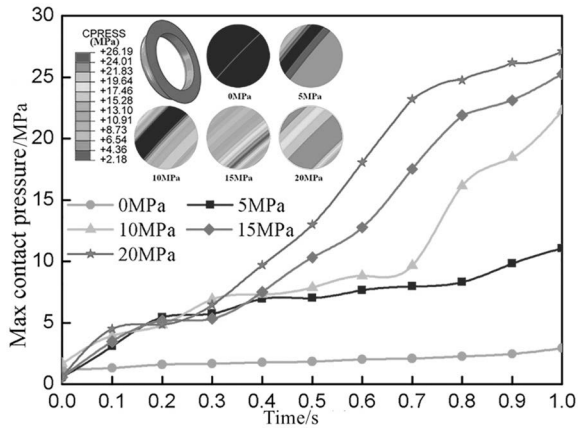


**Fig. 4-16.** The contact pressure distribution on the M.S.S. under different fluid pressures.

0.5 MPa pressure difference in any conditions. Therefore, the sealing performance in this seal range is highly effective.

Figure 4-16 shows the contact pressure distribution on the M.S.S. under different fluid pressures. With time increases, the maximum contact pressure increases on the M.S.S. under different fluid pressures. After 0.4s, the greater fluid pressure is, the greater contact pressure is. The contact pressure on the M.S.S. under different fluid pressures is greater than the corresponding 0.5 MPa pressure difference. Therefore, fluid pressure can enhance the sealing performance of M.S.S.

### *4.3.4 Effect of the inclination angle*

A metal sealing surface uses the cone structure to improve its alignment capability. Figure 4-17 shows the von-Mises stress distributions on the metal sealing surface under different angles. The maximum stress is close to the metal sealing surface, which increases with the angle increases. The stress is concentrated on the surface of the metal ring instead of the inside. With an increase of the angle, the maximum contact pressure on the M.S.S. increases, and a high-stress area appears in the middle of the M.S.S. Over the long-term, the deformation increases.

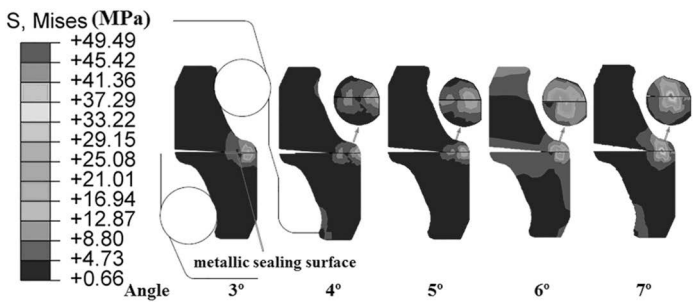


**Fig. 4-17.** The stress distribution on the M.S.S. under different angles.

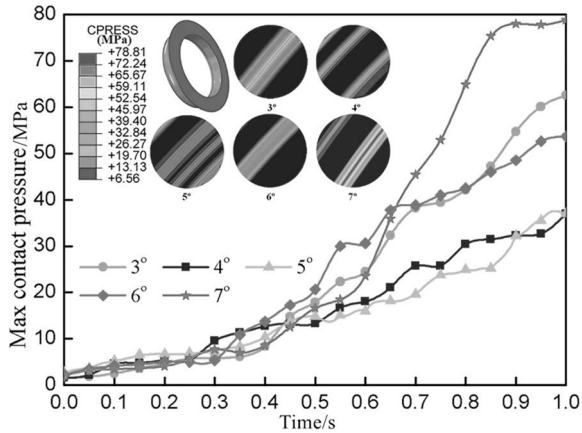


**Fig. 4-18.** The contact pressure distribution on the M.S.S. under different angles.

As shown in Figure 4-18, the maximum contact pressure increases at different angles with time. The growth rate of contact pressure at different angles increase after 0.3s. But with the increase of angle, the increase amplitude of maximum contact pressure is varied. The contact pressure at 7º is the largest, and 4º is the smallest, and 3º is the second-largest. The angle has no linear relationship with the contact pressure. Therefore, it is necessary to choose the appropriate angle according to the fluid pressure utilized in the actual working condition.

### *4.3.5 Effect of the ambient temperature*

The double metal sealing system is not only affected by the high pressures in the deep bore holes, but also by the formation temperature, friction heat, and the heat generated by rotation. Under the action of the thermal load, the temperature distribution is uneven, which can produce thermal stress and thermal deflection.

Due to the uneven temperature distribution of the seal face, thermal stress and thermal deformation occurs. As is shown in Figure 4-19, the von-Mises stress on the

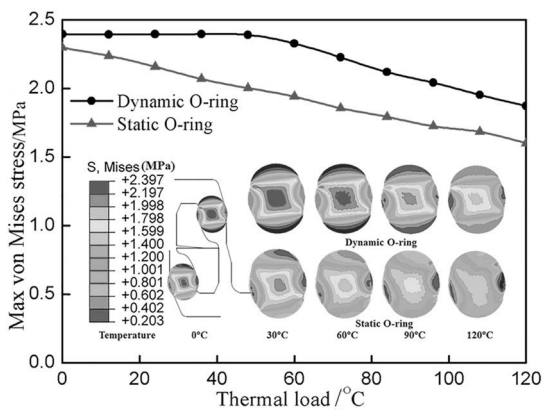


**Fig. 4-19.** The stress distribution on the O-rings under different temperatures.

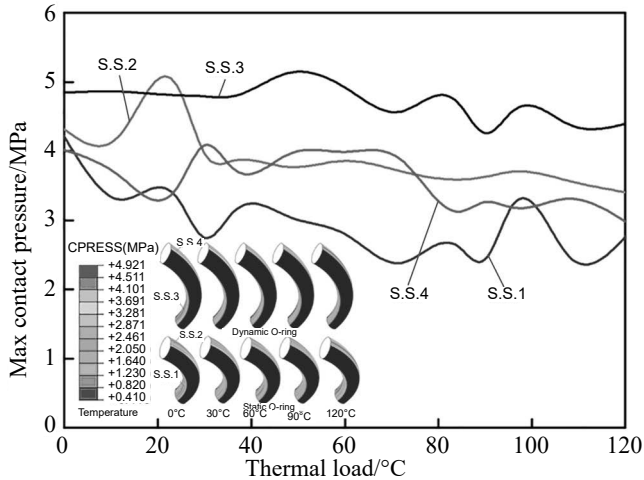


**Fig. 4-20.** The contact pressure on the O-rings under different temperatures.

dynamic O-ring is greater than that on the static O-ring. With the increasing of the thermal load, the stresses on the two O-rings decrease. There is a high-stress area in the inner surface of the O-ring. The low-stress area appears on the non-sealing surface of the O-rings first and then it appears on the sides of the sealing surface.

Figure 4-20 shows that the maximum contact pressure fluctuates randomly within the range of 2–6 MPa when the thermal load is increased. After 20°C, the maximum contact pressure on S.S.3 is biggest; this phenomenon is caused by uneven temperature distribution and structure. Therefore, the thermal load doesn't affect the sealing performance of the double metal seal system as a single independent factor. In order to study the influence of the thermal load on the sealing performance, it is necessary to further explore the thermal coupling deformation.

It is not only necessary to consider the effect of thermal load, but also fluid pressure. The maximum von-Mises stress distribution on O-rings is shown in Figure 4-21. With the increasing of thermal load and fluid pressure, the stress and

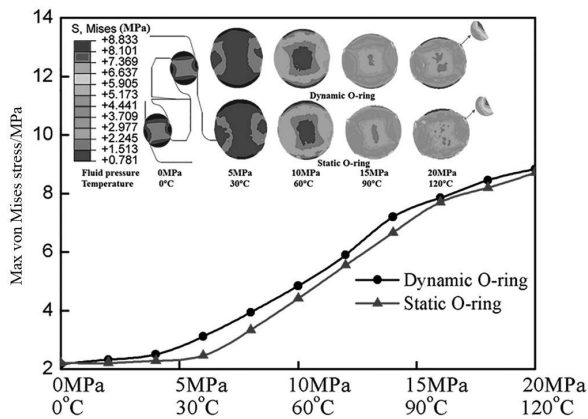


**Fig. 4-21.** The stress distribution on O-rings under different thermal couplings.

deformation on the O-rings increase. Compared to Figure 4-14, it can be found that the von-Mises stress is increased by increasing the thermal load under the same fluid pressure in this case. The high-stress area in the inner surface of the cross-section decreases gradually at first and then a low-stress area appears in the inner surface of the O-rings. The maximum stress is close to the sealing surface. Therefore, material failure is most likely to occur on the edges of the sealing surface.

As is shown in Figure 4-22, the maximum contact pressure on the four sealing surfaces increase linearly with the increasing of fluid pressure under 0.5 MPa pressure difference. As compared with Figure 4-15, contact pressure without thermal load is lesser than the no thermal load condition at the same fluid pressure. 5 MPa fluid pressure and 30°C thermal load is a critical point in this case. After 5 MPa and 30°C, the contact pressure on S.S.2 and S.S.4 are greater than on S.S.1 and S.S.3. The contact pressure on S.S.3 is the least, but it is still greater than the pressure difference in any conditions.

Figure 4-23 shows the contact pressure on the O-rings on M.S.S. in different conditions. For M.S.S., the contact pressure slowly increases at first, then it increases

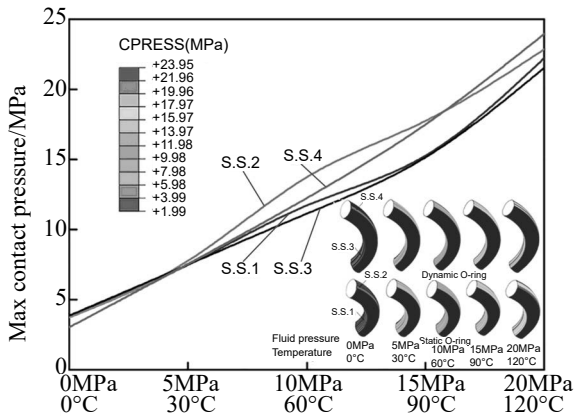


**Fig. 4-22.** The contact pressure on O-rings under different thermal couplings.

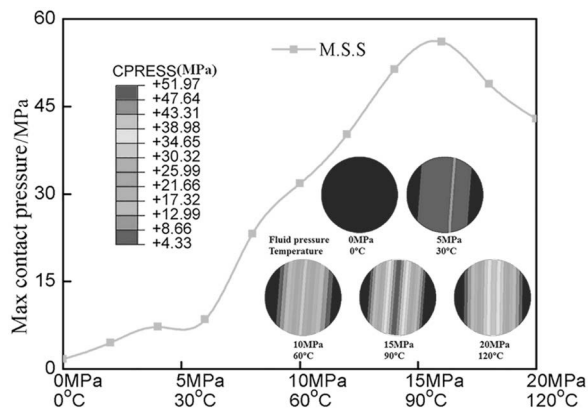


**Fig. 4-23.** The contact pressure on the O-rings in the M.S.S. under different thermal couplings.

rapidly, and finally it decreases with the increasing of fluid pressure and thermal load. Compared to Figure 4-16, in Figure 4-23, the contact pressure decreases when the fluid pressure is greater than 15 MPa and thermal load is greater than 90°C. The reason is that ultra-high pressure and high temperature changes the material's properties.

It is found that the possibility of sealing failure is greater with the increasing of thermodynamic coupling in the actual drilling process. Additionally, the thermal coupling deformation is caused by the interaction between the thermal load and the fluid pressure. Therefore, controlling thermal load under a certain fluid pressure is essential.

## 4.4 HAR and O-ring

### *4.4.1 Sealing performance*

When the roller cone bit is running, the bearing rotates at high speed to generate heat, and the seals work in a high-temperature field. According to the assembly process and operation condition of the seal, the seal is divided into three stages: (1) compression assembly, the sealing ring achieves self-sealing; (2) the sealing ring is further compressed under the action of fluid pressure; (3) thermal expansion is caused by temperature rise, which changes the stress distribution inside the seal. As shown in Figure 4-24, the maximum stress on the HAR sealing ring is greater than that on the O-ring at different stages. In the initial compression stage, a low-stress area is formed in the four sharp corners along the shaft. Because the HAR sealing

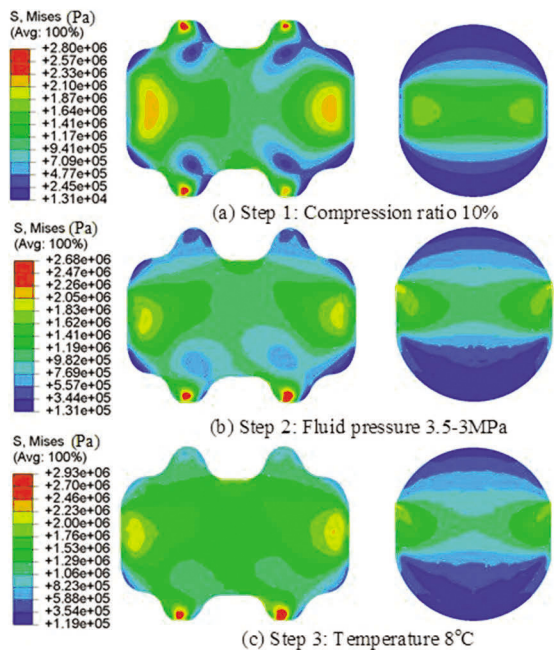


**Fig. 4-24.** The stress distribution on the sealing ring at each stage.

ring is compressed by the movement of the right shaft, the contact surface at the sharp corners had local stress relaxation under friction force. The stress is mainly concentrated inside the cross-section of the O-ring and the HAR seal ring. After the initial compression, two high-stress areas are formed. Under the influence of fluid pressure and temperature, the high-stress areas gradually spread away from the center. However, in the four sharp corners of the HAR sealing ring, excessive compression of rubber material occur easily, and thus, excessive stress appears. Under fluid pressure and temperature, the high-stress area in the sharp corner decreases gradually. Therefore, a HAR sealing ring has a higher failure rate than an O-ring under the same conditions, and the failure area is mainly at the lower sharp corner.

The contact pressure at the cross-section edge of the O-ring and the HAR sealing ring during the three stages are shown in Figure 4-25. The O-ring has two sealing surfaces, while the HAR sealing ring has six. The maximum contact pressure on each sealing surface is greater than the fluid pressure, so sealing can be realized. Moreover, the contact pressure on the HAR sealing ring is greater than that on O-ring. Under fluid pressure and temperature, the contact pressure on sealing surface increases, then improve the sealing performance of the sealing ring. However, the contact pressure on the surface of the HAR ring's S.S.1 and S.S.2 fluctuates greatly. In conclusion, the HAR sealing ring has a better sealing performance. With the increasing of sealing surfaces, the probability of sealing failure decreases. The factors influencing factors the sealing performance of the HAR sealing ring are studied in the following section.

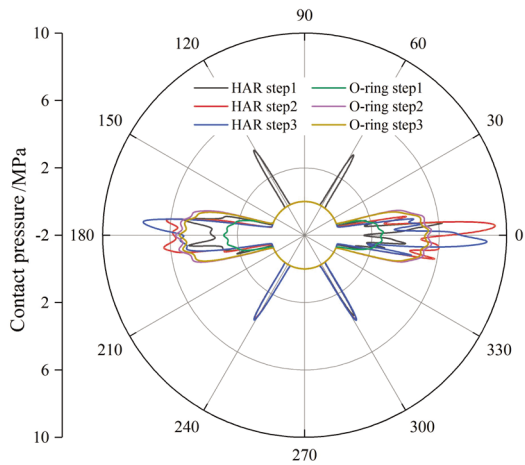


**Fig. 4-25.** The contact pressure curve of the HAR and O ring.

### *4.4.2 Effect of the compression ratio*

Figure 4-26 shows the maximum von-Mises stress inside the HAR ring cross-section at 15% initial compression ratio. With the increasing of the initial compression, the maximum von-Mises stress of the HAR ring increases linearly, and the local low-stress area is formed in the four sharp angles along the shaft direction. As the initial compression increases from 1.5% to 15%, the maximum stress on the cross-

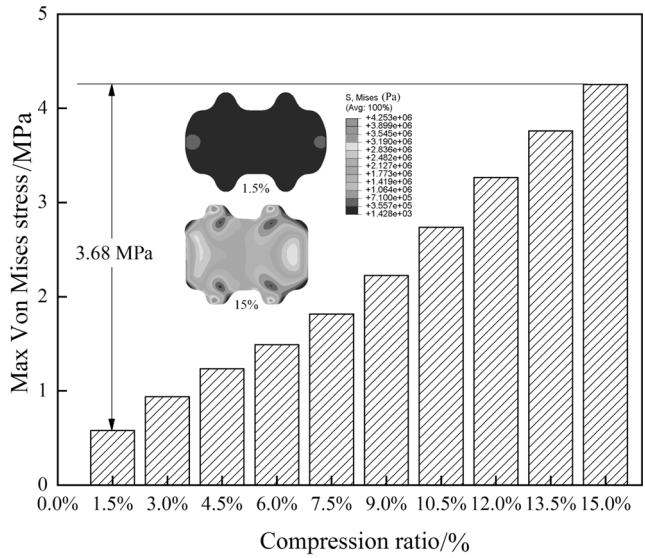


**Fig. 4-26.** The stress on the HAR sealing ring under different compression ratios.

section increases by 3.68 MPa. Figure 4-27 shows the contact pressure curve of the main sealing surface S.S.1 with the initial compression. The larger the initial compression is, the greater the contact pressure on the sealing surface is. The sealing surface contact pressure fluctuation is caused by excessive extrusion of local rubber materials. In conclusion, increasing the initial compression can improve the self-sealing performance of the sealing ring, but the failure rate is correspondingly increased. Therefore, the initial compression ratio should be selected according to the actual application conditions.

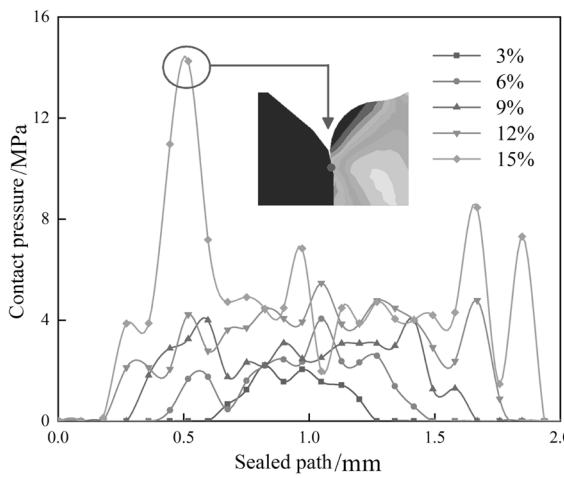


**Fig. 4-27.** The contact pressure on the HAR sealing ring under different compression ratios.

### *4.4.3 Effect of the fluid pressure*

When the initial compression is 15%, the sealing ring pressure between 3–11 MPa, and the pressure difference 0.5 MPa, the contact pressure of the main sealing surface is shown in Figure 4-28. The higher the fluid pressure is, the greater the average contact pressure on the sealing surface is. The deformation of the HAR sealing ring under the fluid pressure is shown in Figure 4-29. When the fluid pressure is greater than the maximum contact pressure on the sealing surfaces S.S.3 and S.S.4, the sealing surfaces are shortened gradually until they disappeared. The two high-stress areas in the cross-section of the HAR sealing ring slowly fused into one high-stress area under fluid pressure. With the increasing of fluid pressure, the contact area between the HAR sealing ring and the fluid pressure is prone to the excessive extrusion of local materials, which leading to the stress concentration in this area.

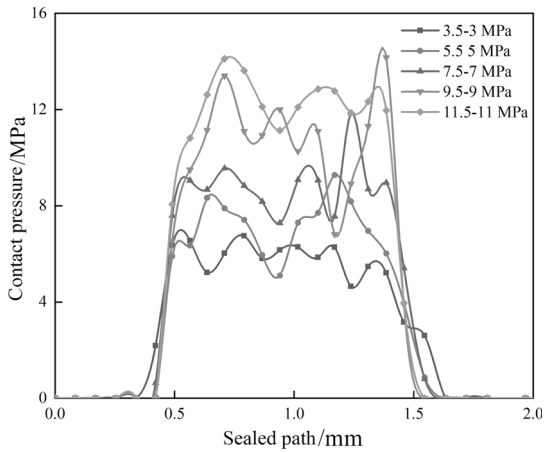


**Fig. 4-28.** The contact pressure on S.S.1 under different fluid pressures.

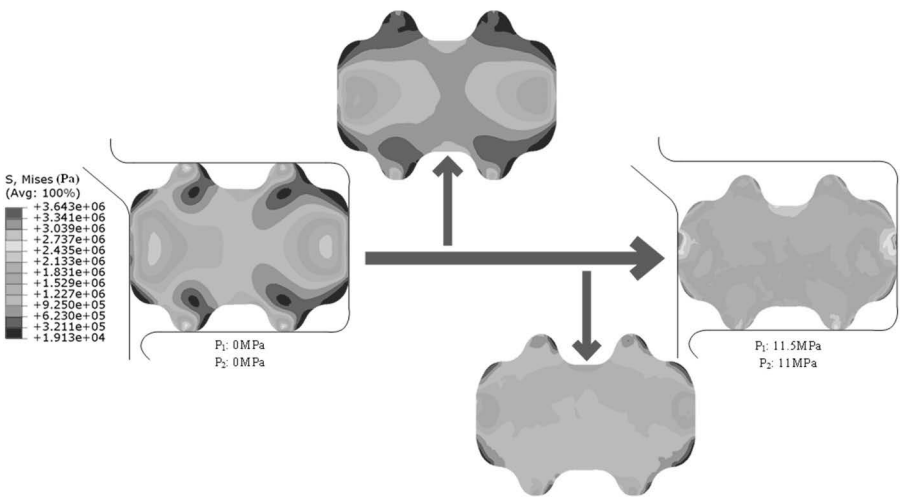


**Fig. 4-29.** The stress on the HAR sealing rings under different fluid pressures.

Figure 4-30 shows the contact pressure curve of the HAR sealing ring. The contact pressures on the sealing surfaces S.S.3 and S.S.4 disappear between 0.15s and 0.2s. That is to say, when the fluid pressure is more than 2.2 MPa, the sealing surfaces on the HAR sealing ring are reduced from 6 to 4. The contact pressure fluctuation on the sealing surface S.S.2 is more than it is on S.S.1, and both fluctuation amounts are greater than the fluid pressure required to achieve sealing. Therefore, increasing the fluid pressure appropriately may reduce the number of sealing surfaces, and increase the contact pressure on the sealing surface, then the sealing performance of the ring will be improved.

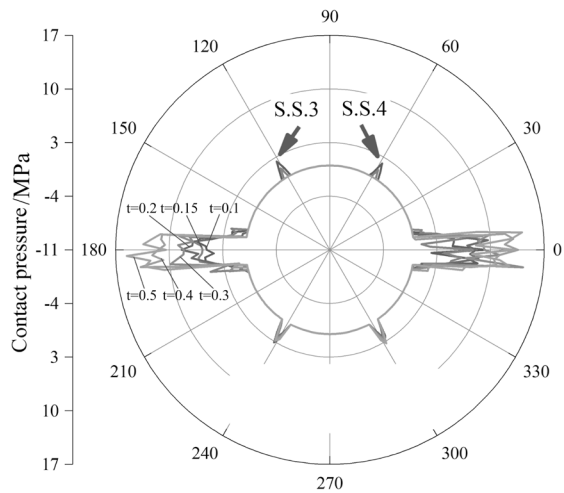


**Fig. 4-30.** The initial contact pressure curve of the HAR sealing ring.

### *4.4.4 Effect of the ambient temperature*

Figure 4-31 shows the von-Mises stress distribution inside the HAR sealing ring cross-section at different temperatures. With the increasing of temperature, the stress on the cross-section of the HAR sealing ring increases gradually. Increasing temperature changes the material properties, and the rubber is more prone to deformation at high temperatures. Stress distribution on the sealing ring is more uniform at a high temperature. However, if the temperature is too high, the stress concentration area easily appeared on the seal surface (A, B, C and D). Figure 4-32 shows the contact pressure with different temperatures, which is located on the main sealing surface S.S.1. With the influence of temperature, although the contact pressure fluctuates, it decreases on the whole. However, the maximum contact pressure at each temperature is higher than the fluid pressure in the same working condition. The HAR sealing ring is more likely to deform and has a reduced sealing performance when working in a high-temperature field. Therefore, the probability of seal failure is greater when it is utilized in high temperatures underground, as the failure area easily appears on the seal surface.

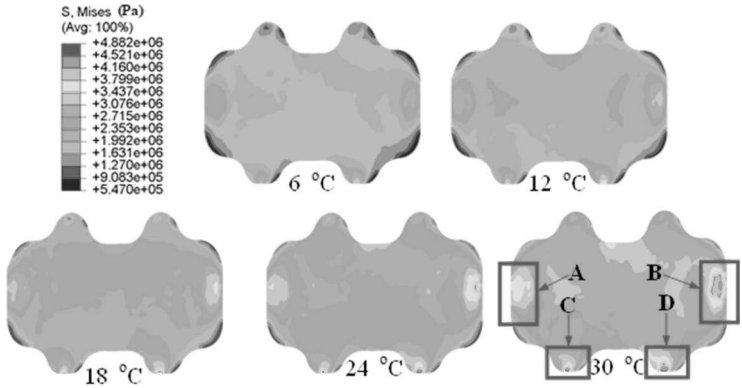


**Fig. 4-31.** The stress distribution with different temperatures.

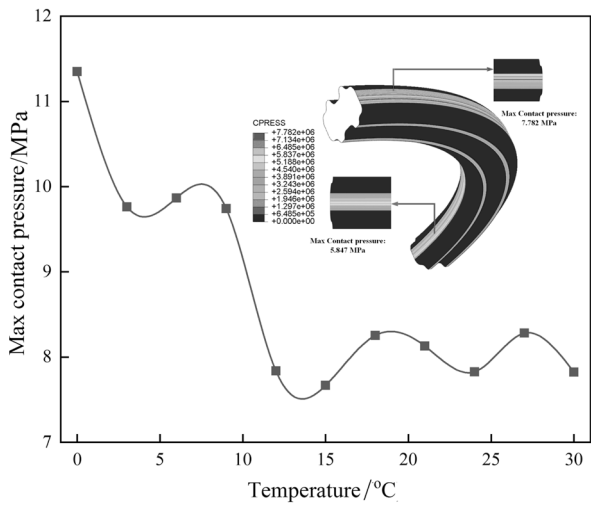


**Fig. 4-32.** The contact pressure distribution with different temperatures.

### *4.4.5 Effect of the friction coefficient*

Figure 4-33 shows contact pressure on the main sealing surface with different coefficients. The contact pressure increases positively with an increase in the friction coefficient. When the friction coefficient increases from 0.1 to 0.5, the contact pressure increases by 1.316 MPa after assembling, and that in increase by 0.748 MPa after fluid pressure. Figure 4-34 shows the contact pressure distribution on the main sealing surface S.S.1 under different friction coefficients. The maximum contact pressure on the sealing surface is higher than the fluid pressure, which means that sealing was achieved. However, the contact pressure fluctuates on the sealing surface.

As shown in Figure 4-35, a stress concentration area is caused by a highly excessive friction coefficient on the contact surface. In assembly process. S.S.3 and S.S.5 are more affected by the friction coefficients and high stress area appears near

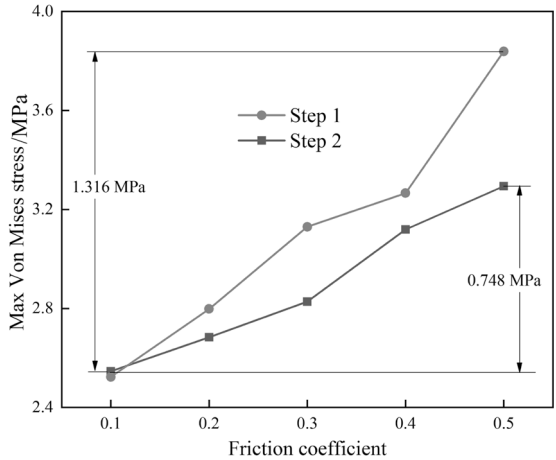


**Fig. 4-33.** The stress on the sealing ring under different friction coefficients.

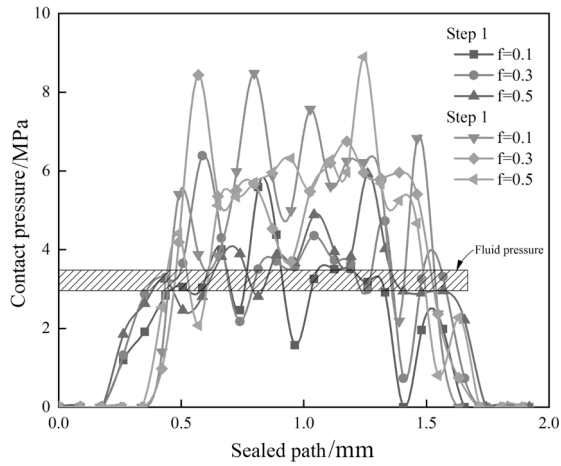


**Fig. 4-34.** The contact pressure on the S.S.1 under different friction coefficients.

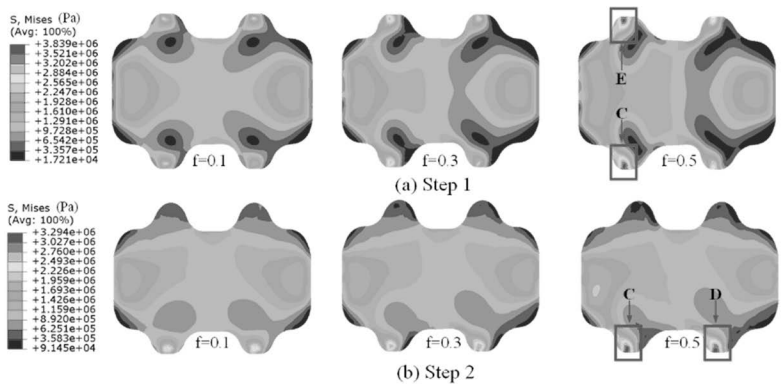


**Fig. 4-35.** The stress distribution on the sealing ring under different friction coefficients.

the sealing surface. In working conditions, the HAR sealing ring is squeezed by fluid pressure in the vertical direction, and the fluid pressure on the upper part is bigger than that on the bottom part. S.S.5 and S.S.6 are more affected by friction coefficients, a high-stress area occurs near the sealing surface area, and cracks, debris, etc. may appear then resulting in sealing failure.

## 4.5 Conclusions

The greater the compression ratio and fluid pressure and angle are, the greater the von-Mises stress on the double metal sealing system. The material of the high-stress area easily becomes loose, causing a loss of stiffness of the material over the long term effect. With the increasing of compression ratio and fluid pressure, the contact pressure on the sealing surfaces increase. Both ambient temperature and load need to be considered in the analysis of sealing performance.

Under the same working conditions, the HAR sealing ring has a better sealing performance than the O-ring. With more sealing surfaces, it can realize multi-stage sealing and increase sealing reliability. The larger the initial compression and fluid pressure are, the greater the contact pressure on the surface of the HAR sealing ring are. In high-temperature working conditions, the failure rate of the HAR sealing ring is higher, and the failure area easily appears on the sealing surface.

## References

[1] Zhang Jie and Hu Yang. 2019. Mechanical behavior and sealing performance of metal sealing system in roller cone bits. Journal of Mechanical Science & Technology 33: 2855–2862.

[2] Yang Junlin. 2017. Research on Metal Seal of Drill Bearing. B.S. Thesis, Southwest Petroleum University, Chengdu, China.

# 5

# Stator Rubber of the Positive Displacement Motor (PDM)

Positive displacement motor (PDM) is a kind of downhole drilling tool, which has been widely used in oil drilling and workover for the advantages of its structure and performance in recent years. It is also used in the geological survey, coal-bed methane, construction pipelines, and defense projects. As shown in Figure 5-1, positive displacement motor is composed of drive shaft assembly, universal coupling assembly, power section assembly, anti-drop assembly, and outlet valve assembly. Power section assembly is the core part of the whole system. It is a displacement engine driven by drilling fluid. There are two core components (rotor and stator). The rotor is a steel screw that coated with wear resistant materials. The stator is a steel pipe, its inner wall bonded by vulcanized rubber lining. Spiral number of the stator is one more than the rotor, such as 1/2, 3/4, 5/6, 7/8, 9/10. The typical cross-section contours of power section assembly as shown in Figure 5-1. The lesser the spiral number, the higher the speed and the lower the torque. The more the spiral number, the lower the speed and the higher the torque. In addition, the hollow rotor can be used to increase the hydraulic horsepower and mud return speed.

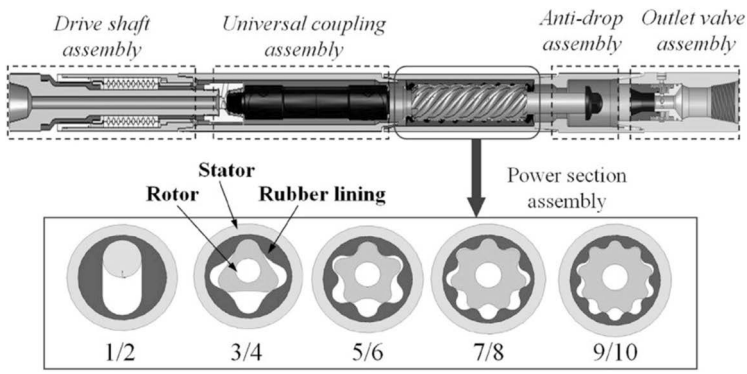


**Fig. 5-1.** The positive displacement motor structure.

The usage of PDM increases gradually with the development of drilling technology. But premature failure of PDM may cause downhole accidents in poor working conditions. According to the accident rate of drilling tools, failure of power section assembly is difficult to be controlled and has a great influence on the drilling. One of the main reasons is that mechanical behaviors of rubber material are more special.

## 5.1 Failure analysis of power section assembly

### *5.1.1 Fault tree model*

From a large number of field investigations and the relevant literature analysis, "Failure of power section assembly" is the top event, and fault tree was established as shown in Figure 5-2. The number of the basic events is 27 and the basic events are named as X1~X27. Table 5-1 shows the basic events and codes. For the fault tree, if logic "AND" is more, the number of the minimal cut set is less. If logic "OR" is more, the number of the minimal cut set is more. Those cut sets can give great insight into the weak link analysis of power section assembly in the design and working process by considering all the aspects related to the top event. It can provide a reference for structure optimization and maintenance.

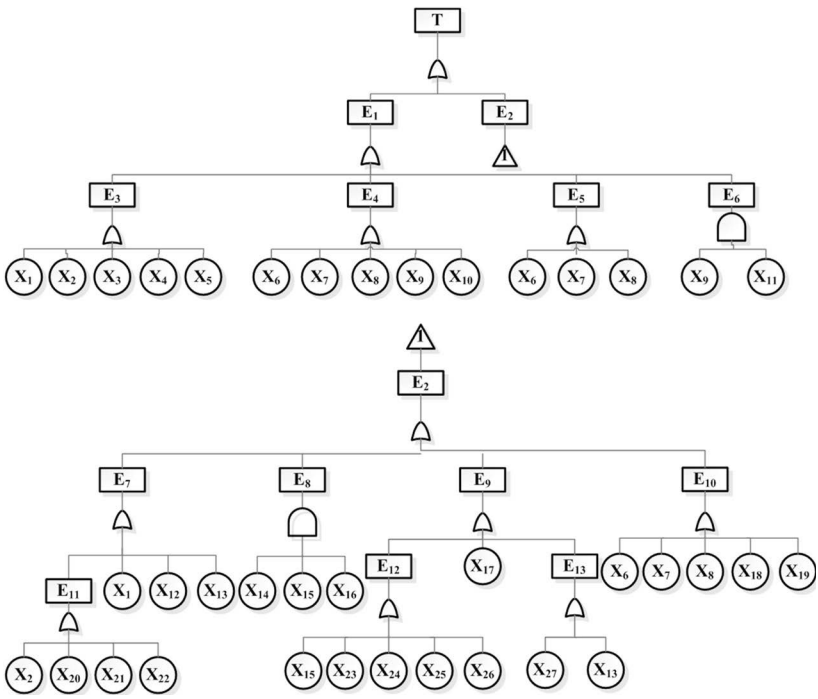


**Fig. 5-2.** The fault tree of power section assembly. ▭ Intermediate event ○ Bottom event △ Logic "OR" ∩ Logic "AND" △ Transfer symbol.

**Table 5-1.** Basic events and codes.

| Code | Basic event | Code | Basic event | Code | Basic event |
|---|---|---|---|---|---|
| T | Failure of power section assembly | $X_1$ | Intermittent drill and frequent braking | $X_{15}$ | Friction heat production |
| $E_1$ | Failure of rotor | $X_2$ | Ultrahigh pressure working environment | $X_{16}$ | Rubber material defects |
| $E_2$ | Failure of rubber lining | $X_3$ | Unstable radial and axial impact load of PDM | $X_{17}$ | Fatigue failure of rubber lining |
| $E_3$ | Joint thread fracture | $X_4$ | Bigger swing of rotor, not uniform speed | $X_{18}$ | Large gap between rotor and stator |
| $E_4$ | Wear and erosion of rotor surface | $X_5$ | Faster speed of rotor and larger pressure drop | $X_{19}$ | Cavitation caused by gas in drilling fluid |
| $E_5$ | Leakage of rotor thread | $X_6$ | Drilling fluid displacement is too large | $X_{20}$ | Stagnation behavior of rotor |
| $E_6$ | Plating peeling and pitting of rotor | $X_7$ | High sand content of drilling fluid | $X_{21}$ | Lager interference between rotor and stator |
| $E_7$ | Wear of rubber lining surface | $X_8$ | Harmful solid of drilling fluid | $X_{22}$ | Larger roughness of rotor surface |
| $E_8$ | Chipping and tear of rubber lining | $X_9$ | Unreasonable coating of rotor surface | $X_{23}$ | Reduced physical properties of rubber in a high-temperature condition |
| $E_9$ | Aging of rubber | $X_{10}$ | High friction of rotor and stator | $X_{24}$ | Bigger interference caused by temperature rise |
| $E_{10}$ | Erosion of rubber surface | $X_{11}$ | Unreasonable grinding process of rotor surface | $X_{25}$ | Lower physical properties of rubber |
| $E_{11}$ | High friction of rotor and stator | $X_{12}$ | Short rubber life | $X_{26}$ | Heat production caused by rubber viscoelasticity |
| $E_{12}$ | Thermal failure of rubber | $X_{13}$ | Large centrifugal force of rotor and stator | $X_{27}$ | Unreasonable design of rubber structure |
| $E_{13}$ | Seal failure caused by rubber deformation | $X_{14}$ | Poor cementing quality of rubber and steel | | |

### *5.1.2 Failure analysis and improvement measures*

As shown in Figure 5-3 and Figure 5-4, failure of the rotor's surface and rubber lining are the main reasons for the failure of the power section assembly. Therefore, the main failure reasons of the rotor's surface and rubber lining should be analyzed and improvement measures should be suggested.

(1) Wear and rust of rotor surface

As high-speed rotation of the rotor is similar to pure roll relative to the stator, the movement process is complicated. Mud is the power fluid of the power section assembly, which contains corrosive liquid and solid particles. Corrosive liquid

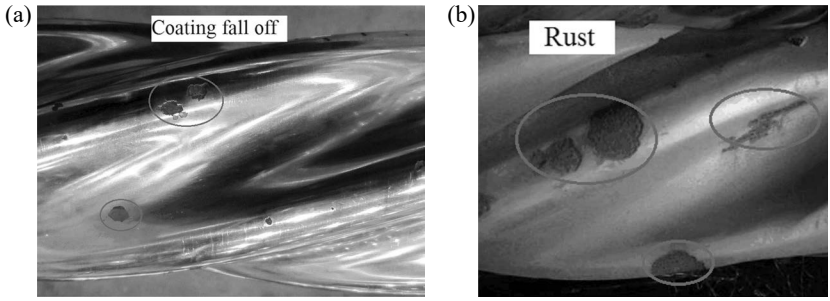


**Fig. 5-3.** Surface failure of the rotor.

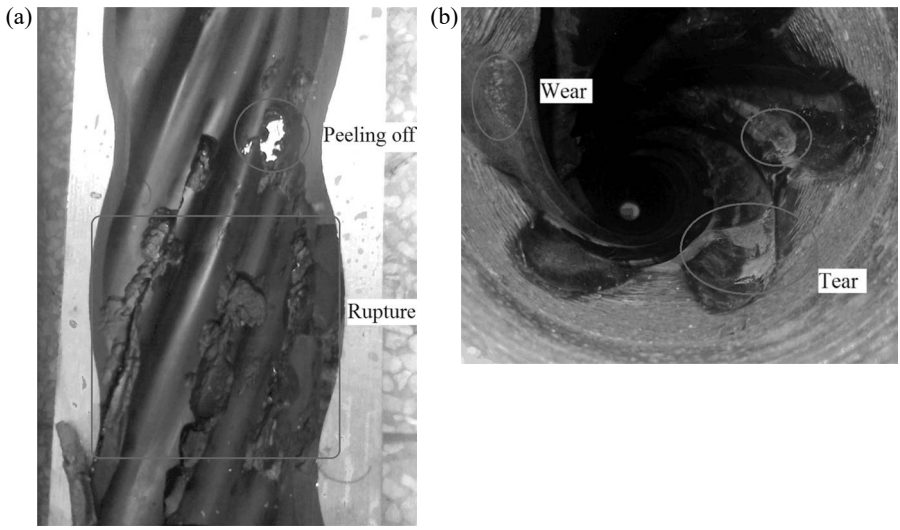


**Fig. 5-4.** The failure modes of the stator rubber lining.

includes additives for drilling technology and natural minerals from strata. The solid particles are mainly broken rock debris which are difficult to separate from the fluid. As shown in Figure 5-3, the main failure causes are wear and rust. They are mainly caused by solid particles and corrosive liquid, respectively. The coating on the rotor surface chips off and holes appear on it. The surface gradually corrodes in a muddy environment.

In order to reduce the surface failure of the rotor, the plating process needs to be improved. The coating material should also be improved to increase the hardness, wear resistance and corrosion resistance. For example, some corrosion-resistant materials can be added to the hard chromium coating. In addition, stainless steel can be used as the rotor material.

(2) Failure of rubber lining

Under the action of mud pressure, interference fit, and rotor movement, if the stress and strain of rubber lining exceed the design limit stress and strain of the rubber

material, tear and rupture will appear as shown in Figure 5-4. The force of the rotor on the rubber lining is a frequency alternating load, which can cause fatigue failure of the rubber lining. The load frequency *f* is:

$$f = \frac{v}{60} N \tag{5-1}$$

where, $\boldsymbol{v}$ is the speed of rotor; $\boldsymbol{N}$ is spiral number of stator [1].

Because of the rising load frequency, the fatigue life of the rubber lining decreases with the increasing of both the stator's spiral number and rotor speed. Under a high-frequency load, micro cracks appear on the concave and convex surface of the stator, because of its deformation. Then, these cracks gradually expand to the surrounding. If the load frequency is lower, the fatigue crack growth phenomenon will not appear. With the increasing of cracks, the coating materials fall off (Figure 5-4). Block peeling off will be more serious if the rubber lining is of low-material quality.

Surface wear of the rubber lining is caused by the action of rotor and mud. If the solid phase content and gravel are too large, this will aggravate the wear of runner lining. The chemistry of the drilling fluid reduces the quality of the physical properties of rubber, and allows of the contraction or expansion of the rubber lining. The change in the lining's volume will affect the fit dimension between the rotor and stator, which intensifies the failure of the rubber lining.

The working performances of the rubber reduce when the environment temperature increases. The environment temperature depends on strata temperature, mud temperature, friction heat, and hysteresis heat. A rise in the environment temperature also increases the interference. Hysteresis heat caused by the viscoelastic material properties of the rubber has been discussed in reference. The thickness of the uniform wall rubber lining is thin and uniform. It is more suited to a high-temperature environment than the general rubber lining.

Some improvement measures should be taken to reduce the failure of the rubber lining. For example, rubber material should be reasonably selected according to the downhole temperature and compound in drilling fluid. The solid content of the drilling fluid should be reduced by the ground solids control equipment. Stated displacement, bit pressure, and other parameters should be used in the drilling process. The bonding quality between rubber lining and steel shell should be improved. In addition, high-temperature-resistant rubber needs to be developed.

## 5.2 Rubber lining of the PDM

Taking the 5/6 positive displacement motor (PDM) (for example), the geometric models of the conventional rubber lining and uniform wall thickness rubber lining are shown in Figure 5-5. The features are:

- The radius of the stator arc $\boldsymbol{r}$ = 14.5 mm;
- The outer diameter of stator shell $\boldsymbol{D}$ = 172 mm;
- The eccentricity of rotor $\boldsymbol{e}$ = 8 mm;
- The density of rubber $\boldsymbol{\rho}$ = 1500 kg/m$^3$;
- The thermal conductivity coefficient $\boldsymbol{k}$ = 0.1465 W/(m•$^o$C);

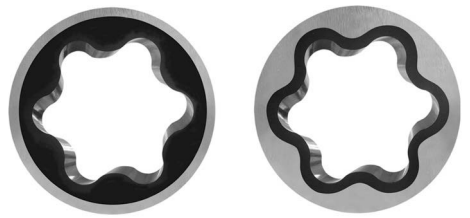


**Fig. 5-5.** The cross-section of the stator.

- The thermal expansion coefficient $\boldsymbol{\alpha}$ = 1e-5;
- The heat transfer coefficient between the linings and drilling fluid $\boldsymbol{h}$ = 20 W/(m$^2$•ºC);
- The specific heat $\boldsymbol{c}$ = 840 J/(kg•ºC);
- The shell material is steel [2].

In light of the geometrical structure, keeping the cross-sections of the linings along the axial the same, two-dimensional models were simulated. Nonlinear material constitutions were involved, the outer shell was fixed, and the initial drilling fluid pressure was applied to the lumen surface of the rubber lining.

## 5.3 Heat source analysis and the heat generation mathematical model

### *5.3.1 Mathematical model of heat generation in rubber bushing*

The heat source of the temperature field in the working process of the stator bushing of the screw tool mainly comes from four aspects. The underground formation temperature is the main heat source which affects its temperature field. Friction heating is caused by the interference fit between the rotor and stator bushing. Friction heating occurs between the high-pressure drilling fluid and the inner wall of the stator bushing. Heat comes from hysteresis loss due to viscoelastic properties of rubber materials.

According to the law of stress and strain of rubber bushing, the stress $\sigma$ and strain $\varepsilon$ are respectively:

$$\sigma = \sigma_{\max} \sin(\omega t + \delta) \tag{5-2}$$

$$\varepsilon = \varepsilon_{\max} \sin \omega t \tag{5-3}$$

where, $\omega$ is the angle frequency. $\delta$ is the loss angle (Lag phase angle).

According to the heating mechanism of the bushing rubber, the energy loss of each unit occurs within one week of rotor rotation in the bushing:

$$Q = 2\int_0^{\pi/\omega} \sigma \frac{d\varepsilon}{dt} dt \tag{5-4}$$

$$Q = \pi E' \varepsilon_{\max}^2 = \pi E \varepsilon_{\max}^2 \tan \delta \tag{5-5}$$

where, $E$' is the loss modulus. $E$ is the elastic modulus. tan $\delta$ is the loss factor. ***t*** is the rotation period. ***n*** is the rotor speed.

The rotor rotates in the bushing for one week, and the energy (heat generation rate at nodes) generated per unit time is:

$$q = \frac{Q}{T} = \pi n E \varepsilon_{\max}^2 \tan\delta \tag{5-6}$$

### *5.3.2 Heat conduction differential equation*

When the screw rotor continuously rotates the lifting fluid in the stator cavity, the joints of the stator rubber bushing have to undergo periodic stress and strain processes, which continuously bear the large deformation of tension and pressure, resulting in hysteresis loss and heat generation. Therefore, the stator temperature field problem can be regarded as the heat conduction problem with an internal heat source. According to the first law of thermodynamics and the Fourier law, the heat equilibrium equation of the unsteady temperature field of the stator of screw drill tool under polar coordinates is as follows:

$$\frac{1}{r}\frac{\partial}{\partial r}\left(\lambda r \frac{\partial T}{\partial r}\right) + \frac{1}{r^2}\frac{\partial^2 T}{\partial \theta^2} + \frac{q}{\rho c} = \frac{\partial T}{\partial t} \tag{5-7}$$

where, $T$ is the temperature °C. $q$ is the heat generation per unit volume, W/m$^3$.

### *5.3.3 Basic assumptions*

During the drilling process, the temperature rise in the stator is caused by the viscoelastic rubber only because of the heat generated by the heat loss, regardless of the thermal radiation between the bushing and the outside world. The working stability of the screw drill tool is in a heat balance state, and the temperature field of bushing is a steady heat conduction. The rubber material of bushing is isotropic, and its characteristics do not depend on temperature. That is, it does not affect the mechanical properties of bushing and neglects the effect of rubber relaxation. There is no temperature gradient along the axial direction, and the stator and rotor fit in the same section.

## 5.4 Thermal mechanical coupling effect

### *5.4.1 Uniform temperature field analysis*

When the initial temperature of the two bushings is set to 20°C, the stress and strain occur inside the bushing when the temperature rises to the downhole ambient temperature. Figure 5-6 shows the thermal stress distribution of the bushing. The maximum thermal stress on both bushings occur at the bottom of the inner surface arc and the minimum value is located at the top of the arc. Along the circumferential direction, the thermal stress on the bushing changes periodically. The maximum thermal stress on the conventional bushing is 0.02126 MPa, and the equal wall thickness bushing is 0.01751 MPa, which is reduced by 17.6%. It shows that

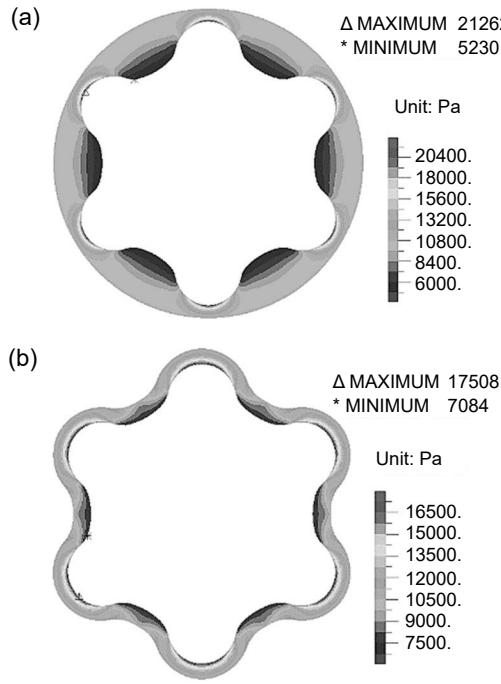


**Fig. 5-6.** Thermal stress distribution on the rubber lining under a uniform temperature rise.

the thermal fatigue life of the equal wall thickness bushing is longer under the same temperature rise. The displacement distribution of the bushing is shown in Figure 5-7. The maximum deformation position of the conventional bushing is at the top of the arc, and the deformation at the bottom of the arc is the smallest, contrary to the distribution of thermal stress. The deformation of equal wall thickness is more uniform along the circumferential direction. The maximum displacement of the conventional type is 0.02468 mm, and the equal wall thickness is 0.01026 mm, which is reduced by 58.4%. It shows that under the same temperature rise, the equal wall thickness bushing is less deformed and uniform, which has better mechanical properties than the conventional type.

Figure 5-8 shows the internal surface thermal stress and displacement variation curves of the two structures when the temperature of the bushing increases uniformly to 45°C, 65°C, 85°C, respectively. On the whole, the thermal stress and displacement of the two structural bushings change periodically. With the increase of temperature, the thermal stress and displacement of bushing increase. Under different temperatures, the peak value of the thermal stress and displacement of equal wall thickness bushing is smaller than that in the normal type, and the minimum value of thermal stress of equal wall thickness bushing is larger than it is in the normal type. The stress difference and displacement difference of the inner surface of equal wall thickness are smaller than that in the conventional type, which indicates that the thermal stress and deformation distribution of the equal wall thickness bushing are more uniform.

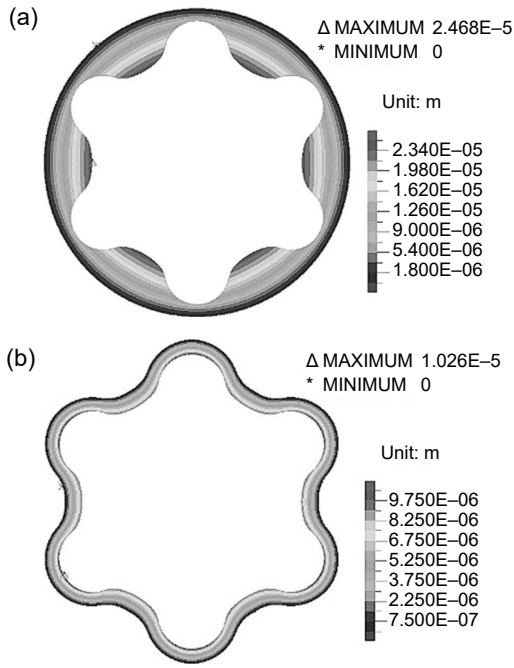


**Fig. 5-7.** The displacement distribution on the rubber lining under a uniform temperature rise.

### *5.4.2 Non-uniform temperature field analysis*

The rotation speed of the rotor is 2 r/s, the underground formation temperature is 65°C and the pressure of the drilling fluid is 50 MPa. Considering the hysteresis heat generation of rubber, the temperature field distribution of the two bushings is calculated as shown in Figure 5-9. The temperature field of the conventional bushing is elliptical in the circumferential direction, and the highest temperature is located in the center of the thickest rubber. The temperature decreases gradually from the center of the ellipse to the outside, and the temperature gradient is steep. The maximum temperature is 95.77°C, and the temperature rise is 30.77°C. The temperature of the thin part of the rubber is lower. When the temperature of the bushing increases, the tensile strength and deflection of the rubber material will decrease sharply, and the bond strength between the rubber and the stator shell will also reduce.

The temperature field of the bushing with equal wall thickness is approximately a symmetrical distribution of the bars at the top of the arc. On the whole, the distribution of the temperature field is more uniform, and the highest temperature is 66.16°C. The temperature rises by 1.16°C, and the temperature gradient is gradual. This has obvious advantages in prolonging the service life and improving the working performance of rubber bushings whose life and working performance are particularly sensitive to temperature.

Table 5-2 shows the comparison of the calculation results of two structural bushings in uniform and non-uniform temperature fields. The maximum thermal

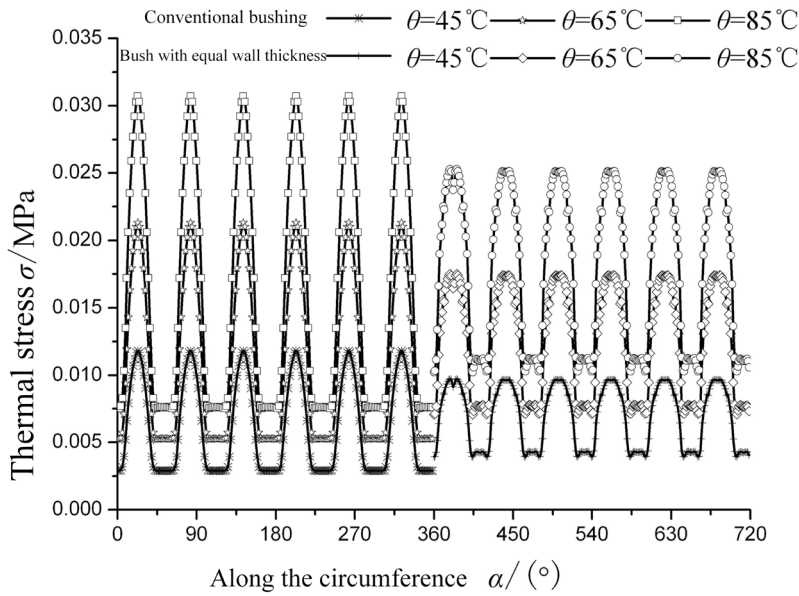


(a) Stress variation curve

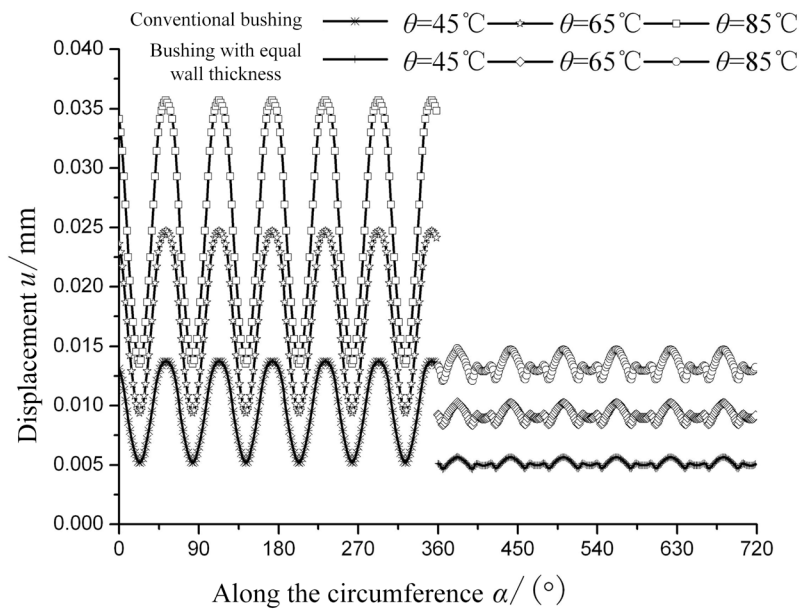


(b) Displacement curve

**Fig. 5-8.** The lining's stress and strain change curves under a uniform temperature rise.

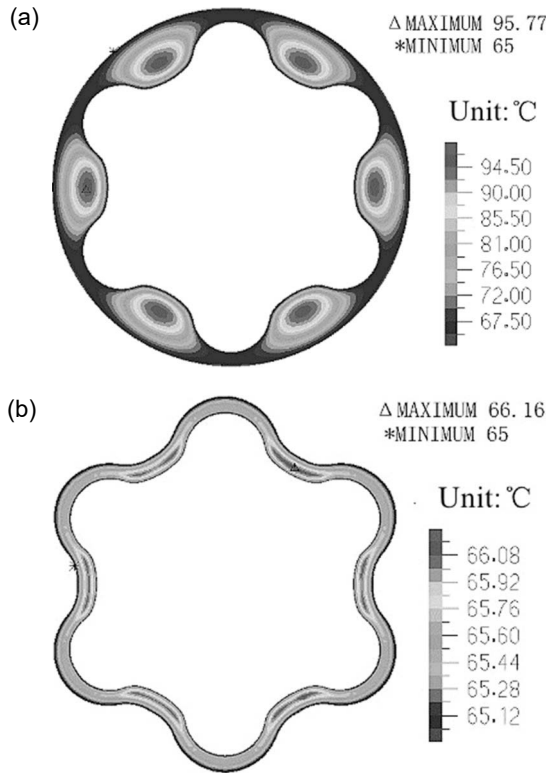


**Fig. 5-9.** The lining's temperature field distribution.

**Table 5-2.** The results of comparing two linings in uniform in an uneven temperature field.

| Temperature field | Bushing type | Maximum temperature rise/ºC | Maximum thermal stress/MPa | Maximum displacement/mm |
|---|---|---|---|---|
| Uniform | convention | 0 | 0.3895 | 0.4523 |
| | equal wall thickness | 0 | 0.3208 | 0.1880 |
| Non-uniform | convention | 30.77 | 0.3874 | 0.4445 |
| | equal wall thickness | 1.16 | 0.3207 | 0.1879 |

stress and displacement of the equal wall thickness bushing are smaller than those of the conventional type both in uniform and non-uniform temperature fields. Considering the lag heat generation of the material, the temperature rise in the equal wall thickness bushing is much smaller than that of the conventional type. The expansion deformation of conventional bushing is large, which increases the interference between bushing and rotor, and then increases friction heat generation.

Figure 5-10 depicts motor failure obtained from a drilling site. Figure 5-10(a) shows that the thermal failure of the rubber lining is basically consistent with the results of finite element analysis, both of which are at the maximum rubber thickness. The hysteresis heat of rubber leads to local holes being generated in the

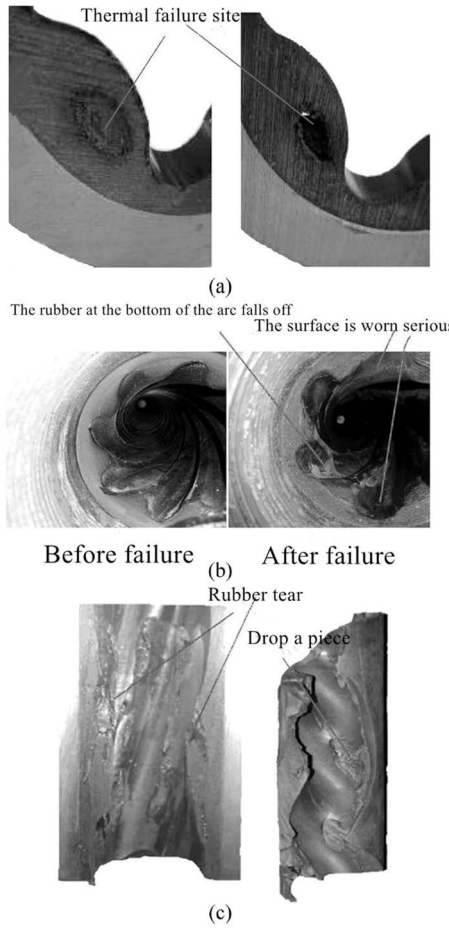


**Fig. 5-10.** The cases where the lining failure.

lining, which greatly reduce the working performance of the screw motor and affect the drilling process. Figure 5-10(b) shows the stator lining inner surface before and after the failure contrast. After the failure of the lining, the inner surface rubber layer at the bottom of the arc falls away and serious friction damage appeared at the top of the arc, which corresponds with the thermal stress field and displacement field of simulation. Due to rubber hysteresis, gas penetration, and rubber stratification, the stator rubber gets torn. Meanwhile, the coupling of thermal stress and temperature increases the degumming and dropping off of the lining during rubber injection if it has production defects, as shown in Figure 5-10(c).

### *5.4.3 Factors influencing the temperature rise*

In order to study the heating principles of rubber bushing, the influence on the temperature rise in the rubber bushing is analyzed from 6 aspects: hydrostatic

pressure, rotor speed, rubber hardness, Poisson's ratio, strata temperature, and differential pressure.

### *5.4.3.1 Effect of the hydrostatic pressure*

Under the action of drilling fluid, the inner cavity deformation of the bushing will directly affect the lag heat generation rate of the rubber body, and then affect the temperature rise in the bushing. The maximum temperature variation curve of bushing with ambient temperature of 65°C and rotational speed of 2 r/s, static pressure of 30 MPa, 40 MPa, 50 MPa, 60 MPa, 70 MPa, 80 MPa is shown in Figure 5-11. The influence of hydrostatic pressure on the temperature rise in the conventional bushing is much greater than that of the isobaric bushing; it is nonlinear, as it is mainly affected by the nonlinearity of rubber material and convection heat dissipation. The influence of hydrostatic pressure on the temperature rise in the equal wall thickness bushing is small. When the pressure is 80 MPa, the maximum temperature is 68.09°C, and the temperature rise is only 3.09°C.

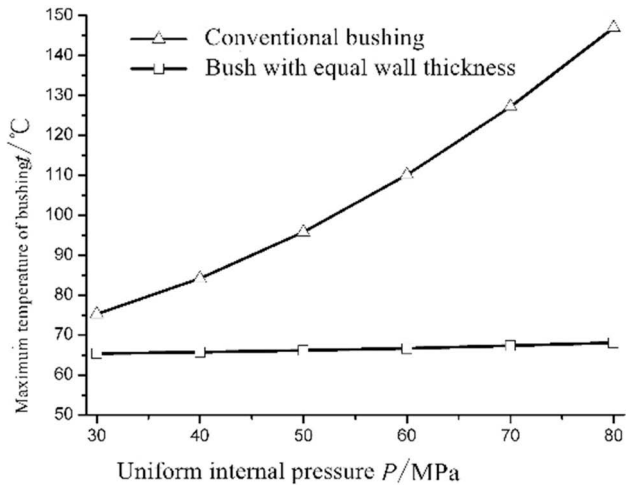


**Fig. 5-11.** The effect of pressures on the temperature rise in the bushing.

### *5.4.3.2 Effect of the rotor speed*

The rotor speed has a great influence on the heating rate of rubber material joints. The greater the rotational speed, the higher the temperature rise in the rubber bushing is. The maximum temperature variation curve of the bushing with a static pressure of 50 MPa and speed of 1 r/s, 1.5 r/s, 2 r/s, 2.5 r/s, 3 r/s is shown in Figure 5-12. The temperature rises of the two types of bushing vary linearly with the rotor speed, and the temperature rise in the conventional bushing varies greatly. However, the temperature rise in the equal wall thickness is small, and the maximum temperature rise is only 1.74°C.

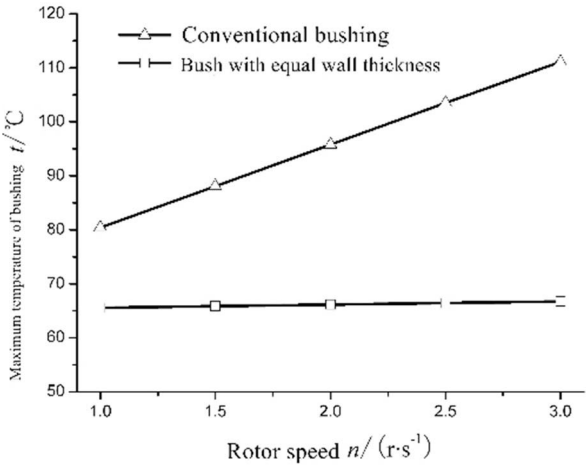


**Fig. 5-12.** The effect of rotor speed on the temperature rise in the bushing.

### *5.4.3.3 Effect of the rubber hardness*

According to the fitting formula, the elastic modulus of rubber material with different hardness and the $C_{10}$, $C_{01}$ value closest to the real experiment are obtained. A rubber material with hardness of 70, 75, 80, 85, 90 was studied. When the strata temperature is 65°C, the variation curve of the maximum temperature of bushing with rubber hardness is as shown in Figure 5-13. With the increasing of rubber hardness, the maximum temperature of the bushing decreases gradually, and the temperature of conventional bushing changes greatly with nonlinear law, and the temperature of the equal wall thickness bushing changes little, which is a mostly horizontal line.

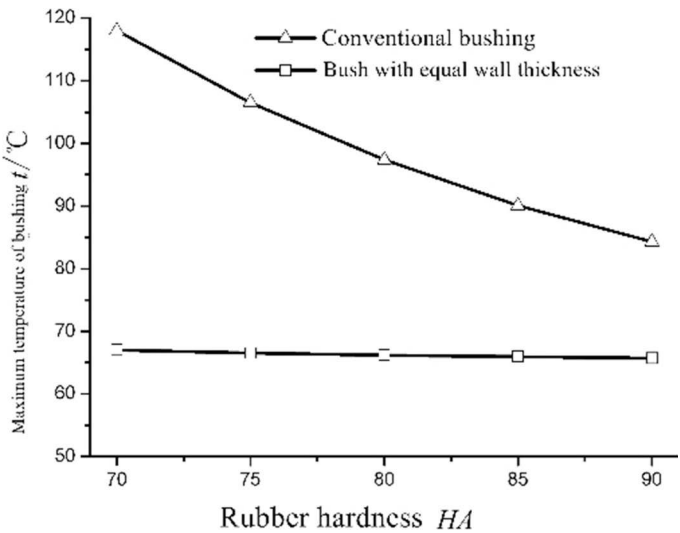


**Fig. 5-13.** The effect of rubber's hardness on the bushing's temperature rise.

*5.4.3.4 Effect of the Poisson's ratio*

Figure 5-14 shows the maximum temperature of the bushing with the rubber poisson's ratio at a speed of 1 r/s. It can be seen that the influence of Poisson's ratio on the temperature rise in the rubber bushing cannot be ignored, and the temperature of both bushings decreases nonlinearly with the increasing of Poisson's ratio. If Poisson's ratio is 0.4999, the rubber is close to incompressible, and there will be no lag heat generation, so the temperature rise in the bushing is close to 0°C. In the selection of the rubber bushing's material, the influence of Poisson's ratio on temperature rise should be taken into account in addition to its mechanical properties.

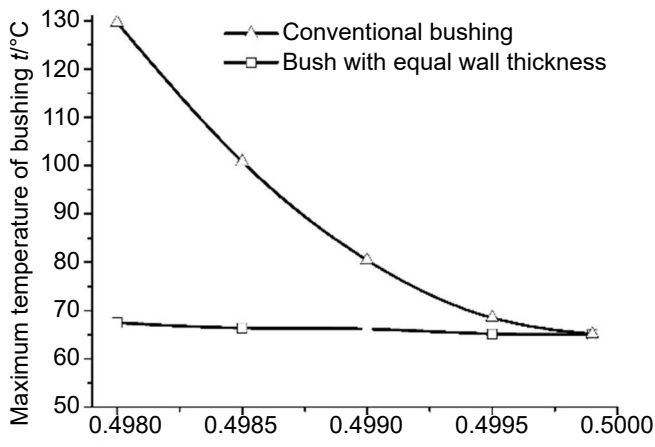


**Fig. 5-14.** The effect of Poisson's ratio on the temperature rise in the bushing.

*5.4.3.5 Effect of the strata temperature*

The downhole temperature is the working environment temperature of screw drilling tool. It affects the initial deformation of bushing, heat dissipation, and convection heat transfer. Because this process is a bidirectional coupling process, it is analyzed only from the angle of unidirectional coupling. Figure 5-15 shows the temperature rise in the rubber bushing at strata temperatures of 25°C, 45°C, 65°C, 85°C, 105°C, and 125°C. The temperature rising of the equal wall thickness bushing does not change much with the strata temperature, which mainly because the bushing is thin and uniform. The temperature rise in conventional bushing decreases with the increase in strata temperature, which is mostly linear law.

*5.4.3.6 Effect of the differential pressure*

Differential pressure is an important parameter affecting the working characteristics of screw drilling tools, which has a great influence on the stress and strain of bushing. The temperature field distribution of the two bushings when the differential pressure is 0.8 MPa as shown in Figure 5-16. When there is differential pressure, the temperature field distribution of the bushing becomes uneven. The highest-temperature region is concentrated in the thickest part of the rubber at the junction

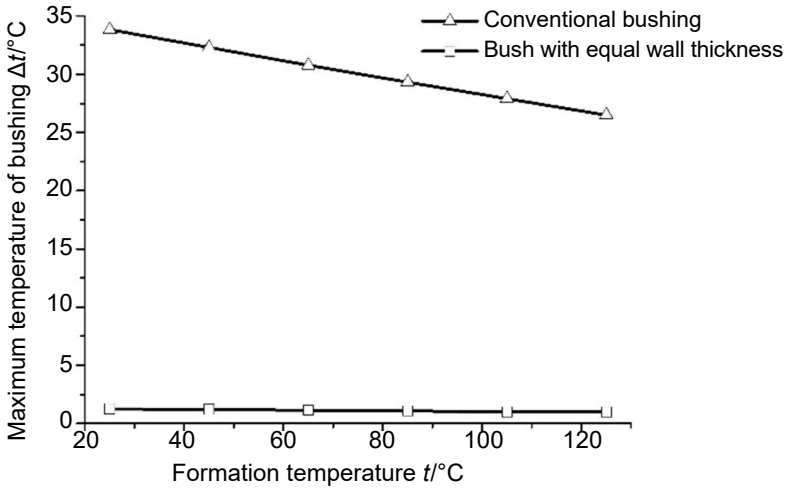


**Fig. 5-15.** The effect of strata temperature on temperature rise.

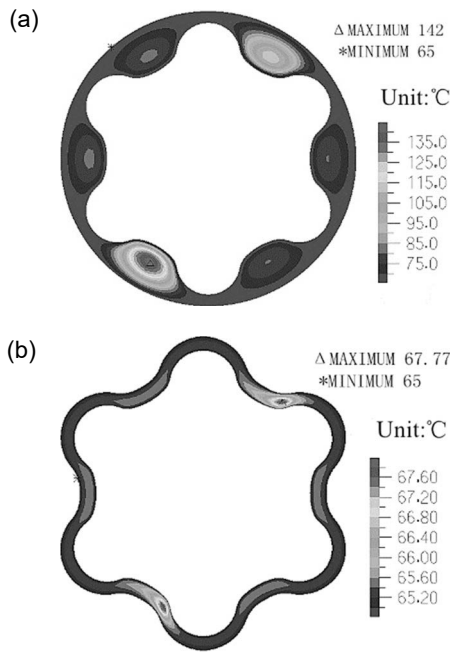


**Fig. 5-16.** The temperature distribution in the lining under the differential pressure 0.8 MPa.

of pressure change, and the temperature field of the two bushings is elliptical. The temperature gradient of conventional bushing is steep. Figure 5-17 shows the maximum temperature rise in the bushing when the rotor speed is 1 r/s, formation temperature as 65°C, and differential pressure is 0.6 MPa, 0.7 MPa, 0.8 MPa, 0.9 MPa, 1.0 MPa. The greater the differential pressure is, the greater the maximum

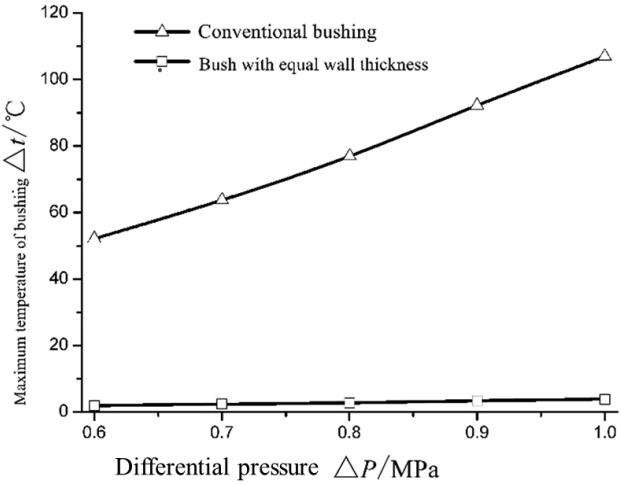


**Fig. 5-17.** The effect of different pressures on the temperature rise in the bushing.

temperature rise in the rubber bushing is, and the greater the nonlinear variation in the temperature is. When the differential pressure is 1 MPa, the temperature rise in the equal wall thickness bushing is 3.84°C, and that in conventional bushing is 107°C, which indicates that the influence of differential pressure on conventional bushing is much greater than that on equal wall thickness. The high temperature in the local area affects the adhesion between the rubber body and the steel body shell. In the design and manufacture of a screw stator, should be paid attention the bonding quality between the rubber bushing and the steel body jacket.

## 5.5 Mechanical behavior without heat effect

### *5.5.1 Stress and strain on the rubber lining*

When the drilling fluid pressure is 50 MPa, effective stress distribution on the rubber lining is as shown in Figure 5-18. The maximum effective stress appears on the bottom of arc, and the minimum effective stress appears on the top of arc. The maximum stress on the conventional rubber lining is 0.42 MPa, the minimum stress is 0.103 MPa. The maximum stress on the uniform wall thickness rubber lining is 0.346 MPa, the minimum stress is 0.14 MPa. The maximum stress on the conventional lining is higher than that on the uniform wall thickness lining by 21.4%. The stress distribution on the uniform wall thickness lining is more uniform, which is very beneficial for improving the service life of rubber lining.

Figure 5-19 shows the maximum shear stress distribution on the rubber lining under drilling fluid pressure 50 MPa. The distribution of maximum shear stress is similar to that of effective stress. The maximum shear stress on the conventional rubber lining is 0.235 MPa, which is higher than that on the uniform wall thickness lining (0.191 MPa) by 23%.

Figure 5-20 shows the deformation of the rubber lining under drilling fluid pressure 50 MPa. For the conventional rubber lining, the maximum deformation

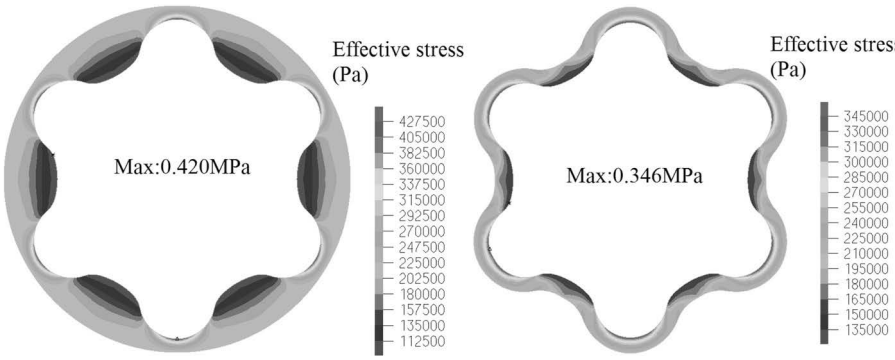


**Fig. 5-18.** The effective stress distribution on rubber lining under 50 MPa.

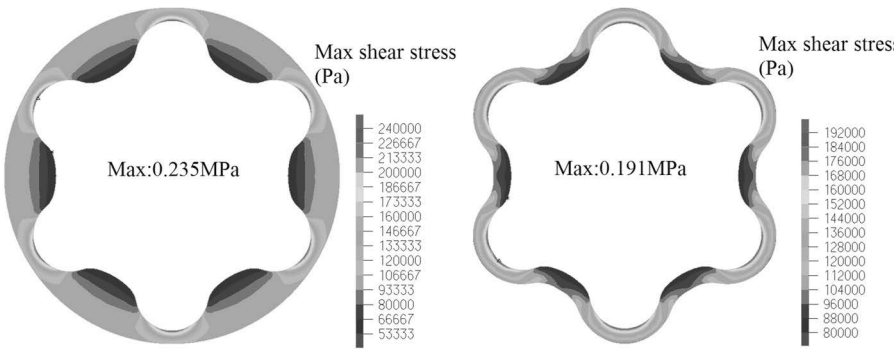


**Fig. 5-19.** The maximum shear stress distribution on the rubber lining under 50 MPa.

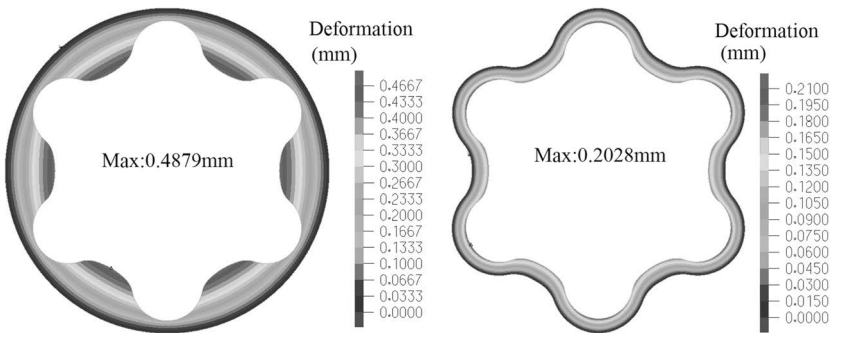


**Fig. 5-20.** The deformation distribution of the rubber lining under 50 MPa.

appears on the top of arc, and the minimum deformation appears on the bottom of arc. The maximum deformation is 0.4879 mm. The deformation distribution of the uniform wall thickness lining is more uniform. This is because the thickness of rubber lining is uniform and thin. The maximum deformation of the uniform wall thickness lining is 0.2028 mm, which is lesser than the maximum deformation of the

conventional lining by 58.4%. If the deformation of the rubber lining is more, which becomes prone to fatigue failure.

### *5.5.2 Effect of the drilling fluid pressure*

Drilling fluid pressure changes the deformation of rubber lining, which in turn influences the interference fit of the rotor and the stator. Figure 5-21 shows the effective stress curves of the lumen surface of the rubber lining. Stress periodically changes along the circumferential direction. The peak stress appears on the bottom of arc, and the valley stress appears the top of arc. With the increasing of drilling fluid pressure, effective stresses increases gradually. Under the same drilling fluid pressure, the maximum stress on the conventional lining is greater than the maximum stress on the uniform wall thickness lining, while the minimum stress on the convention lining is lesser than that on the uniform wall thickness lining.

Figure 5-22 shows the deformation curves of lumen surface of the rubber lining. In the curve, the peak deformation expresses the bottom of arc, and the valley

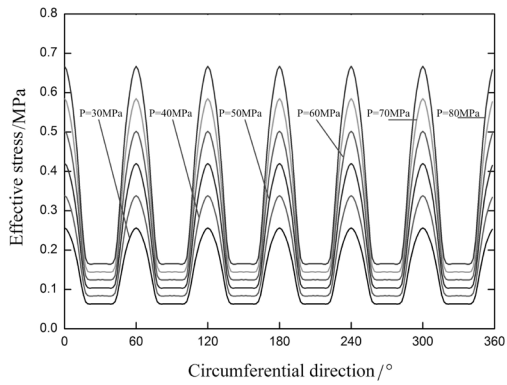


(a) Conventional rubber lining

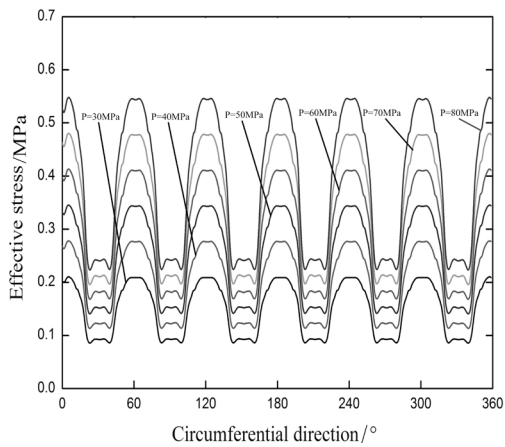


(b) Uniform wall thickness rubber lining

**Fig. 5-21.** The effective stress on the rubber lining under different pressures.

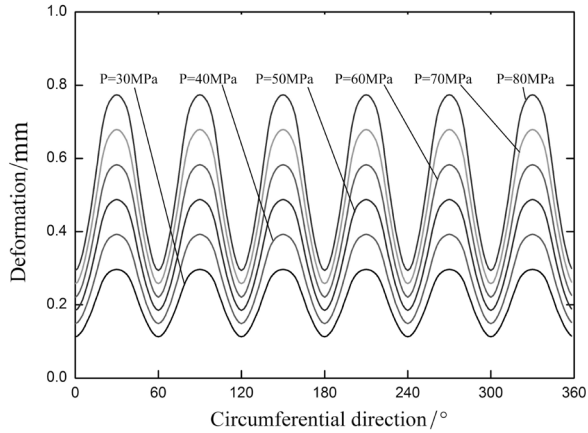


(a) Conventional rubber lining

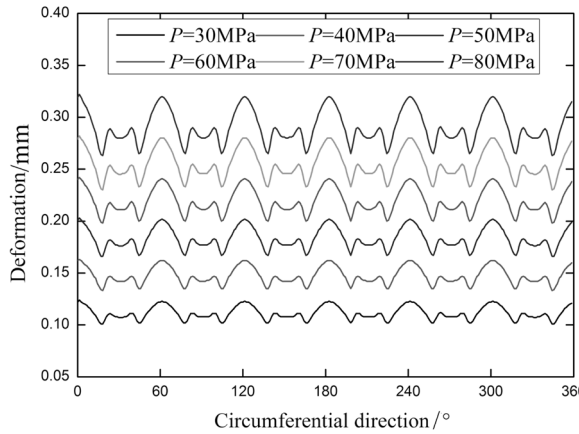


(b) Uniform wall thickness rubber lining

**Fig. 5-22.** Deformation of the rubber lining under different pressures.

deformation expresses the top of arc. Deformation of the rubber lining gradually increases with the increase in the drilling fluid pressure. The difference in peak and valley deformations is very small for the uniform wall thickness lining. Therefore, the deformation of uniform wall thickness lining is more uniform, although there are some fluctuations along the circumferential direction.

### *5.5.3 Effect of the rubber hardness*

Figure 5-23 shows the effective stress on the rubber lining in rubber material with different hardness. With the increasing of rubber hardness, the effective stress on the rubber lining gradually increases. No matter whether it is the conventional lining or uniform wall thickness lining, the change rate of the effective stress is very small. It shows that rubber hardness has a small effect on the effective stress on the rubber lining.

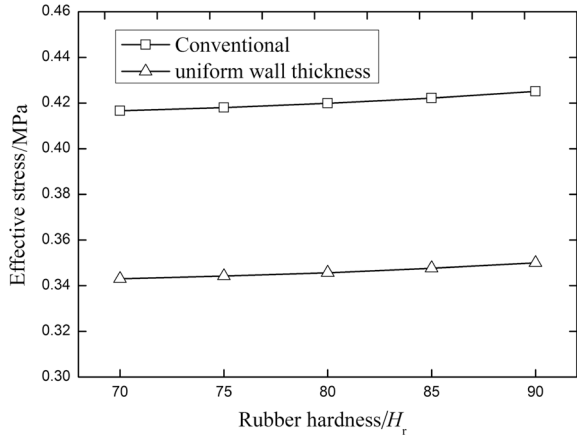


**Fig. 5-23.** The effective stress on the rubber lining under different rubber hardness.

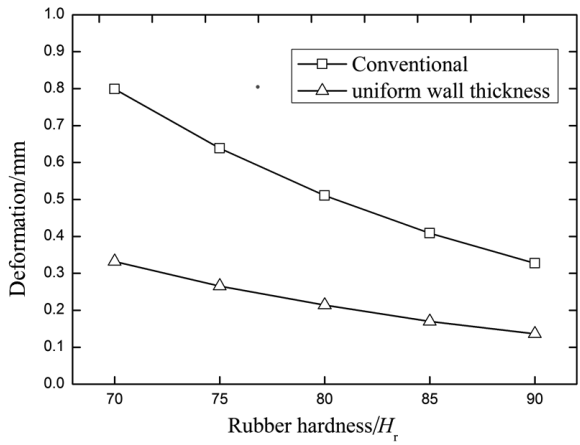


**Fig. 5-24.** The deformation of rubber lining with different rubber hardness.

The rubber's hardness has a great influence on the deformation of the rubber lining. As shown in Figure 5-24, the deformation of rubber lining gradually decreases when the rubber hardness increases. The change rate of the conventional lining is greater than that of the uniform wall thickness lining. With the increasing of the rubber hardness, the deformation change rate gradually decreases.

### *5.5.4 Effect of the downhole temperature*

Downhole temperature is the working environment temperature of PDM. It affects the heat radiation, convection heat transfer, stress, and deformation of the rubber lining. Deformation affects the heat production rate of the rubber material. Therefore, it is a two-way coupling process. After conducting a thermal-structure coupling analysis, the findings of the effective stresses on rubber lining under

different downhole temperatures are shown in Figure 5-25. Effective stresses on the rubber lining decrease when the downhole temperature increases. So, the downhole temperature can reduce the stress on the rubber lining. However, it can also reduce the effectiveness of the material's physical properties, which accelerates the aging of the rubber, and reduce its service life. At present, high-temperature-resistant rubber needs to be developed urgently for the deep well drilling, ultra-well drilling, and geothermal well drilling.

Deformations of the rubber lining under different downhole temperatures are shown in Figure 5-26. Deformation of the rubber lining decreases when the downhole temperature increases. The deformation change of the uniform wall thickness lining is small. The smaller the deformation of the rubber lining is, the bigger the interference between rotor and lining is. Therefore, interference increases when the downhole temperature increases, which is very harmful to the rubber lining when interference is great.

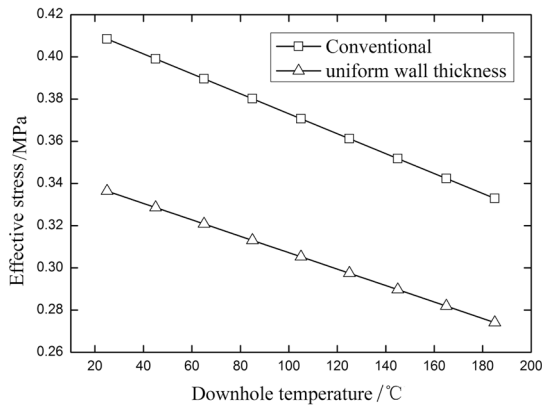


**Fig. 5-25.** The effective stress on the rubber lining under different downhole temperatures.

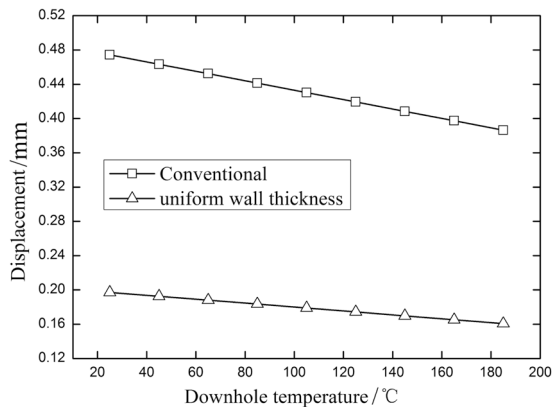


**Fig. 5-26.** The deformation of rubber lining under different downhole temperatures.

### *5.5.5 Effect of the pressure difference*

In the working process, there are six chambers in the cross-section. The pressure difference between the adjacent chambers drives the rotor movement. As shown in Figure 5-27, when the rotor rotates clockwise, the areas of chamber f–a, a–b, and b–c increase, while the areas of chamber c–d, d–e, and e–f decrease gradually. Therefore, the pressure difference should be applied on the inner wall of each chamber after adding an uniform load.

Figure 5-28 shows the effective stress distribution on the rubber lining under various pressure differences. The effective stress distribution on the rubber lining is uneven. Stress on the bottom of arc is greater than on the top of arc. The maximum stress appears on the a–e section. Because the pressure difference between e–f and f–a chamber is the single stage pressure difference of the power section assembly; it

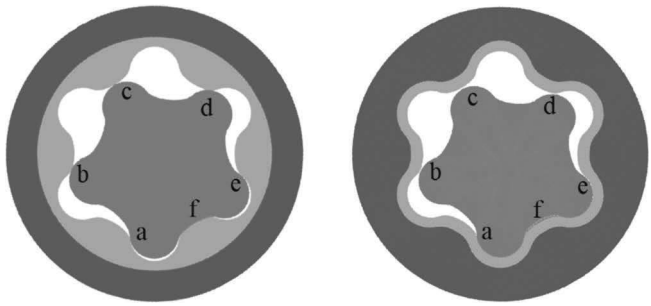


**Fig. 5-27.** A motion model of the rotor in the process.

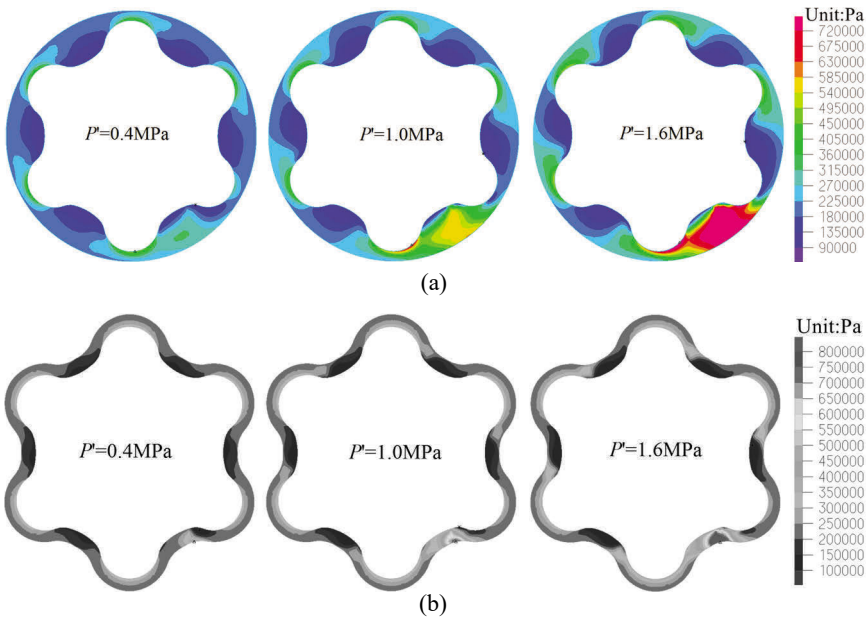


**Fig. 5-28.** The effective stress distribution on the rubber lining.

is more than the pressure difference in the other positions. The maximum stress on conventional rubber lining appears on the inner wall, which aggravates the wear and tear of the rubber lining. While the maximum stress on uniform wall thickness rubber lining appears on the outer wall, it may reduce the bonding strength. Along with the rotor movement, the high-stress area moves along the circumferential direction. Therefore, alternating stress appears on each position of the rubber lining. Then, fatigue failure of the rubber lining occurs. For uniform wall thickness rubber lining, the rubber is easy to fall off from the steel shell. If the speed of the rotor is higher, the failure modes become more apparent.

Effective stress change curves of rubber lining under different pressure differences are shown in Figure 5-29. With the increasing of the pressure difference, the effective stress on the rubber lining increases gradually. When the single stage pressure difference of the power section assembly is less than 0.7 MPa, the stress on the conventional lining is greater than the stress on the uniform wall thickness lining. When pressure difference is more than 0.7 MPa, the stress on the conventional lining is less than the stress on the uniform wall thickness lining. When it comes to the uniform wall thickness lining, the stress change is very small when pressure difference is less than 0.3 MPa. However, stress change rate is relatively constant when the pressure difference is more than 0.3 MPa. So, the uniform wall thickness rubber lining is more prone to failure than conventional lining when the pressure difference is higher.

Figure 5-30 shows the deformation distribution on the rubber lining under various pressure differences. The deformation is more uneven when the pressure difference increases. The maximum deformation appears on the f position. So, the deformation at this position is the most. When the pressure difference is small, the deformation of the uniform wall thickness lining is small and uniform. In the working process of PDM, a severe deformation of the rubber lining can result in hysteresis heat. Thermal failure appears in the conventional rubber lining if the thickness of the petal is too much. The heat emitted from the uniform wall thickness rubber lining is very little, and can be taken care of by convective heat transfer.

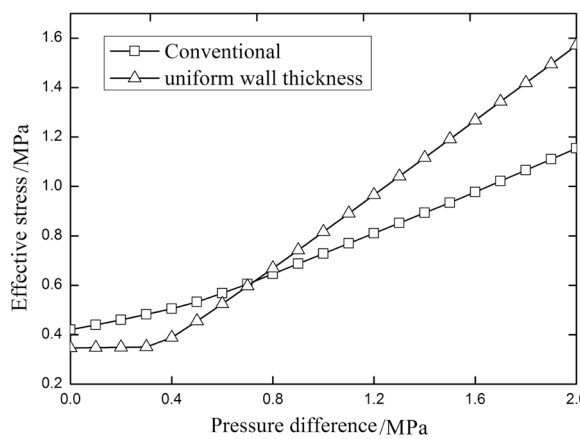


**Fig. 5-29.** The effective stress on the rubber lining under various pressure differences.

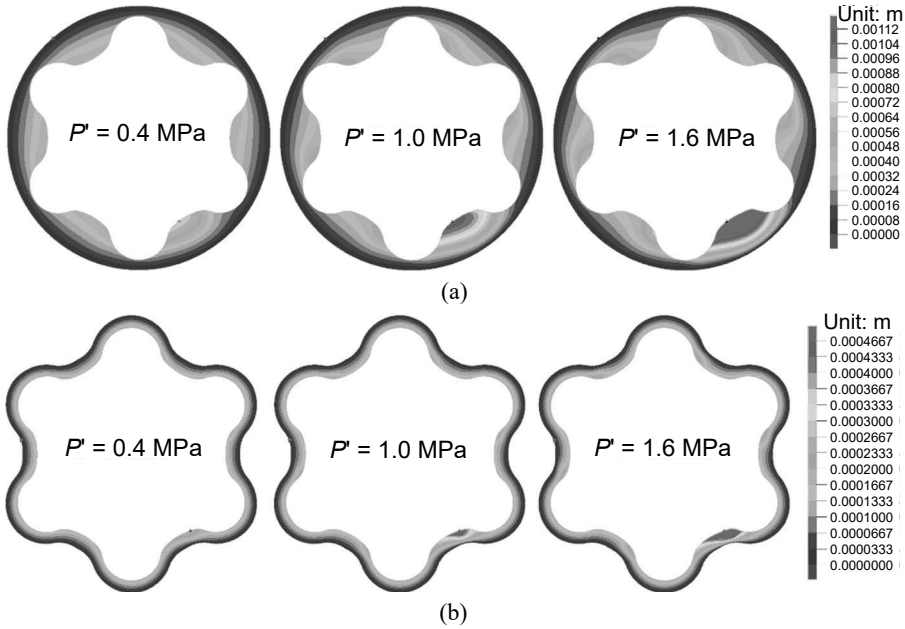


**Fig. 5-30.** The deformation distribution on the rubber lining.

The deformation change curves of the rubber lining under various pressure differences are shown in Figure 5-31. With the increase in pressure difference, the deformation of rubber lining increases gradually with a nonlinear law. The deformation of the conventional lining is more than it is in the uniform wall thickness lining. The deformation change rate of the uniform wall thickness rubber lining is smaller. Therefore, the rubber lining is more prone to failure when the pressure difference increases.

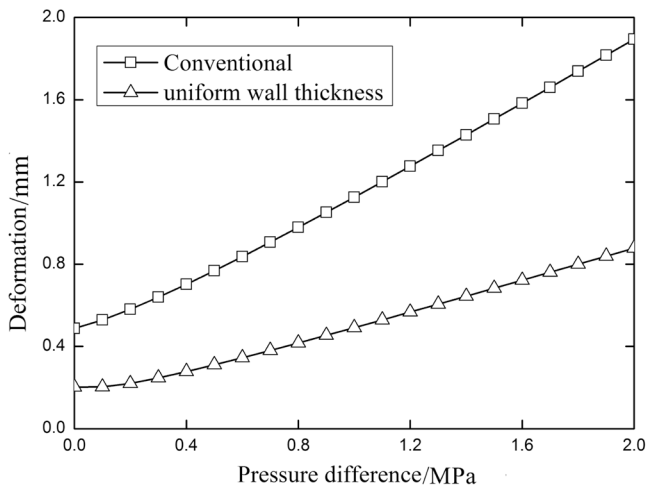


**Fig. 5-31.** The deformation of the rubber lining under different pressure differences.

## 5.6 Conclusions

The higher the temperature is, the greater the thermal stress and deformation of the bushing is. The thermal stress and strain on the equal wall thickness bushing are lesser than those on the conventional type bushing. Considering the delayed heat generation of rubber, the temperature field of the conventional bushing is elliptical along the circumferential direction, and the temperature gradient is steep. The temperature field of the equal wall thickness bushing is approximately a strip symmetrical distribution at the top of the arc.

The temperature rise in the conventional bushing increases with the increase of static pressure, rotor speed and pressure difference, and it decreases with an increase in rubber hardness, Poisson's ratio, and formation temperature. But these parameters have little effect on the temperature rise in wall thickness bushing. The main failure parts are the rotor's surface and the rubber lining. Wear and rust are the main failure causes of the rotor. The main failure causes of the rubber lining are wear, tear, rupture, peeling off, thermal, and fatigue failure.

## References

[1] Li, M.Q. and Zhao, HC. 2008. Failure mechanism and measure analysis of motor stator of screw drill. China Pet Mach. 36(10): 8–11.

[2] Han, C.J., Zhang Han and Zhang, J. 2015. Structural design and sealing performance analysis of biomimetic sealing ring. Appl. Bionics Biomech. 5: 1–11.

# 6

# Sealing Structure of the Pump

## 6.1 Seals for pumps

### *6.1.1 Fracturing pump*

The fracturing pump is a kind of special pump with large displacement and ultra-high pressure, which is mainly used for downhole pressure tests, strata fracturing, and other operations. It is the main production equipment used in extracting shale gas and shale oil. As a key part of fracturing pump, the plunger is located between the power end and the hydraulic end. It is one of the most vulnerable parts of the fracturing pump, which is greatly affected by the alternating force at the power end and the high-pressure impact of the corrosive liquid at the hydraulic end. The fracturing pump is shown in the Figure 6-1.

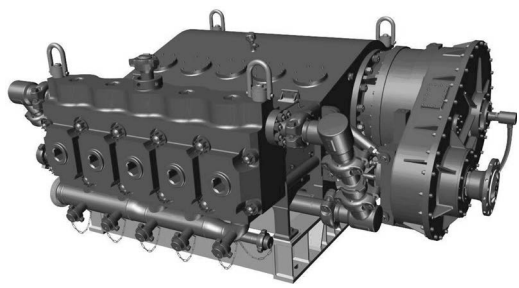

**Fig. 6-1.** The fracturing pump.

### *6.1.2 Mud pump*

The mud pump is the main piece of equipment in the mud circulation system used in oil drilling operations. The mud pump has the functions of being the cooling bit, carrying downhole cuttings, and assisting drilling. The rubber cup on the piston of the mud pump is the key mechanism used for sealing, and its sealing performance directly affects the efficiency of the mud pump, and even the whole drilling process. An investigation of the vulnerable parts of the mud pump revealed that the average

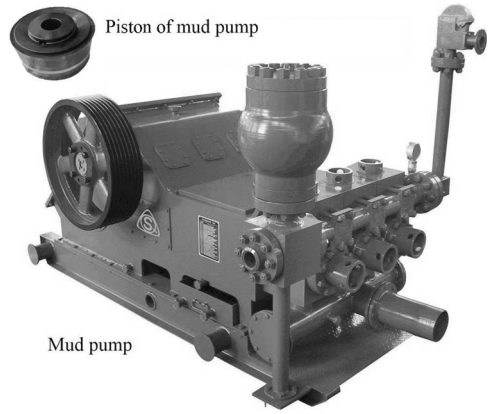


**Fig. 6-2.** The mud pump and piston.

service life of the piston cup is the shortest [1], which is the weakest link in the mud pump. The failure of the piston cup is caused by the wear marks on the sealing surface of the cup due to abrasive wear, resulting in tiny mud leakage. The wear marks continue to expand, eventually leading to piston failure [2]. The mud pump and piston is shown in Figure 6-2.

## 6.2 The plunger seal of the fracturing pump

### *6.2.1 Numerical model*

The fracturing pump analyzed is a 6500 HP five cylinder single acting plunger pump [4], with 275 times/min of impulses and a maximum displacement of 76.0 L/s. The diameter of plunger is designed according to the following formula [5]

$$Q = \left(\frac{N}{2}\right)(\Pi D^2/4)v_p\eta_V \tag{6-1}$$

where, $N$ is the number of piston cylinders of fracturing pump, $n$ = 5. $D$ is the piston diameter of fracturing pump, m. $v_p$ is the average velocity of the piston in the fracturing pump, $v_p$ = 2.7 m/s. $\eta_V$ is the volumetric efficiency of fracturing pump, $\eta_V$ = 0.9.

The diameter of the plunger is 126 mm, and the plunger stroke is 0.295 m. The minimum inner diameter of the sealing ring is 126 mm, and the minimum outer diameter is 166 mm. The side length of the inner and outer rings is $l$ = 10 mm, and the lip angle of the sealing ring is γ = 120°. The interference of the inner and outer rings is $h$ = 0.5 mm, and the friction coefficient is 0.2. The plunger, the support ring, the pressure ring, and the fracturing pump shell are all steel. NBR is selected as the sealing ring material. The two-parameter Mooney-Rivlin model [6] is selected in the simulation analysis. The plunger seal structure and mesh model of the fracturing pump are shown in Figure 6-3. The main dimensions that may affect the mechanical properties and sealing performance of the seal ring of fracturing pump are the support ring angle $\alpha$, pressure ring angle $\beta$, the lip angle of seal ring $\gamma$, the interference amount of seal ring $h$, the seal surface length $l$, friction coefficient $\mu$ and seal ring number $n$.

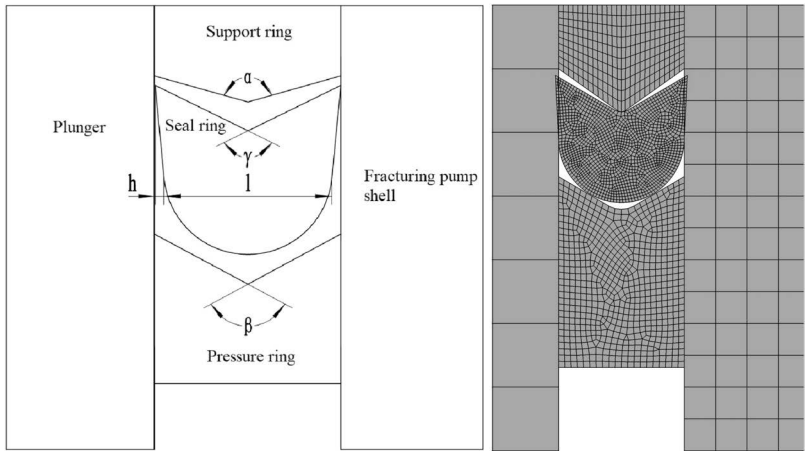


**Fig. 6-3.** The sealing structure and numerical model of the fracturing pump.

## *6.2.2 Structural parameters of the non-sealing ring*

### *6.2.2.1 Effect of the support ring angle*

Because the working load of the fracturing pump in the process of drainage is greater than that in the process of suction, so the numerical simulation analysis under the drainage condition is carried out. In order to analyze the force of the seal ring under different support ring angles $\alpha$, the numerical models with support ring angles of 100°, 110°, 120°, 130°, 140°, and 150° were established, and the seal ring angle $\gamma = 120°$ was selected.

Figure 6-4 shows the von-Mises stress on the seal ring with different support ring angles. The von-Mises stress distribution on the sealing ring is not uniform, and the stress near the sealing surface of the inner ring is higher. The maximum stress with $\alpha = 100° \sim 140°$ appears on the sealing surface of the inner ring, the maximum stress with $\alpha = 100°$ appears at the root of the sealing surface of the inner ring. The maximum stress with $\alpha = 150°$ appears at the lip groove of the seal ring, and the maximum stress is significantly higher than that on other sealing rings.

Figure 6-5 shows the contact pressure distribution on sealing surface under different support ring angles. The maximum contact pressure with different support rings appears at the lip of the sealing ring when the plunger is discharging fracturing fluid. The maximum contact pressure on the support ring angle $\alpha = 140°$ is the greatest, and it on the support ring angle $\alpha = 100°$ is the least.

Figure 6-6 is the contact pressure curve on the axial length of the sealing surface. The contact pressure far away from the lip of the sealing ring gradually decreases, and the stress plateau appears in the middle of the sealing surface. With the increasing of the support ring angle, the contact surface length of the sealing ring becomes larger.

The support ring angle has a certain influence on the von-Mises stress on the sealing surface, and a too large or too small inner ring angle will reduce its mechanical properties. Meanwhile, the support ring angle is one of the important factors affecting its sealing performance.

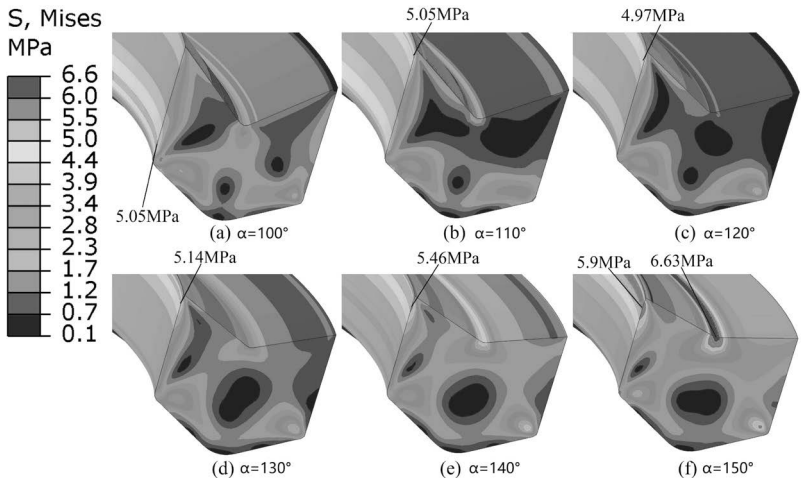


**Fig. 6-4.** The von-Mises stress on the seal ring with different support ring angles.

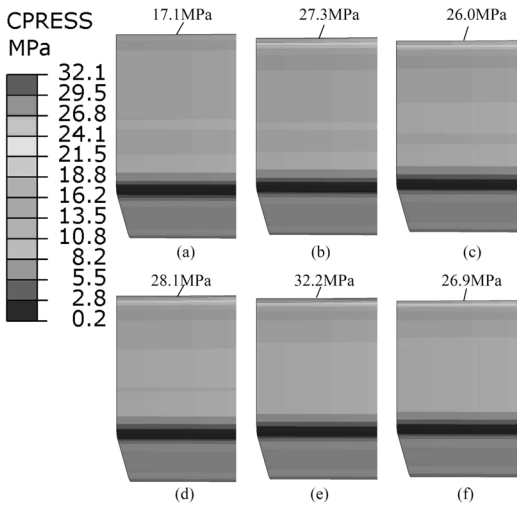


**Fig. 6-5.** The contact pressure distribution on the seal ring with different support ring angles.

### *6.2.2.2 Effect of the pressure ring angle*

Figure 6-7 shows the stress distribution of the sealing rings with different pressure ring angles. The von-Mises stress appears near the lip of the sealing surface, and the difference in the maximum von-Mises stress is small under different pressure ring angles. The contact pressure on the sealing surface is concentrated on the lip of the sealing surface, and the contact pressure varies greatly under different pressure ring angles. The maximum contact pressure is obtained when the pressure ring angle is 120°. With the increasing of the pressure ring angle, the contact surface between the sealing ring and the plunger increases. The contact pressure on the sealing surface decreases with the axial length of sealing surface increase. The pressure ring angle

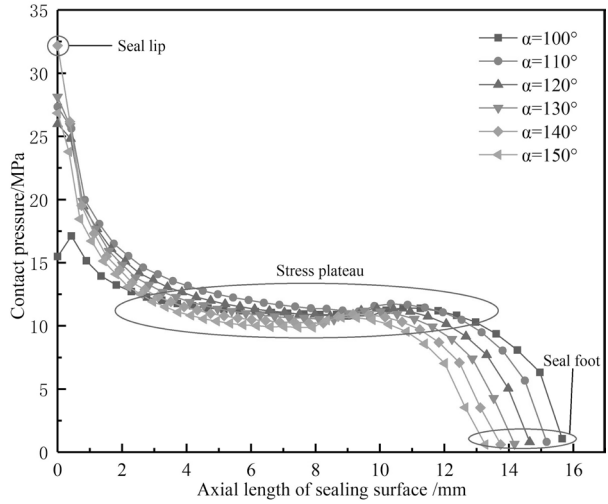


**Fig. 6-6.** The contact pressure curve on the seal ring with different support ring angles.

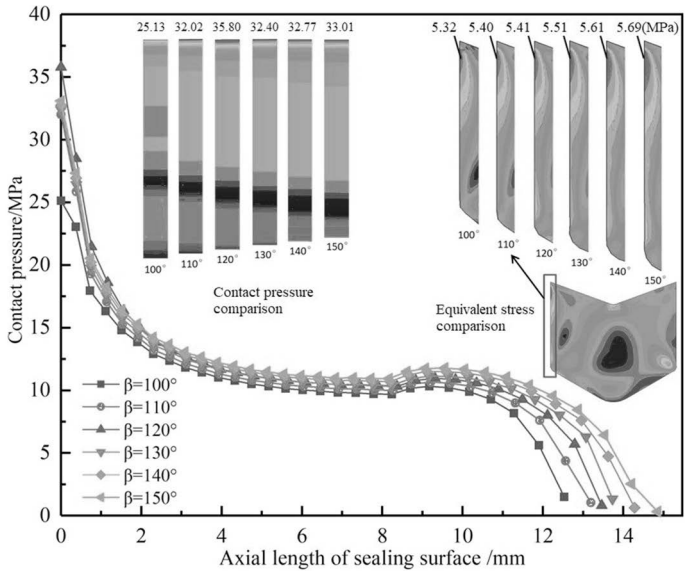


**Fig. 6-7.** Contact pressure and stress of the sealing rings with different pressure ring angles.

has little influence on the maximum von-Mises stress on the sealing surface of the sealing ring, but it has a great influence on the maximum contact pressure.

### *6.2.2.3 Effect of the friction coefficient*

Figure 6-8 shows the stress and contact pressure on the sealing surface of the sealing ring. The maximum von-Mises stresses on the seal ring with friction coefficient 0.05 and 0.10 are on the non-contact surface of the seal ring root, and the stress on the seal ring with larger friction coefficient is more. The maximum stress on the sealing

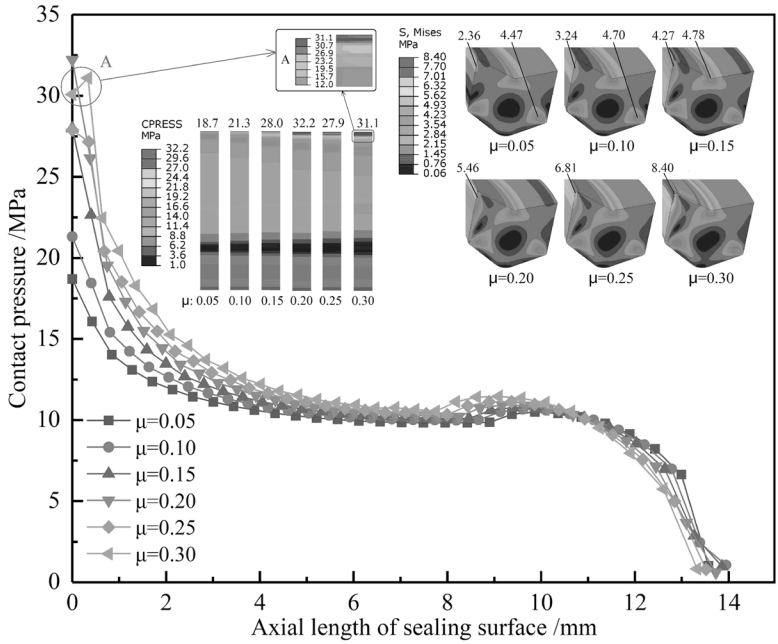


**Fig. 6-8.** Contact pressure and stress of the sealing ring with different friction coefficients.

ring is on the groove of sealing ring lip when the friction coefficient is 0.15. The maximum von-Mises stress on the sealing ring with the larger friction coefficient is greater when the friction coefficient is 0.20, 0.25 and 0.30. The contact pressure on outside the lip of the sealing ring shows little change under different friction coefficients. With the increasing of the friction coefficient, the high contact pressure area on the sealing ring becomes wider. When $\mu$ = 0.05 ~ 0.20, the extremum of contact pressure appears at the lip edge of the sealing surface, and it increases with the friction coefficient increases. When $\mu$ = 0.30, the maximum contact pressure appears near the lip edge of the sealing surface.

Increasing the friction coefficient in a certain range is beneficial for improving the sealing performance of the sealing ring. When the friction coefficient is larger, more heat will be generated when the fracturing pump is working, and the aging of the rubber material will be accelerated.

### *6.2.3 Structural parameters of the sealing ring*

#### *6.2.3.1 Effect of the lip angle*

Figure 6-9 is the contact pressure and stress of the sealing ring with different lip angles. When the lip angle of the seal ring $\gamma$ = 105° and 110°, the maximum von-Mises stress on the seal ring appears in the lip groove. When $\gamma$ = 115° ~ 130°, the maximum von-Mises stress appears on the seal surface of the seal ring in contact with the plunger, and its extreme value is obviously smaller than that of the seal ring with $\gamma$ = 105° and 110°. The maximum contact pressure on the sealing surface

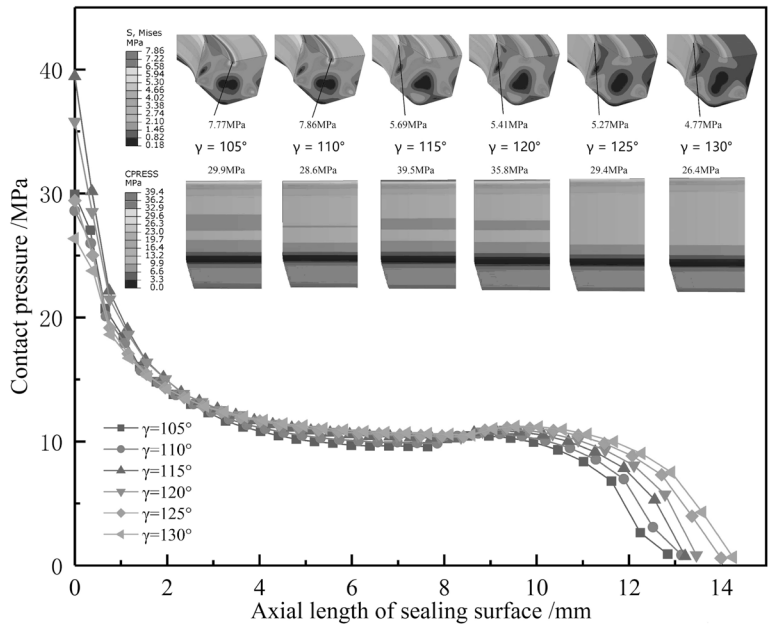


**Fig. 6-9.** Contact pressure and stress of the sealing ring with different lip angles.

appears at the lip of the sealing surface, and that on the sealing ring with the lip angle $\gamma$ = 115° and 120° are the greatest. The contact pressure from the lip to root of the sealing ring gradually decreases under different lip angles. The contact pressure on the lip varies greatly, and the pressure difference in the middle is small and the trend is gentle.

Combined with the analysis results of support ring angle $\alpha$ and seal ring lip angle $\gamma$, when the difference between support ring angle $\alpha$ and seal ring lip angle $\gamma$ is large, the stress concentration phenomenon appears at the seal ring groove, which greatly improves the von-Mises stress extreme value of the seal ring, and the seal ring is more prone to failure.

### *6.2.3.2 Effect of the sealing surface length*

In the actual working of the fracturing pump, due to the vibration of the plunger and the constant wear of the sealing ring, the eccentric phenomenon often occurs between the plunger and sealing ring, which prevents the contact pressure between the plunger and the sealing ring from being a stable value, and the leakage of fracturing fluid easily occurs. The sealing surface length can directly determine the contact surface area between the sealing ring and the plunger. The larger the contact area is, the less sensitive the sealing ring is to the eccentric phenomenon of the plunger. However, the larger the contact area is, the smaller the extreme value of the contact pressure on the sealing surface is, and the insufficient sealing pressure may lead to the fracturing fluid leakage.

Figure 6-10 shows the contact pressure and stress of the sealing ring with different sealing surface lengths. The maximum contact pressure on the sealing

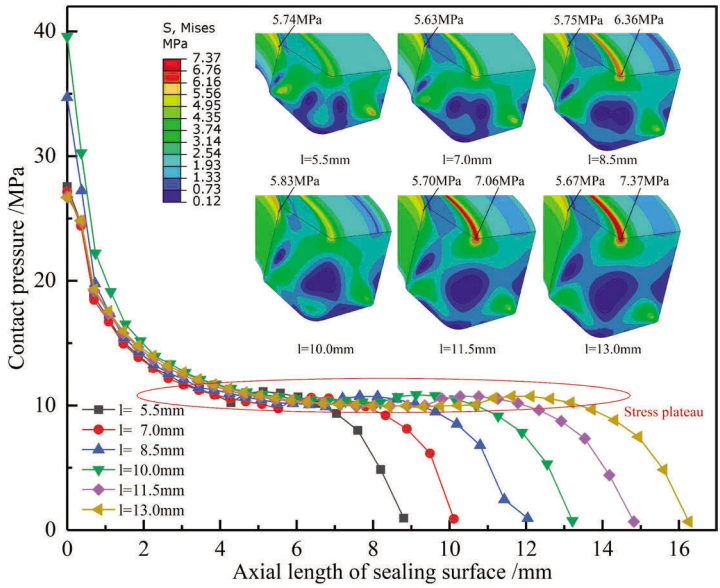


**Fig. 6-10.** Contact pressure and stress of sealing ring with different sealing surface lengths.

ring with $l$ = 5.5 mm, 7.0 mm and 10.0 mm appears on the sealing surface, while that on the sealing ring with $l$ = 8.5 mm, 11.5 mm and 13.0 mm appears on the lip groove of the sealing ring. The maximum contact pressure on the sealing ring with $l$ = 10.0 mm is the highest. With the increasing of $l$, the length of stress gentle zone increases gradually. If the seal ring is too short, it easily causes the leakage of the fracturing fluid. If the seal ring is too long, the contact pressure on the sealing surface will be too low, which will increase the risk of fracturing fluid leakage. At the same time, when stress concentration appears on the seal ring, which may reduces the service life of the seal ring.

### *6.2.3.3 Effect of the interference of sealing ring*

Figure 6-11 shows the contact pressure and stress of the sealing ring with different interferences. The extreme value of stress with the interference of 0.0 mm, 0.2 mm, and 0.4 mm appears near the lip of the sealing surface, and the difference among the three sealing rings is small. The extreme stress with the interference of 0.6 mm, 0.8 mm, and 1.0 mm appears on the lip groove of the sealing ring, and that is significantly higher than that of the other three sealing rings. The contact pressure gradually decreases along the sealing surface from lip to the root, and the contact pressure distributions are almost the same except for the one on the sealing surface lip area. The extreme value of contact pressure with interference 0.4 mm is the highest.

Therefore, the appropriate amount of interference will slightly change the von-Mises stress of the seal ring, but that can significantly change the maximum contact pressure. A bigger interference will reduce the sealing performance of the seal ring. In addition, excessive interference can easily lead to the stress concentration on the lip of the sealing ring.

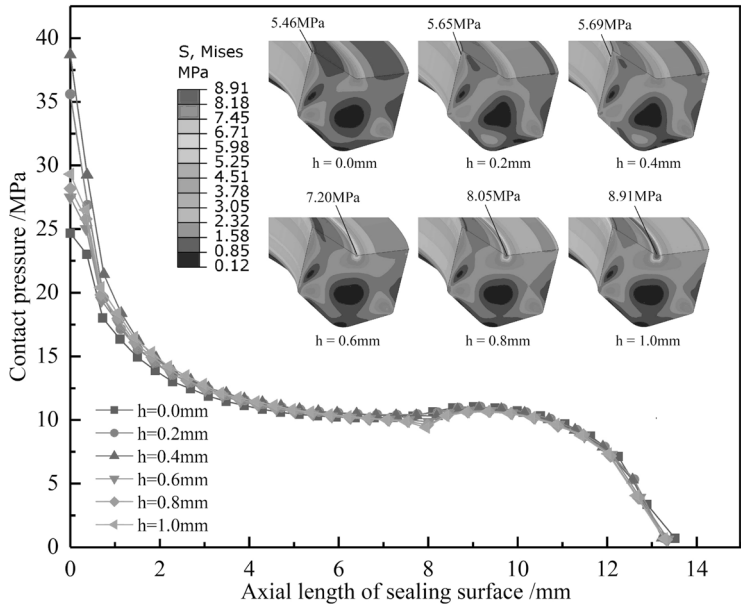


**Fig. 6-11.** Contact pressure and stress of the sealing ring with different interferences.

#### *6.2.3.4 Effect of the sealing ring number*

In order to ensure the sealing performance, many pieces of equipment often use multiple sealing rings to seal the device. The working load of the plunger seal in fracturing pump is very large. The plunger seal is in a high-speed reciprocating motion, and the fluid pressure contains a lot of sediment. Under such bad working conditions, it is very necessary to use multiple sealing rings to seal.

Figure 6-12 shows a the contact pressure and stress of sealing rings with different numbers. The difference of the maximum von-Mises stress on the same number of sealing rings is very small. The maximum von-Mises stress of $n = 4$ is the highest. The maximum von-Mises stress of one sealing ring is the least. The differences between the extreme contact pressure on each sealing structure are small, and the order of these differences from large to small is $n = 1$, $n = 2$, $n = 3$, $n = 4$. When the sealing ring number is greater than 1, the contact pressure on the first sealing ring is the largest, and the contact pressure on the later sealing rings is lesser. Increasing the number of sealing rings has little effect on the von-Mises stress and contact pressure, but that can increase the safety performance of the sealing structure.

## 6.3 Plunger seal of mud pump

### *6.3.1 Numerical model*

The mud pump piston and cylinder liner friction pair is in a very complicated environment in actual working conditions. Therefore, several assumptions were made when establishing the numerical simulation calculation [7]:

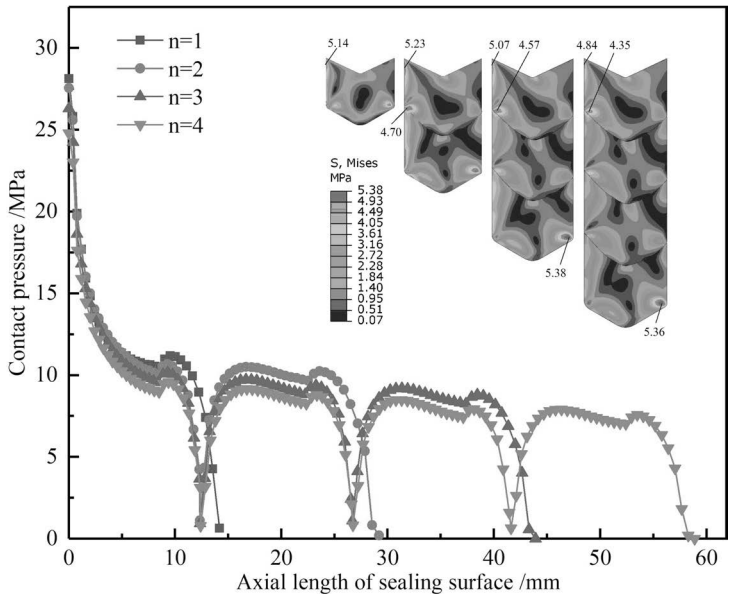


**Fig. 6-12.** Contact pressure and stress on sealing ring with different numbers.

1) The friction pair model of the piston and cylinder liner is an ideal axisymmetric model.
2) The materials used in the piston and cylinder liners and other parts are uniform, continuous, and isotropic.
3) The entire piston cup is made of polyurethane rubber.

BW-160 three-cylinder single-acting pump piston is chosen as the research object. The inner diameter of cylinder liner is 70 mm, the minimum outer diameter of the piston cup is 70 mm, the maximum outer diameter is 71 mm. Which means that the interference is 0.5 mm, and the length from the lip to the root of the bowl is 30 mm. The piston cup is made of polyurethane rubber material, which is a super-elastic material. In the simulation analysis, the Mooney-Rivlin model [8–9] is used, where $C_{10}$ is 2.5 MPa, $C_{01}$ is 0.625 MPa, and the density is 1120 kg/m$^3$. The meshed model and the three-dimensional diagram of the piston are shown in Figure 6-13.

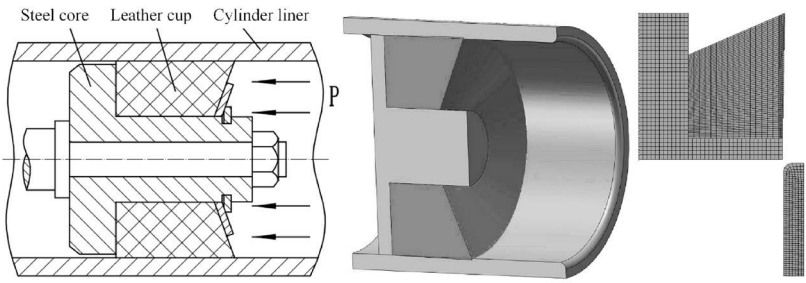


**Fig. 6-13.** The three-dimensional diagram of the mud pump piston.

### *6.3.2 Force of mud pump piston*

As shown in Figure 6-13, the cup tends to squeeze out when the piston completes the action of sucking mud, the piston moves to the left. It completes the action of discharging mud and the leather cup is squeezed inward, when the piston moves to the right.

Figure 6-14 depicts the force diagram of the rubber cup. Figure 6-14(a) represents the force of the cup in the process of sucking mud. Figure 6-14(b) represents the force in the process of mud discharge, and Figure 6-14(c) is the force of the rubber cup size parameters. The force of the rubber cup includes the squeezing force of the steel core and the cylinder liner against the cup, the mud pressure, and the friction when the mud is sucked or discharged.

The factors that may affect the working performance of the rubber piston include the actual working pressure, friction coefficient on the contact surface, the inner wall width of the cup, the sealing surface length, the interference and the cup thickness. These parameters can directly affect the von-Mises stress and contact pressure on the rubber cup, thereby affecting the sealing performance and wear resistance of the rubber cup.

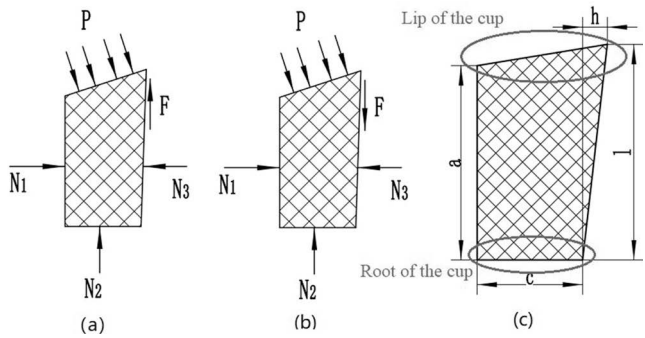


**Fig. 6-14.** The force on the rubber cup.

### *6.3.3 Factors influencing the piston's performance*

#### *6.3.3.1 Effect of the working load*

The working load squeeze the rubber cup and affect its contact mechanical properties. The axial component force causes the cup to be compressed axially, and the radial component force compresses the cup toward the cylinder liner. Figures 6-15 and 6-16 show the von-Mises stress and contact pressure, on the mud pump piston cup under different loads, respectively. Except for the load 0.5 MPa, the von-Mises stress is relatively flat. The change trends of other curves show are all first decrease and then increase with the load increases, the root of the cup and the stress concentration on the lips becomes more and more obvious. The contact pressure of the root of the cup under different loads is the least. As the axial length increases, the contact pressure gradually increases to a stable value, and it finally increases gradually at the lip of the cup, and the increase rate rises with the load increases. Under different loads, the average contact pressure on the cup increases linearly.

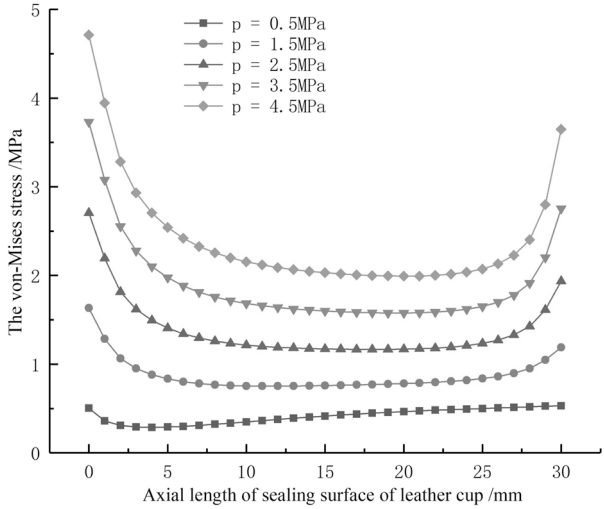


**Fig. 6-15.** The von-Mises stress on the cup under different loads.

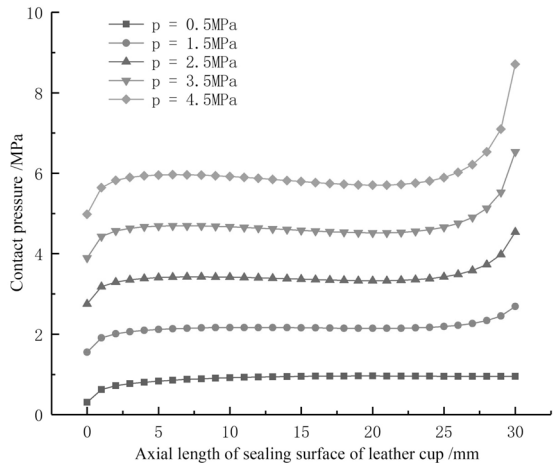


**Fig. 6-16.** The contact pressure on the cup under different loads.

### *6.3.3.2 Effect of the friction coefficient*

Friction is an important factor affecting the force of the rubber cup, and it has a certain restrictive effect on the rubber movement on the surface of the cup. When the mud pump performs the mud discharge stroke, the surface tissue of the cup sealing surface tends to squeeze into the cavity formed by the steel core and the cylinder liner, and the tissue inside the cup tends to squeeze out of the cavity. Then, its deformation affecting the mechanical properties. Figure 6-17 depicts the maximum von-Mises stress and contact pressure on the rubber cup under different friction coefficients. As the friction coefficient increases, the maximum von-Mises stress and contact pressure of the cup gradually increase. The maximum stress with $\alpha$ = 0, 0.05, 0.1,

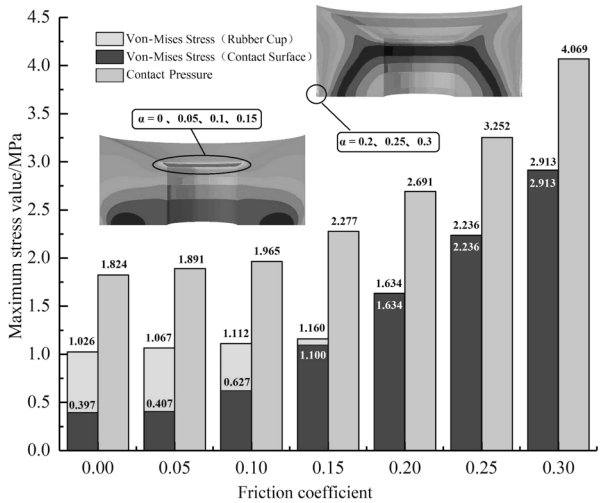


**Fig. 6-17.** Contact pressure and stress on the leather cup under different friction coefficients.

and 0.15 appears on the inner lip of the cup. The maximum von-Mises stress on the cups with $\alpha = 0.2$, 0.25, and 0.3 appears at the root of the sealing surface of the cups, and the extreme stress values change significantly.

The greater the friction coefficient is, the greater the average contact pressure is, which can effectively prevent leakage. However, the maximum von-Mises stress on the contact surface of leather bowl is too high, which will accelerate the fatigue failure of the cup. In addition, an excessive friction coefficient will accelerate the wear of the cup for the generation of heat. When the friction coefficient is small, the stress concentration on the inner wall lip of the rubber cup gradually becomes the main factor affecting the mechanical properties of the cup. The average contact pressure of the leather cup is low, which often leads to leakage. Then, optimizing the size of the cup can increase the contact pressure of the sealing surface of the cup.

### *6.3.3.3 Effect of the inner wall width*

Figure 6-18 shows the stress distribution of the piston cup with different inner wall widths. The stress distribution on the middle of the sealing surface of the cup is relatively uniform, but the stress concentration occurs on the root. An obvious stress concentration is on the root of the sealing surface with inner wall width of 10 mm, 15 mm, and 20 mm. Stress concentration occurs on both the root and lip of the sealing surface with inner wall widths of 25 mm and 30 mm. The difference in the von-Mises stress also becomes greater along the axial length of the cup as the sealing surface increases. The maximum stress difference appears at the lip of the cup. The von-Mises stress on the cup lip with the inner wall width of 25 mm and 30 mm exceeds that of the cup root. The von-Mises stress on the cup lip with the inner wall width of 10 mm is not much different from that on the middle part.

Figure 6-19 shows the contact pressure of the piston cup in the mud pump with different inner wall widths. With the increasing of the inner wall width, stress

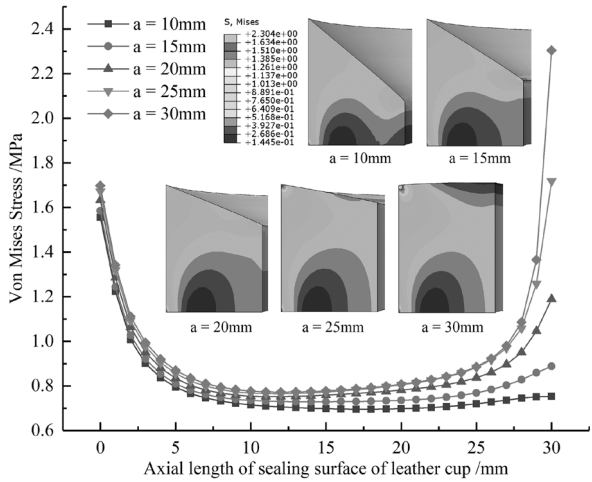


**Fig. 6-18.** The von-Mises stress on a cup with different inner wall widths.

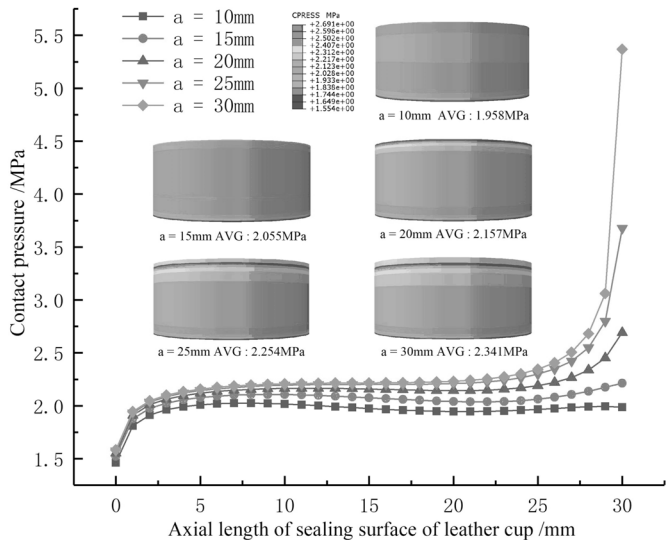


**Fig. 6-19.** The contact pressure on the cup with different inner wall widths.

concentration gradually appears on the lip of the cup, and it becomes more and more obvious. The contact pressure distribution at the lips is roughly the same as the von-Mises stress distribution. But the contact pressure at the root of the cup is lesser and changes slightly with the inner wall width, which is different from the stress concentration phenomenon at the root of the cup. Judging from the average contact pressure on the cup, there is not much difference in the average contact pressure on the rubber cups with different inner wall widths.

Therefore, the inner wall width has little effect on the distribution of the von-Mises stress and contact pressure at the root and the middle section of the cup,

but it has a greater effect on the von-Mises stress and contact pressure on the lip. This is because the lip of the cup and the cylinder liner produce an "edge effect" during the mutual extrusion process, that is, the stress concentration phenomenon appears. As the inner wall width increases, the stiffness of the cup lip increases. The "edge effect" is more obvious, and the cup is more prone to fatigue failure.

### *6.3.3.4 Effect of the interference*

The interference determines squeezing degree between the cup and the cylinder liner, which affecting the contact pressure and the sealing performance of the piston. The greater the interference of the cup is, the greater the average contact pressure and the maximum contact pressure on the sealing surface of the cup are, and the smaller the probability of leakage is. When the interference is too large, the effect of the interference on the piston sealing performance will become smaller. The friction force on the sealing surface of the cup will become larger, which will accelerate the leather cup wear. At the same time, a greater friction will generate more heat, accelerating the aging of the rubber.

Figure 6-20 shows the von-Mises stress on the axial length of the sealing surface of the cup under different interferences. The von-Mises stress first decreases and then increases along the axial length under different interferences. The von-Mises stress appears near the root of the cup and the lip of the cup is larger and the absolute value of the stress gradient is steep. The von-Mises stress in the middle of the cup is smaller and the stress gradient increases with the interference increases. The maximum von-Mises stress value of the cup with interference $h = 0.00$ mm ~ 0.75 mm is located at the root of the sealing surface of the cup, but when $h = 1.00$ mm, the maximum von-Mises stress value of the cup is transferred to the inner lip of the cup. Although the maximum von-Mises stress on the sealing surface of the cup with $h = 1.00$ mm is slightly smaller than that on the cup with $h = 0.75$ mm, the maximum von-Mises stress on the entire cup is higher than that on the cup with $h = 0.75$ mm.

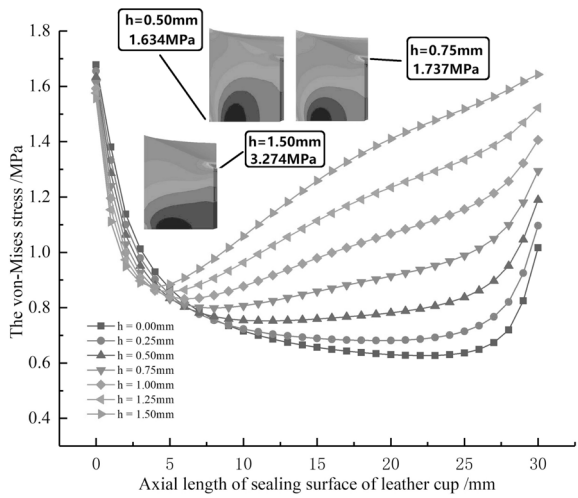


**Fig. 6-20.** The von-Mises stress on cups with different interferences.

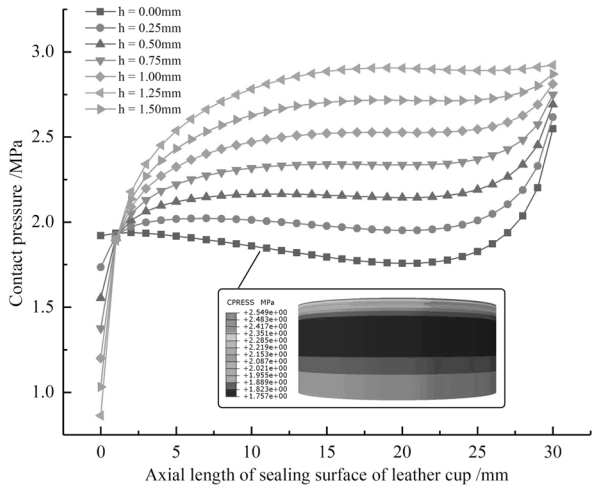


**Fig. 6-21.** The contact pressure on cups under different interferences.

Figure 6-21 shows the contact pressure on the axial length of the cup sealing surface under different interferences. As the interference increases, the maximum contact pressure on the sealing surface of the cup gradually increase, and the contact pressure on the root of the cup gradually decreases. When $h$ = 0.00 mm, the contact pressure at the root of the cup is slightly higher than that on the middle of the cup, while the minimum contact pressure on the contact surface of the other cup appears at the root of the cup. Contact pressure on the middle of the cup with no interference ($h$ = 0.00 mm) is about 1.8 MPa, and the working pressure is 1.5 MPa. Leakage is very easy to occur if the piston is eccentric.

### *6.3.3.5 Effect of the thickness*

Figure 6-22 shows the von-Mises stress of the rubber cup under different thicknesses. The stress distribution on the sealing surface of 18 mm, 23 mm, and 28 mm-thick cups is basically same, and there is little difference in the extreme values of von-Mises stress. The three curves show a trend of first decreasing and then increasing, and a longer gentle-stress zone appears in the middle. For the cup with a thickness 13 mm, a small bulge appears in the middle gentle-stress area, and the lip stress concentration disappears. When the thickness of the rubber cup is 8 mm, the bulge degree of the gentle-stress zone in the middle of the rubber cup increases, the von-Mises stress of the lip continues to decrease, and the stress concentration appears in the lip of the inner wall, but the extreme stress is still at the root of the sealing surface of the rubber cup. Figure 6-23 depicts the contact pressure of the rubber cup under different thicknesses. As the thickness decreases, the contact pressure near the root of the sealing surface of the cup continues to increase, and the contact pressure near the lip of the sealing surface decrease. The smaller the thickness of the cup is, the greater the average contact pressure is.

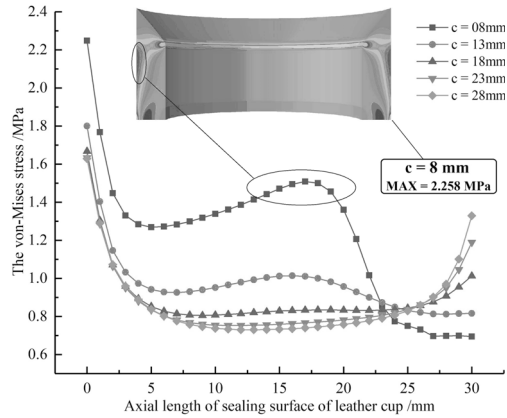


**Fig. 6-22.** The von-Mises stress on cups with different thicknesses.

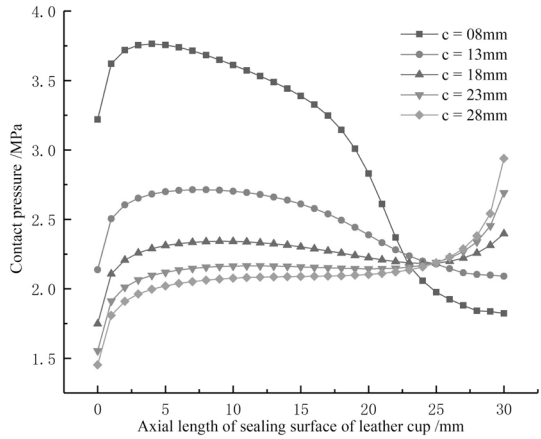


**Fig. 6-23.** The contact pressure on cups with different thicknesses.

### *6.3.4 Improvement of the rubber cup*

The contact pressure on the rubber cup's sealing surface can be improved by optimizing the cup structure parameters. But this method has an upper limit on the optimization of the rubber cup with smooth sealing surface. Three different rubber cup structures (semicircular, trapezoidal and triangular groove structures) and smooth rubber cups are compared in this section. The number of grooves on the three kinds of cups is 4, the width of grooves is 2 mm each, and the distance between grooves is 3 mm.

Figure 6-24 depicts the maximum contact pressure of the four rubber cups during the mud discharge process. The maximum contact pressures on the sealing surfaces of the four cups increase first and then stabilizes. The maximum contact pressure on the smooth cup is lesser than that on the other three cups. The maximum contact pressure on the trapezoidal cup is the most, and the difference between the pressure

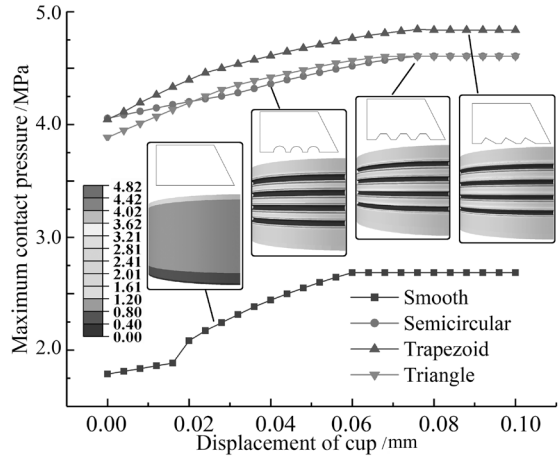


**Fig. 6-24.** The maximum contact pressure on the four types of cups.

levels on the triangular cup and the semicircular cup is small. When the displacement of the smooth cup is small (a small displacement after the mud pump changes from the mud suction stroke to the mud discharge stroke), the maximum contact pressure on the cup is small, only 1.6 MPa ~ 1.8 MPa, while the working pressure of the mud is 1.5 MPa, and the piston movement speed is almost 0. At this time, the mud easily leak from the cup, and more sediment will enter into the sealing surface, which leads to the premature wear failure of the piston cup.

Figure 6-25 shows the von-Mises stress on four cups. The larger stress of the four cups appear near the sealing surface of the cups. The stress of the semicircular groove and trapezoidal groove cups are the highest, followed by the value of the triangular groove, and the smallest value of the smooth cup. The stress extreme value on the semicircular groove and trapezoidal groove cup is concentrated in the groove, while the von-Mises stress on the triangular groove is relatively uniform near the sealing surface, and there is no obvious stress concentration on the groove.

Figure 6-26 shows contact pressure and stress of the four cups. The stress and contact pressure on smooth cups are smaller than that on the other three cups. Among the three kinds of grooved cups, the difference of the maximum von-Mises stress on trapezoidal groove and semicircular groove is large; however, both of them are significantly higher than triangular groove. The difference of the maximum contact pressure on the three kinds of grooved cups is small, but the pressure on the trapezoidal groove is slightly higher than on other two cups.

Therefore, the groove structure can effectively reduce the maximum contact pressure and average contact pressure to improve the sealing performance. However, the groove structure destroys the original sealing surface of the rubber cup, which makes it easier for the lip structure to compress to the root of the cup when discharging mud, which causing additional bending stress on the groove of the cup, resulting in stress concentration at the root of the cup. The root of the groove is prone to failure due to fatigue, cracks directly occur. The addition of a groove structure reduces the contact area between the sealing surface of the cup and the

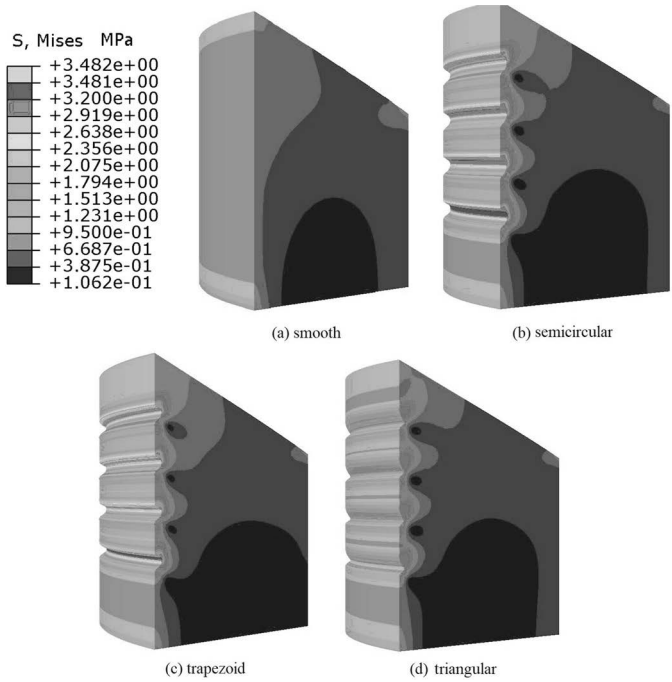


**Fig. 6-25.** A von-Mises stress cloud diagram of four kinds of leather cups.

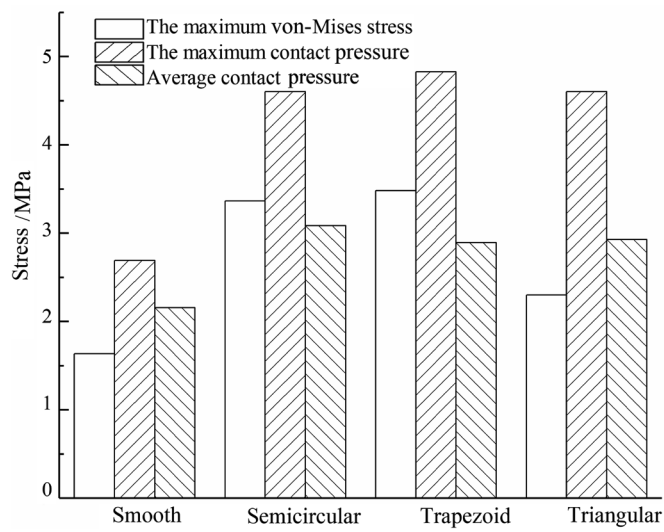


**Fig. 6-26.** Contact pressure and stress on four kinds of leather cups.

inner surface of the cylinder liner, thus increasing the contact pressure on the sealing surface of the cup. The contact pressure of all parts increases, and it is not easy to leak. More importantly, a circle of contact pressure intensive area is formed on the

sealing surface between the two grooves, which enhances the adaptability of the cup to eccentric, vibration, and other working conditions. Theoretically, the groove structure greatly improves the contact pressure on the sealing surface of the cup, the contact pressure between the cup and the cylinder liner is greater, and the cup is more vulnerable to wear. However, in the bad working environment of the mud pump, the mud mixes into the contact surface of the cup and the cylinder liner, making the cup very vulnerable to scratches, while the groove structure can store the mud mixed into the sealing surface, which weakens the influence of sediment on the cup and improves the service life of the cup.

## References

[1] Zhu Xiaomei, Zhang Zhiyi and Li Ben. 2017. Research on the design and application of the piston structure of a new modular drilling mud pump. Technology Wind 4: 97–98 (Chinese).

[2] Zhu Xiaodong. 2012. Failure analysis and optimization measures of mud pump piston. Gansu Science and Technology 28(23): 75–76 (Chinese).

[3] Wang Jie and Xie Yujun. 2008. ANSYS analysis of rubber O-ring. Journal of Liaoning University of Petroleum and Chemical Technology 28(4): 46–49 (Chinese).

[4] Ma Yulong. 2016. Research on hydraulic end of 6500 HP fracturing pump. Lanzhou University of Technology, Machinery 54(11): 21–23 (Chinese).

[5] Zhao Guifeng, Ma Yuhong, Li Yanmin, Luo Jiarun and Du Chang. 2017. Development of a modified Mooney-Rivlin constitutive model for rubber to investigate the effects of aging and marine corrosion on seismic isolated bearings. Earthquake Engineering and Engineering Vibration 16(04): 815–826.

[6] Liao Xintong. 2017. Research on Plunger Seal Structure and Performance of 6500 Hp Fracturing Pump. B.S. Thesis, Lanzhou University of Technology. Lanzhou, China (Chinese).

[7] Ru Shaofeng. 2015. Optimization Design of Mud Pump Piston Biomimetic Surface and Research on Wear-Resistance and Sealing. Ph.D. Thesis, Jilin University, Jilin, China (Chinese).

[8] Zhao Guifeng, Ma Yuhong, Li Yanmin, Luo Jiarun and Du Chang. 2017. Development of a modified Mooney-Rivlin constitutive model for rubber to investigate the effects of aging and marine corrosion on seismic isolated bearings. Earthquake Engineering and Engineering Vibration 16(04): 815–826.

[9] Fan Chengye, Zhuang Zhuo and Huang Kezhi. 2003. The theoretical and finite element solutions of an interference problem of hyperelastic materials. Engineering Mechanics 4: 15–18 (Chinese).

# 7
# Wellhead Blowout Preventer

## 7.1 BOP

### *7.1.1 Overview of a BOP*

The blowout preventer (BOP) is used to control drilling pressure and prevent blowout accidents. It is an important piece of equipment to ensure the drilling safety, oil production, and gas production. There are three kinds of commonly used BOP: ram BOP, annular BOP, and rotary BOP. The ram BOP includes the full seal type, the semi seal type, the shear type and the variable diameter type. According to the shape of the rubber core, the annular BOP includes a conical rubber core, a cylindrical a rubber core and a spherical rubber core. The rotary BOP is mainly used in underbalanced drilling.

#### *7.1.1.1 Semi-enclosed ram BOP*

This ram BOP is widely used in the oil production process because of its strong adaptability, high reliability, and good safety performance. It can seal the high-pressure liquid in the well mainly through the following four sealing areas: the sealing between the ram top and the shell; the sealing between the front of the ram and pipe string; the sealing between the shell and the side door; the sealing between the piston rod and the side door. Among the four seals, the seal between the front of the ram and the pipe string plays an important role. The sealing structure comprises the front rubber, the top rubber, the retainer, and the support plate, and its structure diagram is shown in Figure 7-1.

There are two ways to shut-in the well with the ram BOP: the soft shut-in and the hard shut-in. The hard shut-in is the fastest method to shut the well. It minimizes the volume of kick allowed into the wellbore. The hard shut-in may result in the water hammer pressure increase and damage the BOP.

#### *7.1.1.2 Shear ram BOP*

The shear ram BOP is mainly divided into integral shear gate and split shear gate. During the engineering application, the upper and lower rams are closed to the center of the BOP under the hydraulic push rod, so as to realize the shearing of the drill pipe and the wellhead sealing. The upper and lower parts of the ram are designed

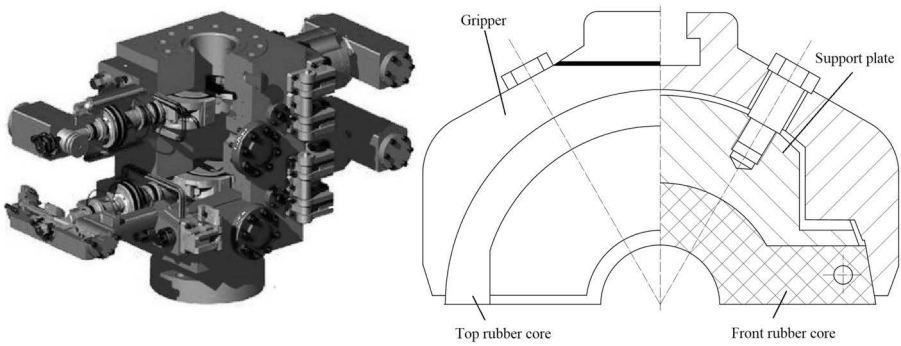


**Fig. 7-1.** A schematic diagram of the ram BOP structure.

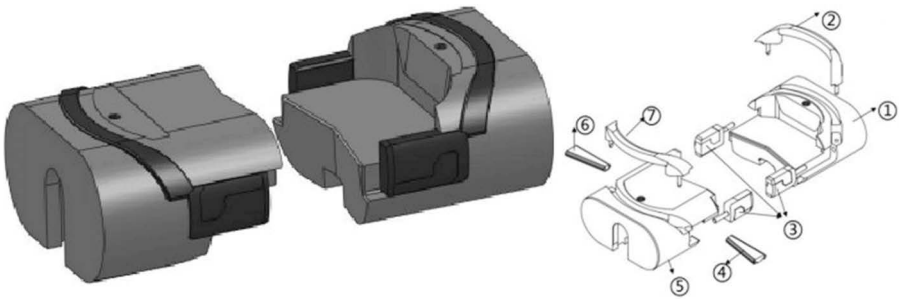


**Fig. 7-2.** The ISR shear ram assembly. ① & ⑤ ram core; ③ side seal block; ② top seal; ④ & ⑥ bottom seal.

with spaces to accommodate the cutting drill pipe. In order to effectively seal the wellhead, the shear ram BOP needs to realize three seals. That is, the ram top and shell—the top sealing strip is a convex surface on the top of the ram to realize the top sealing; ram blade seal—the lower part of the upper ram is provided with a sealing strip, and the upper and lower rams are closed tightly to realize the blade sealing; side door and shell—there are two square sealing blocks on both sides of the ram, which are close to the inner cavity of the U-shaped shell of the BOP to realize the side sealing. Figure 7-2 shows the structural diagram of the ISR shear ram assembly.

### *7.1.1.3 Rotary BOP*

A rotary blowout preventer is used in underbalanced drilling, which is mainly used to control wellhead pressure when negative pressure occurs. The rotary BOP not only seals the drill pipe, but also allows the drilling tool to rotate under the limited wellhead pressure, so as to realize the pressure drilling and partial completion operation [1]. Rotary blowout preventers can be divided into well pressure assisted sealing and hydraulic sealing. They can also be divided into the high-pressure rotary BOP and the low-pressure rotary BOP according to the sealing pressure; or the annular rubber core type and the expansion capsule type according to the sealing method of drill string. A rotary blowout preventer is usually used in combination with ram blowout preventer. In actual drilling conditions, a variety of blowout preventers will be

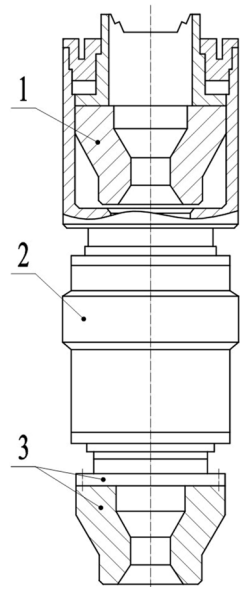


**Fig. 7-3.** The structure of rotary BOP. 1 - upper drive assembly; 2 - outer cylinder; 3 - lower rubber core assembly.

combined into a blowout preventer group according to formation conditions and drilling process requirements. Figure 7-3 is a structural diagram of a rotary BOP [2].

## 7.2 Ram BOP

### *7.2.1 Finite element model*

The front seal of the ram BOP is composed of two independent and symmetrical half rings, which should form a full ring during the operation to ensure the contact seal of pipe string, and be in separation during nonoperation to ensure the smooth passage with the pipe string. Therefore, the following assumptions are made in the finite element analysis of the ram BOP [3]:

1. The rubber core materials of BOP are isotropic, and the factors such as uneven proportioning in the manufacturing process are not considered.
2. The influence of temperature on the performance of sealing material is not considered.

In this chapter, taking 27/8 pipe as an example, the three-dimensional contact numerical calculation model of the ram BOP rubber core and pipe string is established, and the stress of rubber core and pipe string is studied. The rubber material selected is NBR, and the two-parameter Mooney-Rivlin model [4] is used with the parameters of $C_{10}$ = 4.622, $C_{01}$ = –1.548. The material of the support plate is 25CrNiMo. The numerical calculation model of the ram BOP is shown in Figure 7-4.

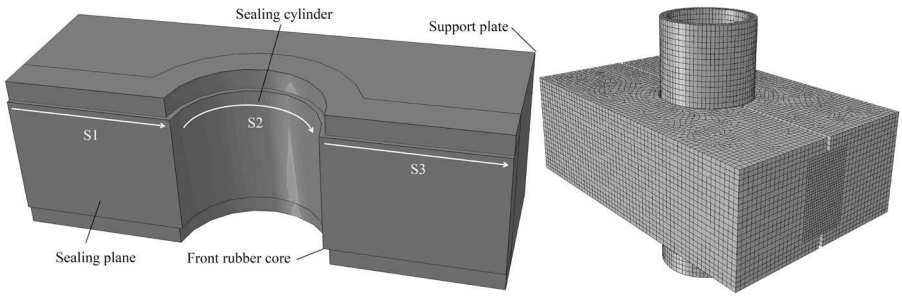


**Fig. 7-4.** The numerical model of ram BOP.

## *7.2.2 Results and discussions*

The ram BOP mainly pushes the ram to the pipe string through the force generated by the hydraulic cylinder, then a large contact pressure between the rubber core and the pipe string occurs. When the contact pressure is greater than the wellbore pressure, the sealing function is realized. Therefore, the external load plays an important role in the sealing performance of rubber core. As the key sealing component of BOP, the rubber core structure will directly affect the sealing performance of the whole BOP. The inner wall of the rubber core cylinder contacts with the pipe string, and its radius directly affects the sealing pressure distribution. The core height determines the sealing area.

So, the load size $p$, inner wall radius of rubber core $a$, and rubber core height $h$ are the important factors affecting the sealing performance of the ram BOP. The factors influencing the ram BOP are shown in Figure 7-5.

### *7.2.2.1 Effect of the load*

Figure 7-6 shows the von-Mises stress on the rubber core under different loads. With the increasing of the load, the von-Mises stress on the rubber core increases obviously, but the stress change at the joint of the sealing plane and the sealing cylinder is not obvious.

Figure 7-7 shows the contact pressure on the rubber core under different loads. Figure 7-8 shows the contact pressure on the rubber core along the paths S1, S2, and S3. The contact pressure between the end of each rubber core sealing plane and the middle of the sealing cylinder is higher, while the contact pressure between the root of the sealing plane and the end of the sealing cylinder is lesser. The contact pressure on the sealing surface generally increases with the load increases.

### *7.2.2.2 Effect of the inner radius of the rubber core*

Figure 7-9 shows the maximum von-Mises stress on the rubber core with different inner radii when the pipe radius is 36.5 mm. The von-Mises stresses on the rubber core with the inner wall radius of 35.5 mm and 36.0 mm are the highest, and that on the inner wall radius of 36.5 mm is the smallest. Figure 7-10 is a contact pressure distribution with different inner radii of the rubber core. The high contact pressure area on the sealing cylinder surface of the rubber core with inner wall radius of 35.5 mm is obviously lesser than that on the other rubber cores, and the contact

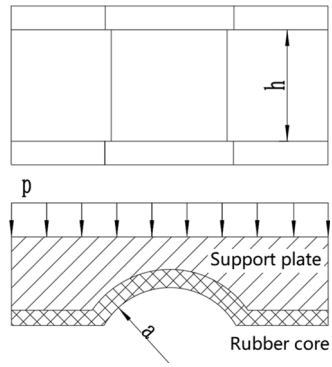


**Fig. 7-5.** The rubber core structure on ram BOP.

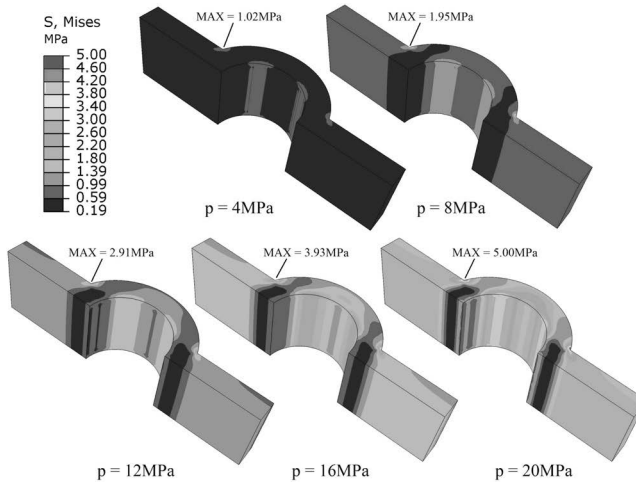


**Fig. 7-6.** The von-Mises stress on the rubber core under different loads.

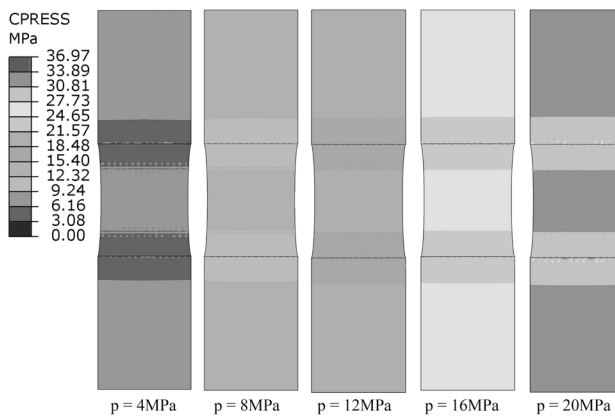


**Fig. 7-7.** The contact pressure on the rubber core under different loads.

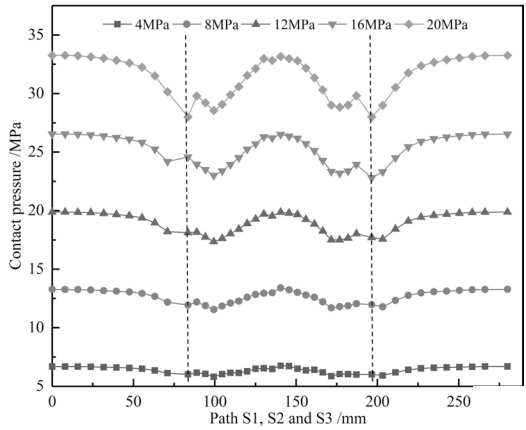


**Fig. 7-8.** Contact pressure curves on rubber core along the paths under different loads.

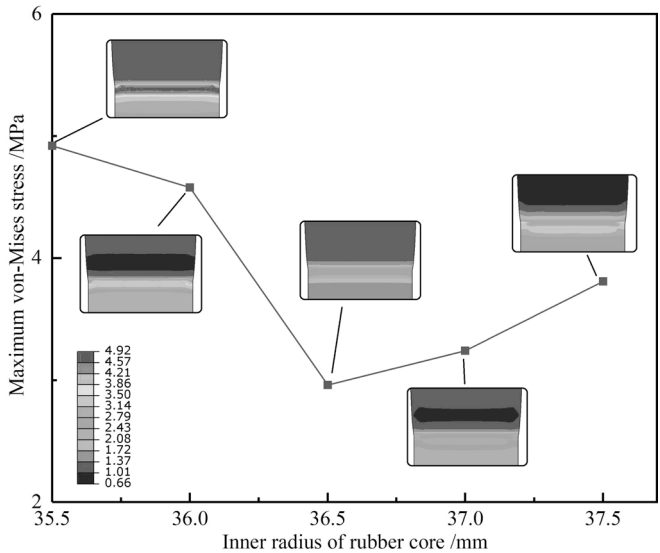


**Fig. 7-9.** The maximum von-Mises stress with different inner radii of rubber core.

pressure on the end of the sealing plane of the rubber core with inner wall radius of 36.5 mm is lesser than that on the other rubber cores. Each curve is roughly in the "W" shape. The minimum contact pressure value of the rubber core with inner wall radius of 35.5 mm is the smallest, and the minimum contact pressure value of the other rubber cores is similar.

### *7.2.2.3 Effect of the rubber core's height*

Figure 7-11 shows the maximum von-Mises stress on the rubber core with different heights. The maximum von-Mises stress on the rubber core appears at the transition part between the plane and the cylinder at the back of the rubber core. The curve of the von-Mises stress extremum of the rubber core shows a "V" shape. The von-Mises

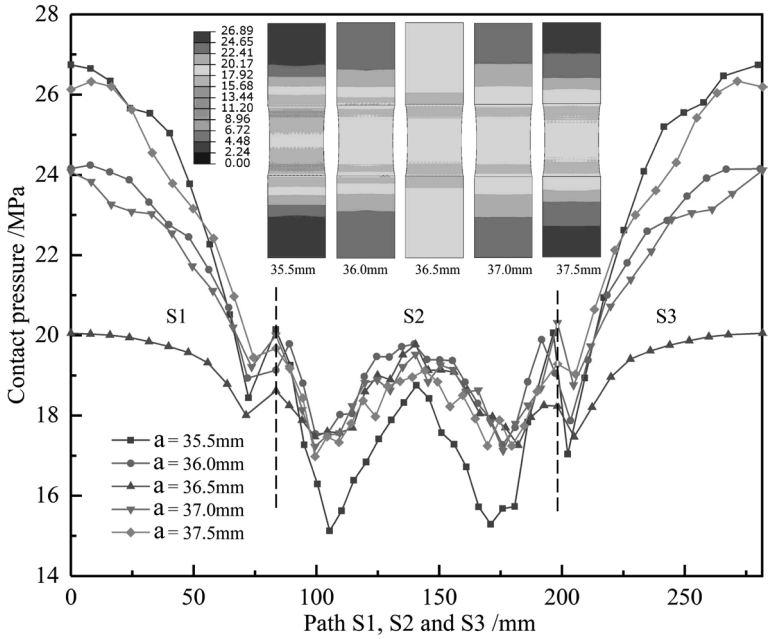


**Fig. 7-10.** Contact pressure distribution with different inner radii of rubber core.

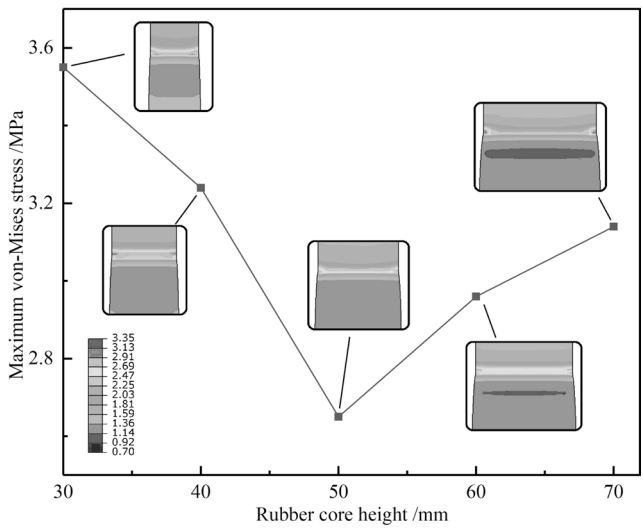


**Fig. 7-11.** The maximum von-Mises stress on rubber cores of different heights.

stress first decreases and then increases with the increase of rubber core height. When the rubber core height is 50 mm, the maximum von-Mises stress is the least.

Figure 7-12 shows the contact pressure distribution of the rubber core at different heights. With the increasing of the rubber core's height, the contact pressure on S1, S2, and S3 increases.

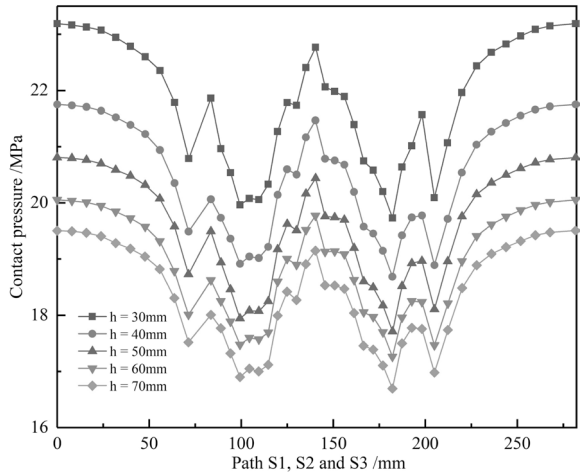


**Fig. 7-12.** Contact pressure distribution on rubber cores of different heights.

The small rubber core's height can effectively change the contact pressure on the rubber core to improve the sealing performance. However, if the rubber core height's is too small, the sealing reliability of the rubber core will be reduced. The vibration and impact generated are more likely to cause local leakage of rubber core.

### *7.2.3 Erosion of the BOP's ram's rubber*

In the hard shut-in process, the well fluid cannot flow past the relief valve. So, when the BOP's rams close rapidly, the fluid's velocity will increase sharply. The BOP's ram's rubber will be abraded by the solid particles in the well fluid. The design of the rubber components to avoid fatigue is one of the critical issues to prevent failures during an operation [5]. The material properties of the rubber control the load/deflection characters of the anti-vibration [6]. The state of the rams' rubber must be assessed to avoid seal failure, which may cause wellhead accidents. It can be seen from the flushing experiment that the well fluid with particles will flush the rams' rubber and flake it, reducing the reliability of the seals [7]. The experimental devices for measuring the erosion are shown in Figure 7-13. The rubber is fixed in-between the casings. Table 7-1 shows the weight of the rams' rubber that was eroded under different air discharges and gravel inputs.

It can be seen from Figures 7-14 and 7-15, that on the seal plane of the ram rubber, there is a clear boundary line between the flushing and no flushing sections. When observing the rubber at the corner of one ram small pits, signs can be seen that indicate the loss of rubber. It can be concluded that a fluid with solid particles damages the BOP's ram's rubber and reduces the seal's reliability. Micro-tearing and micro-deforming occur on the rubber surface through the action of micro-cutting by the flowing abrasive particles that contain a certain amount of kinetic energy [8], which causes the surface and subsurface to generate tensile, compressive, and shearing stresses. Under the continuous and multiple actions of the flowing abrasive grains, cracks appear and grow in the surface or subsurface layers of the rubber. The


**Fig. 7-13.** The experimental devices of erosion.

**Table 7-1.** The erosion of the weight of the rams' rubber in 60 s (g).

| Gravel input (kg/min) | Air discharge ($m^3$/min) | | |
|---|---|---|---|
| | 20.53 | 40.95 | 61.48 |
| 5.00 | 3.1 | 4.8 | 6.3 |
| 15.00 | 4.9 | 7.2 | 10.4 |
| 19.5 | 5.8 | 9.3 | 12.5 |

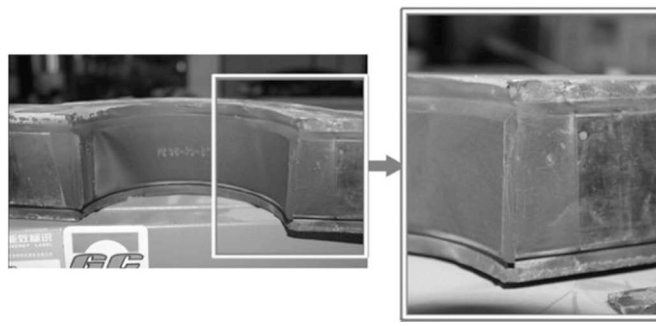

**Fig. 7-14.** The erosion of the ram rubber caused by fluid with solid particles.

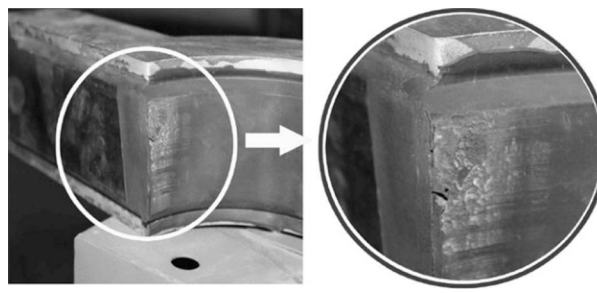

**Fig. 7-15.** The loss of ram's rubber in the form of small pits.

crack growth can appear along the tip of the crack and extend through to the surface under the action of repeated stress, and then the surface layer of the material gets be delaminated [9]. Therefore, the ram's rubber should be checked after a hard shut-in, and if necessary, replaced to ensure the continued safe operation in subsequent operations.

## 7.3 Shearing ram BOP

### *7.3.1 Finite element model*

In the main seal of the ISR shear gate, the seal of the blade is the most important. The blade movement of the lower ram comes into contact with the bottom sealing strip of the upper ram, and the contact pressure is produced by extruding the rubber to realize the sealing effect. Figure 7-16(a) shows a two-dimensional model diagram of the simplified ISR ram bottom sealing.

In this analysis, the Yeoh type is used as the constitutive model of rubber. Rubber's material parameters are shown in Table 7-2.

In practice, the upper and lower ram move synchronously to realize the contact between the blade of the lower ram and the rubber sealing strip. The friction coefficient between steel and rubber is 0.5.

### *7.3.2 Results and discussions*

Due to the extrusion and shearing of the cutting blade on the rubber bottom during the movement of the ram, the maximum stress on the rubber strip is 5.98 MPa. When the shear stress is 6.53 MPa, which is less than the shear strength of the rubber 15 MPa, the rubber will not be damaged. However, if there are solid particles in the migration process of the lower ram, it is easy to scratch the rubber. Figure 7-17 shows the maximum von-Mises stress when the lower ram moves.

The sealing pressure under the no well pressure condition is 4.05 MPa, as shown in Figure 7-18, which is the contact pressure on the lower ram. Figure 7-19 shows the contact pressure on the sealing rubber strip. High contact pressure is generated on the right convex part of the rubber strip and its bottom, which are in contact with the lower ram, and the wellhead pressure is lower than contact pressure to realize effective sealing. When the wellhead pressure increases, the pressure on the well compresses the rubber strip, so that the contact pressure between the rubber and the ram increases, and the sealing force further increases, so as to realize the sealing and play the role of a sealing aid. The contact pressure is always greater than the auxiliary sealing pressure, and the greater the pressure is, the stronger the rubber's sealing ability is.

#### *7.3.2.1 Floating bottom seal structure*

The structure of floating bottom seal is shown in Figure 7-16(b). There is a space of 0.5 mm in height at the top of the rubber strip. When the lower ram extrudes the sealing rubber strip, the rubber strip has a space to retreat.

As the ram moves, the cutting blade squeezes and cuts the rubber bottom surface, which can easily cause rubber tearing and damage. A floating seal structure is used

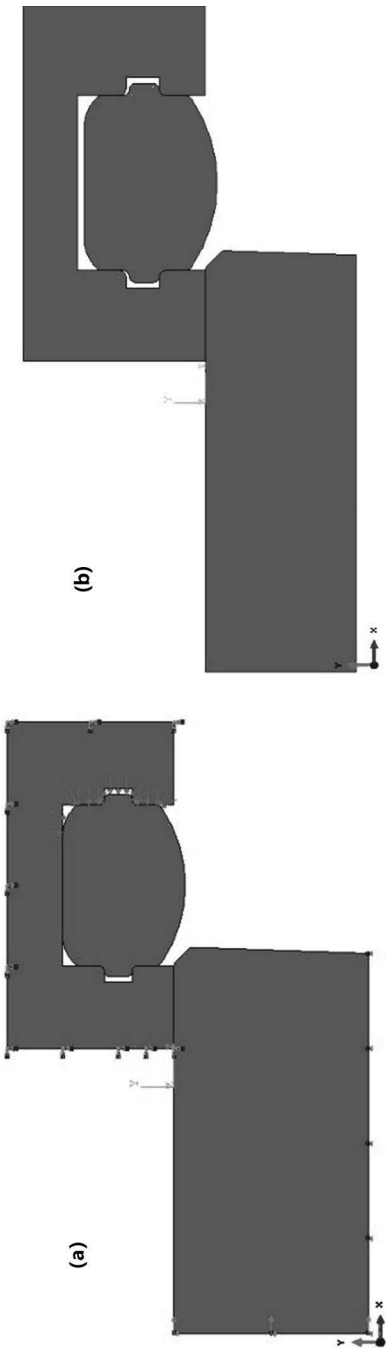


**Fig. 7-16.** A two-dimensional model of the seal structure of the shear ram BOP.

**Table 7-2.** Rubber's material parameters.

| Yeoh | $C_{10}$/Mpa | $C_{20}$/Mpa | $C_{30}$/MPa |
|---|---|---|---|
| 01# | 3.465 | –0.32458 | 5.3805 |

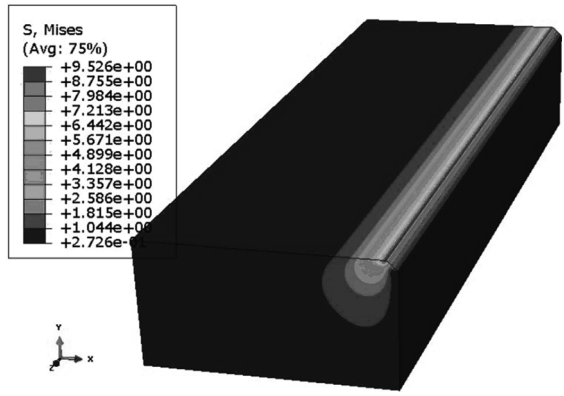


**Fig. 7-17.** The maximum von-Mises stress when the lower ram moves.

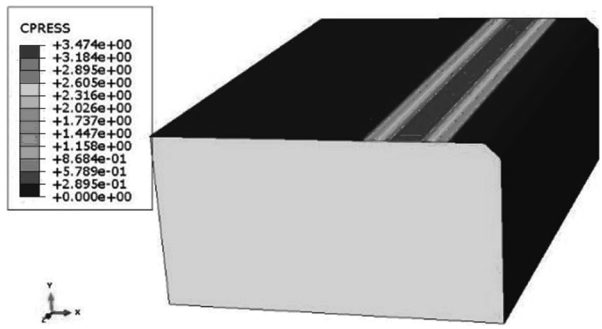


**Fig. 7-18.** The contact pressure on the lower ram.

in the bottom seal. When the ram moves and extrudes the rubber, there is a space to reduce the extrusion shear effect and protect the rubber from being damaged by the ram blade. The maximum shear stress of the non-floating rubber strip is 6.52 MPa, and that of the floating rubber strip is 4.215 MPa, which is 32% less than that of the original structure. Figure 7-20 shows the maximum von-Mises stress when the lower ram moves.

Under the condition of no well pressure, the sealing pressure is 3.879 MPa, which is 5% lower than that on the original structure. Under the condition of well pressure, the well pressure compresses the rubber, which increases the sealing force between the rubber and the ram to realize the sealing. The greater the pressure is, the stronger the sealing ability is. Figure 7-21 is the contact pressure on the lower ram, and Figure 7-22 is the contact pressure on the sealing rubber strip. It can be concluded that the floating sealing structure can not only reduce the extrusion shear damage of the sealing rubber, but also enhance its sealing ability.

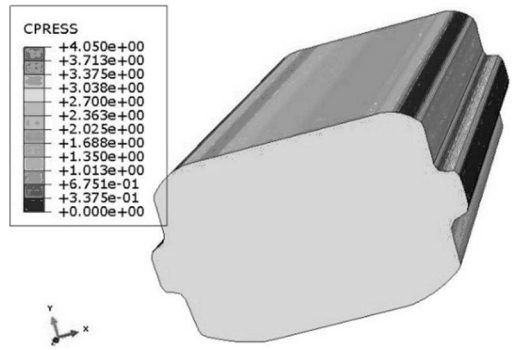


(a) View 1

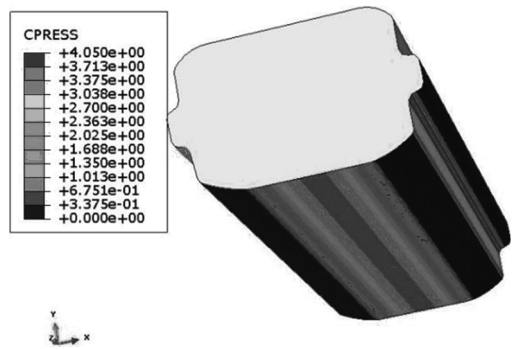


(b) View 2

**Fig. 7-19.** The contact pressure on the sealing strip.

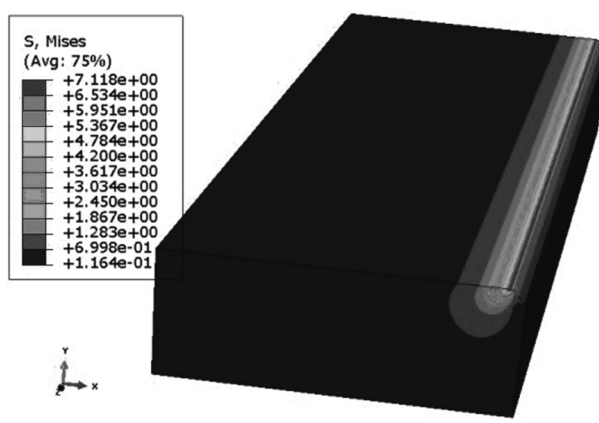


**Fig. 7-20.** The maximum stress value when the lower ram moves.

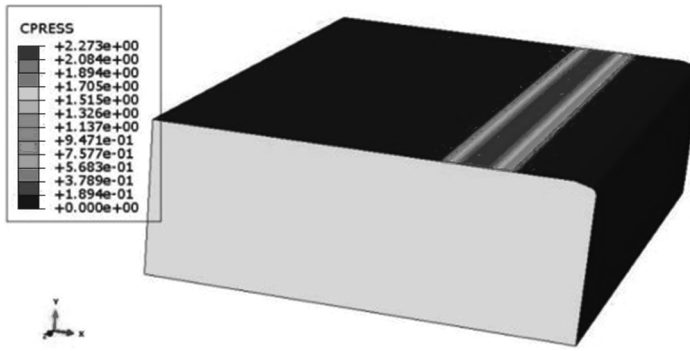


**Fig. 7-21.** The contact pressure on the lower ram.

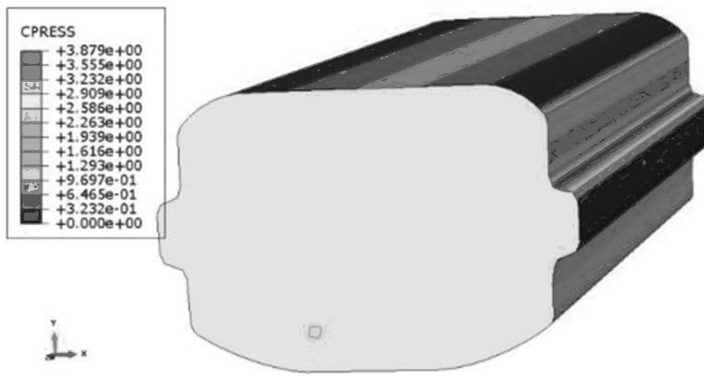


(a) View 1

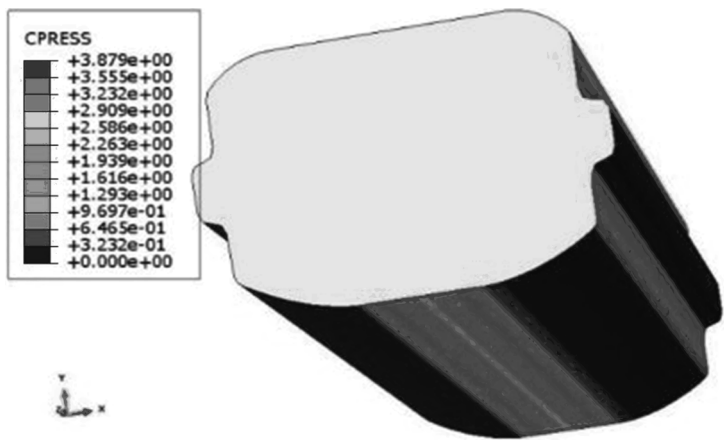


(b) View 2

**Fig. 7-22.** The contact pressure on the sealing strip.

*7.3.2.2 Chamfer of the lower ram*

When the lower ram pushes forward to extrude the rubber, its blade can extrude and shear the rubber. The rubber is easily torn and damaged under the action of shearing. Changing the chamfer of the blade can reduce the shear damage in the process of moving. Taking the floating seal structure for example, the maximum shear stress of the rubber is 3.778 MPa when the chamfer is 15°, which is 8.2% lower than 4.215 MPa when the chamfer is 45°. The rubber is safer and has a longer service life when the optimal chamfer of the lower gate is 15°. Figures 7-23 shows the maximum von-Mises stress on the bottom sealing rubber strip when the chamfer is 15° in the lower ram. Table 7-3 shows the stress peak value of the ram when the edge chamfering of the lower ram is different.

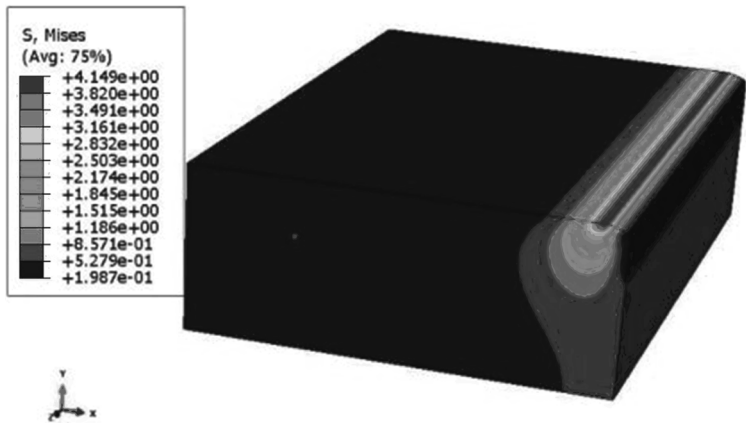


**Fig. 7-23.** The von-Mises stress on lower ram.

**Table 7-3.** The maximum peak stress of rubber and ram under different chamferings of the lower ram blade.

| Chamfer/° | 0 | 15 | 30 | 45 | 60 | 75 |
|---|---|---|---|---|---|---|
| Shear stress of rubber/MPa | 4.125 | 3.778 | 3.883 | 4.215 | 4.159 | 4.131 |
| Von-Mises stress of Ram/MPa | 5.78 | 4.149 | 4.552 | 7.118 | 5.69 | 4.89 |

## 7.4 Rotary BOP

### *7.4.1 Numerical calculation model*

The structural diagram of the sealing core is shown in Figure 7-24(a). The rubber core structure is mainly composed of a rubber core and an iron core. The rubber core is mainly used for sealing and the iron core is mainly used for supporting. When the well fluid intrudes into the cylindrical surface of the rubber core, the iron core can prevent the upper part of the rubber core from being pressed radially. The main sealing surface plays a major role in sealing, which is the first and most important "gate" to prevent leakage. The outer cone and bottom surface make the rubber core press against the drill pipe under the well fluid pressure, and the inner cone will

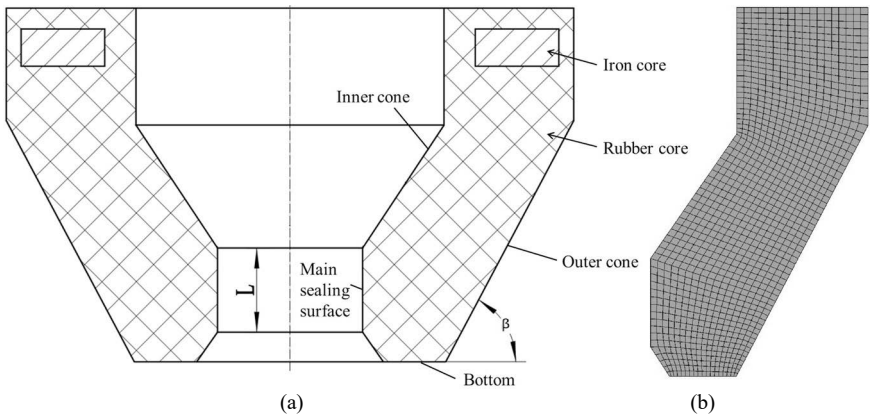


**Fig. 7-24.** A schematic diagram of the rubber core structure.

directly come in contact with the drill pipe to realize the auxiliary sealing function. The length of the main sealing surface of rubber core $L$, the angle of outer cone $\beta$, the friction coefficient $\alpha$, and the well fluid pressure $P$ are all important factors affecting the sealing performance of the rubber core.

A numerical model of rubber core structure is established. The diameter of the main sealing surface of the rubber core is 102 mm, and drill pipe diameter is 127 mm.

The third-order Yeoh model is used, and its coefficients are $C_{10}$ = 3.78 MPa, $C_{20}$ = –4.70 MPa, $C_{30}$ = 7.09 MPa. The sealant core is meshed, and the meshed model is shown in Figure 7-24(b).

## *7.4.2 Results and discussions*

### *7.4.2.1 Effect of the well fluid pressure*

The maximum von-Mises stress on the rubber core under different well fluid pressures is shown in Figure 7-25. The maximum von-Mises stress appears on the joint of the inner cone and the main sealing surface when the well fluid pressure is low ($P$ = 0, 2, 4 MPa). The maximum von-Mises stress appears at the joint of the inner cone and the inner cylindrical surface when the well fluid pressure is high ($P$ = 6, 8, 10 MPa). With the increasing of the well fluid pressure, the growth trend of the maximum von-Mises stress is more gradual in the first stage, and it is steeper when the pressure is greater than 4 MPa.

The maximum contact pressure under different well fluid pressures on the rubber core is shown in Figure 7-26 and the path S is the inner cone and the main sealing surface bus. The maximum contact pressure on the rubber core appears near the contact part of the inner cone and the main sealing surface, and the extreme contact pressure increases with the increasing of the well fluid pressure, the high contact pressure area becomes larger.

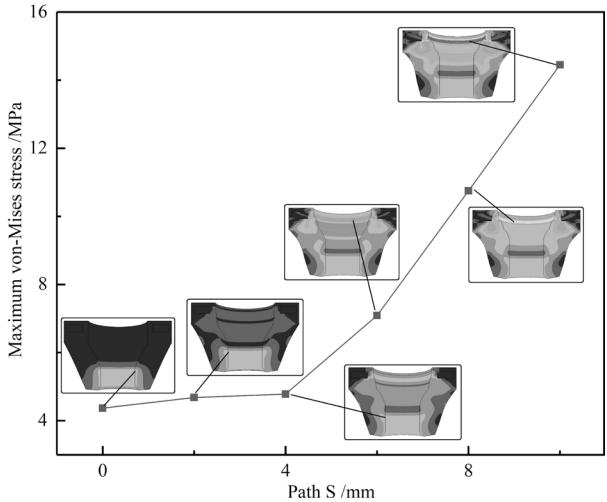


**Fig. 7-25.** The maximum von-Mises stress on rubber core under different well fluid pressure.

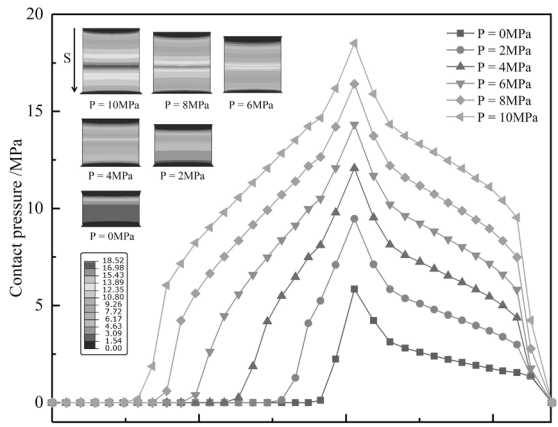


**Fig. 7-26.** The contact pressure on the rubber core under different well fluid pressures.

### *7.4.2.2 Effect of the friction coefficient*

The maximum von-Mises stress on the rubber core under different friction factors is shown in Figure 7-27. The maximum von-Mises stress on the rubber core appears at the joint of inner cone and inner cylinder, and it decreases with the increasing of the friction coefficient. The von-Mises stress on the contact part between the main sealing surface and the inner cone surface decreases with the increasing of the friction coefficient, and the stress change in the other positions is small.

Figure 7-28 shows the contact pressure on the rubber core along the path S under different friction coefficients. The contact pressure first increases and then decreases along the path, and the maximum contact pressure appears on the joint of main sealing surface and inner cone. The extreme value of contact pressure increases the friction coefficient increases.

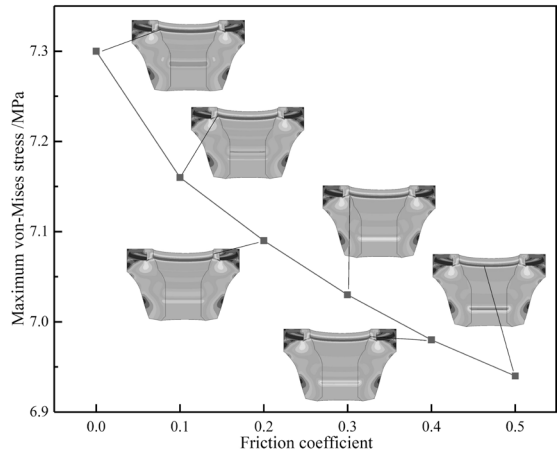


**Fig. 7-27.** The maximum von-Mises stress on the rubber core under different friction coefficients.

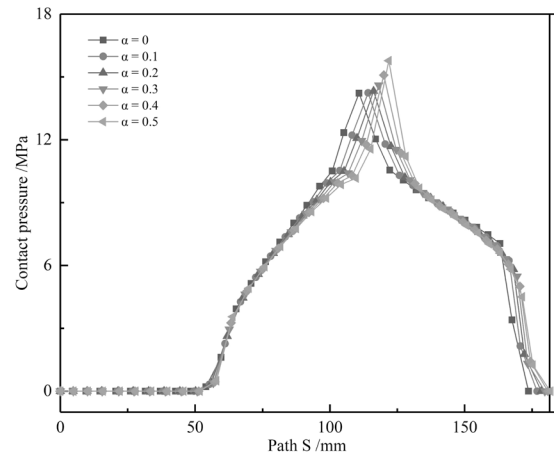


**Fig. 7-28.** The contact pressure on the rubber core under different friction coefficients.

### *7.4.2.3 Effect of length of the main sealing surface*

The main sealing surface is the most critical part of the rubber core sealing, and its structure size will directly affect the sealing performance of the rubber core. Figure 7-29 shows the stress and contact pressure between the length of the rubber core and the main sealing surface. The difference in the maximum von-Mises stress on the rubber core under different lengths of the main sealing surface is very small, which indicates that the length of the main sealing surface has little effect on the mechanical properties of rubber core. From the contact pressure curve, it can be seen that each curve first increases and then decreases. The difference of contact pressure on each curve is small, and the maximum contact pressure extremum on different curves appears on the joint of inner cone and main sealing surface. Effect of the length of the main sealing surface on the mechanical properties and sealing performance of the rubber core is small and almost negligible.

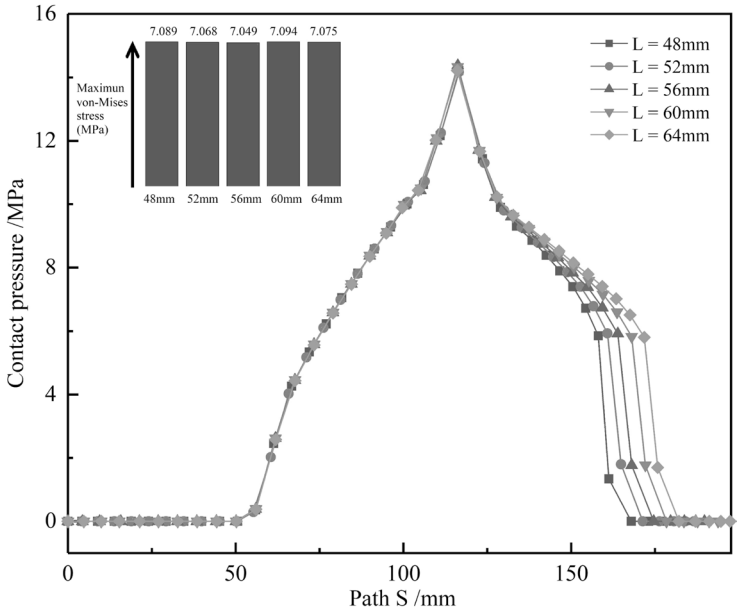


**Fig. 7-29.** Stress and contact pressure on the rubber core under different lengths of the main sealing surface.

### *7.4.2.4 Effect of the outer cone angle*

Figure 7-30 shows the maximum von-Mises stress when there are different outer cone angles. The maximum von-Mises stress decreases with the cone angle of the rubber core.

Figure 7-31 shows the contact pressure on rubber core when there are different outer cone angles. It has a small effect on the contact pressure distribution and pressure value on the rubber core. Therefore, outer cone angle has a greater effect

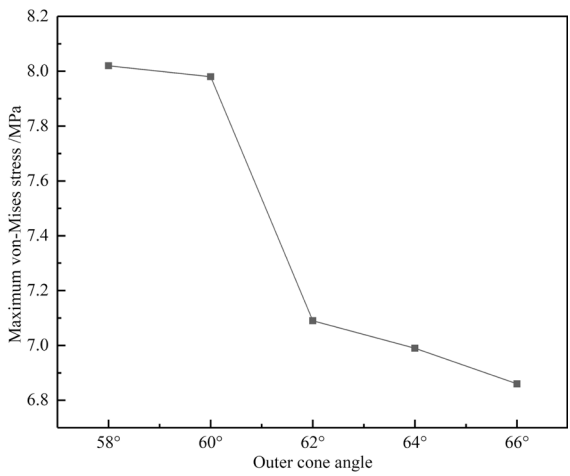


**Fig. 7-30.** The maximum von-Mises stress on the rubber core under different outer cone angles.

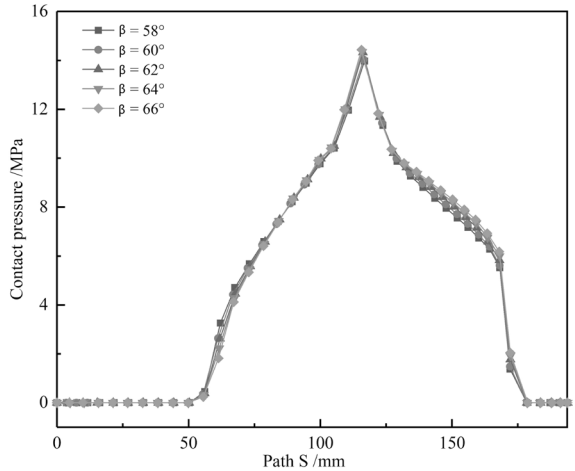


**Fig. 7-31.** The contact pressure on the rubber core under different outer cone angles.

on the von-Mises stress of the rubber core, but have a lesser effect on the contact pressure.

## References

[1] Li Yongping and Jiang Baoyun. 1998. Model XZ-11-05 rotating blowout preventer. Petroleum Machinery 26(10): 33–36 (Chinese).

[2] Dong Yan, Yu Chenglong and Chen Sibo. 2020. Design and laboratory test of new large diameter assembly of DQ-III rotary blowout preventer. Western Exploration Engineering 32(10): 38–40 (Chinese).

[3] Chen ting. 2017. Dynamic Sealing Performance Simulation of Ram Bop Rubber Core Under Pressure. Ph.D. Thesis, Changjiang University, Jingzhou, China (Chinese).

[4] Hu Xia. 2017. Study on Sealing Mechanism of Fz35–105 Ram BOP Rubber Core. Ph.D. Thesis, Changjiang University, Jingzhou, China (Chinese).

[5] Woo, C.S. and Park, H.S. 2011. Useful lifetime prediction of rubber component. Eng. Fail Anal. 18: 1645–51.

[6] Luo, R.K. and Wu, W.X. 2006. Fatigue failure analysis of anti-vibration rubber spring. Eng. Fail Anal. 13: 110–6.

[7] Woo, C.S., Choi, S.S., Lee, S.B. and Kim, H.S. 2010. Useful lifetime prediction of rubber components using accelerated testing. IEEE Trans Reliab. 59: 11–7.

[8] Thakare, M.R., Wharton, J.A., Wood, R.J.K. and Menger, C. 2012. Effect of abrasive particle size and the influence of microstructure on the wear mechanisms in wear resistant materials. Wear. 276: 16–28.

[9] Zhang, S.W. 2004. Tribology of Elastomers. Elsevier Science, New York, USA.

# 8
# Downhole Rubber Packer

## 8.1 Introduction

The packer is an important downhole layered sealing tool in oil and gas well exploitation, which is widely used in completion, fluid injection, fracturing, acidizing, and other processes. At present, the most widely used packers are the compression packer and the expansion packer. The compression packer is compressed and expanded radially by the axial load, and it can achieve sealing after packer contacts with the casing [1]. The rubber cylinder of the expansion packer is filled with fluid pressure, which is deformed and expanded under the pressure, then it comes in contact with the casing to seal the annulus. Figure 8-1 shows the compression packer and expansion packer [2].

The rubber cylinder is one of the core components of the packer [3], and its performance determines service life and reliability. The structural parameters, friction coefficient, and setting load of the rubber cylinder have a great effect on the sealing performance and mechanical performance.

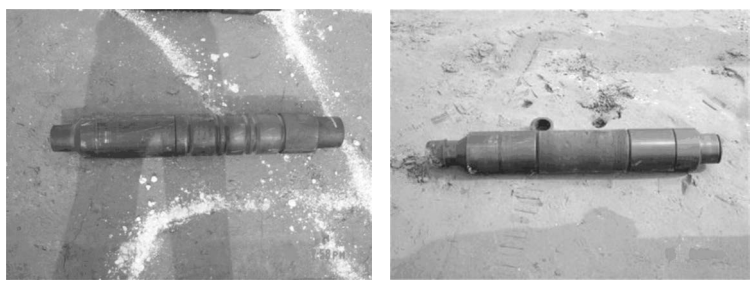

(a) Y111-114 Compression packer (b) K344-110-(114) Expansion packer

**Fig. 8-1.** Compression packer and expansion packer.

## 8.2 Compression packer

### *8.2.1 Finite element model*

The packer's rubber cylinder, center tube, casing, spacer ring, and the other parts are all rotating parts, and the loads received during work are all axisymmetric. A two-dimensional

axisymmetric model is established. The Yeoh model is used. The material constants of the middle rubber cylinder are $C_{10}$ = 0.939841, $C_{20}$ = 0.284971, $C_{30}$ = 0.079314. The material constant of the side rubber cylinder are $C_{10}$ = 1.455628, $C_{20}$ = 1.311081, $C_{30}$ = 0.929566. The parameter size of the compression packer selected is shown in Table 8-1. The finite element model of the middle and three rubber tubes is shown in Figure 8-2.

**Table 8-1.** The packer parameter sizes.

| Part name | Internal diameter (mm) | External diameter (mm) | Height (mm) |
|---|---|---|---|
| Side rubber cylinder | 73.5 | 114 | 85 |
| Medium rubber cylinder | 73.5 | 114 | 70 |
| Central tube | 62 | 73.5 | |
| Spacer ring | 73.5 | 114 | 10 |
| Casing | 124.3 | 139.7 | |

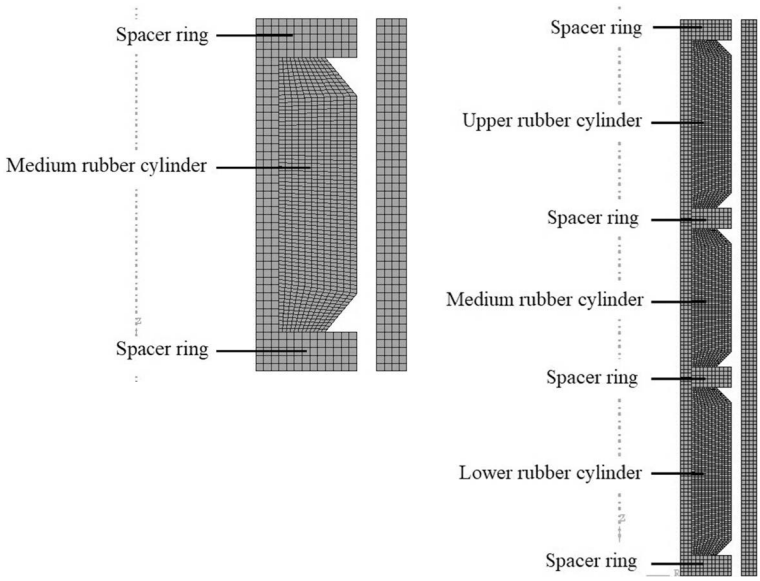


(a) Single rubber cylinder (b) Three rubber cylinders

**Fig. 8-2.** A finite element model of the rubber cylinder.

A fixed constraint is applied to the lower surface of the central pipe, the lower spacer ring, and the casing, and an axial load is applied to the upper surface of the upper spacer ring. The friction coefficient of the contact surface between the upper and lower spacer rings and the central pipe is 0.1. The friction coefficient between the rubber cylinder and casing, center pipe, and upper and lower spacer ring is 0.3.

Model condition assumptions:

1. The plastic tube material is regarded as a volume incompressible material.
2. The influence of temperature change caused by frictional heat on the rubber material is not considered during the working process.
3. The influence of the rubber creep is not considered.
4. The materials used for the center tube, casing, and spacer ring are uniform, continuous, and homogeneous.

### *8.2.2 Effect of structural parameters*

The main structural parameters of the rubber cylinder are the rubber cylinder height, the end face inclination angle and the sub-thickness. Because the sealing function is only the contact surface between the rubber cylinder and the inner surface of the casing, the contact pressure on the surface is discussed. The maximum von-Mises stress and shear stress on the whole rubber cylinder are extracted to discuss the effect of structural parameters on the mechanical properties of the rubber cylinder.

#### *8.2.2.1 Rubber cylinder height*

In Figure 8-3, with the increasing of rubber cylinder height, the length of the contact surface between the rubber barrel and casing's inner wall becomes longer, and the unevenness of the contact pressure's distribution increases. The difference between the contact pressure on loading end and that on the other end of rubber barrel increases, and contact pressure distribution on the middle part of rubber cylinder gradually changes from a straight line to a "concave" curve.

In Figure 8-4, the contact pressure on the rubber cylinder increases with the rubber cylinder height increases from 30 mm to 50 mm. As the packer height continues

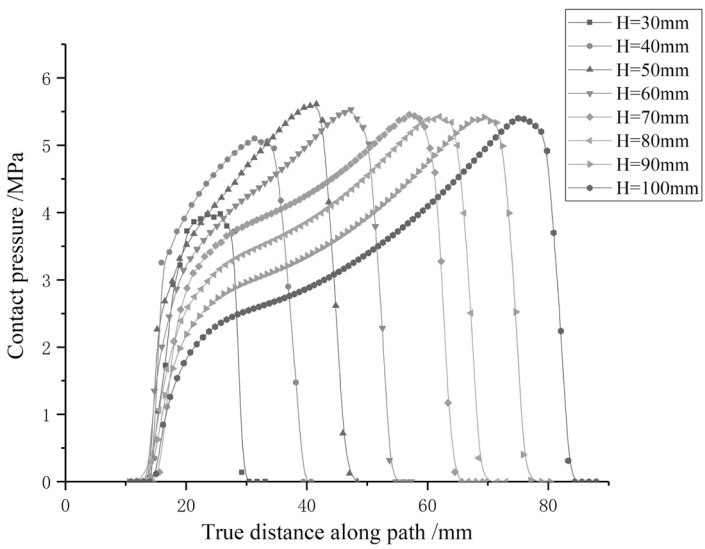


**Fig. 8-3.** The contact pressure distribution on the rubber cylinder with different heights.

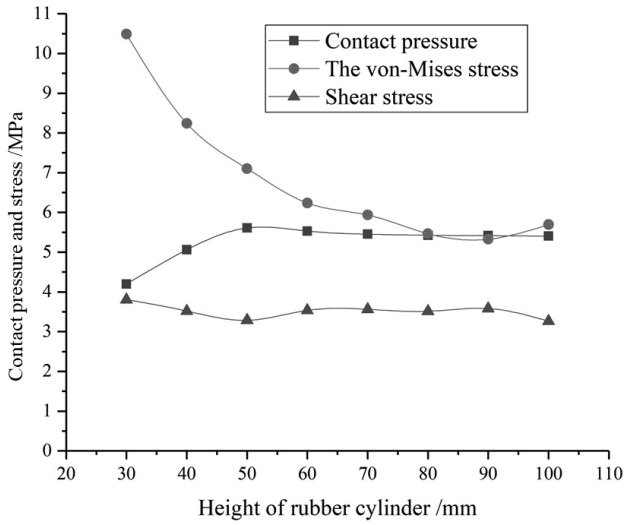


**Fig. 8-4.** The contact pressure and stress on the rubber cylinder with different heights.

to increase, the maximum contact pressure on the packer decreases slowly, and the sealing performance of the packer is affected. When the rubber cylinder height is 90 mm, the von-Mises stress on the rubber cylinder reaches the minimum value. The rubber cylinder height has a small effect on the shear stress.

### *8.2.2.2 End face of the rubber cylinder*

As shown in Figure 8-5, with the increasing of the inclination angle at both ends, the contact length of the rubber cylinder increases. This is because the volume of the rubber cylinder decreases with the increasing of the inclination angle. The volume of the rubber cylinder remains unchanged during the compression process. The greater the inclination angle, the greater the compression distance of the rubber cylinder and the smaller the contact length.

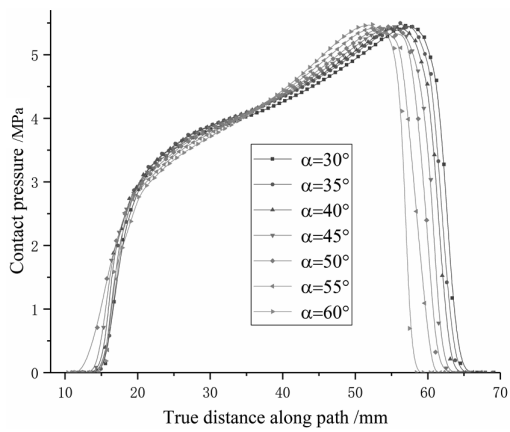


**Fig. 8-5.** The contact pressure distribution on the rubber cylinder with different inclination angles.

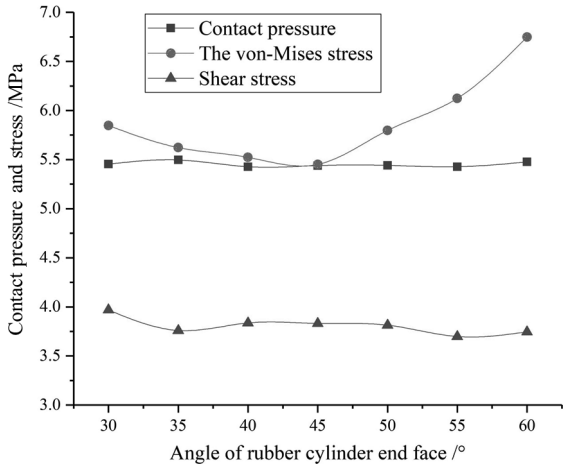


**Fig. 8-6.** The contact pressure and stress on the rubber cylinder at different end face inclination angles.

It can be seen from Figure 8-6 that the inclination angle at both ends of the rubber cylinder does not have a significant effect on the maximum contact pressure on the rubber cylinder. When the inclination angle of both ends is 35°, the maximum contact pressure on the rubber cylinder is slightly larger than that for other angles. When the angle of both ends increases from 30° to 45°, the maximum von-Mises stress on the rubber cylinder decreases, but it increases after 45°. When the inclination angle is 35° and 55°, the shear stress is less than at other angles.

### *8.2.2.3 Rubber cylinder sub-thickness*

It can be seen from Figure 8-7 that with the increase of the rubber cylinder's sub-thickness, the contact pressure on the rubber cylinder at the end far away from the loading end increases obviously. The closer to the loading end is, the contact pressure increases and eventually reaches the maximum value. The contact pressure increases when the rubber cylinder sub-thickness increases, and the contact surface length increases.

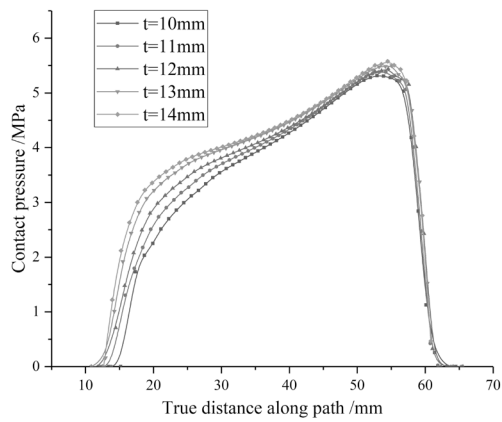


**Fig. 8-7.** The contact pressure distribution of the rubber cylinder under different sub-thicknesses.

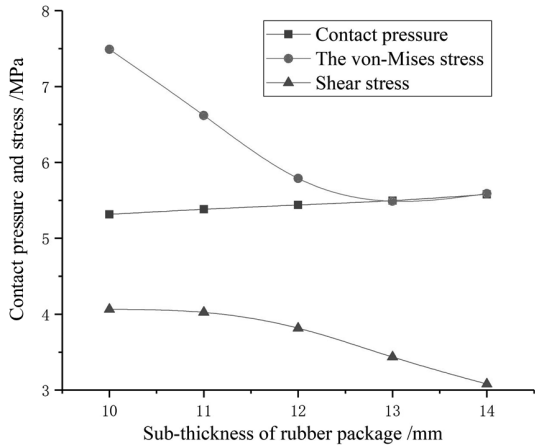


**Fig. 8-8.** The contact pressure and stress on the rubber cylinder under different sub-thicknesses.

In Figure 8-8, the maximum contact pressure on the rubber cylinder increases linearly with the increasing of the rubber cylinder thickness, and the sealing performance of the packer is enhanced. The maximum von-Mises stress on the rubber cylinder decreases gradually, and the decreasing trend becomes slow. The maximum shear stress of rubber cylinder decreases gradually with the increasing of rubber cylinder thickness. And the change rate increases.

*8.2.2.4 Spacer ring diameter at both ends of the rubber cylinder*

In Figure 8-9, with the increasing in the outer diameter of the spacer ring, the contact pressure on the whole contact surface between the rubber cylinder and the inner wall of the casing increases, and the contact surface length changes noticeably.

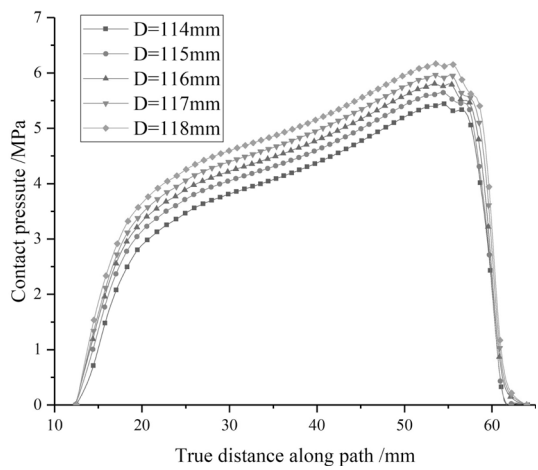


**Fig. 8-9.** Contact pressure distribution on rubber cylinder with different outer diameters of the spacer ring.

In Figure 8-10, the maximum contact pressure increases linearly as the outer diameter of the spacer ring increases, and the sealing performance of the rubber cylinder becomes better. The maximum von-Mises stress on the rubber cylinder does not change significantly. The maximum shear stress on the rubber cylinder increases with the increase in the outer diameter of the spacer ring, but the increase degree is smaller than the maximum contact pressure.

Figure 8-11 shows that the deformation of rubber cylinder with different outer diameters of the spacer ring. With the increase in the outer diameter of spacer ring, the rubber cylinder 'shoulder bulge' phenomenon is alleviated. The reason is that the end of rubber cylinder moves towards the annular space between spacer ring and casing after the rubber cylinder is subjected to axial load. When the outer diameter of spacer ring increases, the annular space becomes smaller, and the gap that can accommodate rubber cylinder becomes smaller, which causing the rubber cylinder being squeezed. The volume flow into the annular space becomes smaller.

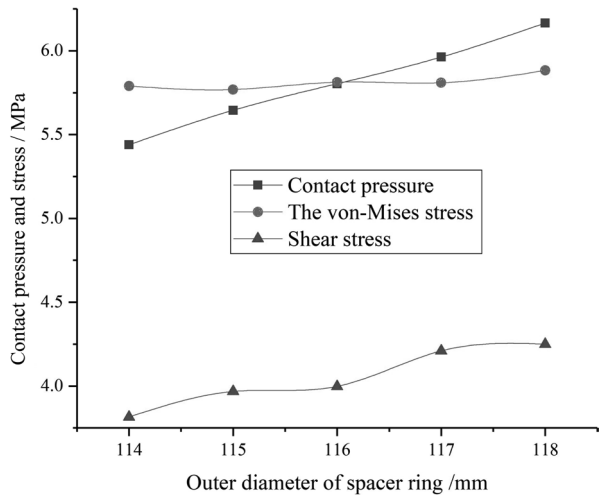


**Fig. 8-10.** The contact pressure and stress on the rubber cylinder with different outer diameters of the spacer ring.

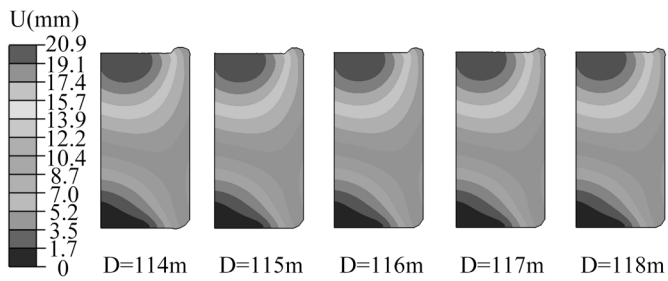


**Fig. 8-11.** The deformation of rubber cylinder with different outer diameters of the spacer ring.

### *8.2.2.5 The friction coefficient*

As shown in Figure 8-12, the contact pressure on the contact surface between the lower rubber cylinder and the inner face of the casing decreases with the increasing of friction coefficient, the length of the contact surface becomes shorter, and the contact pressure curve gradually changes from "saddle shape" to "convex" shape. Then the sealing performance of the upper rubber cylinder becomes worse. The shape of contact pressure curve of the middle rubber cylinder changes, and the difference between contact pressure at the loading end of the middle rubber cylinder and away from the loading end gradually becomes smaller. The contact pressure distribution is more uniform along the path. The contact pressure curve of the upper rubber cylinder is always a "saddle" shape, which is "low in the middle and high at both ends". The contact pressure on both ends of the rubber cylinder is higher and the middle contact pressure is lower, and the contact pressure decreases with the increasing of the friction coefficient.

Figure 8-13 shows the maximum contact pressure on the three rubber cylinders under different friction coefficients. The maximum contact pressure on the three rubber

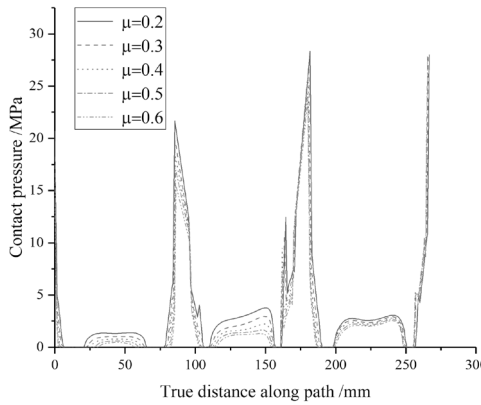


**Fig. 8-12.** The contact pressure curves of the three rubber cylinders under different friction coefficients.

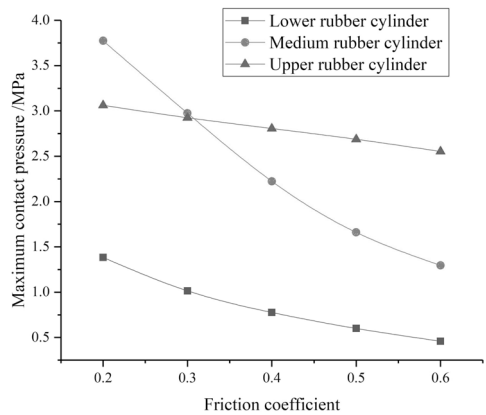


**Fig. 8-13.** The maximum contact pressure with different friction coefficients.

cylinders decreases with the increasing of the friction coefficient. Among them, the maximum contact pressure on the middle rubber cylinder is most obviously affected by the friction coefficient and decreases fastest. The decreasing trend gradually slows down with the increasing of the friction coefficient. The maximum contact pressure on the lower rubber cylinder is least affected by the friction coefficient, and the maximum contact pressure decreases linearly with the increasing of the friction coefficient. The maximum contact pressure on the upper rubber cylinder decreases with the increasing of the friction coefficient, and the decreasing trend gradually slows down.

When the friction coefficient is less than 0.3, the maximum contact pressure on the middle rubber cylinder is greater than that on the upper rubber cylinder, and the middle rubber cylinder plays a major role in the packer sealing process. When the friction coefficient is 0.3, the maximum contact pressure on the upper rubber cylinder is approximately equal to that on the middle rubber cylinder, but the contact pressure curve of the upper rubber cylinder is more uniform. However, when the friction coefficient is greater than 0.3, the maximum contact pressure on the upper rubber cylinder is greater than that on the lower rubber cylinder, and the maximum contact pressure difference on the upper and the middle rubber cylinders increases. The effect of the upper rubber cylinder on the performance of the packer becomes more obvious and plays a major role in the packer sealing in this case.

#### *8.2.2.6 Axial load*

When the friction coefficient of the contact surface between the rubber cylinder and the casing is 0.3, Figure 8-14 shows the deformation of the rubber cylinder under different axial loads. With the increasing of the axial load, the deformation of the rubber cylinder increases. The middle rubber cylinder first contact with the casing and get compacted, and the "shoulder convexity" phenomenon becomes more obvious. Then the upper rubber cylinder comes into contact with the casing, and the lower rubber cylinder finally contacts with the casing.

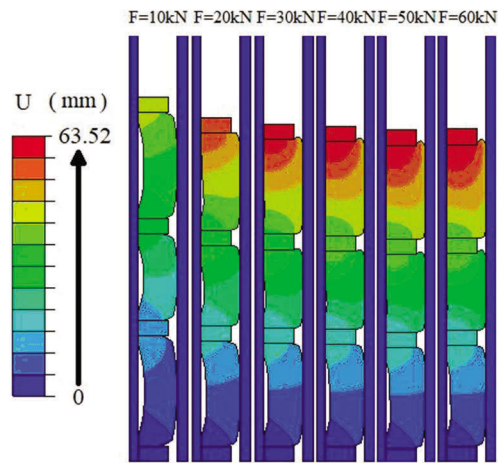


**Fig. 8-14.** Deformation of the rubber cylinder under different axial loads.

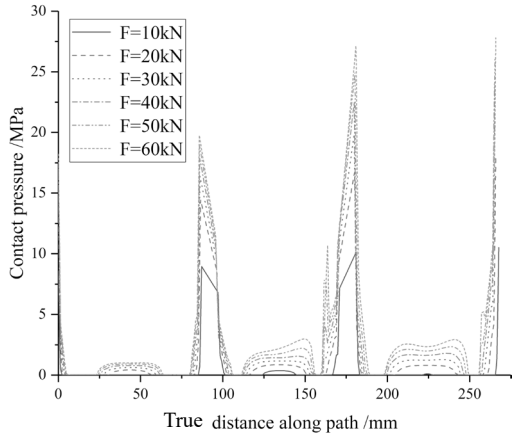


**Fig. 8-15.** The contact pressure curve of rubber cylinder under different axial loads.

Figure 8-15 shows the contact pressure curves of the rubber cylinder. With the increasing of the axial load, the contact pressure and contact length on rubber cylinder increase gradually, the shape of contact pressure curve changes, then the sealing performance of the rubber cylinder is improved. The contact pressure curve of the lower rubber cylinder gradually changes from "convex" shape to "rectangle with fillet at the upper end", and the stress distribution is more average. The contact pressure curve of the middle rubber cylinder changes from "convex" shape to a "rectangle with rounded corners on the upper end" and then to a "saddle" shape with a slight depression in the middle. The stress distribution is more uniform. However, when the load increases to 50 kN, the increase of the contact pressure near the loading end is sharper than that far away from the loading end, and the overall distribution is approximately trapezoidal. This changing trend of the contact pressure distribution curve of upper rubber cylinder with the axial load can also be seen in the middle rubber cylinder.

Figure 8-16 shows the maximum contact pressure between the three rubber cylinders and the casing under different axial loads. The maximum contact pressure

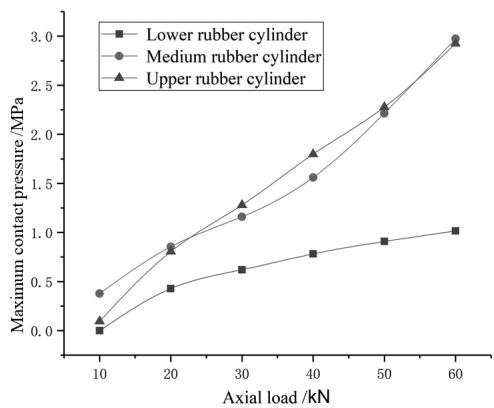


**Fig. 8-16.** The maximum contact pressure on the rubber cylinders under different axial setting loads.

on the three rubber cylinders increases with the increasing of the axial load, and the maximum contact pressure on the upper and middle rubber cylinders is more affected by the axial load than that on the lower rubber cylinder. The increasing trend of the contact pressure on the lower rubber cylinder gradually slows down with the increasing of the load, and finally approaches the linear change. The increasing trend of the contact pressure of the middle and upper rubber cylinders is similar.

## 8.3 Expansion packer

### *8.3.1 Finite element model*

A two-dimensional axisymmetric model was established as shown in Figure 8-17, and the size parameters are shown in Table 8-2.

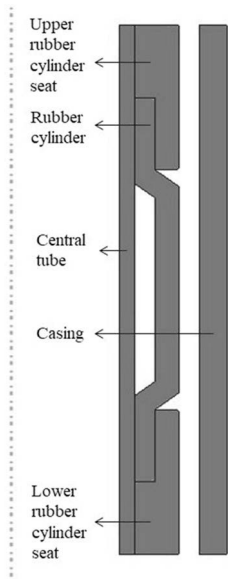


**Fig. 8-17.** A schematic diagram of the calculation model.

**Table 8-2.** The calculation model parameters.

| Structure name | Internal diameter (mm) | External diameter (mm) | Elastic modulus (MPa) | Poisson's ratio | Material constant |
|---|---|---|---|---|---|
| Central tube | 88.5 | 101.6 | 2.1 × 105 | 0.28 | —— |
| Casing | 154.8 | 177.82 | | | |
| Rubber cylinder | 101.6 | 138 | | | |
| Rubber cylinder seat | 101.6 | 138 | —— | 0.49 | $C_{10}$ = 1.53<br>$C_{01}$ = 0.77 |

### *8.3.2 Effect of structural parameters*

#### *8.3.2.1 Inclination of the rubber tube shoulder*

Figure 8-18 shows the contact pressure curve of the rubber cylinder under different shoulder inclination angles. The contact pressure curve between the rubber cylinder and the casing is symmetrically distributed. In the main contact area, the inclination angle of the rubber cylinder shoulder has a small effect on the contact pressure. At the end of the rubber cylinder, when the inclination angle of the rubber cylinder shoulder increases to 45°, the contact pressure changes suddenly, and the position of the contact pressure concentration gradually approaches to the middle with the increasing of the angle.

Figure 8-19 shows the von-Mises stress distribution on the rubber cylinder shoulder under different shoulder angles. With the increase in the inclination angle of the rubber cylinder shoulder, the von-Mises stress concentration area on the rubber cylinder gradually increases, and expands to the contact point between the rubber

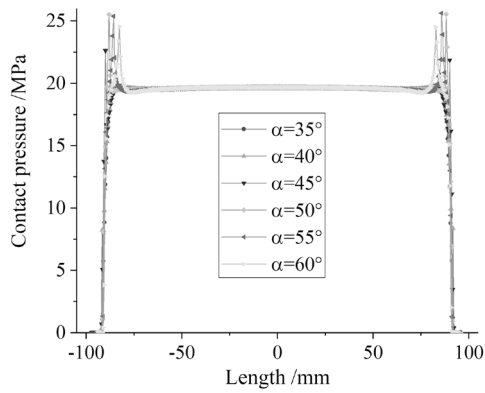


**Fig. 8-18.** The contact pressure curve under different shoulder inclination angles.

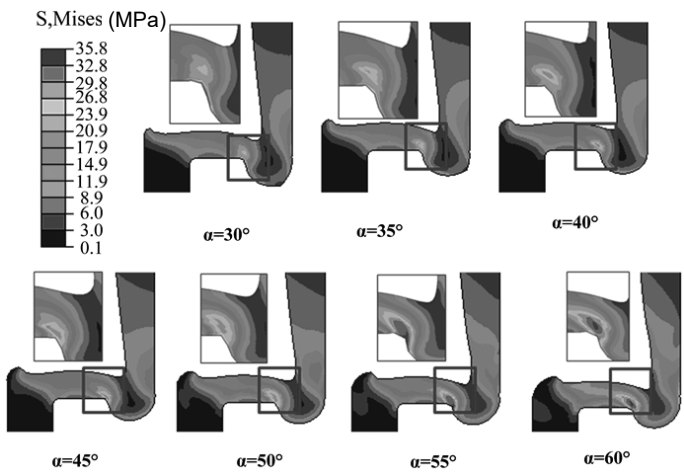


**Fig. 8-19.** The stress distribution on the rubber cylinder shoulder under different shoulder inclinations.

cylinder and the right end of the rubber cylinder seat, and the von-Mises stress also increases. When the inclination angle is less than 35°, there is also a greater von-Mises stress concentration on the contact between the rubber cylinder and the right end of the rubber cylinder seat.

### *8.3.2.2 Thickness*

Figure 8-20 shows the contact pressure curve of the rubber cylinder under different thicknesses. With the thickness of the rubber cylinder increases, the contact pressure distributions between the rubber cylinder and the casing are basically the same. When the thickness is 8 mm, the contact pressure curve of the rubber cylinder is smoother, and the contact pressure between the other two ends is slightly more than the contact pressure on the middle of the rubber cylinder. When the thickness is 12 mm, the contact pressure on the rubber cylinder is slightly lower. Small changes in the thickness of the rubber cylinder have little effect on the contact pressure distribution and size of the rubber cylinder.

Figure 8-21 shows the von-Mises stress distribution on the end of the rubber cylinder with different thicknesses. With the thickness of the rubber cylinder increases, the von-Mises stress concentration area on the rubber cylinder gradually decreases. When the thickness of the rubber cylinder is 10 mm, the maximum von-

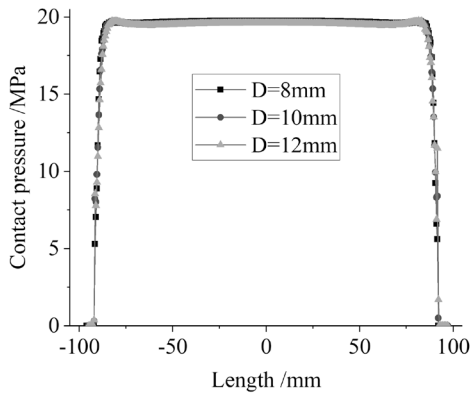


**Fig. 8-20.** The contact pressure curve of the rubber cylinder and casing under different thicknesses.

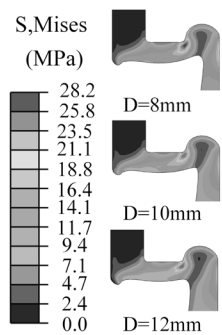


**Fig. 8-21.** The von-Mises stress distribution on the end of a rubber cylinder with different thicknesses.

Mises stress value of the rubber cylinder is 28.2 MPa. When the thickness of the rubber cylinder is 12 mm, the von-Mises stress value of the rubber cylinder is the smallest, 26.3 MPa. When the thicknesses of the rubber cylinder are 8 mm and 10 mm, the von-Mises stress difference is small, but the stress concentration area on the 8 mm cylinder is larger. The change in the von-Mises stress distribution is due to the increasing of rubber cylinder's thickness. Under the same internal pressure, the deformation of the rubber cylinder with a greater thickness is less.

#### *8.3.2.3 Length*

Figure 8-22 shows the contact pressure curve between rubber cylinder and casing with different rubber cylinder lengths. With the increase in the rubber cylinder length, the contact pressure curve undergoes no obvious change. The curves are all slightly convex "saddles" at both ends and like "saddles", and the contact pressure curve in the middle section is flat. The contact pressure increases with the rubber cylinder length increases, but the change amount is less.

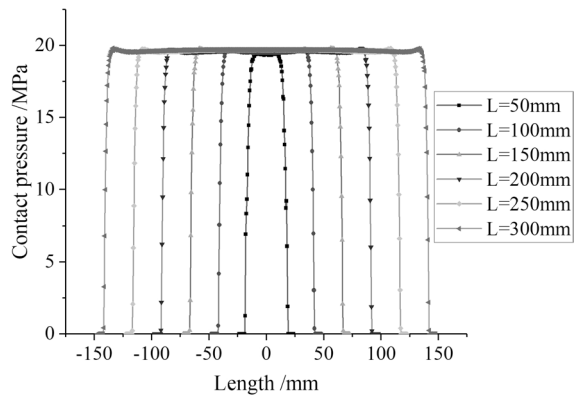


**Fig. 8-22.** The contact pressure curve between rubber cylinder and casing with different lengths.

### *8.3.3 Effect of other parameters*

#### *8.3.3.1 Chamfering of the rubber cylinder seat*

Figure 8-23 shows the contact pressure distribution on the rubber cylinder under different chamfer sizes. The contact pressure distributions of the rubber cylinder are basically the same even with the change in the chamfer size. So, the change of the chamfer size of the rubber cylinder base will not cause the contact pressure between the rubber cylinder and the casing to change noticeably.

Figure 8-24 shows the von-Mises stress distribution on the rubber cylinder's end under different chamfering sizes. The von-Mises stress concentration area is mainly concentrated at the end of the rubber cylinder and the right corner of the rubber cylinder. When the chamfer increases from 0 to 1 mm, the von-Mises stress concentration area becomes smaller and the maximum stress decreases. The stress concentration on the rubber cylinder is alleviated. As the chamfer of the rubber cylinder seat increases, the stress concentration area on the rubber cylinder becomes larger, the von-Mises stress concentration area gradually transfers from the rubber

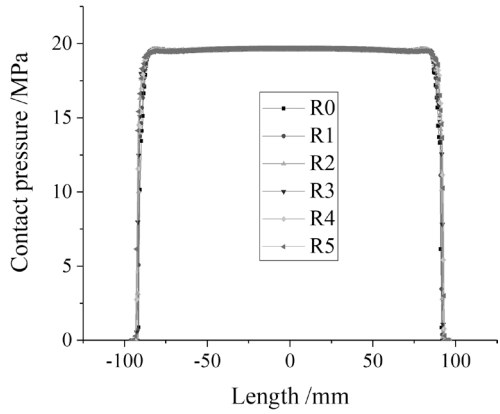


**Fig. 8-23.** Contact pressure curve between rubber cylinder and casing with different rubber cylinder seat chamfer sizes.

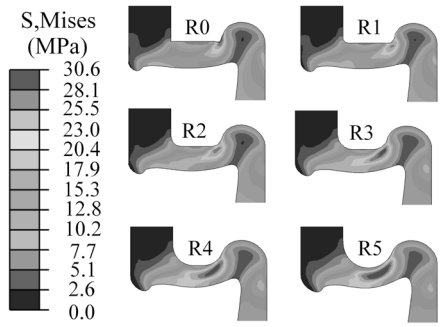


**Fig. 8-24.** The stress distribution on the end of rubber cylinder with different chamfer sizes of the rubber cylinder seat.

cylinder near the outer surface to the inner part of the rubber cylinder, and the degree of the von-Mises stress concentration gradually increases.

### *8.3.3.2 Gap between the rubber tube and the casing*

Figure 8-25 shows the contact pressure curve between rubber cylinder and casing with different distance. As the distance between rubber cylinder and casing increases, the contact pressure distribution between the rubber cylinder and the casing are almost the same. They are all "saddle-shaped" with high ends and a flat middle section. A small change in the distance between the rubber cylinder and the casing has no obvious effect on the contact pressure between the rubber cylinder and the casing.

Figure 8-26 shows the von-Mises stress on the end of the rubber cylinder with different distances. With the increase in the distance between the rubber cylinder and the casing, the stress concentration area on the rubber cylinder shoulder becomes larger and more obvious. A greater distance between rubber tube and casing causes more deformation. Therefore, the distance between packer and casing can be reduced as far as possible.

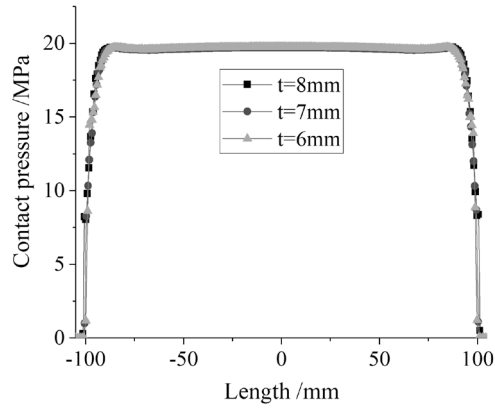


**Fig. 8-25.** Contact pressure curve with different distances between the rubber cylinder and the casing.

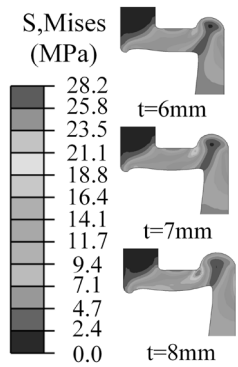


**Fig. 8-26.** Stress with different distances between the rubber cylinder and the casing.

# References

[1] Pan Bo, Wu Wei and Li Decai. 2020. Effect of new anti-outburst mechanism on sealing properties of the packer rubber. Machinery Design & Manufacture (10): 232–235 (Chinese).

[2] Ma Li. 2017. The Mechanical Behavior Numerical Simulation and Revise of Expandable Packer. B.S. Thesis, Xi'an Petroleum University, Xi'an, China (Chinese).

[3] Zhang Zhi, Zhu Xiaohua and Xu Jianbo. 2019. Structural parameters optimization of compression packer rubber based on orthogonal test. Natural Gas Industry 39(03): 80–84 (Chinese).

# Index